

The time structure of extensive air showers of ultra-high energies with the Telescope Array

Rosa MAYTA PALACIOS

*A thesis submitted in fulfillment of the requirements
for the degree of Doctor of Science*

Department of Physics
Osaka City University

February, 2020

Abstract

The extensive air shower, or simply the air shower, is a swarm of particles generated by a high-energy cosmic-ray that hits the atmosphere. Because of their extremely small flux, a direct detection of high-energy cosmic rays is not realistic, and the air shower detection technique is the unique solution to observe them. It is known that the particles in an air shower reach the ground in a rather "thin" structure compared to its lateral spread, and therefore we can determine the arrival direction of the primary cosmic ray from the relative time differences of shower particle arrivals at different positions on the ground. To improve the accuracies in determining the arrival directions and primary energies, the details of air shower structure, including the curvature of the shower front and the thickness of the shower disk as a function of the distance from the center of the shower (the air shower core) are very important, in particular for air showers initiated by ultra-high energy cosmic rays (UHECRs), cosmic rays with energies greater than 10^{18} eV. The center-of-mass energy of the interaction of a UHECR and the atmospheric nucleus is greater than that of the present accelerators (e.g. LHC), and we can only use hadronic interaction models to infer the cosmic ray interaction by extrapolating the accelerator data. Telescope Array constructed in Utah USA is the largest air shower observatory in the northern hemisphere aiming at clarifying the origin of UHECRs. The air showers induced by UHECR above 10^{18} eV can create a large extensive shower in the order of 10^{12} secondary particles. This analysis of temporal shower classified data, that was taken by the Telescope Array Surface Detector from May 2008 to May 2019 that have zenith angle $0 < \theta \leq 60^\circ$. By analyzing the waveforms measured by FADCs, we defined two quantities characterizing the shower structure, the curvature of the shower front and the thickness of the shower disk. This analysis is the first time performed by selecting the data sample of high-quality from the Telescope Array events under several geometrical conditions and energies. Firstly we studied the

curvature of the shower front with the arrival time distribution of particles by using the empirical AGASA function of residual time. Second, it was studied the thickness of shower disk in a sampling region of core distance by using the FADC pulse signals. From both analyses, it was found the features of shower front and shower disk have a clear zenith angle dependence but it was also found an azimuthal asymmetry around its shower axis. This feature of extensive air showers is observed with the same tendency compared with data analysis reported in 2016 by the Auger group. The study of the extensive air showers of UHECRs was studied by analyzing 3 different energy intervals for above in averaged at 10^{19} , $10^{19.30}$ and $10^{19.75}$ eV respectively. It was no found significant energy dependence based on the 3 energy intervals.

Acknowledgements

Firstly, I would like to express my gratitude to Prof. Shoichi Ogio for the privilege of working in the high energy group laboratory and for the opportunity to be part of the Telescope Array Collaboration during the last 3 years, and my sincere thanks to Prof. Yoshiki Tsunesada for his guidance and for his many corrections, support in the present work.

Next I would also like to thank for the entire Telescope Array Collaboration for the helpful discussion. In particular to Dr. Dmitri Ivanov, who is one of the developer of analysis software and for his helpful comments during my analysis. I also express my appreciation to Profs. Charles Jui, John Matthews for their kindly support at during some meetings.

During the analysis work report in the Telescope Array in SD group meeting, I had the opportunity to get the support from the researchers of ICRR, especially I would like to thank Toshiyuki Nonaka, Kazumasa Kawata, Takashi Sako, Eiji Kido, Masahiro Takeda, Toshihiro Fujii, Daisuke Ikeda and Yuichiro Tameda for their co-operation and helpful discussions.

It was sad during my stay to see some members of leaving high energy group OCU from whom I learned much, so my thanks also extend to Prof. Yoshio Hayashi, Dr. Naoto Sakaki, Dr. Bokkyun Shin, and M.Sc. Yoshinori Takagi.

I would also like to thanks the office mates at Osaka City University, Dr. Jihyun Kim and my fellow graduate students, M.Sc. Keitaro Fujita, M.Sc. Yugo Omura, Mr. Ryota Fujiwara, Mr. Yuta Tanou, Mr. Kei Nakai, Mr. Hiroyuki Matsumiya, Mr. Koki Sato, Mr. Yuto Arai and Mr. Ryo Fukushima from whom I learned many things and share good times and good environment.

Finally, I am very grateful to my family especially to my parents Justiniano Mayta and Basilia Palacios for their support and encourage as well as to my sisters and my brother Yolanda, Sonia and Hugo.

The Telescope Array experiment is supported by the Japan Society for the Promotion of Science (JSPS) through Grants-in-Aid for Priority Area 431, for Specially Promoted Research JP21000002, for Scientific Research (S) JP19104006, for Specially Promoted Research JP15H05693, for Scientific Research (S) JP15H05741 and JP19H05607, for Science Research (A) JP18H03705 and for Young Scientists (A) JPH26707011; by the joint research program of the Institute for Cosmic Ray Research (ICRR), The University of Tokyo; by the U.S. National Science Foundation awards PHY-0601915, PHY-1404495, PHY-1404502, and PHY-1607727; by the National Research Foundation of Korea (2016R1A2B4014967, 2016R1A5A1013277, 2017K1A4A3015188, 2017R1A2A1A05071429); by the Russian Academy of Sciences, RFBR grant 16-02-00962a(INR), IISN project No. 4.4502.13, and Belgian Science Policy under IUAP VII/37 (ULB). The foundations of Dr. Ezekiel R. and Edna Wattis Dumke, Willard L. Eccles, and George S. and Dolores Doré Eccles all helped with generous donations. The State of Utah supported the project through its Economic Development Board, and the University of Utah through the Office of the Vice President for Research. The experimental site became available through the cooperation of the Utah School and Institutional Trust Lands Administration (SITLA), U.S. Bureau of Land Management (BLM), and the U.S. Air Force. We appreciate the assistance of the State of Utah and Fillmore offices of the BLM in crafting the Plan of Development for the site. Patrick Shea assisted the collaboration with valuable advice on a variety of topics. The people and the officials of Millard County, Utah have been a source of steadfast and warm support for our work which we greatly appreciate. We are indebted to the Millard County Road Department for their efforts to maintain and clear the roads which get us to our sites. We gratefully acknowledge the contribution from the technical staffs of our home institutions. An allocation of computer time from the Center for High Performance Computing at the University of Utah is gratefully acknowledged.

Contents

Abstract	iii
Acknowledgements	v
Contents	vii
List of Figures	ix
List of Tables	xvii
List of Abbreviations	xix
1 Introduction	1
2 Overview of cosmic ray physics and air shower phenomenon	5
2.1 Energy spectrum of cosmic rays	7
2.2 Acceleration Mechanisms	9
2.3 Possible origins of UHECRs	12
2.3.1 Sites of cosmic ray acceleration	12
2.3.2 Top-down Model	15
2.4 Extensive Air Showers	16
2.4.1 Electromagnetic cascade	19
2.4.2 Hadronic component	21
2.5 Characteristics of EAS	23
2.5.1 Time structure	25
Shower front	25
The thickness of the shower disk	26
2.6 Observation of extensive air shower	28
Surface detector	29
Fluorescence detector	30
3 The Telescope Array	33
3.1 Fluorescence Detector and the energy calibration	35
3.1.1 Event reconstruction and energy determination by FD	38
3.2 The description of Surface Detector	40
3.2.1 Calibrations and trigger judgement	43
Monitoring data acquisition	45
3.2.2 Event reconstruction using surface detectors	47
4 MC simulation and data status	53
4.1 Extensive air shower simulations	53
4.2 Detector simulation	55
4.3 Data and Monte Carlo of TA SD comparison	56
4.4 Resolutions	58
4.5 Event selection and data cuts criteria	59
4.6 Events after passing the selection criteria	63
4.7 Trigger condition of SDs	64
5 Shower front curvature analysis with TA SD data	67
5.1 Time structure of the shower front	67
5.1.1 Definiton of hit time t_{hit}	68
5.1.2 Definition of residual time (t_d)	70
5.1.3 Examples of events shower using TA SD data	72
5.2 Residual time dependence on zenith angle (θ)	77

5.2.1	Residual time parameters A and B	84
5.3	Residual time dependence on zeta angle (ζ)	85
5.4	Results of shower front analysis	87
5.4.1	Curvature of the early part of shower front	87
5.4.2	Curvature of the intermediate part of the shower front	89
5.4.3	Curvature of the late part of the shower front	90
5.5	Results of residual time dependence on zeta angle (ζ)	91
5.6	Results of residual time dependence on energy	92
5.7	Summary of θ , ζ angle and energy dependence	93
6	Shower disk thickness analysis using SD data	97
6.1	Definition of risetime (t_R)	98
6.2	Quality of waveform to determine the risetime	99
6.2.1	Bad quality of FADC signals	103
6.3	Risetime dependence of zenith angle	105
6.4	Analysis of azimuthal angle (ζ)	107
6.5	Thickness of shower disk dependence on ζ	111
6.5.1	Thickness parameter parameterized to zeta angle	113
6.6	Summary of thickness dependence on zeta angle	119
6.7	Thickness of shower disk dependance on energy	122
7	Summary and conclusions	125
7.1	The curvature of the shower front	126
7.2	Comparison of risetime investigation with other experiment	127
7.3	Asymmetry in the curvature of the shower and the thickness of shower disk	129
7.4	Future prospects	132
A		135
A.1	Rise time measured by Haverah Park experiment	135
A.2	Angular resolution	136
A.3	Resolution of core location	137
A.4	Residual time for averaged energy $\sim 10^{19.0}$ eV	138
A.5	Residual time for averaged energy $\sim 10^{19.3}$ eV	139
A.6	Residual time for averaged energy $\sim 10^{19.8}$ eV	140
A.7	Lateral distribution for averaged energy 10^{19} eV	141
A.8	t_R distribution for averaged energy $10^{19.0}$ eV	142
A.9	t_R distribution for averaged energy $10^{19.75}$ eV	143
	Bibliography	145

List of Figures

2.1	The cosmic ray spectrum as a function of energy-per-nucleus, observed from earth compiled using various experiments [21].	8
2.2	The energy spectrum measured by TA experiment derived from 11 years 2008/05/11 to 2019/05/11.	9
2.3	A sketch describing the diffusive shock acceleration. Downstream and upstream show the shocked and yet to be shocked part of the medium respectively. Left panel: in the rest frame of the shock front, the upstream and the downstream are moving at velocity U and $(1/4)U$, respectively. Middle panel: in the rest frame of the upstream gas, the shock front is moving at velocity $(3/4)U$. Right panel: in the rest frame of the downstream, the shock is moving at velocity $(3/4)U$ [24] [27].	10
2.4	Hillas plot of maximum energies of particles accelerated from various objects [29].	13
2.5	Cloud chamber photograph of cascade shower through several thicknesses of material from a an incident proton with energy ~ 4 GeV (1964)[41]	17
2.6	Left: type of secondaries produced when 1st interaction of primary, encoded in track color, red: e^\pm , γ , green: μ^\pm , blue: hadrons. Right: air shower of primary proton of 10^{15} eV simulated.	18
2.7	a) Heitler model for electromagnetic cascade. b) Heitler-Matthews model for hadronic cascade.	20
2.8	a): Lateral Distribution Function at ground level and b): longitudinal distribution of particle density for CR proton of 10^{19} eV. [50]	24
2.9	Scheme of shower front. Left figure: a) representation of front as plane. Right figure: b) shower front representated as curved front.	26
2.10	Scheme of shower front with the representation of the residual time (t_d) and the thickness of the shower disk as (t_R).	27
2.11	Detection of an UHECR by observing an EAS with surface detector and fluorescence detector [56].	28
2.12	Secondary particles initiated by UHECR detection with ground array technique. a) A surface detector used by TA experiment based on plastic scintillation [58]. b) Water Cherenkov detector used by Pierre Auger experiment by observing cherenkov light [59].	29
2.13	Fluorescence detection technique. Fluorescence detection is most accurate method, but duty cycle is $\sim 10\%$ [60].	30
2.14	Telescope Array measurement of the UHECR mass composition. Plot of mean of X_{\max} vs. energy for 10 years of data. The black points with error bars are the data and red and blue points represent the hadronic model predictions for the proton and iron primary particles [61].	31
2.15	Updated mass composition measurements from TA 10 years hybrid data using mean and fluctuations of X_{\max} . The black stars are the data and the colors dots the MC simulated elements presented for energies $10^{18.2} - 10^{19.1}$ eV [63, 64].	32

3.1	Map of the Telescope Array in the western deserts of Utah, USA. The TA experiment is composed by TA surface detector TA-SD (red, closely spaced symbols) and fluorescence telescopes TA-FD (blue symbols) [65].	34
3.2	A description of fluorescence detector technique [60].	35
3.3	The air fluorescence spectrum of two experiments AIRFLY [66] and FLASH [67], range of wavelength is from 290 nm \sim 430 nm. Maximum fluorescence band is 337.1 nm emitting from N ₂ 2P [68]	35
3.4	A picture of BRM FD station (left) with the schematic view of the 2 FD telescope tower (right). Two telescope in one tower, the upper FD views 3° \sim 18.5° and the lower FD views 17.5° \sim 33°. Total 6 towers in a station.	37
3.5	Light track on the camera (left) and an illustration of geometry of an air shower track as viewed by a FD. The color of the light track indicates the sequence of trigger time on each pixel. The track \hat{t} is unit vector which point along the shower in the direction which the shower travels, \mathbf{c} points from the FD to the point on the ground where de shower impacts (core), \mathbf{R}_p is the impact parameter, and ψ in the SDP angle. Each PMT that observes the shower has viewing angle χ_i and triggers at times t_i . The time τ_i is the difference btw the PMT trigger and the light travel time from the shower axis [70, 63].	38
3.6	Calculated longitudinal shower profile. The flux and uncertainty vs. function of shower depth for each tube along the shower detector plane. The solid lines show the simulated flux generated for the best profile fit. Red is the contribution of fluorescence flux, blue the contribution of Rayleigh scattered flux and green is Cherenkov flux contribution [63].	39
3.7	The energy calibration: the plot shows the scatter of E_{FD} versus E_{SD} [71].	40
3.8	Layout of the TA-SD. Square symbol denote 507 SDs. There are three subarrays controlled by the communication towers denoted by triangles. The star symbols represent the FD telescopes [72].	41
3.9	A description by main components of a surface detector deployed.	42
3.10	A cartoon for the description of inside scintillation box with scintillator plates, WLS fibers and PMTs. A total of 104 WLS fibers are laid on each layer to collect and transmit scintillation light to a PMT. Above picture shown the WLS fibers end collected to be connected to a PMT.	43
3.11	Mean energy deposition in a different medium by a vertical muon plotted versus muon kinetic energy. The minimum ionizing energy occurs at 300 MeV (0.3 GeV) [73].	44
3.12	The BR communication tower CT [75].	45
3.13	Sample of monitor data during 26 Sep. 2019 - 04 Oct. 2019 UTC. The number of detected GPSs is shown in the 1 st panel from the top. The 2 nd panel shows the communication status. The 3 rd panel, battery voltage, solar panel voltage and battery current. The temperature measured is shown in 4 th panel. The 5 th and the 6 th panel shows the pedestal value and 1 MIP FADC value, respectively. The 7 th panel describes the Level-0 and Level-1 trigger rate. There is a day-night variation in 1 MIP FADC value which has temperature dependence.	46
3.14	A typical TA SD counter signal monitored over a 10 min cycle from level-0 trigger events obtained as 1-MIP monitor data (yellow area). The black dashed area corresponds to pedestal histogram scaled in the same interval [72].	47

3.15	Example of one shower event recorded in 2019/05/04 $E=10^{19.10}$ eV and direction (θ, ϕ) : $(43.8^\circ, 256.9^\circ)$. The display represents the triggered TA SD, the color shows the relative hit time and the size of circles as proportional to the number of charged particles (VEM).	48
3.16	Side view of shower front at the time t_0 . And the geometry variables description.	49
3.17	(a) : Plot of plane fit (start residual time with respect to the shower plane vs core distance). (b) : Plot of lateral distribution fit to the AGASA function. The color of dots represent the relative hit time as displayed on the event map (Figure 3.15).	51
3.18	TA SD UHECR Energy estimation table [79].	52
4.1	Description of thinning method [80]. The thick and thin solid lines show the primary and secondary particle tracks, respectively.	55
4.2	The distribution of primary energy $E > 10^{18.85}$ eV and zenith angle condition $\theta < 55^\circ$ for data of TA SD and MC SD reconstructed. The comparison corresponds from May 11,2008 to May 11, 2014.	57
4.3	The comparison of reconstructed zenith angle (left) and azimuth angle (right) of data and MC, black and red dots respectively.	57
4.4	The comparison of $\chi_G^2/\text{d.o.f}$ (left) $\chi_{LDF}^2/\text{d.o.f}$ (right) values distribution for data and MC.	57
4.5	Left: Histogram of opening angle, and the blue dash line at 68% for a bin average of energy $E \sim 10^{19.05}$ eV and $\sigma_\theta \simeq 1.2^\circ$. Right: Histogram of resolution of core location for a bin average energy $E \sim 10^{19.05}$ eV and $\Delta R \simeq 140$ m.	59
4.6	Left plot shows angular resolution versus energy. Right plot shows resolution of core location.	59
4.7	Distribution of primary energy in the interval of $10^{19.15} - 10^{19.45}$ eV for data of TA SD and MC SD reconstructed respectively. The comparison corresponds from May 11,2008 to May 11, 2014.	62
4.8	The comparison of reconstructed zenith angle (left) and azimuth angle (right) of data and MC, black and red dots respectively. The distributions are for energy range $10^{19.15} - 10^{19.45}$ eV.	62
4.9	The comparison of $\chi_G^2/\text{d.o.f}$. (left) and $\chi_{LDF}^2/\text{d.o.f}$. (right) distribution for data and MC. The distribution is for energy range $10^{19.15} - 10^{19.45}$ eV.	62
4.10	Distribution of core distance R comparison for data and MC. The distribution is for energy range $10^{19.15} - 19.45$ eV.	63
4.11	Number of SDs hit for low energy range of $10^{18.90} - 10^{19.08}$ eV. For various intervals in $\text{sec}\theta = 1.0 - 2.0$ in step of 0.2.	65
4.12	Number of SDs hit for higher energy range interval $10^{19.15} - 10^{19.45}$ eV. For various intervals in $\text{sec}\theta$ in step of 0.2.	65
4.13	Number of SDs hit for the highest energy interval of $10^{19.45} - 10^{20.05}$ eV. For various interval in $\text{sec}\theta$ in step of 0.2.	65
5.1	Left panel: a typical waveform recorded in TA SD counter, the y-axis represents FADC counts versus number of bin. Right panel: FADC waveform in units of time, the blue line is the hit time.	68
5.2	The arrival time distribution represented by FADC traces of each SD, the three set of plots represent event showers particles delay. Left figure shows an event recorded in 2008-10-09 with direction $\theta = 1.2^\circ$ and $\phi = 350.7^\circ$ and energy $10^{19.1}$ eV. Middle figure shows an event with zenith and azimuth angle of $(\theta, \phi) = (46.8^\circ, 263^\circ)$ with primary energy $10^{19.0}$ eV recorded in 2017-04-15. Right set of plots correspond to an inclined shower event recorded in 2017-02-13, with arrival direction $(\theta, \phi) = (59.5^\circ, 315.3^\circ)$ and energy $10^{19.0}$ eV.	70

5.3	Scheme of shower development in the atmosphere and the parts of curvature of shower front.	71
5.4	Residual time vs. core distance, the y-error bars is the the residual time error measured by Equation (3.10). The red and black line is the simple AGASA fitting function. The color shows the triggered, the latest is marked in red. Event recorded in 2014-07-23 $(\theta, \phi) = (7.9^\circ, 88.6^\circ)$ ($E = 10^{19.38}$ eV)	72
5.5	This event air shower is the highest primary energy found $E = 10^{20.25}$ eV observed with 18 SDs triggered. The left top show the map event display where color bar show the arrival time sequence. Bottom figure shows the lateral distribution fitted with the AGASA LFD function. Right plots show all FADC traces showing the arrival delay.	74
5.6	This plot is the corresponding residual time measured for the large air shower detected versus the distance to core. Primary energy $E = 10^{20.25}$ eV and arrival direction $(\theta, \phi) = (19.6^\circ, 192.4^\circ)$	74
5.7	One event shower sample recorded in 2019-04-18 at 16:42:57.524175 $(\theta, \phi) = (42.9^\circ, 136.9^\circ)$ with primary energy of $10^{19.30}$ eV. Left top: show the event map. Left bottom: Scatter plot of particle density versus distance to shower axis. Right panel: the footprint recorded represented by the waveforms traces.	75
5.8	Distribution of the residual time respect to the air shower plane measured by the event recorded in 2019-04-18 $(\theta, \phi) = (42.9^\circ, 136.9^\circ)$ $E=10^{19.30}$ eV. The red line is the AGASA fitting function for the early hit SDs and the black line the AGASA function fitted for late SDs hit.	75
5.9	This example represents to an inclined event shower $(\theta, \phi) = (50.5^\circ, 314.6^\circ)$ of energy $E = 10^{19.40}$ eV with 14 SDs triggered. Left top figure is showing the event map where the arrow show the direction of UHECR event and the dash line shows the separation from the early and late hits SDs. Bottom left show the particle density versus to core distance. Right panel shows the corresponding FADC traces showing the delay time distribution.	76
5.10	The residual time distribution as function of R for inclined shower $(\theta \sim 50^\circ)$ with $E = 10^{19.40}$ eV, the positive x-axis represents the curvature for early SDs hit and the negative x-axis are the latest arrival particles.	76
5.11	Example of residual time distribution as a function of distance from the shower core for a specific zenith interval in $\sec\theta = 1.18 - 1.20$ ($\theta = 32.1^\circ \sim 33.5^\circ$) including early and late part of shower front. The black dots is the residual time for each SD and blue dots correspond to the average of t_d in an interval of R of 100 m, and the y-axis error bar correspond to RMS.	77
5.12	This set of plots correspond t_d vs. R for zenith angle intervals in $\sec\theta = 1.00 - 1.18$ divided in step of 0.02.	78
5.13	Left plot is an example of residual time distrubution for $\sec\theta = 1.0 - 1.2$ and the two histograms attached to it represents to the distribution of t_d in a bin of 100 m which is shown the red circle.	79
5.14	Left panel is an example of $\sec\theta = 1.8 - 2.0$ inclined event showers. Right plots are the respective histograms of red circles bins of t_d	79
5.15	Residual time distribution in function of distance of core position of an interval of energy $10^{18.90} - 10^{19.08}$ eV and zenith angle interval of $\sec\theta = 1.0 - 1.2$. The red line is the fitted line of AGASA residual time function.	80
5.16	Particle density distribution as function of distance of core position for the interval of energy $10^{18.90} - 10^{19.08}$ eV and zenith interval $\sec\theta = 1.0 - 1.2$ of each SD (black dots) and the blue dots are the average of particle density binned in each 200 m.	80

5.17	Left panel: residual time distribution versus core distance, the red line is the residual time AGASA function fitted from 500 to 2500 m. Right panel: particle density versus distance to core, and the red line is the AGASA LDF fitted to the averaged of ρ binned in intervals of R . From top to bottom various zenith angle, $\sec\theta = 1.2 - 2.0$ in step of 0.2. Corresponding to interval of energy $10^{18.90} - 10^{19.08}$ eV.	81
5.18	Left panel: residual time distribution versus distance to the shower core, the red line is the residual time AGASA function fitted from 500 to 2500 m. Right panel: particle density versus distance to the shower core, and the red line is the AGASA LDF fitted to the averaged of ρ binned in intervals of R . From top to bottom various zenith angle, $\sec\theta = 1.0 - 2.0$ in step of 0.2. Corresponding to interval of energy $10^{19.15} - 10^{19.45}$ eV.	82
5.19	Left panel: residual time distribution versus distance to the shower core, the red line is the residual time AGASA function fitted from 500 to 2500 m. Right panel: particle density versus distance to the shower core, and the red line is the AGASA LDF fitted to the averaged of ρ binned in intervals of R . From top to bottom various zenith angle, $\sec\theta = 1.0 - 2.0$ in step of 0.2. Corresponding to the highest interval of energy $10^{19.45} - 10^{20.05}$ eV.	83
5.20	Parameters A and B as function of $\sec\theta$, blue dots represent for average energies in $\log(E/eV) = 19.0$. Parameter A represents the power-law of curvature shower and B parameter is the power-law of particle density.	84
5.21	Values of χ^2 from the AGASA residual time function fitted and the $\sec\theta$ analyzed in the energies $10^{18.90} - 10^{19.08}$ eV.	84
5.22	Description of early and late SD hits and the zeta angle (ζ) on the shower planes definition. The left figure is a side view of air shower curvature with "early" side, and "late" side. Right figure describes the ζ angle definition representing the early/late part of the shower.	85
5.23	Residual time distribution versus distance of core shower. From left to right, the early part of shower corresponding the interval of zeta angle $ \zeta \leq 60^\circ$, the intermediate part of showers $60^\circ < \zeta < 120^\circ$, and the late part of the curvature $120^\circ \leq \zeta \leq 180^\circ$	86
5.24	Particle density versus distance to core. From left to right plots, particle density for the early, intermediate and the early part of showers. For energy in averaged at $10^{19.0}$ eV. In the interval of zenith $1.0 \leq \sec\theta \leq 1.2$	86
5.25	Parameters A and B as function of $\sec\theta$ for showers of early part of shower front for interval of energy $10^{18.90} - 10^{19.08}$ eV.	87
5.26	The curvature of shower front in function of core distance for "early" part of the shower for 3 intervals of energy. In each plot, the color from light to dark blue represents the $\sec\theta$ binned from vertical to inclined shower respectively. Energy interval in logarithmic scale 18.90 – 19.08 (left), higher energy band 19.15 – 19.45 (middle), and the highest energy band 19.45 – 20.05 (right).	88
5.27	Parameters A and B of residual time function versus $\sec\theta$ for "early" part of the shower.	88
5.28	The curvature of shower front as function of core distance for "intermediate" part of the shower for various zenith intervals. Energy interval in logarithmic scale 18.90 – 19.08 (left), higher energy band 19.15 – 19.45 (middle), and the highest energy band 19.45 – 20.05 (right).	89
5.29	Parameters A and B of residual time function versus $\sec\theta$ for " intermediate " part of the shower.	89

5.30	The curvature of shower front as function of core distance for "late" part of the shower for various zenith intervals. Energy interval in logarithmic scale 18.90–19.08 (left), higher energy band 19.15–19.45 (middle), and the highest energy band 19.45–20.05 (right).	90
5.31	Parameter A and B of residual time function versus $\sec\theta$ for "late" part of the shower for different energy intervals.	90
5.32	Results of constants of p_0 , p_1 of A (left) and p_0 of B (right) respect to the zeta angle ($\cos\zeta$). Top to bottom different energy intervals. . .	91
5.33	Results of constants of p_0 , p_1 of A (left) and p_0 of B (right) respect to averaged energy. Top to bottom different zeta angle intervals. . . .	92
5.34	Curvature of shower front for 5 intervals of zenith angle (by blue color degree, dark blue for large zenith). Top to bottom are for different energy intervals. Left to right presents in different intervals of zeta angle.	93
5.35	Results of A (left) and B (right) parameters for various zenith angle intervals binned. Top to bottom early, intermediate and late zeta angle intervals, each one for 3 bands of energies.	94
6.1	An example of FADC waveforms of one vertical event shower. The black area fill represents the upper layer and the red area is the lower layer of the SD counter.	98
6.2	(Left) Typical FADC waveforms of a TA SD counter as a function of time-bin. The black and red lines represent the upper and lower layers response signals of PMTs of one SD. (Right) The accumulated waveforms of the left figure.	99
6.3	An example of an event map with 16 SDs triggered. Around the map, the waveforms FADC with the integration of signals. The black star mark is the core location and the waveforms correspond to all SDs close to the core. The SDs marked in circles with red represent those weak signals and those with black circles are possible accidental particles.	100
6.4	These plots are the scatter plot is the risetime versus R measured for the upper and lower layer.	100
6.5	The FADC waveforms and the corresponding integration of the weak signals at higher distance to core the color marked match with the map event display.	101
6.6	The FADC waveforms and the corresponding integrated signal, the color marked matches with the map event display.	102
6.7	Example of weak signal (upper panel) and the integrated signal (low panel) the color marked matches with the event map display.	103
6.8	Two example of interrupted waveforms during collecting data at CT. Left figure shows the waveform interrupted after 1 frame at 129 bin and continue at bin 450 ($\sim 9 \mu s$) and collecting this accidental-signal. Right figure is other example when the first FADC signal is weak, the total bins are 1675 which correspond $33.5 \mu s$ and the second big pulse is at bin 1330.	104
6.9	A FADC trace belongs to a high signal pulse, but the signal is interrupted after the 2nd. frame.	104
6.10	The distribution of risetime as function of distance to core for an fix interval of energy of $18.90 \leq \log(E/eV) \leq 19.08$ and zenith angle in $1.0 < \sec\theta \leq 1.1$ ($0^\circ < \theta \leq 24.6^\circ$). Left and right plots correspond to upper and lower layer, the black and the red dots represent the averaged of risetime in a bin of 100 m. Both is fitted with a linear function in R range of 500 - 1200 m.	105
6.11	Mean of risetime for SDs binned in R and $\sec\theta$ for an interval of energy $18.90 \leq \log(E/eV) \leq 19.08$. Left plot is fitted with a linear function in a range of 500 - 1200 m. Right plot is fitted each zenith interval with a quadratic polynomial function in the range 100 to 1500 m. . .	106

6.12	The superposition of results of the slope, a , and the offset, b versus $\sec\theta$ of 3 intervals of energy averaged in $10^{19.0}$, $10^{19.30}$ and $10^{19.75}$ eV.	106
6.13	Particle density distribution averaged as function of core distance binned in bins of 150 m, and various zenith intervals in $\sec\theta$ $1.0 < \sec\theta \leq 2.0$ in steps of 0.2. Lateral distribution of particles in the interval of energy $18.90 \leq \log(E/eV) \leq 19.08$ (left), $19.15 \leq \log(E/eV) < 19.45$ (middle), and $19.45 \leq \log(E/eV) \leq 20.05$ (right).	107
6.14	An event map display with the zeta angle projected on the ground.	108
6.15	An example of ζ distribution for early ($\zeta = -60$ to 60), intermediate ($\zeta = \pm 60$ to ± 120) and late ($\zeta = 120$ to -120) triggered SDs for fix interval in energy $10^{19.15} - 10^{19.45}$ eV and zenith angle $1.0 \leq \sec\theta \leq 1.2$	108
6.16	Histograms of ζ distribution in bins of $\log(E/eV)$ for various zenith angle intervals. Left column of plots show at interval $18.90 \leq \log(E/eV) \leq 19.15$. Middle column of plots show at interval $19.15 < \log(E/eV) < 19.45$. Right column of plots at interval $19.45 \leq \log(E/eV) \leq 20.05$. From top to bottom binned: $1.0 \leq \sec\theta \leq 1.2$, $1.2 < \sec\theta < 1.4$, $1.4 < \sec\theta < 1.6$, $1.6 < \sec\theta < 1.8$ and $1.8 < \sec\theta \leq 2.0$	109
6.17	Scatter distribution of core distance (R) values and azimuthal angle (ζ) in bins of $\log(E/eV)$ for various zenith angle intervals. Left plots correspond to energy interval $18.90 \leq \log(E/eV) \leq 19.15$. Middle plots in bins at interval of $19.15 < \log(E/eV) < 19.45$. Right plots in energy bins $19.45 < \log(E/eV) \leq 20.05$. From top to botom: $1.0 \leq \sec\theta \leq 1.2$, $1.2 < \sec\theta < 1.4$, $1.4 < \sec\theta < 1.6$, $1.6 < \sec\theta < 1.8$ and $1.8 < \sec\theta \leq 2.0$	110
6.18	Scheme of shower shape and the effect of zeta angle projected on the ground.	111
6.19	The scatter plots of the risetime vs. core distance for an interval of the energy of $10^{19.15} - 10^{19.45}$ eV. Divided into 5 intervals of zenith angle from top to bottom in $\sec\theta = 1.0 - 2.0$ in steps of 0.2. From left to right different intervals of zeta angle for "early", $ \zeta \leq 60^\circ$, (left), "intermediate", $60^\circ < \zeta < 120^\circ$, (middle), and "late", $120^\circ \leq \zeta \leq 180^\circ$ (right). Each plot with linear fits in the range of R of 500 - 1200 m.	112
6.20	Thickness parameter a and azimuthal angle ζ , for the interval of energy $10^{19.15} - 10^{19.45}$ eV, and zenith angle band in $\sec\theta : 1.0 - 1.2$. Left plot a vs. zeta, the upper layer FADC traces result (black dots) and the lower layer FADC traces result (red dots). Right plot a vs. $\cos\zeta$, the upper and lower layer results are represented by black and red dots respectively.	113
6.21	The values of offset, b , respect to zeta angle ζ , for the interval of energy $10^{19.15} - 10^{19.45}$ eV, and zenith angle band in $\sec\theta = 1.0 - 1.2$	114
6.22	Thickness parameter a as function of ζ (left plot) and $\cos\zeta$ (right plot) for various $\sec\theta$ for the lower energy interval $10^{18.60} - 10^{18.85}$ eV. Top to bottom plots for intervals of $\sec\theta = 1.2 - 2.0$ in steps of 0.2. The results for upper layer (black mark) and lower layer (red marks).	115
6.23	Thickness parameter a as function of ζ (left plot) and $\cos\zeta$ (right plot) for various $\sec\theta$ for the lower energy interval $10^{18.85} - 10^{19.15}$ eV. Top to bottom for intervals of $\sec\theta = 1.2 - 2.0$ in steps of 0.2. The results for upper layer (black mark) and lower layer (red marks).	116
6.24	Thickness parameter a as function of ζ (left plot) and $\cos\zeta$ (right plot) for various $\sec\theta$ for the lower energy interval $10^{19.15} - 10^{19.45}$ eV. Top to bottom for intervals of $\sec\theta = 1.2 - 2.0$ in steps of 0.2. The results for upper layer (black mark) and lower layer (red marks).	117

6.25	Thickness parameter a as function of ζ (left plot) and $\cos\zeta$ (right plot) for various $\sec\theta$ for the lower energy interval $10^{19.45} - 10^{20.05}$ eV. Top to bottom for intervals of $\sec\theta = 1.2 - 2.0$ in steps of 0.2. The results for upper layer (black mark) and lower layer (red marks).	118
6.26	Thickness parameter (a) versus zeta angle (left) and $\cos\zeta$ (right) for various $\sec\theta$ in each plot. From top to bottom, 4 intervals of energy $10^{18.60} - 10^{18.85}$ eV, $10^{18.85} - 10^{19.15}$ eV, $10^{19.15} - 10^{19.45}$ eV, and $10^{19.45} - 10^{20.05}$ eV. All evaluated for linear fits in a range of 500 - 1200 m.	120
6.27	Thickness parameter a as a function of energy measured by lower layer signals for various $\sec\theta$ intervals. Top plot is the result of early part of shower. Middle plot is the intermediate part of shower. Bottom plot is for late part of shower results.	123
7.1	The evolution of the curvature of shower front for various $\sec\theta$ in lower energy interval of $10^{18.90} - 10^{19.08}$ eV. The area of curvature shows the fluctuation of all event showers in the $\sec\theta$ binned presented by the RMS in the y-error bar and the dots is the average of t_d	126
7.2	Left panel: Risetime calculated by TA SD. Right panel: The risetime measured by AUGER experiment by water-Cherenkov detector.	127
7.3	The asymmetry along the azimuthal angle calculated for 5 intervals in $\sec\theta$ for TA SD (left). Asymmetry measured by Auger experiment (right).	128
7.4	Side view of definition of the azimuthal angle (ζ) (left image) and the front view of the zeta angle projected on the ground. The color shows the early part of the shower (dark purple), intermediate (purple) and late triggered part of the shower (light purple).	129
7.5	Residual time (left) and risetime (right) distribution as function of distance to shower axis. The early shows the dark color, and the late part of shawer shows by the ligh color.	130
7.6	Averaged of residual time and risetime as function of distance to core for energy $10^{19.45} - 10^{20.05}$ eV. Left panel: residual time for early, intermediate and late part of curvature of shower. Right panel: risetime distribution for early, intermediate and late SDs triggered.	131
A.1	Rise time measured by Haverah Park experiment [90].	135
A.2	Histograms of opening angle σ_θ for various energy bins.	136
A.3	Histograms of ΔR for various energy bins.	137
A.4	t_d vs. R profile for energy interval $10^{18.90} - 10^{19.08}$ eV for early(left), intermediate(middle), and late(right) side showers.	138
A.5	t_d vs. R profile for energy interval $10^{19.15} - 10^{19.45}$ eV for early(left), intermediate(middle), and late(right) side showers.	139
A.6	t_d vs. R profile for energy interval $10^{19.45} - 10^{20.05}$ eV for early(left), intermediate(middle), and late(right) side showers.	140
A.7	ρ vs. R profile for energy interval $10^{18.90} - 10^{19.08}$ eV for early(left), intermediate(middle), and late(right) side showers.	141
A.8	t_R vs. R profile for energy interval $10^{18.85} - 10^{19.15}$ eV for 5 intervals of zenith angle and 6 intervals of zeta angle.	142
A.9	t_R vs. R profile for energy interval $10^{19.45} - 10^{20.05}$ eV for 5 intervals of zenith angle and 5 intervals of zeta angle.	143

List of Tables

4.1	Table of TA SD Monte Carlo simulated condition.	56
4.2	List up of shower events collected in 11 years of data by TA SD used in the curvature shower front analysis, listed up by intervals of energy and zenith angle ($0^\circ < \theta \leq 60^\circ$).	63
4.3	List up of shower events collected in 11 years of data by TA SD for the analysis of the thickness of shower disk, listed up by intervals of energy and interval of zenith angle ($0^\circ < \theta \leq 60^\circ$).	64
5.1	Table of functions found of p_0 and p_1 of A and p_0 of B for different energy intervals.	95
5.2	Table of functions found of p_0 and p_1 of A and p_0 of B for different zeta angle intervals.	95
6.1	Summary of function fitted in the a and $\cos\zeta$ for the energy interval $10^{18.85} - 10^{19.15}$ eV for each interval of $\sec\theta$	121
6.2	Summary of function fitted in the a and $\cos\zeta$ for the energy interval $10^{19.15} - 10^{19.45}$ eV for each interval of $\sec\theta$	121
6.3	Summary of function fitted in the a and $\cos\zeta$ for the energy interval $10^{19.45} - 10^{20.05}$ eV for each interval of $\sec\theta$	122

List of Abbreviations

CR	Cosmic Ray
UHECR	Ultra High Energy Cosmic Ray
CMB	Cosmic Microwave Background
AGASA	Akeno Giant Air Shower Array
AGASA LDF	Akeno Giant Air Shower Array Lateral Distribution Function
TA	Telescope Array
TALE	Telescope Array Low Extension
EAS	Extensive Air Shower
GZK	Greisen-Zatsepin-Kuzmin
EeV	10^{18} eV
ZeV	10^{21} eV
FADC	Flash Analog to Digital Converter
SD	Surface Detector
FD	Fluorescence Detector
LHC	Large Hadron Collider
CORSIKA	COsmic Ray SIMulations for KAascade
VEM	Vertical Equivalent Muon
MIP	Minimum Ionizing Particle
LDF	Lateral Distribution Function
GH Function	Gaisser-Hillas Function
CLF	Central Laser Facility (centre of TA site)
IMC	Inverse Monte Carlo (reconstruction method)
GPS	Global Positioning System
CTD	Central Trigger Distributor
Auger	Pierre Auger Observatory

Chapter 1

Introduction

The cosmic ray (CR) is a crucial clue to understand high-energy phenomena in the Universe. One of the goal in the cosmic ray physics is to reveal the origins of cosmic rays by observing their energy spectrum, mass composition, and arrival direction distributions. Cosmic rays in the energy range below about 10^{14} eV are studied with direct observations by balloon-borne or satellite-borne experiments. However, for cosmic rays above 10^{14} eV a large detection area and/or long exposure times are required because of the steep falling primary energy spectrum. A large detection area can be realized with observations of "*extensive air showers* EASs" with ground-based detectors. Such a high energy cosmic ray produces secondary particles through the interaction with the atmospheric nucleus.

The Telescope Array (TA) has been designed to study cosmic rays with primary energy greater than 10^{18} eV by using the hybrid detection technique with the fluorescence detectors (FD) and the surface detectors (SD). The Telescope Array experiment is operating since its complete layout in 2008 allowing a complete and detailed three-dimensional reconstruction of shower front with high space-time resolution. Currently TA SD array is the largest plastic scintillation detector array, and shower geometry reconstruction are using "AGASA functions". But these functions were obtained by smaller air shower arrays than TA, and from studies for low energies than those by TA. Therefore, the studies of these functions by TA SD itself, is important. The Akeno Giant Air Shower Array (AGASA) experiment, which had studied primary cosmic rays of energies above 3×10^{18} eV with a large surface plastic scintillation detector array covering 100 km^2 , presented summarized characteristics of EASs. One of them is an empirical function of shower front curvature, which is

known as the AGASA function of "time delay". From observations, AGASA group proposed an empirical parabolic and axisymmetric function centered around the shower axis. Another formulated feature by AGASA is the shower disk thickness. Since secondary shower particles generated by repeated interactions have different originating altitudes and transverse momenta, the shower as an aggregate of the secondary particles has a lateral extension, and also the particle density distribution behind the shower front has a finite extension. We can parameterize the distribution behind the front as "thickness of the shower disk", and it is larger with increasing the radial distance of the shower axis.

The time structure empirical formulas used by AGASA had been obtained with Akeno 1 km and 20 km² array, which were much smaller than TA SD array, and these were applicable to showers with energies below 10¹⁹ eV. Then, for TA SD we need new formulas applicable to more larger primary energies, based on much higher event statistics and more detailed studies. In this context, shower parameters are studied by using the TA SD data. To determine these features of air showers, here I used timing information measured as FADC traces. One of the observables focused on the arrival time distribution of the shower particles to study the curvature of the shower front. Another feature is the thickness of the shower disk. In this thesis I present the results of these shower properties, and their energy and arrival direction dependencies. The TA SD array covering an area of 700 km² consists of 507 detectors arranged in a square grid on the ground with 1.2 km spacing. Each detector contains two layers of a plastic scintillator, and each layer has an area of 3 m² and a thickness of 1.2 cm. The output signal from a PMT for each layer is digitized by 12bit Flash Analog to Digital Converters (FADC) with 50 MHz sampling rate. The minimum recording time range for a waveform is 2.56 μ s. The judgements of signal recording and event triggering are made based on two different threshold, and the lowest 0.3 minimum ionizing particles (MIP) for level-0 trigger, and the other is 3.0 MIPs for level-1 trigger. When three or more adjacent SDs have the level-1 trigger within 8 μ s window, an event trigger called level-2 trigger is established. All level-0 triggered waveforms within ± 32 μ s from the event trigger time are sent to the DAQ host and stored.

Using 11 years of the SD data from 2008-05-11 to 2019-05-10, I analyzed the

shower front temporal structure. In this thesis, Chapter 2 gives an overview of cosmic rays and extensive air showers, UHECRs physics and review of recent results. Descriptions of the Telescope Array experiment and general analysis of air shower reconstructions for FD and SD data are described in Chapter 3. Chapter 4 is focussed to describe a general air shower simulation and data collected with 11 years observations. Air shower analysis of the shower front curvature and the shower disk thickness are given in Chapters 5 and 6 respectively. Chapter 7 gives discussions and conclusions of this work.

Chapter 2

Overview of cosmic ray physics and air shower phenomenon

The cosmic ray (CR) was discovered by V.F. Hess, an Austrian-American physicist, in 1912. Hess measured the rate of production of ionization (ion pairs $\text{cm}^{-3} \text{s}^{-1}$) as a function of altitude using the electroscope with his balloon experiments reaching over 5 km [1]. Since the total amount of matter from the top of the atmosphere decreases with increasing altitude, and the intensity of radiation from Earth decreases, the result discovered by Hess clearly showed the rate of ionization was some three times that at sea level and concluded that penetrating radiation was entering the atmosphere from outer space. His measurement was also taken at night showing that the Sun is not the only source of radiation, thus, the ionizing radiation permanently are hitting the Earth's atmosphere.

Over the next two consecutive decades, with the invention of Geiger counter enabled later the discovery of the extensive air showers (EAS) by P. Auger [2] which are secondary nuclei generated by the primary cosmic rays generated in the atmosphere. Further studies of cosmic rays radiation led to the discovery of new exotic particles such as positron, muon, and pion (later also kaon and sigma). The existence of some of these particles had been predicted by pioneering efforts in quantum physics (e.g. [3]), and these experimental discoveries (e.g. positron, [4] and muon [5]) provided the necessary basement for successful development of the theory. Experimental particle physics emerged as a consequence of the discovery and study of cosmic rays.

Later lead to the discovery of ultra high energy cosmic rays (UHECRs) typically

carry energy over 10^{18} eV and while more higher are very rare. An ultra high energy primary produces a cascade of secondary particles, EAS, in the atmosphere of the Earth, and the secondary particles reach the ground level, which makes it possible to obtain the information of the primary particle using an array with separated detectors on the ground. B. Rossi [6] pioneered the surface detection technique, and later the ground array experiment called Volcano Ranch detected primary cosmic ray particles above 10^{20} eV [7].

At the present, the highest energy given to particles accelerated at the most powerful accelerator on Earth is around only 10 TeV by the Large Hadron Collider [8], while the highest energy cosmic ray observed so far is above 10^{20} eV. The detection of ultra-high energy particles resulted in substantial theoretical and experimental efforts aimed at establishing their sources and the mechanisms of the acceleration and the propagation from their sources to the Earth. These tasks are currently addressed by measuring and interpreting the primary cosmic ray energy spectrum (flux), the mass composition, and the arrival directions. Such measurements are made indirectly by observing and reconstructing the extensive air showers.

Over the past 50 years, a big experimental challenge was found from an important theory in ultra high energy cosmic rays. In 1966, Greisen [9], and Zapsepin and Kuzmin [10] predicted a strong suppression (GZK cutoff) in the cosmic ray flux at 6×10^{19} eV due to pion production through the Δ resonance in the interaction of protons with the cosmic microwave background of the 2.4×10^{-4} eV CMB radiation ($p + \gamma_{CMB} \rightarrow \Delta \rightarrow \pi + p$) [11, 12, 13], which corresponds to $2.7 K = 2.4 \times 10^{-4}$ eV blackbody radiation [14].

For that purpose, several early experiments were carried out as the Volcano Ranch [7], SUGAR [15] and Yakutsk [16] reporting events above the 6×10^{19} eV threshold challenged. The High Resolution Fly's Eye (HiRes) experiment implemented an air fluorescence technique pioneered Cornell university [17], and HiRes reported seeing an event of energy 3×10^{20} eV, which is the highest measured particle energy to date. In the cosmic ray field, such primaries are called *super-GZK* particles. Later, with higher statistics sample of $> 10^{19}$ eV to prove the existence of the GZK cutoff was a pressing challenge for this research field. The first experiment, sufficiently large to measure cosmic ray flux at $E > 10^{19}$ eV, was the Akeno Giant Air

Shower Array (AGASA) [18] (with an area of 100 km²). The experiment reported a continuing unbroken spectrum beyond the predicted GZK threshold [19]. On the other hand, HiRes was operated for nine years (1997-2006) collecting accumulative exposure more than twice that collected by AGASA above the GZK threshold, and reported the existence of the GZK cutoff in the resulting cosmic ray spectrum [20]. Therefore, the results and the statements by these two experiments contradicted. In order to solve this contradiction, these two experiment groups joined to make a collaboration called "Telescope Array (TA)" with their experimental skillful techniques, a scintillation detector array by AGASA and fluorescence telescopes by HiRes, the TA collaboration carries out a huge "hybrid" experiment.

At present, the ultra high energy cosmic rays (UHECR)s considered with energies $> 10^{18}$ eV are still not fully understood, the aim of the present experiments of the TA in the northern hemisphere and Pierre Auger Observatory in the southern hemisphere experiments is to reveal the mysteries by observing the spectrum, the anisotropy and the mass composition of UHECRs with hybrid detectors.

2.1 Energy spectrum of cosmic rays

The differential cosmic ray spectrum is given in Figure 2.1. The CR flux decreases by approximately 30 orders of magnitude over 12 decades from about 1 particle cm⁻² s⁻¹ for energies $E \sim 100$ MeV to in a 1 km² detector, ~ 1 particle per day for $E > 10^{18}$ eV, ~ 1 particle per year for $E > 10^{19}$ eV, and ~ 1 particle per century for $E > 10^{20}$ eV. The energy spectrum form is,

$$dN/dE \propto E^{-\alpha}, \quad (2.1)$$

where α is the index of the spectrum and shows the steepness of the falling of the flux. The energy spectra is measured by direct detection with balloon space and through the extensive air showers (EAS) by indirect detection of cosmic rays with ground-based observations. The flux has been scaled by $E^{2.6}$ for a better visualisation of some of detailed features. The flux drops at the rate of ~ 2.6 orders of magnitude per energy decade from the solar energetic particle origin (the lowest

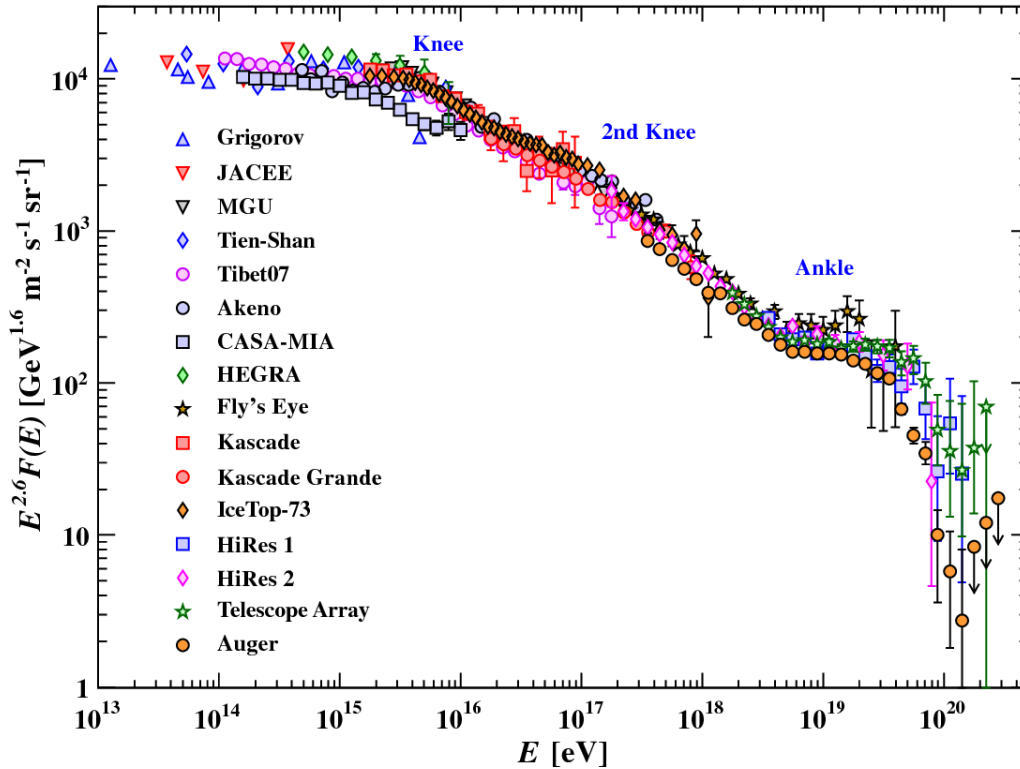


FIGURE 2.1: The cosmic ray spectrum as a function of energy-per-nucleus, observed from earth compiled using various experiments [21].

energy region of the spectrum) until to the "knee" at $E \simeq 3 \times 10^{15}$ eV. The spectrum gets steeper with α increasing to 3 at higher energies than knee. Cosmic rays at the knee energy arrive on the Earth's atmosphere at the rate of ~ 1 particle $\text{m}^{-2}\text{yr}^{-1}$ and are studied with ground based experiments such Tibet AS γ array, which is currently working with enough efficiency at the knee energy. The exact location of the knee is also considered to depend on the particle species, as particles with the higher charge peaks at the higher energies. It is believed that the origin of these cosmic rays around "knee" is associated with galactic objects such as supernova remnants (SNRs). Another characteristic of Figure 2.1 is known as "second knee" at $\sim 8 \times 10^{16}$ eV which makes the spectrum even steeper, and this steepening can be explained by the idea that this structure is due to the knee of heavy primaries [22].

At $10^{18.69}$ eV another structure called "ankle", a flattening of the spectrum decreasing the index from $\alpha = 3.28$ to 2.68 [23] with increasing energy, recently reported from TA surface detector data of 11 years. Figure 2.2 shows this result, multiplied E^3 to zoom up the features at the ankle and at higher energies. The solid line is a fit with the broken power law, where slopes are represented by p_1 , p_2 and

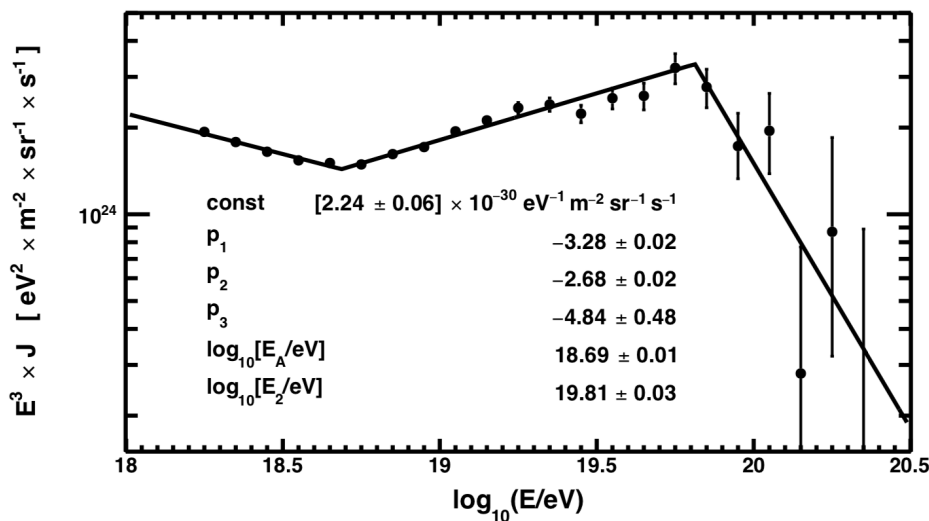


FIGURE 2.2: The energy spectrum measured by TA experiment derived from 11 years 2008/05/11 to 2019/05/11.

p_3 . The second break point was found at $E = 10^{19.81}$ which is expected as the GZK cutoff [9, 10] where the spectrum become even steeper to $\alpha = 4.84$.

2.2 Acceleration Mechanisms

The acceleration of cosmic rays is generally explained by the repeated crossing of charged particles in astrophysical shocks. It was proposed by Fermi in 1949 [24], and depending on the geometries of moving plasma, the two processes known as the *first* and the *second order* Fermi accelerations are defined. Both acceleration mechanisms predict a power-law cosmic ray energy spectrum. However, the *first order* is the most promising one to explain the ultra-high-energy cosmic ray flux, even though it does not manage to predict the observed spectral index [25]. The *diffusive shock acceleration* is a realistic model based on astrophysical the *first order* Fermi acceleration.

The diffusive shock acceleration involves the propagation of a strong shock in the interstellar medium, in which a particle gains an energy by a bouncing off a random magnetic turbulence. The shock can be defined as a non-linear disturbance that transfers energy and momentum to the particle. A downstream, an upstream and a shock front region are shown Figure 2.3. The definitons of the condition in

three different frames of reference are shown in this Figure 2.3. The shock front is defined as the boundary of the shock. The downstream is the shocked part of the medium, while upstream is the region where the shock has not interacted with the medium yet. In the rest frame of the shock front, it can be seen that the upstream approaches at speed U towards the shock front. The mass is conserved through the shock front and so $\rho_1 v_1 = \rho_2 v_2$, where, ρ_1 , ρ_2 and v_1 , v_2 being the mass densities and the velocities of the upstream and the downstream, respectively. If we assume the shock front is in a fully ionized monoatomic ideal gas, the specific heat ratio (γ) of the medium is $\gamma = 5/3$. In a strong shocks, the compression factor results in $\rho_2/\rho_1 \approx (\gamma + 1)/(\gamma - 1) = 4$ (more details in [26]). Therefore, one gets $v_2 = (1/4)v_1 = (1/4)U$ (as seen in Figure 2.3). In the rest frame of the upstream gas, the downstream approaches the shock front at speed $|v_1 - v_2| = (3/4)U$. This is the

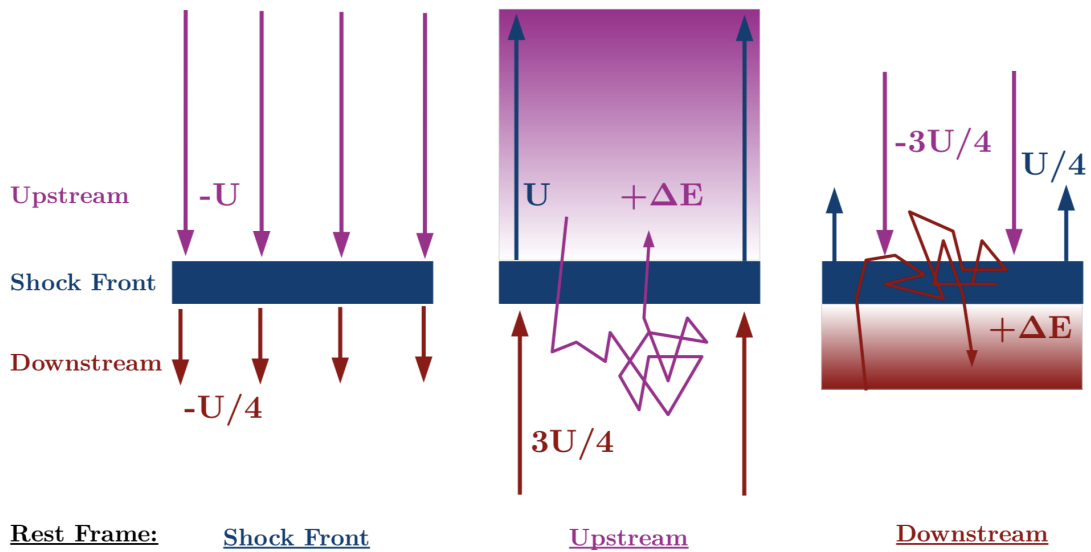


FIGURE 2.3: A sketch describing the diffusive shock acceleration. Downstream and upstream show the shocked and yet to be shocked part of the medium respectively. Left panel: in the rest frame of the shock front, the upstream and the downstream are moving at velocity U and $(1/4)U$, respectively. Middle panel: in the rest frame of the upstream gas, the shock front is moving at velocity $(3/4)U$. Right panel: in the rest frame of the downstream, the shock is moving at velocity $(3/4)U$ [24] [27].

same the rest frame of the downstream, where the upstream is seen as approaching in speed $(3/4)U$. In this case, a particle always gain an energy when even the particle crosses at the shock front from the upstream to the downstream and returns to the

upstream bounced by the downstream magnetic field. It can be shown that in the single round trip cycle around the shock front the particle's averaged energy gain is,

$$\left\langle \frac{\Delta E}{E} \right\rangle = \frac{4V}{3c}, \quad (2.2)$$

where $V = (3/4)U$ is the velocity of the downstream gas in the rest frame of the upstream (*i.e.*, in the laboratory frame) [28]. After each crossing, the average energy of the particle can be defined as $\langle E \rangle = \beta \langle E_0 \rangle$, where E_0 is the initial energy and β is a dimensionless constant. Now we define the probability of the particle remaining in the system after each crossing is P . Taking into account turbulent magnetic fields formed as a result of instabilities in the medium, which allow particles to cross the shock, a particle crosses the shock front k times. Then the average energy of the particle reaches $\langle E \rangle = \beta^k \langle E_0 \rangle$, and the number of particles remaining in the system will be $N = P^k N_0$. Where N_0 is the initial number of particles. Combining these two relations one can obtain the number of particles remaining in the system after k crossing with energy E as:

$$\frac{\ln(N/N_0)}{\ln(\langle E \rangle / \langle E_0 \rangle)} = \frac{\ln P}{\ln \beta}. \quad (2.3)$$

Using the Equation 2.3 and a relation between the integral spectrum $N = N(\geq E)$ and the differential spectrum $n(E)$, $N = \int_E^\infty n(E) dE$, one can obtain the following power-law relation,

$$n(E) dE \propto E^{-1 + \ln P / \ln \beta} dE. \quad (2.4)$$

The value of β can be obtained as $1 + U/c$ using the Equation (2.2). It can be calculated that the number of particles crossing the shock front with relativistic speeds is $\rho c/4$, where c is the velocity of light and n is the number density of particles. It can be seen from Figure 2.3 that the number of particles advected away in the downstream region would be $\rho U/4$. Therefore the probability of escaping the system is U/c and hence the probability of remaining in the system would be $P = 1 - U/c$. Putting the values of β and P back in Equation (2.4), one would get the power law index of -2 for non-relativistic shocks, where $U \ll c$. Since by the Equation (2.2) that the energy gain is proportional to the velocity of the shock, this

process is called the first order Fermi acceleration. In the case of the second order Fermi acceleration, the energy gain is proportional to the square of the velocity of the shock. This is caused by an assumed geometry of an acceleration site such as a definite size of a moving magnetized cloud. In the case of the first order Fermi acceleration, we generally assume that the shower front is infinitely two-dimensional plane, the depth of the downstream region is infinite and particles return to the upstream region with probability P . Details can be found in [28].

2.3 Possible origins of UHECRs

Origins of UHECR are still unknown. There are two different types of proposed models for the explanation of the existence of UHECRs. One idea to explain the origin of UHECR is that they are accelerated by astrophysical objects, and this "bottom-up" model is widely discussed and accepted by the scientific community. The other idea is associated with new physics beyond the standard model, and it is known as "top-down model".

2.3.1 Sites of cosmic ray acceleration

Cosmic rays can be accelerated via Fermi mechanisms as described in the previous section 2.2 in various known astrophysical environments. The main requirement here is that the particle's Larmor radius of gyration in the magnetic field presents around a source cannot exceed the physical size of the source for the acceleration. The Larmor radius is defined as the radius of the circular motion of a charged particle in a uniform magnetic field. The maximum attainable energy (E_{\max}) for a particle with this scenario is given by the following equation,

$$E_{\max} = Ze\beta cBL, \quad (2.5)$$

where the particle of charge Ze is moving at velocity βc in a magnetic field of B of an object of scale length L . For a given source property particles with larger Z , and such as heavier nuclei can be accelerated to higher energies than lighter nuclei.

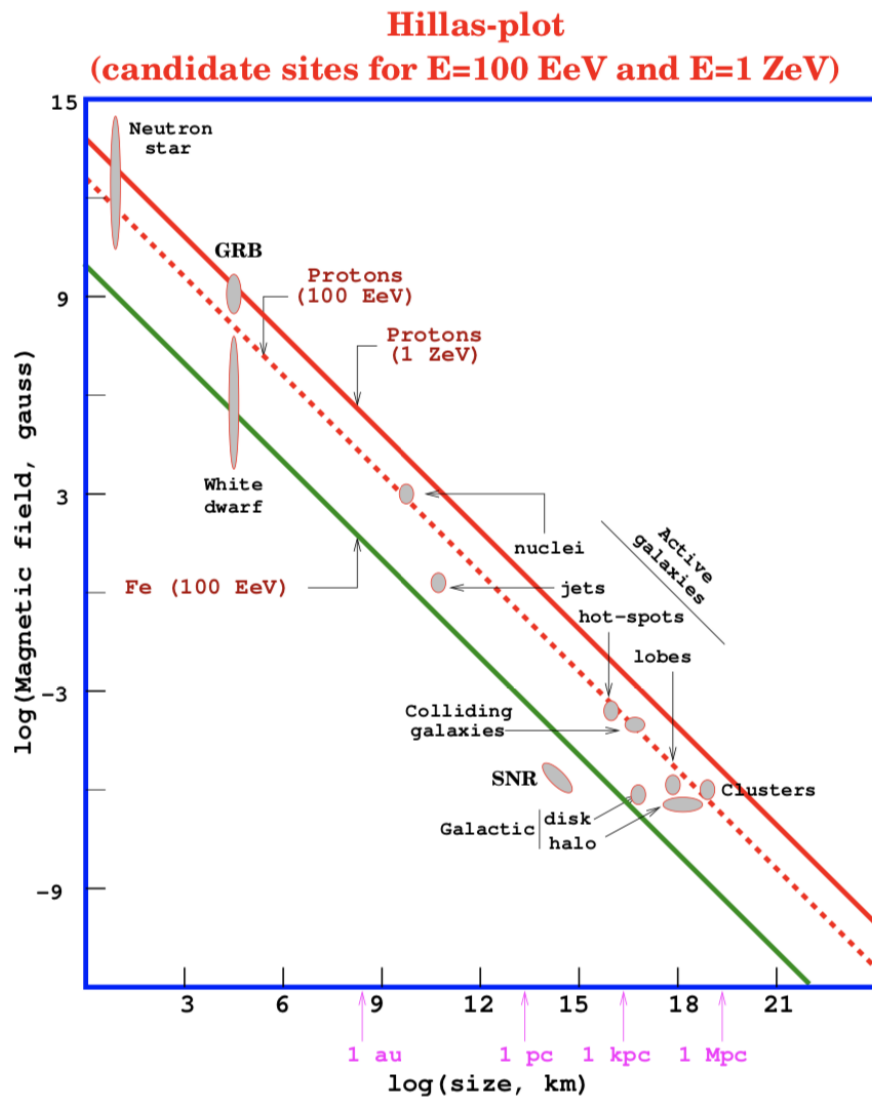


FIGURE 2.4: Hillas plot of maximum energies of particles accelerated from various objects [29].

Possible source candidates based on this criteria are shown in Figure 2.4 called Hillas plot, which is a handy tool to characterize the candidates to accelerate CRs. It displays the various acceleration sites with their magnetic field strength B and physical size L . It also shows lines for required B and L to accelerate particles to 100 EeV ¹ and 1 ZeV ². For protons the lines for $E_{\max} = 1$ ZeV (solid) and for 100 EeV (dashed) and for Iron nuclei the green line for $E_{\max}=100$ EeV (solid) are shown. Sources lying upper left of a specified maximum energy line are able to accelerate CRs up to the energy. Although for the acceleration of highest energy

¹1E = 10^{18}

²1Z = 10^{21}

CRs, not all of the source types are suitable, they can contribute to the acceleration of CRs in different energy ranges. Sources can be divided into two main categories namely "galactic" and "extragalactic". The major and possible galactic sources are SNRs, pulsar wind nebulae (PWNe), pulsars, binary systems, and young stars. The E_{\max} to be reachable by the galactic sources is a matter of debate, however, it is generally believed that they can significantly contribute up to PeV energies of the CR spectrum. The highest energy part of the CR spectrum is believed to be due to extragalactic sources. Proposed extragalactic sources are active galaxies, starburst galaxies, cluster of galaxies and gamma-ray bursts (GRBs).

Active Galaxies

Active Galaxy is believed to be one of the most powerful source of energy in the current Universe. An active galaxy has a compact region at the center, called "active galactic nucleus" (AGN) which produces much higher emission luminosity than that to be attributed to its stellar content, stellar remnants and interstellar medium. Each AGN consists of supermassive black hole with around 10^6 to 10^9 solar masses at central region, with an extension of often only 1 pc in diameter. The currently believed classification scheme for the many observed subclasses of AGNs is based on the mass of the central black hole, its evolutionary status, its accretion speed, and on the orientation of the galaxy and the emitting regions with respect to the line of sight. Charged particles are accelerated by electric fields induced by rotating magnetic fields. Candidates of AGNs within 100 Mpc can be correlated with UHECR, suggested by GZK suppression, through the position of AGNs and the cosmic ray arrival direction [30]. However, AGN with the hot spots are very rare and usually exist far from the earth. The nearest concentration of AGNs concentrated around large scale structure with the typical length of 5 – 15 Mpc in the local universe including galaxy clusters as Centaurus and Virgo [31].

Starburst galaxies

Starburst galaxies are young and characterized by their comparatively high star formation rate, which is associated to the high density of massive, hot stars and thus a comparatively high supernova rate. One example of the starburst galaxies is M82

in which the gas pressure is 100 times greater than in the local neighborhood and its forming stars at about the same rate as the milky way in a region about 600 parsec across[32]. In recent studies, Pierre Auger experiment reported a correlation between cosmic rays with energies above 39 EeV with 23 nearby Starburst galaxies (SBGs) [2]. And some of the SBGs on their list including the brightest M82 from the northern sky [33].

Gamma-ray bursts

Gamma-ray bursts (GRBs) are the most energetic phenomena observed in the Universe. The widely accepted current understanding of these highly transient bursts is given by the fireball model [34] (for other interpretations see [35, 36]), which assumes that a central object produces an ultrarelativistic outflow of an optically thick plasma shell, which emits the GRB as soon as it becomes optically thin. The short duration of GRBs (milliseconds to a few hundred seconds) hints at very compact progenitors. The mean distance of these progenitor objects has been measured to be $z = 2.8$ with at least 7% of the GRBs originating at $z > 5$ [34]. Typically, 10^{51} to 10^{54} erg s^{-1} are released within seconds up to tens of seconds. This prompt emission is followed by an afterglow of less energetic photons, which extends long after the initial burst and can last for days, from these events scientifics have suggested that GRBs can produce cosmic rays during this huge energy release. Since for highest energy UHECRs sources are required to exist within GZK horizon of about 50 Mpc, and the rate of GRBs is 1 per 100 years in such volume, the arrival direction distribution would have a strong anisotropy for highest energy UHECRs.

2.3.2 Top-down Model

An alternative theory about the UHECR origin is the top-down model which describes, that the decay or the annihilation of super heavy relic particles generate CRs at ultra high energies [37]. This model is based on new physics beyond the standard model for the existence of such massive particles or topological defects.

In this model, UHECR sources are hypothetical particles and/or topological defects which are expected to be generated at the beginning of the Universe. Decays or annihilations of the super heavy particles or the high density topological defects can induce cascades of UHE particles [38]. Some types of the topological defects are expected to decay to super heavy gauge bosons or Higgs bosons. A succeeding hadron jet induced by these particles decays to gamma-rays, electrons and neutrinos with only a few percent of nucleons. If this contribution dominates the CR spectrum above GZK cutoff, a transition of mass composition is expected at GZK energy, 4×10^{19} eV. Thus with the some kind of propagation models of UHE gamma rays, the topological defect scenario suggests that proton is the dominant component in energy region less than GZK energy, and gamma ray is dominant above this energy. When the super heavy relic particles are rich abundance at the galactic halo and providing UHECRs, the mass composition is not changed as a function of energy because of enough short distances to avoid the GZK mechanism.

Z-burst model:

In Z-burst model, UHECRs are generated via interactions between UHE neutrinos and cosmic background relic neutrinos [39]. In general, these interactions via the decay of Z^0 products UHE photons.

2.4 Extensive Air Showers

Once an UHECR reaches the Earth, the UHECR hits the earth's atmosphere and generates an extensive air shower, a cascade of huge number of particles. As it was explained in the introduction the air shower phenomenon was studied in the earliest by pioneers B. Rossi and later by P. Auger using several types of detectors from Geiger-Muller counters, sophisticated total absorption calorimeters, time track detectors and so on to observe and measure this phenomenon [40]. One example of a cascade shower is shown in Figure 2.5 observed in 1947 by a cloud chamber when a low energy hadron passing through by interacting with lead plates. The ionisation process creates tracks in the cloud chamber.

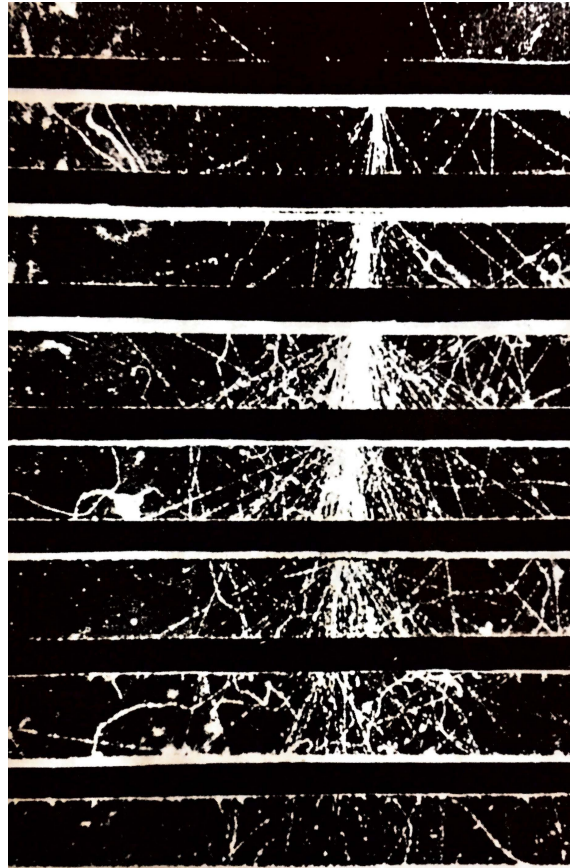


FIGURE 2.5: Cloud chamber photograph of cascade shower through several thicknesses of material from a an incident proton with energy ~ 4 GeV (1964)[41]

An extensive air shower, EAS, is initiated by a high energy particle interacting with a nucleus in the upper layers of the atmosphere at an altitude of 20 km (~ 50 g cm $^{-2}$ vertically) which depends on energy and the type of primary particle. The rate of arrival of primary cosmic rays with energy above 10^{14} eV is too low to be detected by direct measurements using balloons or satellites at the top of the atmosphere. When high energy cosmic ray particles enter the atmosphere, they interact with nuclei in the air and produce cascades of secondary particles. The produced secondary particles called “air shower” are strongly collimated along the direction of the incoming particle because of their relativistic energies. They interact on average after one interaction length.

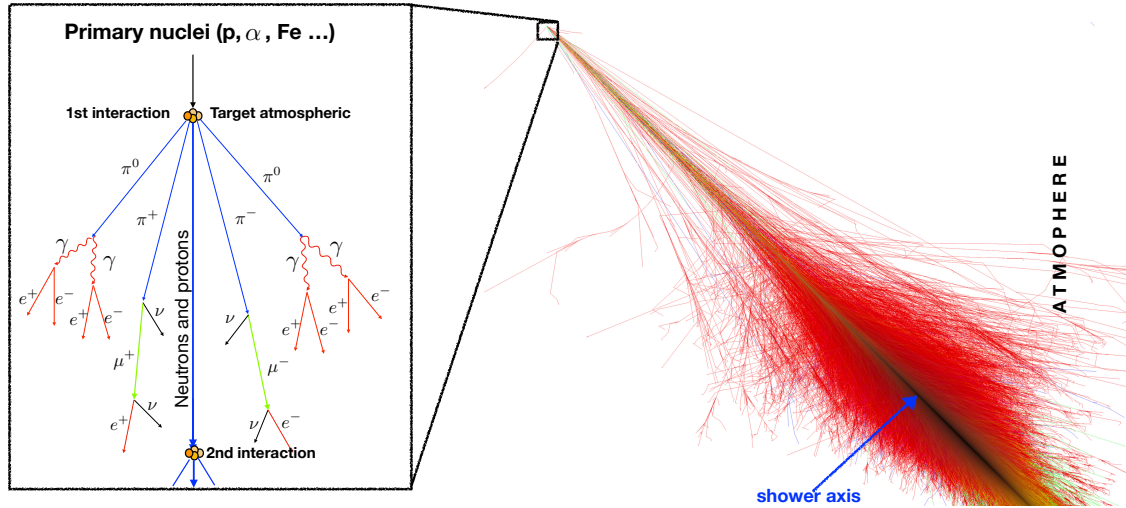
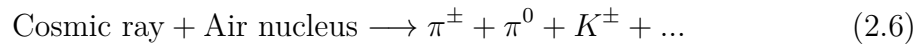


FIGURE 2.6: Left: type of secondaries produced when 1st interaction of primary, encoded in track color, red: e^\pm , γ , green: μ^\pm , blue: hadrons. Right: air shower of primary proton of 10^{15} eV simulated.

This iterative process results in an avalanche of secondaries that traverse the atmosphere with nearly the speed of light in the vacuum. Since the physical length between interactions decreases with (air) density, it is useful to express it in terms of the product of density and distance, called atmospheric depth X . For vertical incidence, the atmospheric depth at sea level is $X_{\text{air}} \approx 1030 \text{ g/cm}^2$. Figure 2.6 shows an EAS initiated by an extremely energetic CR nucleus followed by hadron multiple productions, the elementary interaction of which is,



with **electromagnetic cascades** and **hadronic multiparticle** production [42]. Typically, the first interaction occurs within $\sim 100 \text{ g cm}^{-2}$ with respect to the top of the atmosphere. Extensive air showers produced by $E > 10^{18}$ eV cosmic rays are cascades of billions of secondary particles, and the maximum number of secondary charged particles in an EAS, which called "shower size" (N_{max}) is known to be proportional to its primary energy, E_0 , with

$$N_{\text{max}} \simeq \frac{E_0 \text{ in eV}}{1 \text{ GeV}}. \quad (2.7)$$

An air shower is extensive due to the transverse momentum of secondary particles

and the multiple scattering of electrons components. As result, its lateral spread reaches several square kilometers for UHE primaries.

Numerical models calculations as well as hadronic physics experiments covers by LHC Large Hadron Collider have been used to analyze the shower measurements to investigate the properties of the incoming CRs. However, a centre-of-mass energy of p-p collision is $\sqrt{s} \simeq 14$ TeV which corresponds to an energy of 10^{17} eV in the laboratory frame is the maximum energy reached by LHC [43]. Thus the interaction models are extrapolated from accelerator measurements to interpret EAS, and then there are systematic uncertainty on the hadronic processes for UHECR EAS with primary energies higher above 10^{17} to 10^{20} eV are not yet well understood [44]. In this context it is important to explore experimentally using many techniques to study the properties of UHE EAS.

2.4.1 Electromagnetic cascade

The electromagnetic (EM) cascade is part of an EAS initiated by a hadron CR as the example in the Figure 2.6. Primary gamma-ray generates a pure EM cascade. The EM consists of γ -rays and leptons (mostly electrons and positrons). In typical EASs induced by hadronic primaries the start point of EM cascade are neutral pions (π^0), which immediately decay due to its shorter lifetime (8.4×10^{-17} s) into a pair of gamma-rays

$$\pi^0 \rightarrow 2\gamma \quad (2.8)$$

A gamma ray produces e^\pm pairs when passing near nuclei, and e^\pm re-generate gamma-rays via bremsstrahlung. Thus, repeating these processes, a developing electromagnetic subcascade is built along the trajectory in the atmosphere. The EM components in Figure 2.6 right panel is shown in red. The electromagnetic cascade grows via pair-production and bremsstrahlung. The radiation length λ (from the Figure 2.7 (a), λ is the distance denoted with the red arrow), then λ_r^e is the grammage path length over which e^\pm loses $1/e$ of its energy (this radiation length λ_r^e is ~ 36 g/cm² in air). And assuming $\lambda_r^e = \lambda_r^\gamma$ and considering the primary energy E_0 and if we assume the energy of a particle is equally divided into 2 particles at the pair-creation and bremsstrahlung, the number of particles and the energy of each particle

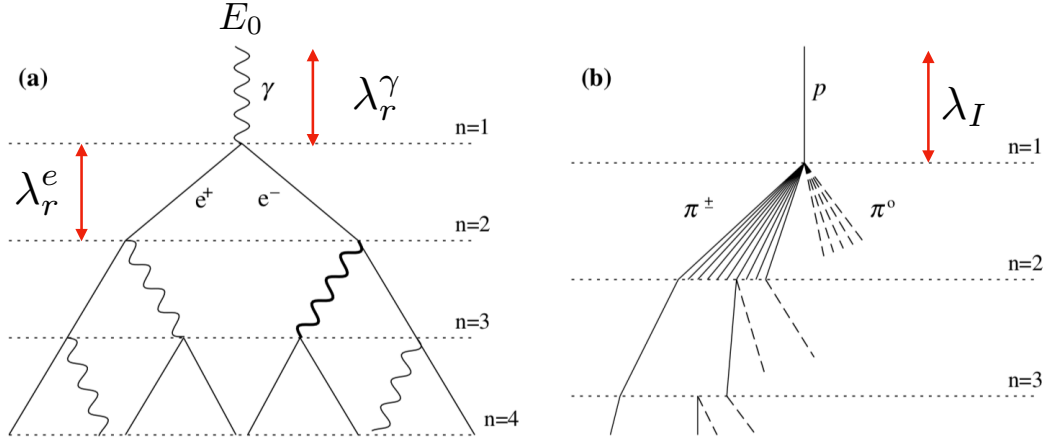


FIGURE 2.7: **a)** Heitler model for electromagnetic cascade. **b)** Heitler-Matthews model for hadronic cascade.

at the n 's step are 2^n and $E_0/2^n$, respectively. Multiplication causes the energy of the particles are too low for pair-creation or bremsstrahlung. It called critical energy, E_c , below which radiative energy loss by bremsstrahlung less than ionization energy loss. $E_c = 85$ in the air. E_c is considered the minimum energy at the particles reached through the multiplication process. The Heitler model describes the electromagnetic cascade development in the left panel of Figure 2.7. When EM starts with an energy E_0 and the critical point the EM cascade reaches the maximum size $N = N_{\max}$ of all particles (electrons and photons), therefore, $E_0 = E_c N_{\max}$. The number of generations n needed to reach this maximum size depends on the total energy E_0 as describe in the diagram **(a)** of Figure 2.7. Since the number of particles doubles at each generation, one has at maximum, $N_{\max} = 2^n = E_0/E_c$, therefore, $n = \ln(E_0/E_c)/\ln(2)$. The maximum size occurs at a slant depth $X_{\max}^\gamma = n \times \lambda_r \times \ln(2) = \lambda_r \times \ln(E_0/E_c)$ [42].

The energy loss of an electron with bremsstrahlung is proportional to its energy:

$$-\frac{dE_e}{dx} = \frac{E_e}{\lambda_r^e} \quad \text{with} \quad \lambda_r^e \sim 36 \text{ g/cm}^2 \quad \text{in air} \quad (2.9)$$

For pair creation, the relevant free path for γ 's is given by $\lambda_r^\gamma = (7/9)\lambda_r^e$. The elongation rate Λ for electromagnetic cascade is defined as

$$\Lambda = \frac{dX_{\max}}{d\log_{10} E_0} = \frac{\ln 2}{\log_{10} 2} \times \lambda_r \simeq 85 \text{ [g/cm}^2\text{]}. \quad (2.10)$$

The contribution of EM charged particles to showers induced by primary CRs of $E > 10^{18}$ eV is calculated about 85% to 90% of primary energy [45], and these results can be verified experimentally by counting muons [46]. The energy deposits in the atmosphere along a shower axis important in energy determination of the primary particle with the atmospheric fluorescence technique. This method of the primary energy estimation does not strongly rely on the details of the first interaction and the subsequent processes in the hadronic core, which constrains the systematic uncertainty due to the models to 5% [45].

2.4.2 Hadronic component

The hadronic air-shower is produced by a reaction by a charged particle with atmospheric nucleus via strong interaction. When the charged particle is the primary particle were a nucleus of energy E_0 and the mass number A , the EAS should be viewed as a simple superposition of A showers with the primary energy of E_0/A each [47]. The hadronic interactions then continue in the narrow region around the shower axis (direction of the primary particle) thus forming the *hadronic core* until their energies are depleted. The secondaries are pions with $\sim 90\%$ (π^\pm, π^0), $\sim 10\%$ kaons (K^\pm, K^0) and light baryons (p, \bar{p}, n, \bar{n}) are created (equation 2.6). The multiplicity of the hadron particles follow an approach to similar Heitler model and it has been described by Matthews [42]. Shown in **(b)** Figure 2.7 (right), when a hadron with energy E enters the atmosphere, it travels \sim one interaction length λ_I and collides with a nucleus in the air according Equation 2.6. Through the interaction at the level where $n = 1$, if one assumes multiplicity $N = 3$ (in the graph $N = 12$) the primary hadronic energy is split into three equal parts to two charged pions and a neutral pion. The neutral pion has a very short lifetime $\tau_{\pi^0} = 8.4 \times 10^{-17}$ s and decays into two photons. Photons will then create electromagnetic showers like introduced before (as seen in Figure 2.7 **(a)**). The charged pions are assumed to travel a constant distance which is related to the interaction length λ_r and then conduct hadronic interactions as indicated at level $n = 2$. If the number of the

charged particles produced at each level is N_{ch} , the average energy per pion E_π is

$$E_\pi = \frac{E_0}{\left[(3/2)N_{\text{ch}}\right]^n} \quad (2.11)$$

The size of the shower keeps growing since there are more and more hadronic interactions. However, the lifetime of charged pions is $\tau_{\pi^\pm} = 2.6 \times 10^{-8}$ s, low energy pions have larger probability of decaying than interacting. The energy of pions at this level is called the critical energy E_c^π , and if one assumes γ is the Lorentz factor of the pion, one gets

$$\lambda_I/\rho = \gamma c\tau \quad (2.12)$$

where ρ is the density of the atmosphere and E_c^π is approximately ~ 30 GeV. The interaction length can be calculated from the cross-section and here can be treated roughly as 80 g/cm^2 . Charged pions and kaons decay to muons and also creates neutrinos (ν) in these processes, $\pi^\pm \rightarrow \mu^\pm + \nu_\mu/\bar{\nu}_\mu$ and $K^\pm \rightarrow \mu^\pm + \nu_\mu/\bar{\nu}_\mu$. Thus the number of muons at the critical level is,

$$\ln N_\mu = \ln N_\pi = n \ln N_{\text{ch}} = \beta \ln E/E_c^\pi \quad (2.13)$$

where $\beta = \ln(N_{\text{ch}})/\ln[(3/2)N_{\text{ch}}] \sim 0.85$ from simulations. Therefore the number of muons in the hadronic shower is proportional to the logarithmic primary energy. The muons as secondaries CRs are usually close to the minimum ionizing energy of 100 MeV to 1 GeV, which make long-lived (muon mass and lifetime are ~ 106 MeV and $\tau_{\pi^\pm} = 2.2 \times 10^{-6}$ s) and penetrating [48].

Therefore, muons (as well as electrons and gamma) can make a significant contribution to the signal measured by the ground array detectors. Also, the ground arrays can be designed to measure the electromagnetic component separately from the muonic component: counters that register signals from the muons only can be placed underground for shielding them from the EM component [16].

2.5 Characteristics of EAS

There are two characteristics based on radiation models assuming the air shower is developing along their travel these properties are: the lateral distribution development which is perpendicular to the shower of particles travel and the longitudinal development along the shower axis through the radiation length.

Lateral distribution development

The tranverse development of EM shower, the total number N_e of charged particles at the shower maximum is approximately 2/3 per GeV of primary energy. We will also assume equal numbers of 30 MeV positrons and electrons among charged particles, neglecting an admixture of muons, an excess of electrons and variations of energies between the particles. Such a simple model serves as a precursor to a future full scale shower development and radiation simulation similar to a study of the properties of electromagnetic showers in dense media performed in [49]. Lateral particle density ρ_e is parameterized by the age parameter s of the shower ($s = 1$ for the shower maximum) and the Molière radius R_M

$$\rho_e = K_N(\Gamma, N, s) \left(\frac{R}{R_M} \right)^{s-2} \left(1 + \frac{R}{R_M} \right)^{s-4.5} \quad (2.14)$$

where $K_N(\Gamma, N, s)$ that function depends on Γ function, N total number of charged particles and s age of air shower. R is the distance from the shower axis. The Molière radius for air is approximately given by $R_M = 74(\rho_0/\rho)$ m, with ρ_0 and ρ being the air densities at sea level and the altitude under consideration, respectively. As a shower travels towards the Earth and enters denser layers of the atmosphere, the age parameter increases while the Molière radius drops. Both processes affect the spread of the lateral distribution.

EM shower longitudinal development

The longitudinal development which is understand as the rise and fall of the number of charged particles is frequently approximated by a parametrized GaisserHillas

function (GH Funtion) form,

$$N_e(X) = N_{\max} \left(\frac{X - X_0}{X_{\max} - X_0} \right)^{(X_{\max} - X_0)/\lambda_r} \exp\left(\frac{X_{\max} - X}{\lambda_r} \right) \quad (2.15)$$

where X_0 is the first interaction point of primary particles, and λ_r is the attenuation length in g/cm^2 . The parameter X used above is the grammage distance that an EAS has traveled in the atmosphere. That is known as *slant depth* in unit of g/cm^2 .

Using Monte Carlo simulation is possible infer the properties of lateral distribution of each type of particles on the ground as seen in the Figure **a** 2.8 and the longitudinal development of different kind of particles in the air which is shown in the Figure **b** 2.8. According the MC simulation and air shower models the hadron component is composed of long-lived secondary particles (baryons, charged mesons) that travels along shower axis and contributes to signals at the core. Figure 2.8 shows an example of CR with proton primary of 10^{19} eV generated by using monte carlo simulation package CORSIKA [50]. The lateral distribution in the plot **a**, the type of secondary particle density changes with respect to core distance for gamma and electrons are larger than muons. In case of longitudinal development plot, the number of hadrons, muons, and electrons in the x-axis have been scaled respectively.

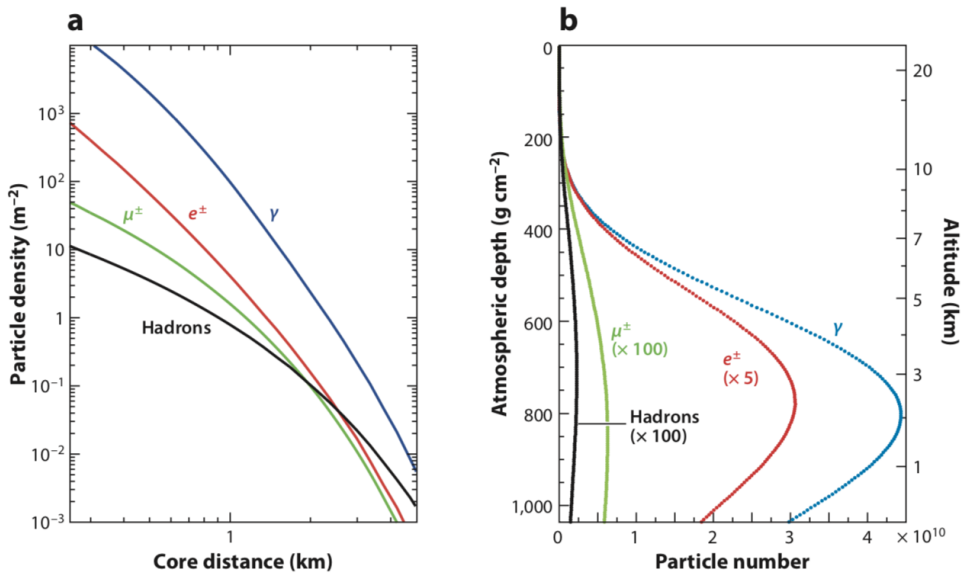


FIGURE 2.8: **a:** Lateral Distribution Function at ground level and **b:** longitudinal distribution of particle density for CR proton of 10^{19} eV. [50]

2.5.1 Time structure

The study of extensive air showers of the highest energies is difficult because the atmosphere is part of detector and the interpretation of measurement is indirectly. A complex chain of interactions occurs in the atmosphere and the remains of particles are caught by detectors as footprint of the shower on the ground. From this sample footprint on detectors, the properties of the air shower development can be deduced. In this sense based on experimental observation by using large array of detectors are necessary to study the characteristic of particles on the ground. The detectors record the particle number densities (or the energy deposition into detectors) and the particle (signal) times. The time profile of signal recorded it is considered the main observable to understand the extensive air shower phenomenology of UHECR on this present study. For this purpose it was taken into account two scenarios; **1)** the curvature of the shower front by using the residual time with respect to the shower plane and **2)** the thickness of the shower disk by analyzing the observable rise time based on the accumulated waveforms from the signals.

Shower front

The basic analysis of shower front is very important because the shower arrival direction of EASs is reconstructed from the relative arrival times of the signals. Then the precision of arrival direction is very important because is controlled by the time profile. The traditional method is simple considering the shower front is completely plane and it consists on any pair of detectors A and B determine the arrival direction cosine along the direction from A to B as $c(t_B - t_A)/\overline{AB}$, where c is the speed of the light and t_A and t_B are the trigger times for detector A and B respectively, and \overline{AB} is the distance between them. Then any two independent direction cosines determine an unique arrival direction (as seen on Figure 5.3). The shower front can be approximated a plane but based on several air shower experiments for instance Volcano Ranch and AGASA experiments [7, 51] was observed from the plane shower front there is a fluctuation of the shower particles around the average [51]. Therefore, a more realistic model of the shower front is curved shower front moving at the speed of light as observed on the right Figure 2.9.

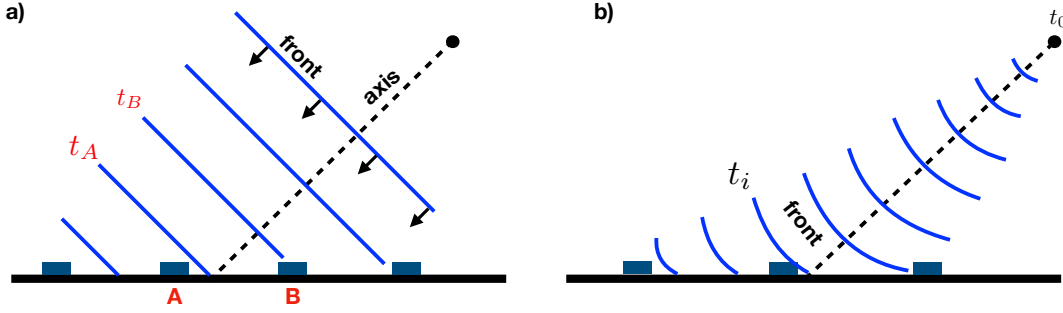


FIGURE 2.9: Scheme of shower front. Left figure: **a)** representation of front as plane. Right figure: **b)** shower front represented as curved front.

The results presented by the Akeno air shower experiment, in the shower analysis it is presented an empirical formula (Equation (2.16)), $t_d(R, \rho)$ is the delay time of the first particle observed by each detector from the plane shower. And $\sigma_d(R, \rho)$ is the uncertainty of t_d expressed in the Equation (2.17),

$$t_d = 2.6 \left(1 + \frac{R}{30\text{m}}\right)^{1.5} \left(\frac{\rho}{\text{m}^{-2}}\right)^{-0.5} \text{ ns} \quad (2.16)$$

$$\sigma_d = 2.6 \left(1 + \frac{R}{30\text{m}}\right)^{1.5} \left(\frac{\rho}{\text{m}^{-2}}\right)^{-0.3} \text{ ns} \quad (2.17)$$

where R is the distance in meters from the shower axis and ρ is the particle density in units of number of particles per unite of m^2 [52, 51]. And the particle density $\rho(R, \theta)$ is introduced by AGASA experiment and it is referred the lateral distribution function AGASA LDF by,

$$\rho = C \left(\frac{R}{R_M}\right)^{-1.2} \left(1 + \frac{R}{R_M}\right)^{-(\eta(\theta)-1.2)} \left(1 + \left[\frac{R}{1000\text{m}}\right]^2\right)^{-0.6} \quad (2.18)$$

where $\eta(\theta) = 3.97 - 1.79[\sec(\theta) - 1]$. R_M is the Molière unit (91.6 m at Akeno site of AGASA experiment), calculated the from the radiation length at the site of experiment. And C is the normalization factor.

The thickness of the shower disk

In the same region of shower disk, it is formed the thickness of the shower composed by the secondary particles remained, this temporal property in the front curvature is not well understood yet. In the earliest studies, it was suggested to use the pulse

widths to observe the thickness of the shower disk and measure it respect to air shower impact parameter. As result, this fluctuation of thickness had not have dependence only on impact to parameter, but it also depends on shower size, and zenith angle [53]. In the earliest studies, it was suggested to use the pulse widths to observe the thickness of the shower disk and measure it respect to air shower impact parameter. As result, this fluctuation of thickness had not have dependence only on impact to parameter, but it also depends on shower size, and zenith angle [53]. This study was observed with few shower events data by Haverah Park shower array with energy target of $\sim 10^{18}$ eV by using water-Cherenkov detectors [54]. In their observations [52, 55] the thickness of the shower disk increases with distance from the shower axis (more detail of this observation see Appendix A.1). Since there is not enough studies about it, the basic idea of the thickness comes from shower disk, there is in the front of EAS a thin plane like pancakes which is the thickness of the shower disk as shown in the Figure 2.10.

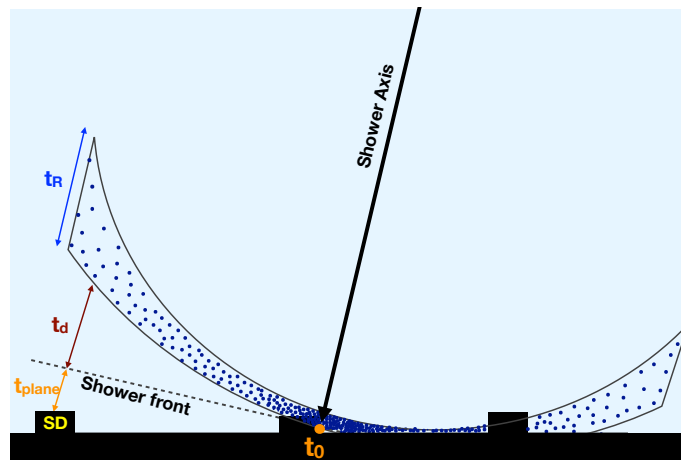


FIGURE 2.10: Scheme of shower front with the representation of the residual time (t_d) and the thickness of the shower disk as (t_R).

Figure 2.10 represents the time structure showing the time delay t_d or residual time between the shower plane and the shower disk and the thickness of the shower disk which is represented by t_R . To quantify this feature of thickness of shower disk is based in the Haverah Park experiment thought his measurement by using the risetime t_R by using the signal height between 10% to 50% of the full integrated signals [54].

In the Chapters 5 and 6 will be explained in detail about the shower front disk and thickness structure because these are the central part of analysis study.

2.6 Observation of extensive air shower

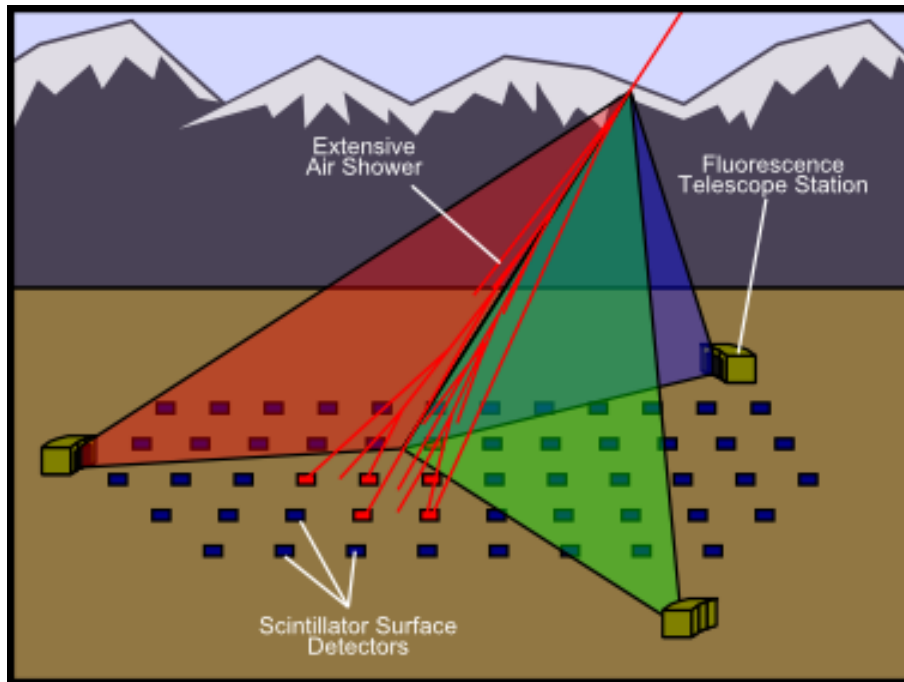


FIGURE 2.11: Detection of an UHECR by observing an EAS with surface detector and fluorescence detector [56].

To observe EASs, there are several techniques and in case of UHECR a large array of hybrid detectors are used to detect the secondary particle of extensive air shower. Therefore, these arrays are deployed in high altitudes in order to observe the depth of the shower maximum X_{\max} of the shower by Fluorescence detector. And the main technique to detect the secondary particles are either using scintillation counters or by using Water Cherenkov Detectors (WCDs). In the first, PMTs detect the light from scintillation, while in the second, they detect the Cherenkov light produced by the secondary particles in water. The time and charge information of the signal observed by the PMTs is then utilized to estimate the shower properties. A schematic of the technique is shown in the Figure 2.11.

Surface detector

The traditional technique that measure the secondaries using a lot of surface detectors (SDs) spread on the ground. The typical SDs consist of scintillation matter as plastic and water as describe in the Figure **a)** and **b)** 2.12 respectively. The best merit of an air shower array is to observe UHECRs with duty factor of detector array is close to 100%. The vast majority of the energy in EASs is carried to the ground by photons, electrons and positrons (e^- , e^+), and muons (μ^+ and μ^-)[57, 16]. A typical detector is a scintillation counter sensitive to charged particles and muons. To measure muons, we can use special scintillation counters shielded by lead, soils, rocks or other dense materials. Moreover, to measure a hadron flux in the vicinity of shower axis, hadron calorimeters had been used in several experiments.

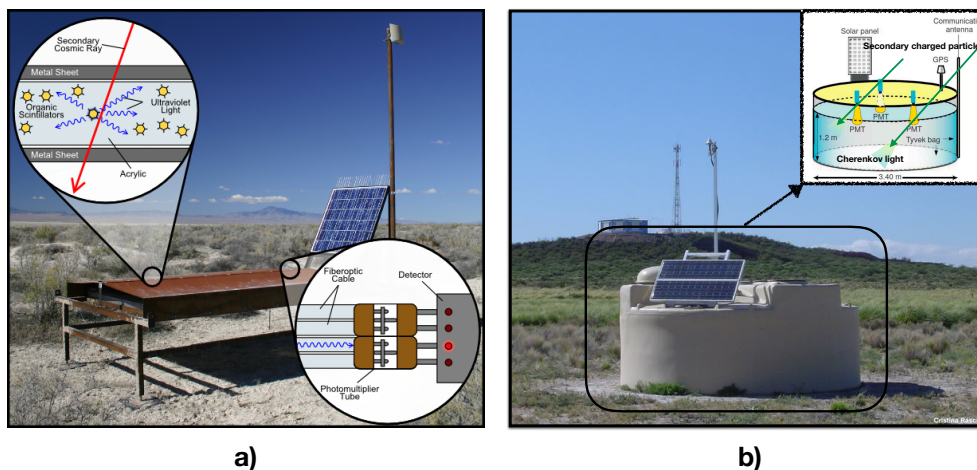


FIGURE 2.12: Secondary particles initiated by UHECR detection with ground array technique. **a)** A surface detector used by TA experiment based on plastic scintillation [58]. **b)** Water Cherenkov detector used by Pierre Auger experiment by observing Cherenkov light [59].

In air shower array, an arrival direction of EASs is reconstructed from a timing distribution of each surface detector because a front of EAS has a thin plane like pancakes. The energy of a primary particle is estimated from the air shower size which is estimated by the shower lateral density distribution of the shower. However, it is difficult to avoid an uncertainty of from hadron interaction models, because a particle distribution of EASs is relatively large dependent on hadron interaction models. Reconstruction of the ultra-high energy cosmic rays (energy and direction)

relies on measurements of the atmospheric extensive air shower (EAS), induced by the primary particles by using SD array.

Fluorescence detector

The Figure 2.13 shows the detection technique with fluorescence photon from air shower. After high energy particles penetrate the atmosphere, atmospheric molecules, for example nitrogens or oxygens, are excited and emitted ultra-violet fluorescence photons with wavelengths, $300 \sim 400$ nm. In other word, the atmosphere plays a role of scintillators. When a single electron with the kinetic energy of 80 MeV passes through 1 m in the unit atmosphere of 1 atm, 4 fluorescence photons are emitted.

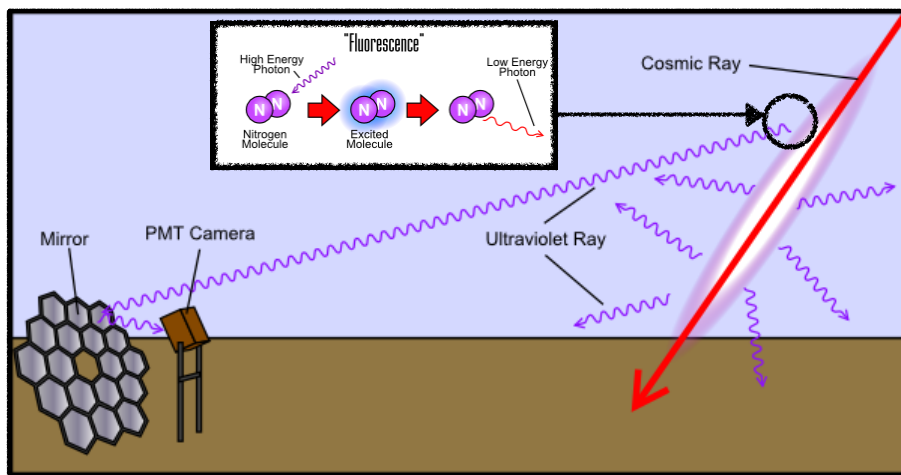


FIGURE 2.13: Fluorescence detection technique. Fluorescence detection is most accurate method, but duty cycle is $\sim 10\%$ [60].

Since the fluorescence photon emission is isotropic, we observed the fluorescence photons from all direction of UHECRs within effective area. In general, there are two steps of data analysis in the fluorescence technique to obtain the information of primary cosmic rays, as follows,

- geometrical reconstruction
- longitudinal development reconstruction

The merit of fluorescence detection technique is to detect all processes of longitudinal developing. The fluorescence detector must be operated in moonless nights. Therefore the duty circle of fluorescence detection technique is $\sim 10\%$.

However, the rich information of primary cosmic rays is measured the mass composition as well the energy of UHECR by the fluorescence technique. In order to measure the primary energy and X_{\max} , it is needed estimate the fluorescence yields, scattering of ultra-violet photons, reflectivities of mirror, the transmittance of filters and quantum efficiencies of photomultiplier tubes. The UHECR mass composition is

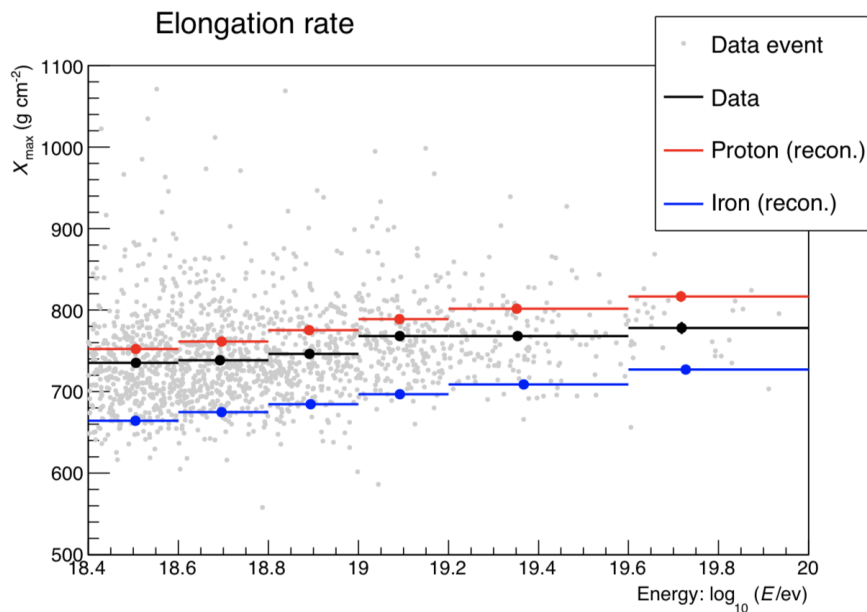


FIGURE 2.14: Telescope Array measurement of the UHECR mass composition. Plot of mean of X_{\max} vs. energy for 10 years of data. The black points with error bars are the data and red and blue points represent the hadronic model predictions for the proton and iron primary particles [61].

currently inferred, through the fluorescence detector, measurements of the position of the shower maximum X_{\max} by using the Equation (2.15). The current report of the TA experiment shows the mean X_{\max} measured with fluorescence detectors in stereo mode as shown in Figure 2.14, this result is in favor of light elements for $E > 10^{18.4}$ eV [61] by using 10 years of data. This figure presents the recent result from the TA experiment and it shows the mean of the observed and the simulated X_{\max} versus energy bins. This result is not completely in agreement with the parallel experiment Auger, measured in the southern hemisphere, where is in favor of heavy elements for energies higher $10^{18.33}$ eV [62]. The possible conflict in the measurement of X_{\max} could be attributed to the high energy interaction model [61].

Figures 2.15 show the measurement of X_{\max} (left) and $\sigma(X_{\max})$ with hybrid events mode, TA BR/LR FD telescopes in coincidence with SD array. The black star mark shows the observed data and the color dots marks are the MC simulations for different elements from light to heavy, p, He, N, and Fe, all presented in the energy range of $10^{18.2} \leq E < 10^{19.1}$ eV.

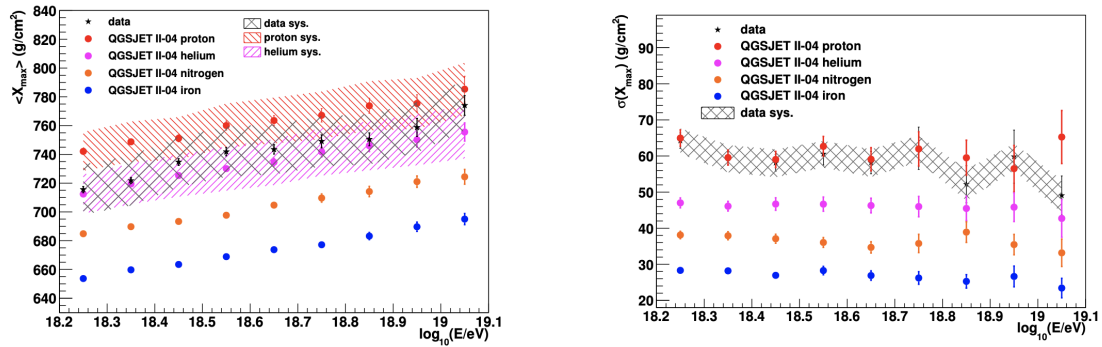


FIGURE 2.15: Updated mass composition measurements from TA 10 years hybrid data using mean and fluctuations of X_{\max} . The black stars are the data and the colors dots the MC simulated elements presented for energies $10^{18.2} - 10^{19.1}$ eV [63, 64].

Chapter 3

The Telescope Array

The Telescope Array (TA) constructed in Utah USA is the largest observatory in the northern hemisphere aiming at clarifying the origin of UHECRs in wider energy higher than $E > 10^{18.2}$ eV, by measuring the energy spectrum, mass composition and anisotropies in their arrival directions. The TA experiment based on the indirect method of cosmic ray detection covers an area of 700 km² and its location Millard County, Utah, in the middle of the array is located the Central Laser Facility (CLF) at 39°11'20" North, 112°54'31" East, and whose altitude 1370 m above the sea level which corresponds at 876 g/cm²). The data have been recorded since 11st May 2008. Firstly TA contains two types of detectors: Surface detectors (SD), which are deployed in an array of 507 counters, and each counter consists of plastic scintillators with optic fiber that counts charged particles on the ground with 1200 m spaced on a square grid. And the Fluorescence Detector (FD) is the other types of detectors mainly to study longitudinal information of the air shower and enable the determination of calorimetric energy of the shower. However the duty cycle of fluorescence telescope is limited by weather condition and the main operation is during dark, moonless and clear nights which reduces to an observation of $\sim 10\%$. Figure 3.1 shows the current map of the TA experiment the red area represents the TA-SD layout with the three TA-FD telescopes represented with blue symbols. In this analysis, it uses data from surface detectors, which have almost $\sim 100\%$ duty cycle. This chapter will be introduced information on individuals components of the TA experiment including its calibration and the trigger judgment. A brief description of the fluorescence detector will be described. As well as the description of energy calibration of SD based on the calorimetric energy measured by FD is

explained. Afterward, it is dedicated to the surface detector, the event trigger and reconstruction will be explained.

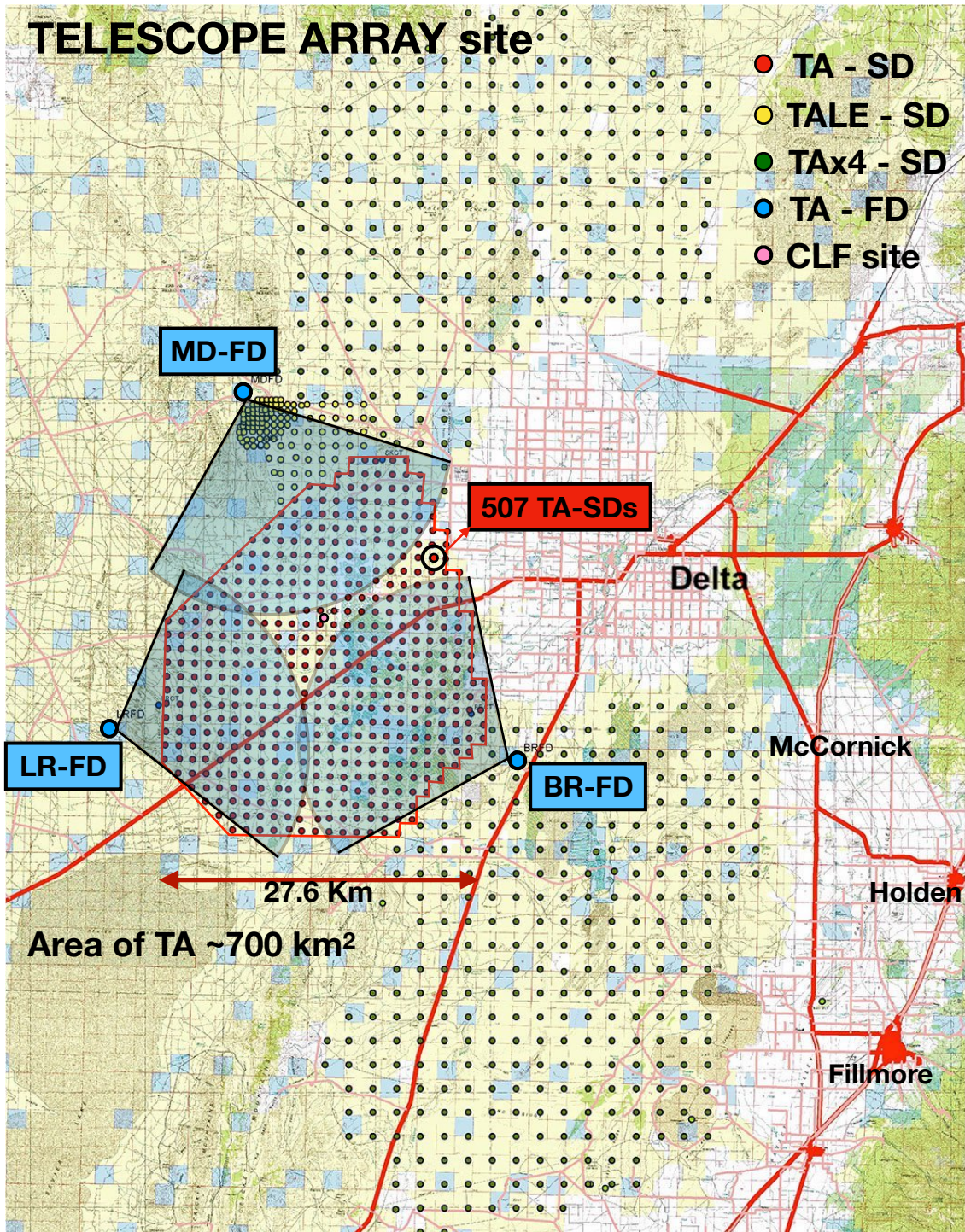


FIGURE 3.1: Map of the Telescope Array in the western deserts of Utah, USA. The TA experiment is composed by TA surface detector TA-SD (red, closely spaced symbols) and fluorescence telescopes TA-FD (blue symbols) [65].

3.1 Fluorescence Detector and the energy calibration

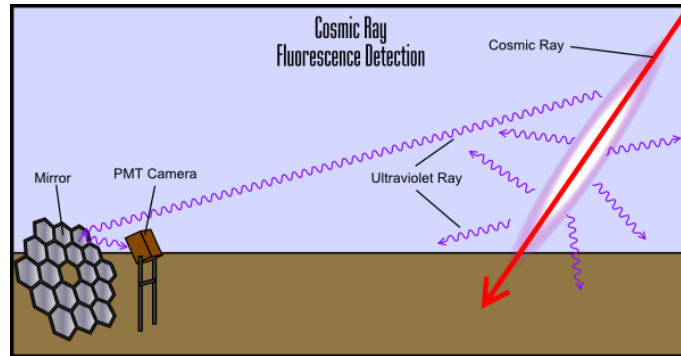


FIGURE 3.2: A description of fluorescence detector technique [60].

The charged particles in the extensive air shower excite nitrogen molecules in the atmosphere as represented the Figure 3.2. A fraction of the energy deposited in the air is then re-emitted during the de-excitation of the nitrogen molecules. The emission is a band spectrum with many lines from 300 - 420 nm in condition of 304 K and 1 ATM (see the Figure 3.3).

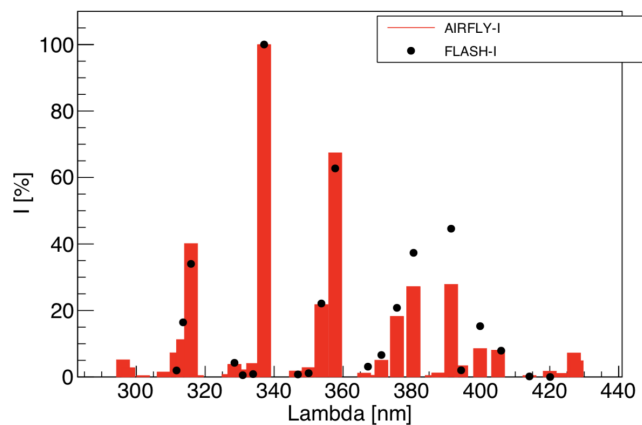


FIGURE 3.3: The air fluorescence spectrum of two experiments AIRFLY [66] and FLASH [67], range of wavelength is from 290 nm ~ 430 nm. Maximum fluorescence band is 337.1 nm emitting from N_2 2P [68]

Figure 3.3 shows the efficiencies of fluorescence photon emission versus the relative intensity. In this result presents 34 bands of the wavelength of air fluorescence in a range of 290 nm to 420 nm. Maximum intensity is 337.1 nm emitted from N_2 2P 0-0 band [68].

The number of fluorescence photons (N_λ) emitted is proportional to the energy that is deposited by charged particles from the air shower in the atmosphere ($\frac{dE}{dX}$). The fluorescence yield Y quantifies the relationship between the intensity of the fluorescence photons and the energy loss of the charged particle.

$$N_{i\lambda} = \frac{dE}{dX} Y_{i\lambda}(H_i) S_\lambda(H_i) dl_i \quad (3.1)$$

where λ is the photons wavelength and i is the i^{th} segment of the telescope and S_λ is the emitted spectrum response on its height (H_i), dl_i is the length of segment. The emission of fluorescence photons is isotropic and only a fraction of them can be observed using, the Fluorescence detector (FD). The expected signal, the number of photon $N_{i\lambda}$ at a FD, with aperture A_i is calculated by,

$$N_{i\lambda} = N_{i\lambda} T_{i\lambda}^{Rayleigh}(r_i) T_{i\lambda}^{Mie}(r_i) \frac{A_i}{4\pi r_i^2} \quad (3.2)$$

here r_i is the distance from the segment to telescope, $T_{i\lambda}^{Rayleigh}(r_i)$ and $T_{i\lambda}^{Mie}(r_i)$ are a transmittance of Rayleigh and Mie scattering for the wavelength propagating in a r_i . A_i is an effective area of the telescope. The effective area discussed here is defined as an area assumed the combined mirror as a single spherical mirror[69].

The fluorescence detector must be operated in moonless nights. Consequently the duty circle of fluorescence detection technique is only 10%. The atmospheric parameters must be monitored to estimate a yield of the fluorescence light and the transmittance of Rayleigh scattering. Therefore the transmittance is measured by Light Detection And Ranging (LIDAR) system at the start and the end of daily operation of FD. LIDAR is host in the CLF site.

The Telescope Array has 3 FDs at the perimeter of SD array. The FD station northwest corner of the SD array (MD station) consists of 14 telescope refurbished of High Resolution Fly's Eye (HiRes) experiment and the southeast (BRM station Figure 3.4) and southwest (LR station) FD are new developed stations composed of 12 fluorescence telescope in each. Right side of Figure 3.4 shows a schematic of FD frame equipped with a pair of FD telescopes.

A FD telescope consists of a primary mirror and a photomultiplier tube (PMT)

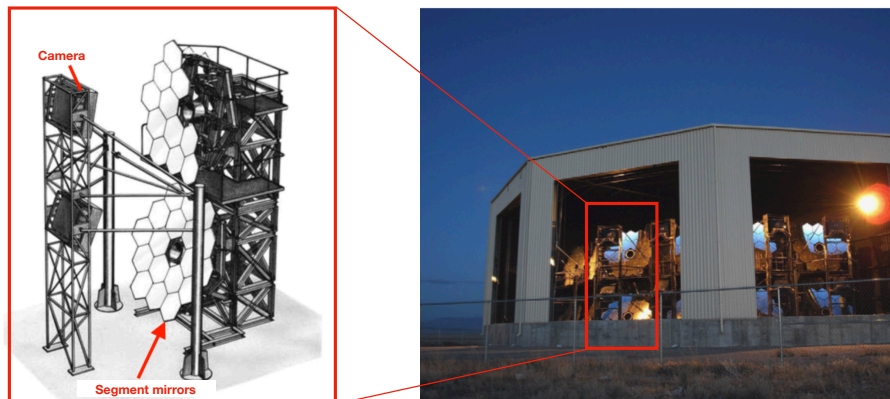


FIGURE 3.4: A picture of BRM FD station (left) with the schematic view of the 2 FD telescope tower (right). Two telescope in one tower, the upper FD views $3^\circ \sim 18.5^\circ$ and the lower FD views $17.5^\circ \sim 33^\circ$. Total 6 towers in a station.

camera. The mirror is designed to detect EASs from a distance of 30 km and with the primary energy of 10^{20} eV. The mirror diameter and radius of curvature were determined to be 3300 mm and 6067 mm. A primary mirror is composed of 18 segment mirrors; the distance between the parallel sides of the segment segment is 660 mm. A PMT camera consisting of 16×16 hexagonal PMTs is set at a distance of 3 m away from the mirror. The Field of View (FoV) of each PMT with mirror is approximately 1° , and an FoV of FD telescope is 15° in elevation and 18° in azimuth. The FoV centers of the upper and lower FDs are 10.5° and 25.5° in elevation. Thus, total FoV of a station is $3^\circ \sim 33^\circ$ in elevation and 108° in azimuth. Then the sensitive part of FD is focus in the PMT camera, and each camera is composed by 16 by 16 PMTs. The left side of Figure 3.5 shows the projection on the sky of the signal produced by one event shower, the colored circles represent "good" PMTs, the of diameter of each circle is proportional to N_{pe} and the color represents weighted average signal time: the earliest signals are blue with the last signals (some $13 \mu\text{s}$ later in this example) colored orange. PMTs that are designated "noise" and excluded from the reconstruction are marked with the symbol \times . And each gives the signal that is digitised with a 10Mhz FADC.

3.1.1 Event reconstruction and energy determination by FD

The start time of each triggered PMT is used to determine the arrival direction of the air shower by treating the shower development as a series of point source travelling along the shower axis. The plane that contains both the shower axis and the telescope is named the shower detector plane (SDP) and shown in Figure 3.5 (right). In the measurement the shower detector plane SDP is taken into account \hat{n} , shower direction (θ, ϕ) , SDP angle ψ , shower impact parameter R_p , core location and arrival time. Once the SDP is known, the shower impact parameter and the

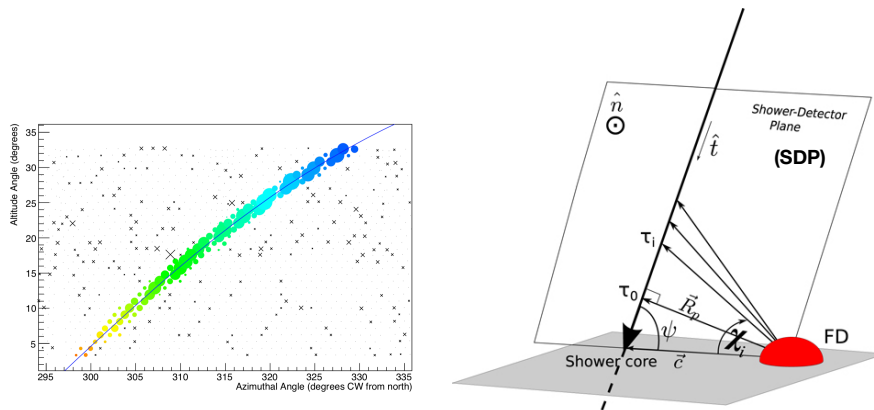


FIGURE 3.5: Light track on the camera (left) and an illustration of geometry of an air shower track as viewed by a FD. The color of the light track indicates the sequence of trigger time on each pixel. The track \hat{t} is unit vector which point along the shower in the direction which the shower travels, \vec{c} points from the FD to the point on the ground where the shower impacts (core), R_p is the impact parameter, and ψ is the SDP angle. Each PMT that observes the shower has viewing angle χ_i and triggers at times t_i . The time τ_i is the difference between the PMT trigger and the light travel time from the shower axis [70, 63].

SDP angle are calculated by the time vs. angle fit. The expected trigger time of PMT i is [63],

$$\tau_i(\chi_i; R_p, \psi, t_0) = t_0 + \frac{R_p}{c} \tan\left(\frac{\pi - \psi - \chi_i}{2}\right) \quad (3.3)$$

The predicted values τ_i are then compared to measured values by calculating χ^2 . The best fitted values of t_0 , R_p and ψ are found when χ^2 is minimized. Then this is the reconstruction of the shower based on FD signals, which is named as the mono-reconstruction. In addition, it is possible to combine SD and FD for the reconstruction, which is called the hybrid reconstruction. The hybrid analysis

requires at least one FD and one SD station to be triggered. The shower axis therefore can be reconstructed with a better precision by including the start time of the SD stations that are not on SDP in the fitting process.

Once the shower geometry is known, the signal in each pixel is converted in flux: an example of a shower profile which describes the energy deposited along the slant depth (the depth of atmosphere) is shown in Figure 3.6. The shower profile is fitted with the GH function. The calorimetric energy (E_{cal}) of the primary UHECR is reconstructed by integrating the curve [70]. However, during the shower

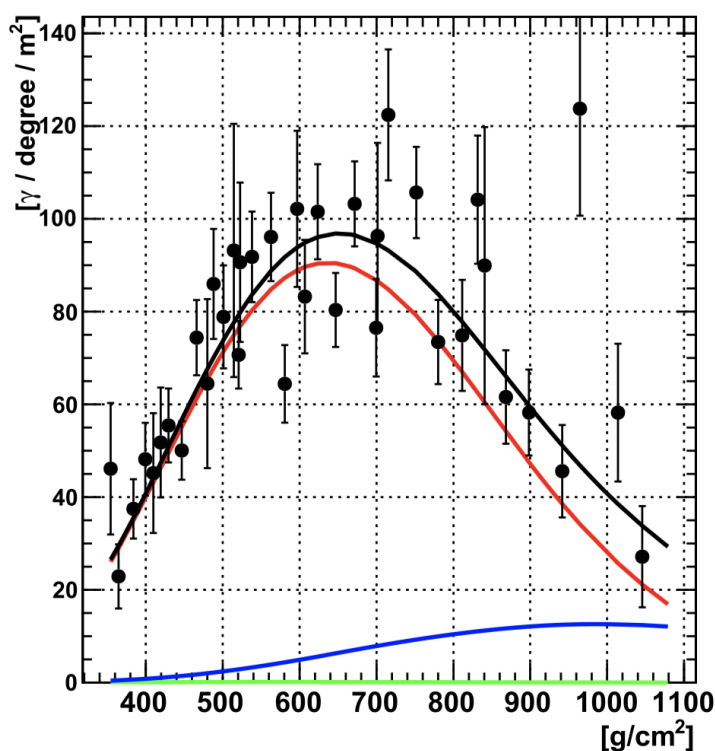


FIGURE 3.6: Calculated longitudinal shower profile. The flux and uncertainty vs. function of shower depth for each tube along the shower detector plane. The solid lines show the simulated flux generated for the best profile fit. Red is the contribution of fluorescence flux, blue the contribution of Rayleigh scattered flux and green is Cherenkov flux contribution [63].

development, the energy of neutrinos, neutrons and almost all energy of muons electrons cannot be measured by using FD. This fraction of energy is known as the invisible energy or "missing energy" and the fraction depends on the primary energy and the mass composition of the cosmic ray. Using Monte Carlo simulations, that has large uncertainty from hadronic models in the air shower simulation, the correction

has to be made. Thus the energy calibration is by using TA SD energy E_{SD} , which is evaluated using MC means depend on hadronic model and by other side it is compared with the calorimetric energy known as E_{FD} of TA FD energy deposited in the atmosphere (Figure 3.7). In order to match the TA FD energy, from TA SD energies determined need to be reduced by a factor $1/1.27$. In other words, when

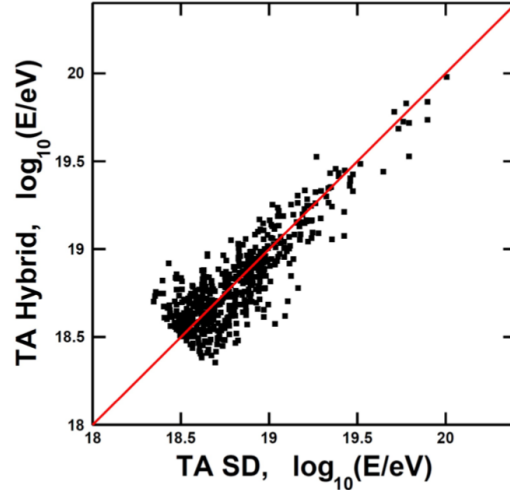


FIGURE 3.7: The energy calibration: the plot shows the scatter of E_{FD} versus E_{SD} [71].

the energy estimation procedure derived from the MC CORSIKA surface detector Monte-Carlo is applied to the real data, the predicted event energies are on average 27% higher than those of the fluorescence detector:

$$E_{MC,SD} = 1.27 \times E_{FD} \quad (3.4)$$

Figure 3.7 shows the energy of the TA SD plotted versus the energy of the TA FD, by hybrid analysis, in case of TA SD need to be reduced by a factor 1.27. Since the plot is log-log, the symmetry around the $Y = X$ line indicates that the event energies are matching on the average.

3.2 The description of Surface Detector

The 507 surface detectors are arranged in a square grid on the ground with 1200 m spacing. The TA SD has been operating more than 11 years. The layout of the

detectors have been proved to be fully sensitive for the detection of showers from hadronic primaries with energy above 10^{18} eV and zenith angle $0 - 60^\circ$. The Figure 3.8 shows the SD array, it is divided into three subarrays, and each subarray is controlled by its trigger-decision electronics at the communication tower via wireless LAN communication; the SK (Smelter Knoll), BR (Black Rock) and LR(Long Ridge) Communication Tower (CT). The subarrays have 148, 170 and 189 SDs respectively. Each SD is powered by a battery, which is charged during the daylight with a solar panel that gives a power of 125W.

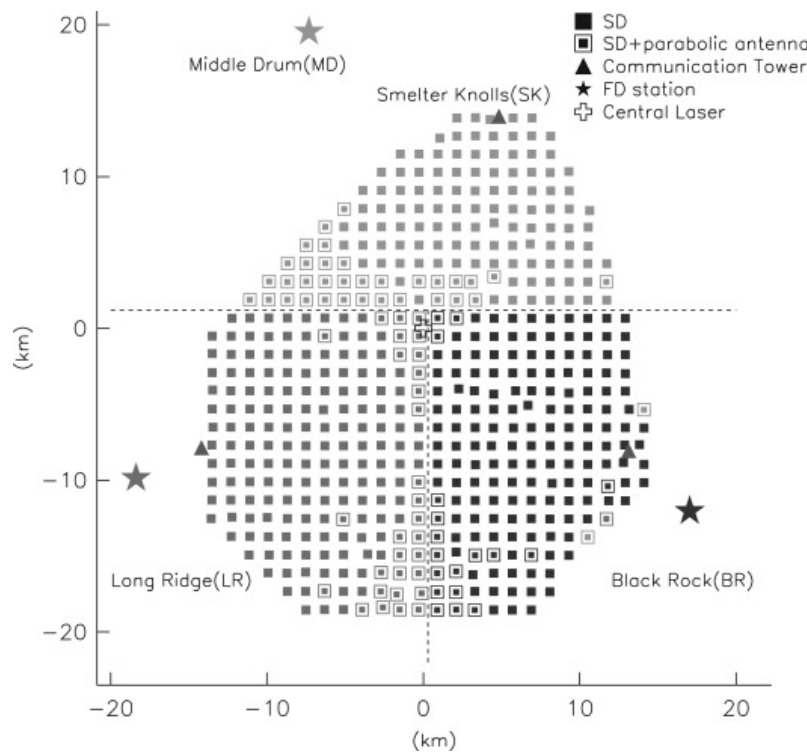


FIGURE 3.8: Layout of the TA-SD. Square symbol denote 507 SDs. There are three subarrays controlled by the communication towers denoted by triangles. The star symbols represent the FD telescopes [72].

Figure 3.9 shows the external parts of a surface detector. The sensitive part is the scintillator box of 3m^2 in dimension, which contains the scintillator and the photomultiplier tubes (PMTs). A square solar panel 1 m on one side is mounted on the platform to supply to the electronics. The electronics and the battery are contained in a box made of with 1.2 mm thick stainless steel is placed near to solar panel. And the communication antenna is mounted on a 3-m long iron pole as shown in Figure 3.9. The figure 3.10 shows the schematic of the inside of a

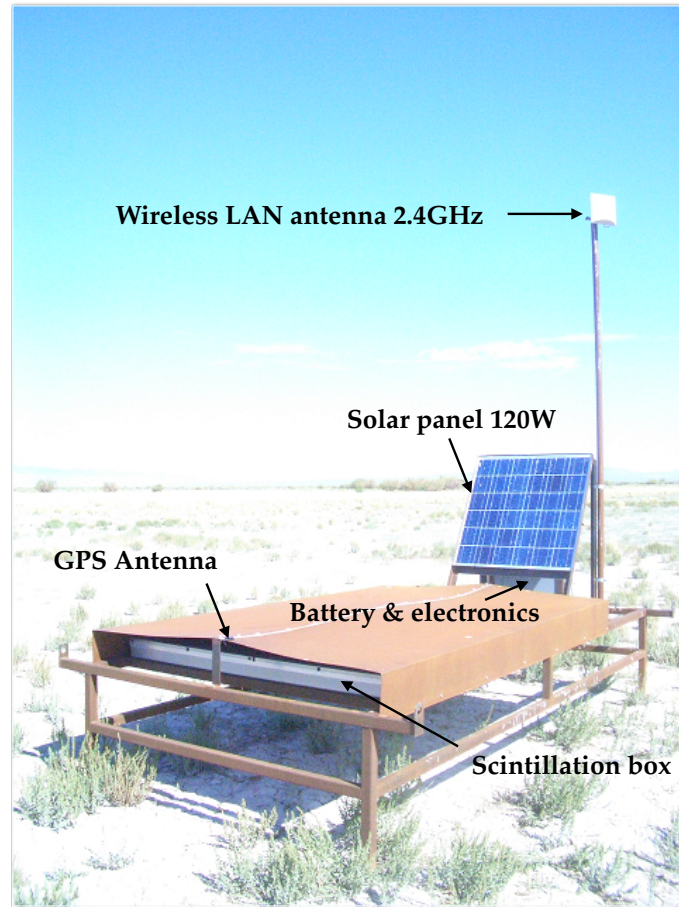


FIGURE 3.9: A description by main components of a surface detector deployed.

scintillator box. Each surface detector box consists of two layers (upper and lower) of plastic scintillator, which use polyvinyl toluene (C_9H_{10} , $1.032g/m^2$). Each layer of scintillator has an area of $3 m^2$ and a thickness of 1.2cm. A stainless-steel (SUS) plate has 1 mm in thickness and is inserted between layers. As described in Figure 3.10 each scintillator layer consists of two segments is $1.5 m \times 1.0 m$. On the top side of the plastic scintillator slab, there are grooves in parallel along the length of the slab where is setup 104 wavelength-shifting (WLS) fibers (Y-11; Kuraray). The segment is wrapped with two layer of Tyvek sheet. The end of WLS fibers from both edges of the slabs are collected together and connected to a PMT(9124SA; Electron tubes Ltd.) for each layer (upper and lower). The PMTs operate at 1000 V and provide a gain of 1.2×10^6 per photoelectron. When the shower of particles hit on the plastic detector by ionization process light will be generated and those will be collected and transmit to the PMT. The output signals from PMTs are digitized by

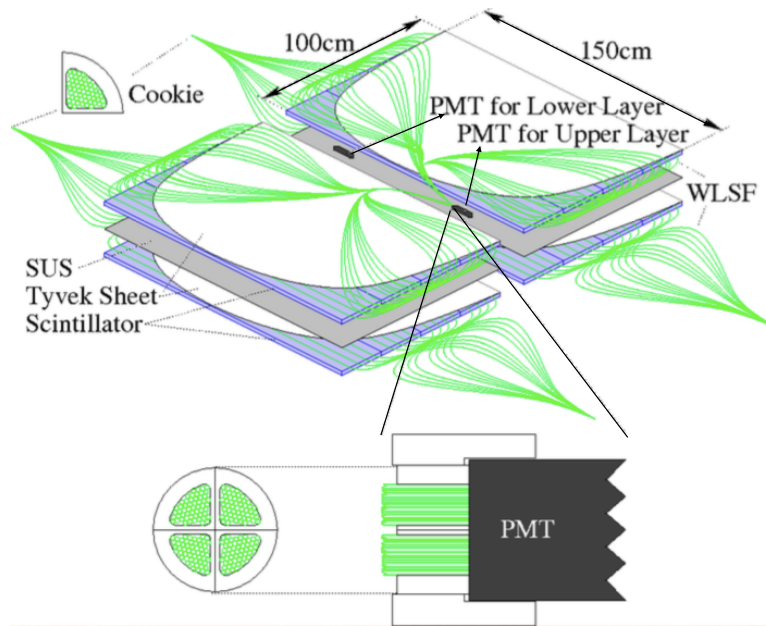


FIGURE 3.10: A cartoon for the description of inside scintillation box with scintillator plates, WLS fibers and PMTs. A total of 104 WLS fibers are laid on each layer to collect and transmit scintillation light to a PMT. Above picture shown the WLS fibers end collected to be connected to a PMT.

Flash Analog Digital Converters FADC in 12bits(channels) (AD9235RU-65; Analog Devices) with a 50 MHz sampling rate on the CPU board. The digitized PMT signal is called the waveform. The waveform is recorded with $2.56 \mu\text{s}$ wide that correspond in length 128 time bin, where each FADC bin is 20 ns.

3.2.1 Calibrations and trigger judgement

The calibration is based on the energy deposition of a vertical muon. Then it is defined the vertical-equivalent muon (VEM) unit of energy deposition to be $1 \text{ VEM} = 2.05 \text{ MeV}$, which is the most probable energy deposition for a vertical muon at the minimum ionizing energy (300 MeV or 0.3 GeV) (Figure 3.11). Cosmic ray muons travel at relativistic speeds at ground level, and are typically minimum ionizing particles. A commonly used approximation for dE/dx is $2 \text{ MeV}/(\text{g}/\text{cm}^2)$.

Each SD electronics suite also has a Field-Programmable Gate Array (FPGA) that continuously monitors the FADC waveforms to monitor pedestals and to determine whether the event trigger condition is met. When an SD measures a signal

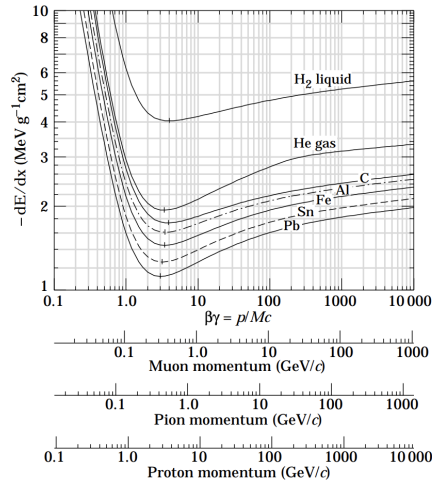


FIGURE 3.11: Mean energy deposition in a different medium by a vertical muon plotted versus muon kinetic energy. The minimum ionizing energy occurs at 300 MeV (0.3 GeV) [73].

above threshold, it can announce it to a remote Data Acquisition (DAQ) via radio communication. A SD can record two types of low-level triggers:

- A level 0 trigger, in which an integrated signal exceeding 15 FADC counts above pedestal is measured (~ 0.3 MIP Minimum Ionizing Particles).
- A level 1 trigger, in which an integrated signal exceeding 150 FADC (equivalent to 3 MIPs) counts above the pedestal is measured.

These remote DAQ locations are referred to as communication towers (CTs), as they monitor and receive data from many SDs and make the decision about high-level triggers based on the low-level trigger logic of all SDs that it communicates with. If three or more adjacent SDs announce level 1 triggers within an $8\mu\text{s}$ window then

- a level 2 event trigger, in which the CT directs all SDs that observed level 0 with $\pm 32\mu\text{s}$ of the event to send the waveform data to CT for storage.

Each SD has an onboard GPS unit to time-stamp event triggers, so the time of particle passage is also recorded by each SD and included as part of the event information. Figure 3.12 shows one of the communication towers. The communication and data transfer between a SD and a communication tower is done through a directional antenna equipped on 2.4 GHz wireless LAN modem (ADLINK540F). For the



FIGURE 3.12: The BR communication tower CT [75].

communication, a custom-made DAQ process is used [74]. The tower-to-tower communication is performed in 5.7 GHz band to avoid interference in the tower-to-SD communication.

Monitoring data acquisition

The TA SD unit constantly accumulates monitoring data every 10 min. cycle, during in a day 144 cycles are registered. Figure 3.13 shows an example of a SD with ID 0712 monitored. The monitoring data is divided into 600 subsets and all the subsets are sent along with the level-1 trigger tables every second. The acquisition and transfer of the monitoring data are synchronized by the GPS 1 second pulse (1-PPS). The monitoring data consists of the histograms and the status variables of every SD. Figure 3.13 shows of the time variations of the monitoring data. Muons at the minimum ionizing energy (around 300 MeV) are the most abundant atmospheric particles which penetrates the TA SD scintillator. So the level-0 triggers are dominated by minimum ionizing particles. Histograms of the level-0 signals (1 MIP) are used for determining the detector gain in FADC counts per MeV of energy deposition in each SD. The histogram is generated by integrating FADC counts of waveforms with the time window ranges between -4 bins from trigger timing and +8 bins after trigger timing. Here 1 bin corresponds to 20 ns. The pedestal histogram is also calculated to determine the base line of the FADC counts. Figure 3.14 shows an example of signal distribution by atmospheric charged particles, the integrated FADC value from level-0 used to estimate the total energy deposited

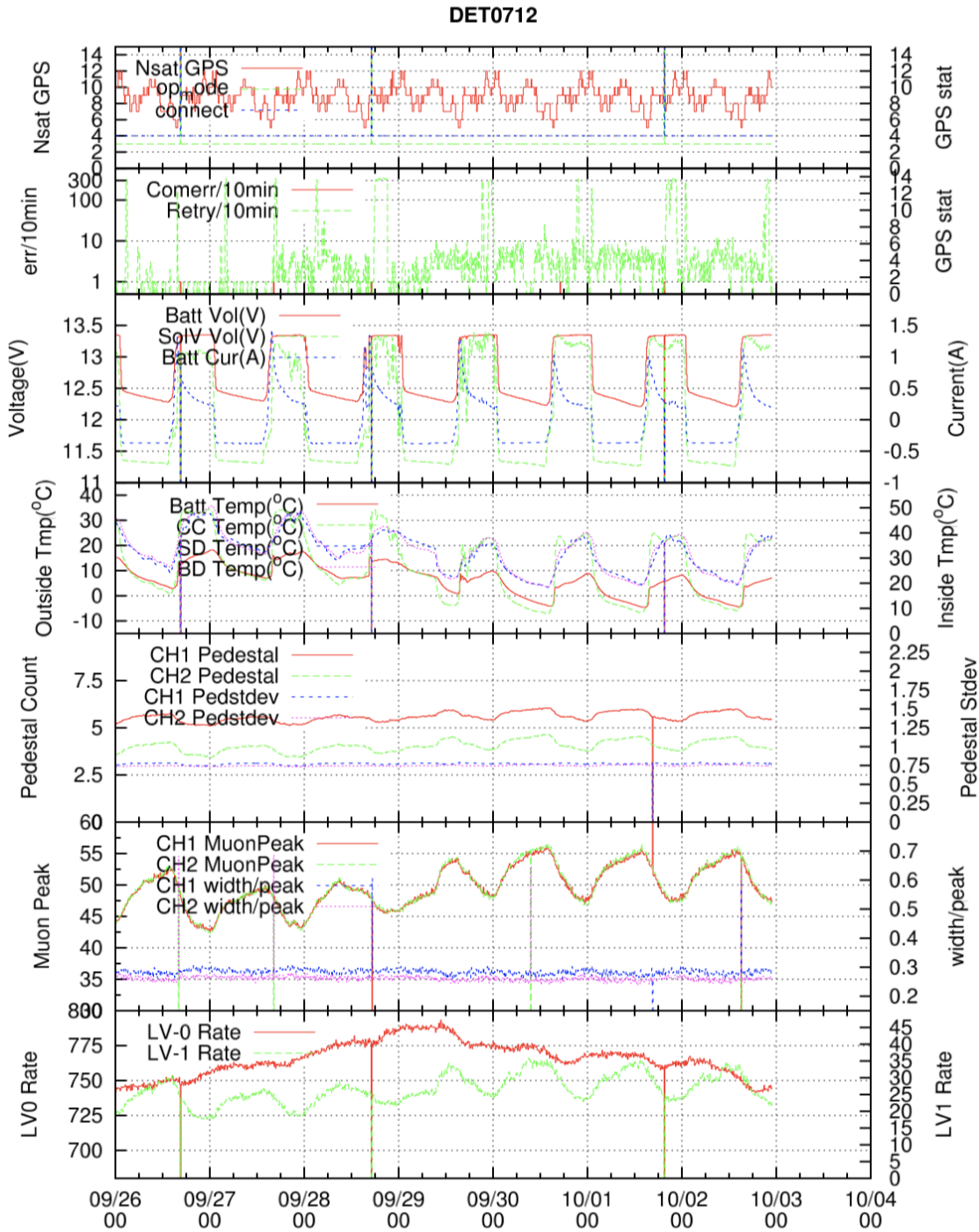


FIGURE 3.13: Sample of monitor data during 26 Sep. 2019 - 04 Oct. 2019 UTC. The number of detected GPSs is shown in the 1 st panel from the top. The 2 nd panel shows the communication status. The 3 rd panel, battery voltage, solar panel voltage and battery current. The temperature measured is shown in 4 th panel. The 5 th and the 6 th panel shows the pedestal value and 1 MIP FADC value, respectively. The 7 th panel describes the Level-0 and Level-1 trigger rate. There is a day-night variation in 1 MIP FADC value which has temperature dependence.

[72]. The histogram shape consists of energy loss distribution and zenith angle distribution of atmospheric muons, the position dependence (non-uniformity) of the response of the SD, Poisson distribution of the number of photoelectrons generated at the surface of the PMT and so forth [76]. The MIP peak value histogram as shown in the 6th panel of figure 3.13. This MIP FADC value variation is caused mainly by the variation of outside temperature. To understand the status of the GPS module, the visible number of satellites and conductivity of the antenna are read out in every 600 s.

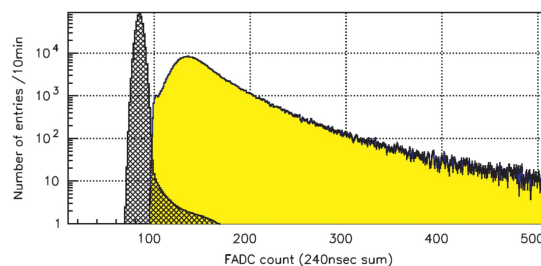


FIGURE 3.14: A typical TA SD counter signal monitored over a 10 min cycle from level-0 trigger events obtained as 1-MIP monitor data (yellow area). The black dashed area corresponds to pedestal histogram scaled in the same interval [72].

3.2.2 Event reconstruction using surface detectors

The TA SD air shower events are reconstructed in four steps [77]. At first the SD signals that are related to air shower events are selected. Then the event geometry is determined by the arrival time distribution of air shower particles at the SDs. Following that, the lateral distribution of air shower particles is obtained in the signal size at each SD. Finally, the energy is determined by reconstructed parameters, using the energy scale obtained by the hybrid observation.

Signal selection

The first scheme of the event reconstruction is signal selection. For each event, all the detector waveforms are scanned by 80 ns (4 time bins) sliding window. If all 4 time bins of the sliding window exceed the pedestal by 5σ in both upper and lower layers, the first time bin is regarded as the time of the signal. Here σ is the RMS of the pedestal per one time bin. Then if all 4 time bins of the sliding window

are no longer larger than 5σ , the time bin is considered as the signal end. This process separates the waveform into the multiple pulses in one waveform and reduce background signals from the random atmospheric muons, which occur at a rate of $700 \text{ Hz} \times 64 \mu\text{s} \simeq 0.05$ per counter within one event time period ($\pm 32\mu\text{s}$). After that, all pulses within $10 \mu\text{s}$ of the start time of the signal are summed and the integrated FADC values are obtained in each detector. Lastly, the average pedestal values are subtracted from the integrated FADC values, and they are converted to VEM units using calibration data. Next, the SD which belongs to the air shower event is selected by determining a cluster which is contiguous in space and time. If the distances of the SDs are into $\sqrt{2}$ times of the detector separation unit (1200 m), the SDs are included in a cluster in space. Also if the time difference of the SDs are within their spatial separation divided by the speed of light, the SDs are included in a cluster in time. This procedure can exclude random atmospheric muons, which occurs uniformly in space and time. Figure 3.15 shows a display of sample clustered SDs decided by the above procedure by the event map.

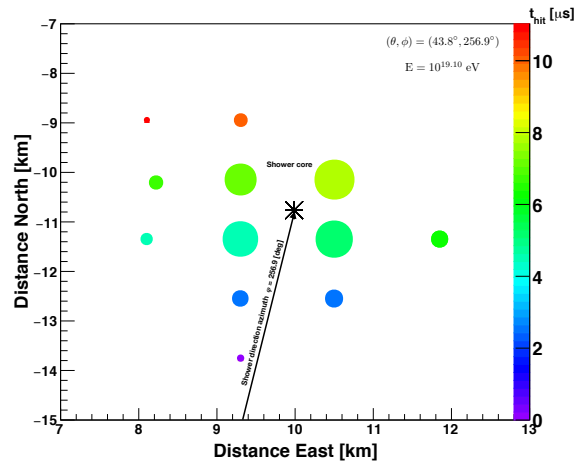


FIGURE 3.15: Example of one shower event recorded in 2019/05/04 $E=10^{19.10}$ eV and direction (θ, ϕ) : $(43.8^\circ, 256.9^\circ)$. The display represents the triggered TA SD, the color shows the relative hit time and the size of circles as proportional to the number of charged particles (VEM).

Event geometry determination

Figure 3.16 represents the shower front description when the core of the shower hit the ground. The direct observables, when the shower footprint the ground, are

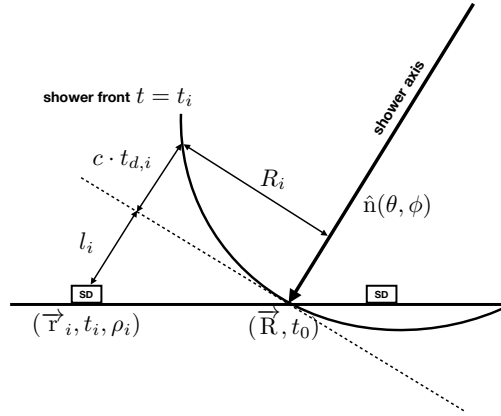


FIGURE 3.16: Side view of shower front at the time t_0 . And the geometry variables description.

the relative time t_i and the particle density ρ_i on each i SD, they are the starting values to reconstruct the geometry of a event shower. The first approximation of core location is derived from the center-of-gravity, where $\vec{R}_{COG} = (x_{COG}, y_{COG})$ and this vector is defined as;

$$(\vec{R}_{COG})_k = \frac{\sum_{i=1}^N \rho_i (r_i)_k}{\sum_{i=1}^N \rho_i} \quad (3.5)$$

this calculation is from the first calculation of the first moments of the pulse height distribution ρ , measured by N SDs. The 5 parameters related to the air shower event geometry are decided by detector time distribution and the particle density fitting respectively; the time t_0 when the core of the shower hits the ground, the core position $\vec{R} = (R_x, R_y)$, zenith angle θ and azimuth angle ϕ . The parameters are obtained while minimizing the function:

$$\chi_G^2 = \sum_{i=0}^N \frac{(t_i - t_i^{Fit})^2}{\sigma_{t_i}^2} + \frac{(\vec{R} - \vec{R}_{COG})^2}{\sigma_{\vec{R}_{COG}}^2}, \quad (3.6)$$

where t_i is the i^{th} detector trigger time and t_i^{Fit} is the time of the i^{th} detector as predicted by the fit function. The form t_i^{Fit} is,

$$t_i^{Fit} = t_0 + \frac{l_i}{c} + t_{d,i} \quad (3.7)$$

here l_i is the distance between the detector and the shower front plane at $t_0 = 0$,

$$l_i = (\vec{r}_i - \vec{R}) \cdot \hat{u} \quad (3.8)$$

where $\vec{r} = (x, y)$ is the detector position and $\hat{u}(\theta, \phi)$ is the unit vector of the shower axis projected onto the ground, $t_{d,i}$ is the residual time, the predicted function is the modified function from the Equation 2.16 explained from Section 2.5.1, respect to shower front curvature effect and the function is tuned for TA SD data. The empirical functions of residual time and its uncertainty that well describe the TA SD data are,

$$t_{d,i} = (8 \times 10^{-4})a(\theta) \left(1 + \frac{R_i}{30\text{m}}\right)^{1.5} \rho_i^{-0.5} \quad (3.9)$$

$$t_{\sigma,i} = (7 \times 10^{-4})a(\theta) \left(1 + \frac{R_i}{30\text{m}}\right)^{1.5} \rho_i^{-0.3} \quad (3.10)$$

$$a(\theta) = \begin{cases} 3.3836 - 0.018148\theta & : \theta < 25 \\ c_3\theta^3 + c_2\theta^2 + c_1\theta + c_0 & : 25^\circ \leq \theta < 35^\circ \\ \exp(-3.2 \times 10^{-2}\theta + 2.0) & : \theta > 35^\circ \end{cases}$$

where c_0 , c_1 , c_2 and c_3 are constants,

$$c_0 = -7.761668 \times 10^{-2}, c_1 = 2.99113 \times 10^{-1}$$

$$c_2 = -8.79358 \times 10^{-3}, c_3 = 6.51127 \times 10^{-5}.$$

And the σ_t is defines as

$$\sigma_i = \sqrt{\sigma_e^2 + t_{\sigma,i}^2}, \quad (3.11)$$

where $\sigma_e = 20$ ns is the resolution due to electronics. And $\sigma_{\vec{R}_{COG}} = 170$ m, which is the uncertainty of the center-of-gravity of pulse height distribution. Figures (a) and (b) 3.17 show an example of the event time fit and the lateral distribution funtion fit respectively.

Lateral Distribtution Fit

The next step to event reconstruction is the Lateral fit and the energy reconstruction. Based on AGASA experiment [18] to fit the shower size by using the definition of lateral profile

$$\rho = C \left(\frac{R_i}{91.6\text{m}}\right)^{-1.2} \left(1 + \frac{R_i}{91.6\text{m}}\right)^{-(\eta(\theta)-1.2)} \left(1 + \left[\frac{R_i}{1000\text{m}}\right]^2\right)^{-0.6} \quad (3.12)$$

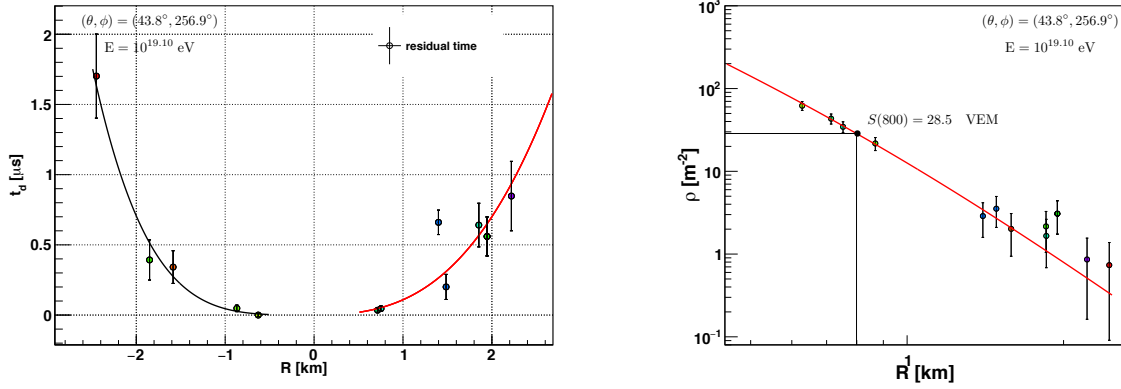


FIGURE 3.17: **(a)**: Plot of plane fit (start residual time with respect to the shower plane vs core distance). **(b)**: Plot of lateral distribution fit to the AGASA function. The color of dots represent the relative hit time as displayed on the event map (Figure 3.15).

where $\eta(\theta) = 3.97 - 1.79[\sec(\theta) - 1]$.

The uncertainties on [78] the pulse height density are adjusted to fit TA SD data by $\sigma_\rho = \sqrt{0.56\rho + 6.3 \times 10^{-3}\rho^2}$. The last two parameters of the geometry reconstruction is the obtention of LDF factor C and the core location \vec{R} by minimizing the function,

$$\chi_{LDF}^2 = \sum_{i=0}^N \frac{(\rho_i - \rho_i^{Fit})^2}{\sigma_{\rho_i}^2} + \frac{(\vec{R} - \vec{R}_{COG})^2}{\sigma_{\vec{R}_{COG}}^2} \quad (3.13)$$

After the time and lateral distribution fit, the primary cosmic ray energy is calculated from the integrated FADC values at 800 m from shower axis, called $S800 = \rho^{Fit}(800 \text{ m})$, and $\sec\theta$. For the corresponding conversion to energy relation, it was used a large statistics of MC set to reconstruct the energy estimation E table from these two parameters ($S800$ and reconstructed $\sec\theta$). Figure 3.18 represent the Energy table estimation, where y-axis in log scale is the $S800$ versus $\sec\theta$ and the bin color represent the correspondent energy. More details of Energy reconstruction is studied in [77].

It was explained in the Section 3.1.1, by comparison between TA SD energy derived by MC TA CORSIKA and the TA FD energy deposited the energy is estimated. As result the determination of energy for the event reconstruction of surface detector the energy has been reduced by a factor of 1/1.27.

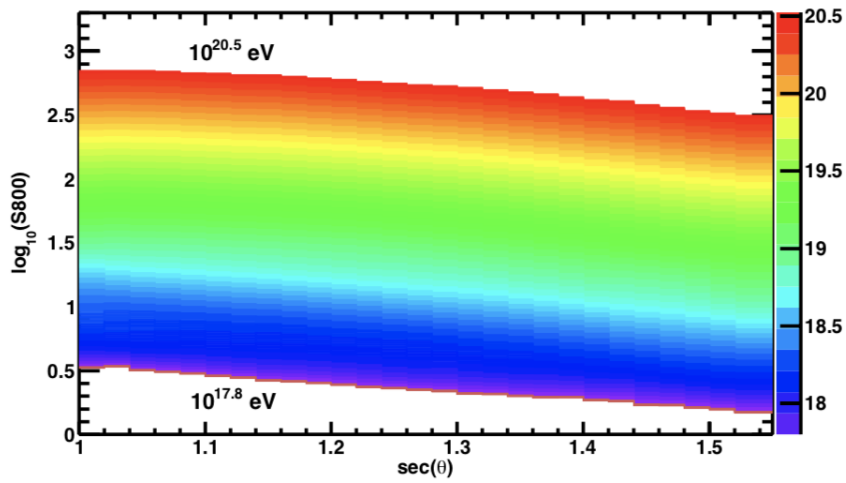


FIGURE 3.18: TA SD UHECR Energy estimation table [79].

Chapter 4

MC simulation and data status

This chapter describes the simulation technique for TA SD Monte Carlo (MC) to generate extensive air showers above 10^{17} eV using CORSIKA and simulation of the response of the TA surface detector to secondary particles by using Geant4 package. It also includes the comparison of the simulated distribution of MC and those of data to get the validation of how faithfully represents the data. The analysis of the curvature of the shower front, based on the residual time function, leads to the improvement in the angular resolution. Then, the analysis of time structure requires to know the accuracy in the determination of geometry as the angular resolution and core location resolution, then this chapter also shows the resolution of geometry for different energies binned.

In the sections that follow, it is described the events selection and the data cut criteria as well the data condition after cut selection.

4.1 Extensive air shower simulations

In this section we describe shortly the EASs simulations for TA SD. EASs are simulated with the Cosmic Ray Simulations for KASCADE (CORSIKA) package [80]. It was used Monte Carlo model QGSJET II-03 [81] as reference model for high energy hadronic interactions. The air shower MC with tracking all secondary particles, where 10^{11} particles are generated at shower maximum for a 10^{20} eV event, requires too large calculation time. For a single CPU core, one shower simulation for $E \sim 10^{20}$ eV takes part of a decade [82]. In monte carlo is popular used the method

called thinning, which particles are removed from consideration in the shower generation and other particles in similar regions of phase space are given weights to account for the loss.

But the thinning method does not fully reproduce the TA SD signal. The TA SD measures the lateral distribution of air shower particles at the ground [83]. The measured particles include those far from the shower axis (\sim km), where the average number of particles at a TA SD in a shower event is less than unity. The thinning approximation causes larger artificial fluctuation of the number of particles than non-thinned air showers [84].

In order to make more accurate simulation of the TA SD, dethinning method is applied, where each group of thinned particles was regenerated from its weighted representative (developed by [82, 84]). The idea of replacing the information lost in thinning is to start with a thinned shower, maintain the average density of particles, and smooth the distribution to get the correct amount of fluctuations. A brief description of thinning is described. Let E_0 and ϵ denote the primary energy cosmic ray energy and thinning level parameter. The simulation is generated for a given ϵ value, which is 10^{-6} for TA SD MC. For each step of the interaction of each shower particle, two situations are possible; 1) $\sum_j E_j < \epsilon E_0$ and 2) $\sum_j E_j > \epsilon E_0$ where j describes the secondary particles generated in the interaction and E_j is the energy of each particle. If $\sum_j E_j < \epsilon E_0$, one secondary particle survives with probability $p_i = E_i / \sum_j E_j$. If $\sum_j E_j > \epsilon E_0$, one of the secondary particles of energies $E_i < \epsilon E_0$ survives in the secondary particles with probability $p_i = E_i / \epsilon E_0$ and all particles with $E_i > \epsilon E_0$ are kept. In both cases, surviving particles have the weight of $w_i = 1/p_i$. The weight of a particle reaching the end of the simulation after passing through numbers of interaction steps is $w_{i,total} = \prod_k 1/p_k$, where k describes each step. This algorithm conserves the total energy; the weighted sum is equal to the energy of the primary particle that initiated the shower. In the dethinning method, $w - 1$ particles are inserted to every ground particle of weight w generated by the simulation with thinning. When this is completed the weight of each particle is set to 1. To insert these particles we use the following procedure [82].

1. An arbitrary vertex point on the trajectory of the weighted particle is chosen.

2. A point in a cone centered on the particle's trajectory is chosen, weighted by a 2-dimensional Gaussian distribution with a sigma of a few degrees. This will be the inserted particle's trajectory.
3. Project the inserted particle to ground level, assign it a time and energy, and add it to the particle list of the dethinned shower.
4. Perform steps 2 and 3 for $w - 1$ times.

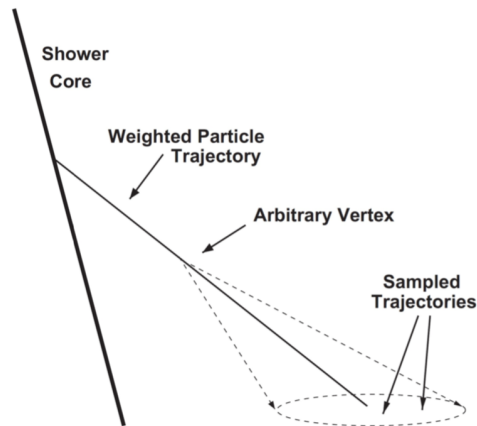


FIGURE 4.1: Description of thinning method [80]. The thick and thin solid lines show the primary and secondary particle tracks, respectively.

Figure 4.1 shows the geometry to describe the procedure. The dethinning CORSIKA simulations are used for the TA-SD simulations. Each CORSIKA shower is used repeatedly with random different core positions to reduce the calculation time. For SD simulations with proton (p) primaries, each proton shower is also used repeatedly with random different zenith and azimuthal angle.

4.2 Detector simulation

After generated the events showers, the energy deposit processes on each TA-SD is simulated by GEANT4 (simulation package) in geometry and materials. Deposited energies in scintillator layers for a given particle type, momentum and trajectory. Then, energies deposited in the scintillators and time dependent SD calibration information are combined for simulation of digital output waveforms by SD electronics.

All trigger conditions processes are described in Section 3.2.1 is also included in the calculations. For each condition, two dimensional histograms of energy deposition in upper and lower layers are generated and recorded as same FADC waveforms format as the real data.

Finally, the output file of an air shower event simulated by CORSIKA consists in the position, momentum and timing $(x, y, z, p_x, p_y, p_z, t)$ of each particle on the ground is recorded. Where p_n means the momentum in the n direction and t the relative time when reaches on the ground. The following Table 4.1 summarizes the input parameters to generated events of TA SD.

Parameters	Sampling method
Primary	Proton
Energy	$E^{-2.81}: 10^{18.65} \text{ eV} \leq E < 10^{19.75} \text{ eV}$ $E^{-5.1}: 10^{19.75} \text{ eV}$
Zenith angle	$\theta: 0^\circ - 60^\circ$ ($\sin\theta\cos\theta$ uniformly distributed)
Azimuth angle	$\phi: 0 - 360^\circ$ (random distributed)
Core position	Randomly distributed inside a circle of 25 km radius (from CLF).

TABLE 4.1: Table of TA SD Monte Carlo simulated condition.

4.3 Data and Monte Carlo of TA SD comparison

This section describes the condition of Telescope Array of Surface Detector data by comparing with MC simulations to ensure that the MC simulations used in the event reconstruction reproduce accurately the observable data. The condition of MC data was described in the Table 4.1 and it was applied the same reconstruction procedure for the MC dataset. The following set of Figures 4.2, 4.3 and 4.4 show the typical distribution of reconstructed parameters of TA SD data during 6 years from May-11-2008 to May-11-2014. These distributions include the TA standard analysis condition in the process of reconstruction, the geometry reconstruction is validated for zenith angle $\theta < 55^\circ$ and energy $E > 10 \text{ EeV}$ [85].

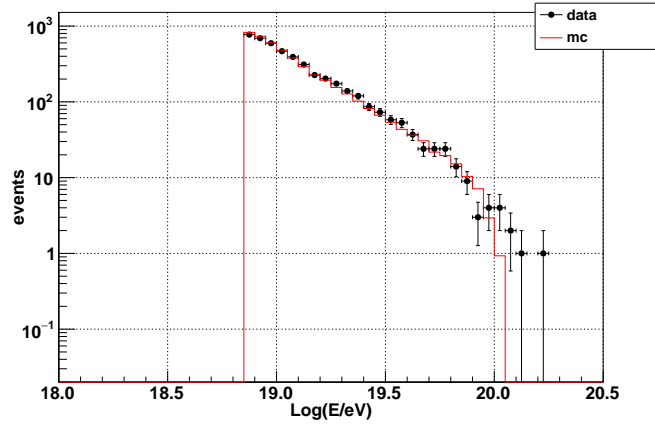


FIGURE 4.2: The distribution of primary energy $E > 10^{18.85}$ eV and zenith angle condition $\theta < 55^\circ$ for data of TA SD and MC SD reconstructed. The comparison corresponds from May 11, 2008 to May 11, 2014.

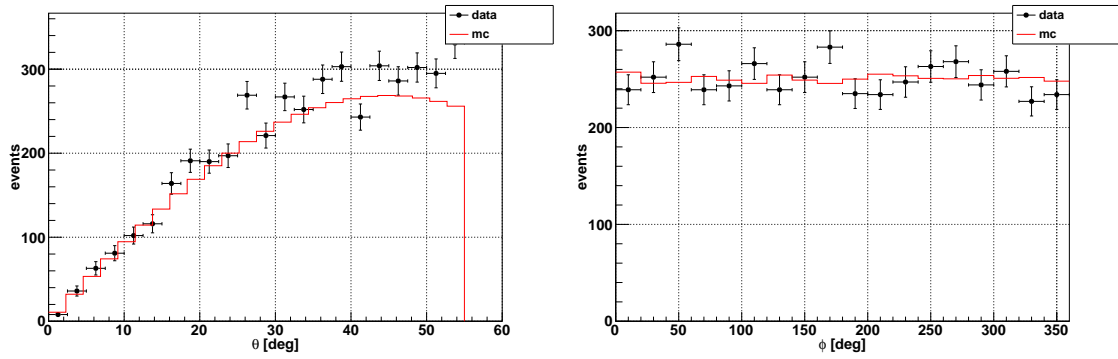


FIGURE 4.3: The comparison of reconstructed zenith angle (left) and azimuth angle (right) of data and MC, black and red dots respectively.

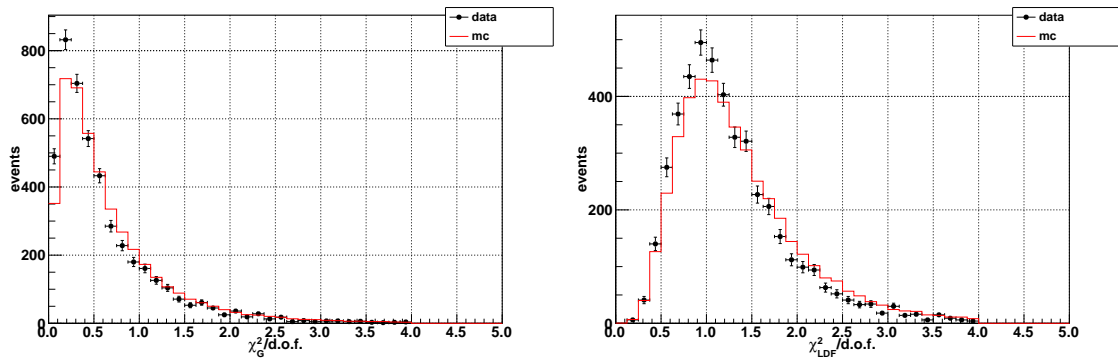


FIGURE 4.4: The comparison of $\chi_G^2/\text{d.o.f}$ (left) $\chi_{LDF}^2/\text{d.o.f}$ (right) values distribution for data and MC.

Figure 4.2 shows the energy distribution above $10^{18.85}$ eV, which is from the

low energy used in the analysis. Figures 4.3 show the zenith and azimuth angles distribution, and Figure 4.4 gives the distribution of $\chi_G^2/\text{d.o.f}$ and $\chi_{\text{LDF}}^2/\text{d.o.f}$ values of geometry and lateral distribution fitting.

4.4 Resolutions

In order to see the resolution of TA SD, which is reconstructed Monte Carlo parameters set compared with the true variables (thrown), this process is made with the same data reconstruction programs and it is applied the quality cuts as in the data.

The angular resolution is characterized by considering the distribution of the opening angle (σ_θ) between the shower direction thrown $\hat{n}_{\text{thr.}}$ and the direction reconstructed $\hat{n}_{\text{rec.}}$,

$$\sigma_\theta = \cos^{-1}(\hat{n}_{\text{rec.}} \cdot \hat{n}_{\text{thr.}}) \quad (4.1)$$

where $\hat{n}_{\text{rec.}}(\theta_{\text{rec.}}, \phi_{\text{rec.}})$ and $\hat{n}_{\text{thr.}}(\theta_{\text{thr.}}, \phi_{\text{thr.}})$ are the unit vectors. For the determination of resolution of core location is used the definition of,

$$\Delta R = \sqrt{(X_{\text{rec.}} - X_{\text{thr.}})^2 + (Y_{\text{rec.}} - Y_{\text{thr.}})^2} \quad (4.2)$$

Figures 4.5 show two examples of the histograms of opening angle and ΔR of air shower for a certain energy bin, more plots for different bins is shown in Appendix A. In both cases of histogram were chosen the 68% confidence limits for TA-SD the angular resolution and the core location resolution.

Figure 4.6 of right panel shows the summary of angular resolution for different energy bin calculated from histograms of opening angle and the bias of core location at 68% as shown on Figure 4.5, the resolution of arrival direction vary from 1.3° to 0.9° for highest energy. In our analysis of data for shower structure was used mainly three energy range around 10^{19} , $10^{19.3}$ and $10^{19.8}$ eV respectively as shown by color range. The resolution of core position is summarized on right side of Figure 4.6, the core position is found typically with a resolution of ~ 140 m for low energy $10^{18.8}$ eV and for highest energy at 10^{20} eV is ~ 240 m. More details can be found in the appendix A.2 and A.7.

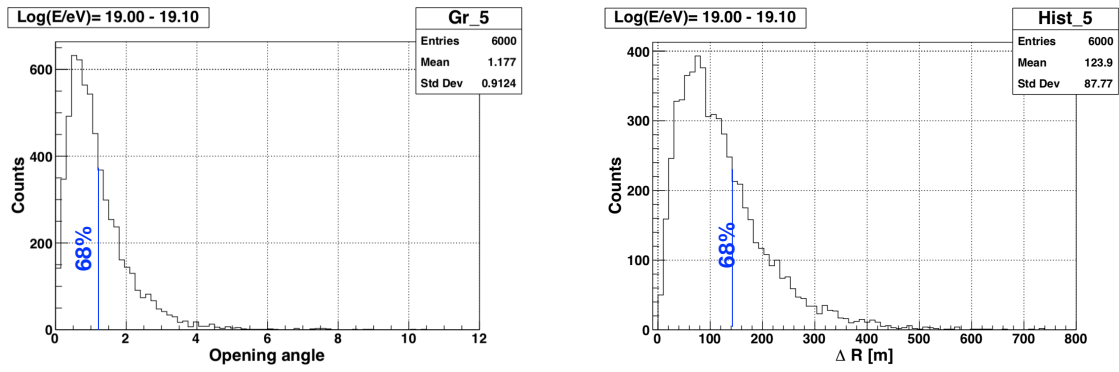


FIGURE 4.5: Left: Histogram of opening angle, and the blue dash line at 68% for a bin average of energy $E \sim 10^{19.05}$ eV and $\sigma_\theta \simeq 1.2^\circ$. Right: Histogram of resolution of core location for a bin average energy $E \sim 10^{19.05}$ eV and $\Delta R \simeq 140$ m.

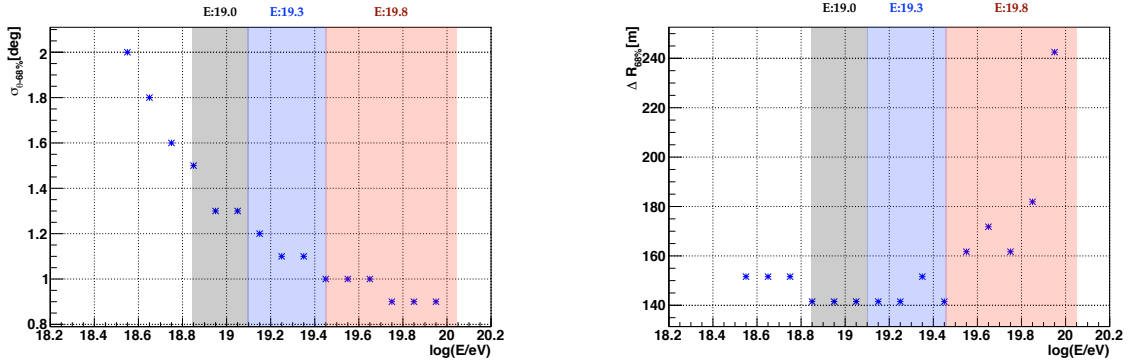


FIGURE 4.6: Left plot shows angular resolution versus energy. Right plot shows resolution of core location.

4.5 Event selection and data cuts criteria

During the geometry and energy reconstruction of the event showers, there are contaminations of inaccurately reconstructed events even if reconstruction process are successfully finished. Those events misreconstructed could have large fluctuations on the determination of different variables. Therefore, it is necessary to exclude these inaccurately reconstructed events from the analyzed event data set. The main quality cuts have been designed and optimized in the event reconstruction process by [77]. TA SD has the standard selection cut of events $\chi_G^2/\text{d.o.f.} < 4$ and $\chi_{\text{LDF}}^2/\text{d.o.f.} < 4$ both reduced by χ^2 (per degree of freedom) values of geometry and lateral distribution fits. The uncertainty of S800, which is the final cut to improve the energy resolution, given by the fractional uncertainty on S800 based on the normalization

constant of the AGASA LDF (denoted by C), which is a fit parameter proportional to S800 (particle density evaluated at 800 m). This fractional is given by,

$$\sigma_{S800}/S800 = \sigma_C/C, \quad (4.3)$$

where, σ_C is the fit parameter uncertainty given by MINUIT (math library) when the χ^2 of Equation (3.13) is minimized. An additional quality cut is for well events reconstruction, it is the border cut, where the event core position should be 1200 m inside of the TA array as well the minimum number of SDs triggered is 5 to higher for any event reconstructed, these standard selection criteria is described in details [86] for TA SD reconstruction.

Besides to main quality cuts described above, in the our main analysis of study time structure, it was considered other quality cuts for the respective analysis. In both the shower front and thicknes of the shower disk which were considered some selection rules based on geometrical parameters as well energies. The following section will describe the summary of the selection of shower events in order to study time structure. Those are applied in the 11 years of TA SD data from 2008-05-11 to 2019-05-10.

Selection rules of the shower front curvature

Measurements of residual time, t_d , based on observations of nearly 9097 events above $10^{18.90}$ eV without any selection, collected in 11 years after passing standard selection cut as described previously. It was analyzed 3 intervals of energy $18.90 \leq \log(E/\text{eV}) \leq 19.08$ with 4640 events, $19.15 \leq \log(E/\text{eV}) < 19.45$ with 2478 events, and $19.45 \leq \log(E/\text{eV}) \leq 20.05$ with 795 events. The next list up shows the summary of the standard selection cut and the total interval of the zenith angle analyzed.

- Zenith angle cut: $0^\circ < \theta \leq 60^\circ$
- Border cut: 1.2 km inside of array
- Geometry and LDF fit quality cut, $\chi_G^2/\text{d.o.f.} < 1.5$, $\chi_{LDF}^2/\text{d.o.f.} < 4$ (d.o.f is the number of degrees of freedom).

- Numbers of SD triggered 6 or more.
- The uncertainty estimation of lateral distribution fit ($\sigma_{800}/S(800)) < 25\%$.

Selection rules for the thickness of the shower disk

It was used a total of 23773 events collected for the analysis of the thickness of shower disk by measuring the risetime, t_R , above $10^{18.60}$ eV. The following intervals of energy $18.60 \leq \log(E/eV) \leq 18.85$ with 16882 events, $18.85 < \log(E/eV) < 19.15$ with approximately 7603 events, $19.15 < \log(E/eV) < 19.45$ with 2478 events, $19.45 \leq \log(E/eV) \leq 20.05$ with 795 events, being the last 3 intervals of energy the main used in the analysis. The following list up shows the standard event selection cuts and selection of SDs cut.

- Zenith angle cut: $0^\circ < \theta \leq 60^\circ$.
- Border cut: 1.2 km inside of array
- Geometry and LDF fit quality cut, $\chi_G^2/\text{d.o.f.} < 1.5$, $\chi_{LDF}^2/\text{d.o.f.} < 4$ (d.o.f is the number of degrees of freedom).
- Numbers of SD triggered 6 or more
- For the integration of the waveform was used all continuous waveforms stores independently as upper/lower layers (cutting $\sim 11\%$ of total SD data due to discontinues waveforms).
- To reduce accidental muons signal: hit time of up/lo layer rejection ($t_{\text{up}} - t_{\text{lo}}) \leq 200$ ns (cutting $\sim 5\%$ of total SD data).

The following Figures 4.7, 4.8, and 4.9 show an example of the interval of energy $10^{19.15} - 10^{19.45}$ eV used for the analysis, the distribution of energy, zenith angle, azimuth angle, $\chi_G^2/\text{d.o.f.}$ and $\chi_{LDF}^2/\text{d.o.f.}$ parameters are reconstructed by data and MC after selection cuts. The distribution of MC is normalized to data numbers of events, the number of events during May 11 2008 to May 11 2014 is 1148 events.

Figure 4.10 shows the distribution of core distance calculated for data and MC for each SD for the same condition of energy interval of $10^{19.15} - 10^{19.45}$ eV.

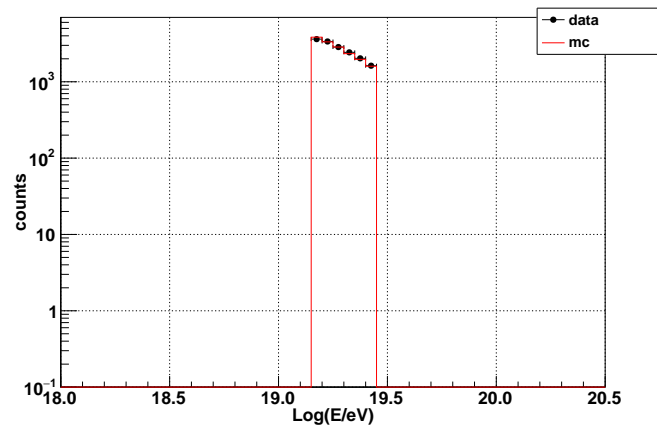


FIGURE 4.7: Distribution of primary energy in the interval of $10^{19.15} - 10^{19.45}$ eV for data of TA SD and MC SD reconstructed respectively. The comparison corresponds from May 11, 2008 to May 11, 2014.

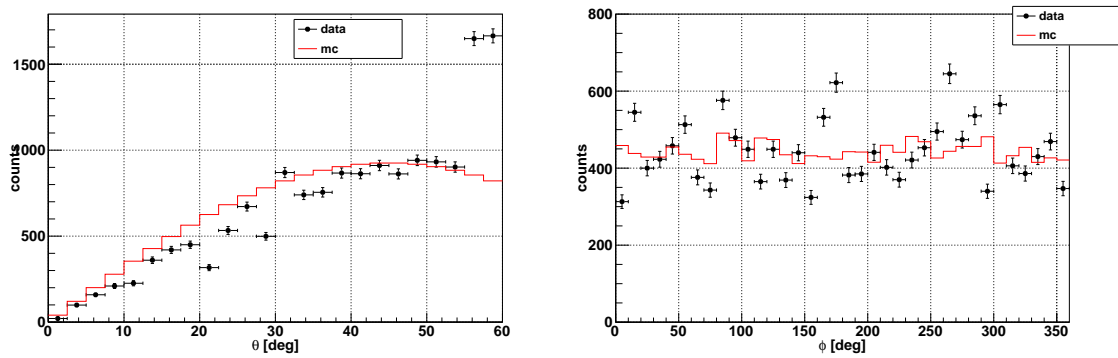


FIGURE 4.8: The comparison of reconstructed zenith angle (left) and azimuth angle (right) of data and MC, black and red dots respectively. The distributions are for energy range $10^{19.15} - 10^{19.45}$ eV.

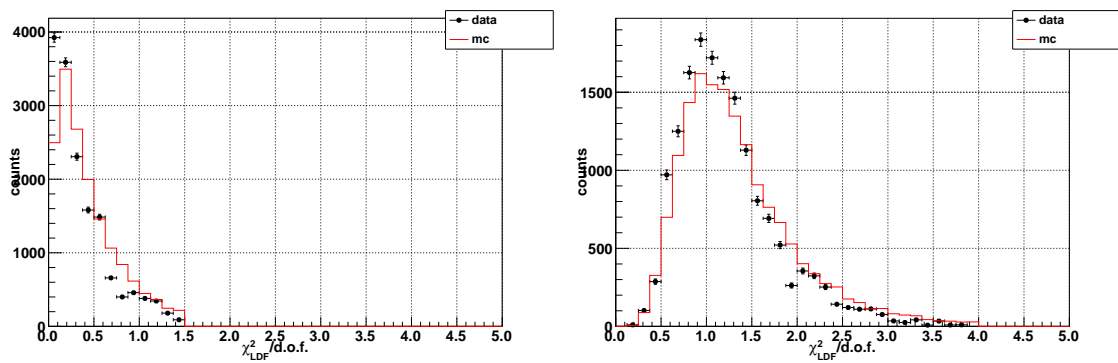


FIGURE 4.9: The comparison of $\chi_G^2/\text{d.o.f.}$ (left) and $\chi_{LDF}^2/\text{d.o.f.}$ (right) distribution for data and MC. The distribution is for energy range $10^{19.15} - 10^{19.45}$ eV.

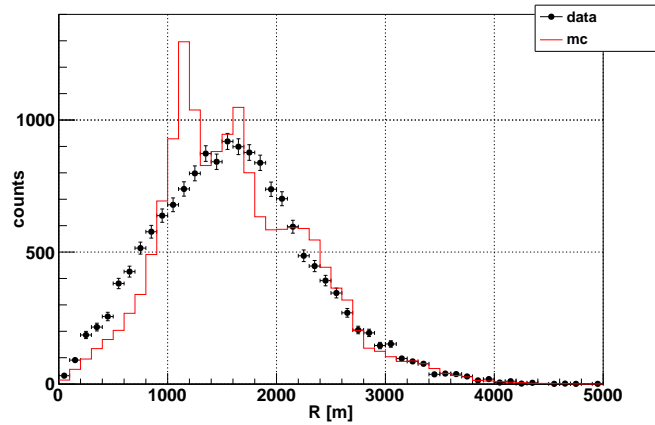


FIGURE 4.10: Distribution of core distance R comparison for data and MC. The distribution is for energy range $10^{19.15} - 19.45$ eV.

4.6 Events after passing the selection criteria

The following Table 4.2 describes in detail the shower events of TA SD data after passing the selection criteria and the total events without the cuts, according to the intervals of energy and zenith angle for the analysis of the curvature of shower.

$\sec(\theta)$	θ [deg]	$10^{18.90} - 10^{19.08}$ eV	$10^{19.15} - 10^{19.45}$ eV	$10^{19.45} - 10^{20.05}$ eV
1.0 - 1.2	0 - 33.6	1077/1562	538/799	183/293
1.2 - 1.4	33.6 - 44.4	716/949	363/503	117/165
1.4 - 1.6	44.4 - 51.3	472/634	224/316	88/127
1.6 - 1.8	51.3 - 56.2	402/521	187/234	60/81
1.8 - 2.0	56.2 - 60.0	302/380	207/262	47/66
totals		2969/4046	1519/2114	495/732

TABLE 4.2: List up of shower events collected in 11 years of data by TA SD used in the curvature shower front analysis, listed up by intervals of energy and zenith angle ($0^\circ < \theta \leq 60^\circ$).

The next Table 4.3 shows the summary of events after selection cut and the total events without cut in the different intervals of energy and zenith angle in the range $0 < \theta \leq 60^\circ$ used in the analysis of the thickness of the shower disk.

$\sec(\theta)$	$10^{18.60} - 10^{18.85}$ eV	$10^{18.85} - 10^{19.15}$ eV	$10^{19.15} - 10^{19.45}$ eV	$10^{19.45} - 10^{20.05}$ eV
1.0 - 1.2	2856/4250	1758/2541	538/799	183/293
1.2 - 1.4	2231/3100	1171/1563	363/503	117/165
1.4 - 1.6	1577/2083	773/1037	224/316	88/127
1.6 - 1.8	1041/1361	642/848	187/234	60/81
1.8 - 2.0	674/883	500/644	207/262	47/66
totals	8379/11677	4664/6633	1519/2114	495/732

TABLE 4.3: List up of shower events collected in 11 years of data by TA SD for the analysis of the thickness of shower disk, listed up by intervals of energy and interval of zenith angle ($0^\circ < \theta \leq 60^\circ$).

4.7 Trigger condition of SDs

This section is illustrated the trigger condition of SD for several intervals of zenith angle and energy, same used in the analysis for the curvature of shower front and thickness of shower disk.

Figure 4.11 shows the histogram of SDs triggered by a low energy interval of $10^{18.90} - 10^{19.08}$ eV for the curvature of shower front analysis. For close to vertical shower the typical number of SDs hit is 10 SDs, while increasing the zenith angle the average number of SDs triggered is 12. In the plot also shows the number of events in the corresponding interval of zenith angle.

The histogram of SDs triggered for a higher interval of energy is between $10^{19.15} - 10^{19.45}$ eV as shown in Figure 4.12. In this interval of energy, the number of SDs for vertical showers is about 12 SDs and for inclined showers, the number in average is 17 SDs. The number of events in each condition of zenith angle interval also decreases for large zenith angle.

The highest interval of energy is between $10^{19.45} - 10^{20.05}$ eV, for the analysis of the curvature of shower front and the thickness of shower disk, is shown in Figure 4.13. The frequency of events is low but the distribution of SDs triggered for vertical goes from 8 to 16 SDs, and for large zenith is in average of 20 SDs hit.

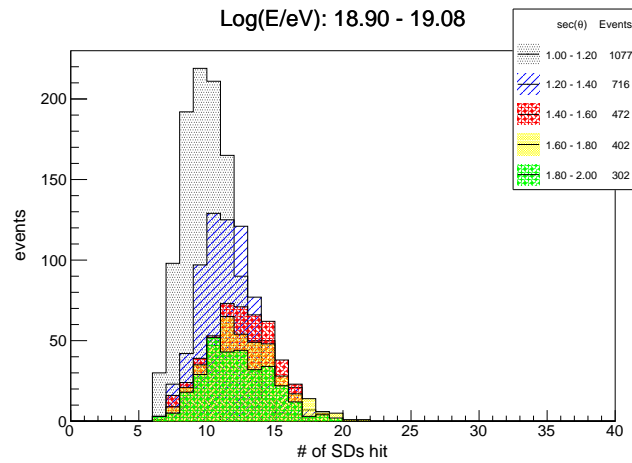


FIGURE 4.11: Number of SDs hit for low energy range of $10^{18.90} - 10^{19.08}$ eV. For various intervals in $\sec\theta = 1.0 - 2.0$ in step of 0.2.

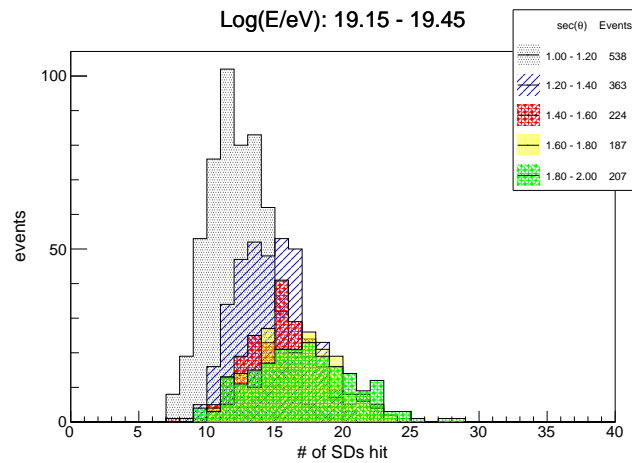


FIGURE 4.12: Number of SDs hit for higher energy range interval $10^{19.15} - 10^{19.45}$ eV. For various interval in $\sec\theta$ in step of 0.2.

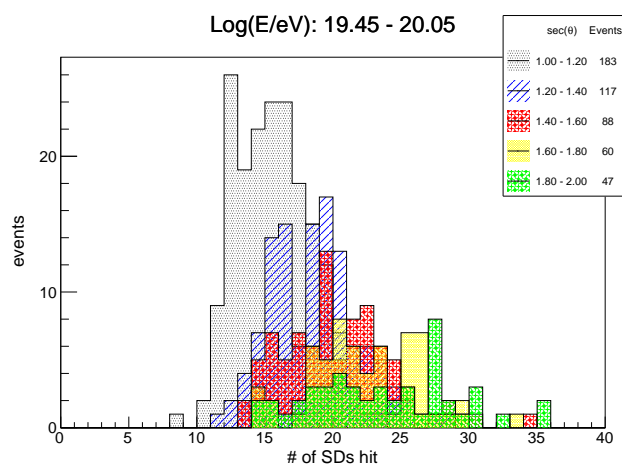


FIGURE 4.13: Number of SDs hit for the highest energy interval of $10^{19.45} - 10^{20.05}$ eV. For various interval in $\sec\theta$ in step of 0.2.

Chapter 5

Shower front curvature analysis with TA SD data

This chapter is dedicated to study the relative times of arrival of shower particles at large distance (500 to 2500 m) from the shower axis. Based on air shower events selected from the data taken at the Telescope Array Surface Detector, using the array of 507 scintillation detectors. The importance of know in details the characteristics of air showers phenomenology at very UHECR with energies higher than 10^{18} eV and with enough statistics. The particles which are detected in an EAS array have travelled out to a large radial distances from an origin in the core region of the shower. The electron-photon from EM component is in general the product of cascades which have been laterally dispersed by Coulomb scattering, while a significant portion of a lateral spread of the muons is due to the transverse momentum imparted to them at production. These two types of particles electrons and muons are generated along the entire length of the core of shower and combine to form the shower front.

5.1 Time structure of the shower front

The early investigations the time structure with highest energies was made by several experiments leaded by [87, 55, 88]. However, this work is merely based on experimental data and with enough statistics and the main deal is present the characteristics of showers front based on the study of AGASA function of residual time

and understands its phenomenology by analyzing the dependencies on several geometrical parameters. For this purpose, it is introduced the basic description of the components of residual time which conform the analysis starting from the signal of FADC trace, hit time, time at core position and so on.

5.1.1 Definiton of hit time t_{hit}

The stamp time on surface detector is stored on the waveform trace which is represented in the example of the left Figure 5.1, where y-axis is the FADC counts and x-axis number of bins. The typical waveform is stored in one frame 128 FADC bins. Right side of Figure 5.1 is the the waveform accumulated in unit of microsecond since 1 bin is equivalent to 20 ns, then the maximum value of waveform is stored in 2.56 microseconds. The hit time is occurred at the point the waveform start to rise and it is measured when the signal is greater than 0.3 minimum ionizing particles (MIP) and this is calculated by

$$t_{\text{hit}} = \left(\frac{\text{clkcnt}}{\text{mclkcnt}} \times 10^6 + 0.02 \times \text{Start Bin}_{\text{rise}} + \text{SDtime}_{\text{corr.}} \right) [\mu\text{s}], \quad (5.1)$$

here the relative time is synchronized using GPS by PPS signals, then the relative time is denoted clock-counts (clkcnt) and the maximum-clock-count (mclkcnt) which correspond to 50 MHz sub-clock and the Start Bin_{rise} is considered at 0.3 MIP and SDtime correction due to GPS time offset (-260 ns) and the SD trigger time offset correction (-600 ns).

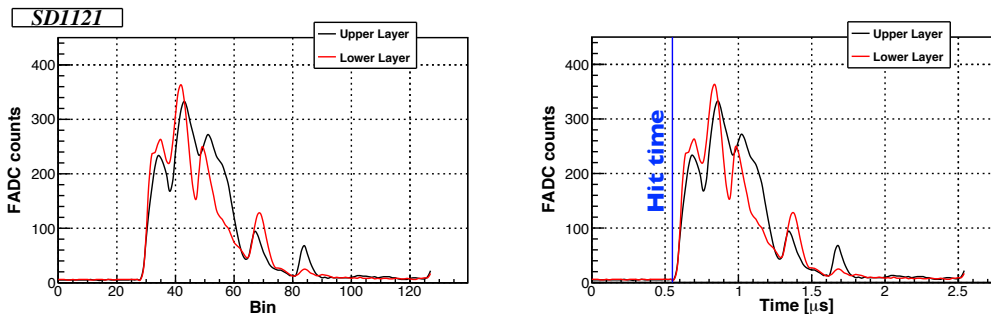


FIGURE 5.1: Left panel: a typical waveform recorded in TA SD counter, the y-axis represents FADC counts versus number of bin. Right panel: FADC waveform in units of time, the blue line is the hit time.

The arrival time of the incoming shower front is deduced from the one set of the signals pulse printed on the ground and collected by SD ground detectors. To measure the temporal characteristics, it can be considered the delays of particles arrival times with respect to the earliest arrival in the set of individual events. The following Equation describes the arrival time distribution.

$$\tau_i^n = t_i^n - t_{\text{earliest}}^n \quad (5.2)$$

Where τ_i^n and t_i^n are the delay and the absolute arrival time respectively of the i^{th} particle in the n^{th} event. As a result, it is possible determine the delay distribution in the individual events. The following examples of arrival distribution are measured from TA SD data for specific events.

Figure 5.2 shows three examples of delay of particles by shower events recorded by TA SD with different zenith angle for energies around of $10^{19.0}$ eV. The left plot shows the waveforms for an event with zenith angle close to **vertical shower** with $\theta \sim 1^\circ$, this event shower counts 8 SDs triggered and whose arrival time vary from $0 \sim 1.2$ [μs] this time is very short due this shower almost vertical and all arrival time sequence is very close each other SD. The second case corresponds to an event of **middle zenith angle** $\theta \sim 47^\circ$ with 10 SDs triggered and the time arrival duration is ~ 11.4 [μs] between the first SD hit and the last SD hit. And the right set of plots is an example of a typical **inclined shower** event with $\theta \sim 60^\circ$ with 13 SDs hit where the time duration of arrival time of inclined event is a little longer than the previous events with approximately 14 [μs].

It is important to clarify that the time delay distribution or sequence of SD hit respect to the first particle "locally detected", it does not precisely describe the particle distribution of the one event shower [89], for this purpose, the residual time definition is introduced to understand the properties of the temporal structure of the shower front curvature.

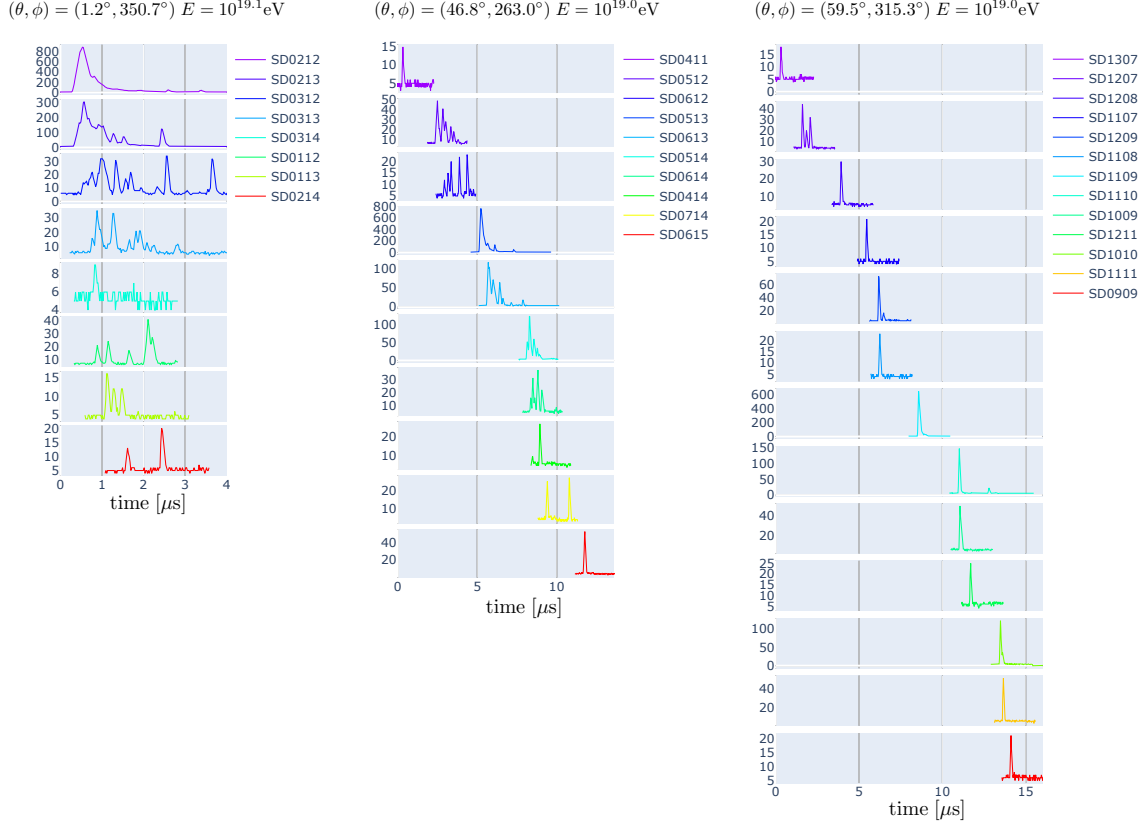


FIGURE 5.2: The arrival time distribution represented by FADC traces of each SD, the three set of plots represent event showers particles delay. Left figure shows an event recorded in 2008-10-09 with direction $\theta = 1.2^\circ$ and $\phi = 350.7^\circ$ and energy $10^{19.1} \text{ eV}$. Middle figure shows an event with zenith and azimuth angle of $(\theta, \phi) = (46.8^\circ, 263^\circ)$ with primary energy $10^{19.0} \text{ eV}$ recorded in 2017-04-15. Right set of plots correspond to an inclined shower event recorded in 2017-02-13, with arrival direction $(\theta, \phi) = (59.5^\circ, 315.3^\circ)$ and energy $10^{19.0} \text{ eV}$.

5.1.2 Definition of residual time (t_d)

In order to analyze the shape of the arrival time distribution, it has been considered the time fluctuation respect to the "zero" time or the time at the lowest point from the shower front. The "zero" time or time at core position is denoted by t_0 . The residual time t_d around the shower plane is found by the hit time t_{hit} and times at core location t_0 and time plane-SD t_{plane} as shown in Figure 5.3. The spread of the arrival time is related to the geometry of each event of the shower, where t_{plane} is estimated by l/c , where $l(\theta, \phi)$ is the distance from the shower plane to the SD along the shower axis direction, and if one assumes particles travel in the speed of

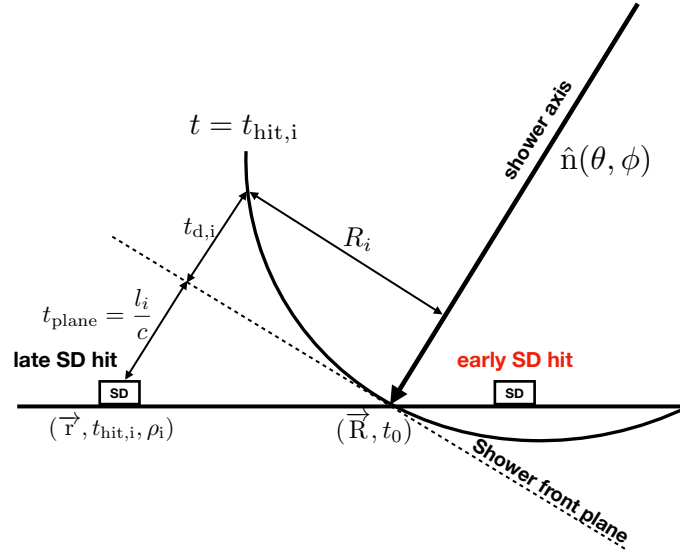


FIGURE 5.3: Scheme of shower development in the atmosphere and the parts of curvature of shower front.

the light c . The following equation describes experimentally the residual time,

$$t_d = t_{\text{hit}} - t_0 - t_{\text{plane}}. \quad (5.3)$$

The time at core location (t_0) is obtained in the event geometry reconstruction process which was described in the Section 3.2.2. The representation of the curvature of the shower front is described by the residual time as a function of the core distance R .

As first approximation to study the residual time distribution is based in the empirical AGASA function [51],

$$t_{d,i} = 2.6 \times \left(1 + \frac{R_i}{30\text{m}}\right)^A \left(\frac{\rho_i}{\text{m}^{-2}}\right)^B [\mu\text{s.}] \quad (5.4)$$

since the residual time Equation has dependence on particle density (ρ), in the following analysis it is used the AGASA lateral distribution function given by

$$\rho_i = C_n \left(\frac{R_i}{91.6\text{m}}\right)^{-1.2} \left(1 + \frac{R_i}{91.6\text{m}}\right)^{-(\eta(\theta)-1.2)} \left(1 + \left[\frac{R_i}{1000\text{m}}\right]^2\right)^{-0.6} [\text{VEM}/\text{m}^2] \quad (5.5)$$

Figure 5.4 (left) is an example of curvature of shower front measured by the residual time distribution vs. core distance. Figures 5.4 (right) show the FADC signals with the respective delay time distribution by using TA SD data.

This shower event was registered in 2014-07-23 $(\theta, \phi) = (7.9^\circ, 88.6^\circ)$ ($E = 10^{19.38}$

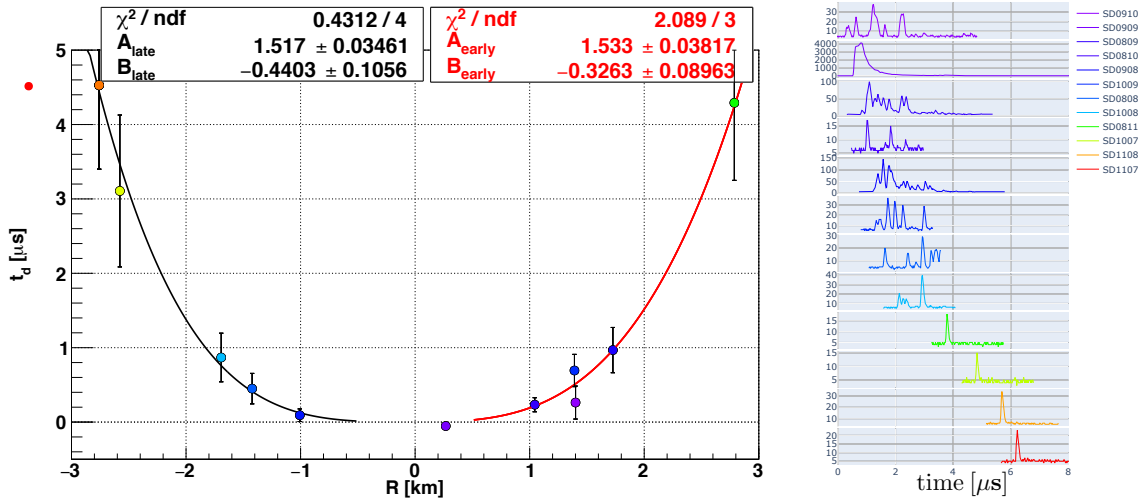


FIGURE 5.4: Residual time vs. core distance, the y-error bars is the the residual time error measured by Equation (3.10). The red and black line is the simple AGASA fitting function. The color shows the triggered, the latest is marked in red. Event recorded in 2014-07-23 $(\theta, \phi) = (7.9^\circ, 88.6^\circ)$ ($E = 10^{19.38}$ eV)

eV), in this event 12 SDs are hit, it is clearly seen the distribution becomes wider with increasing core distance. The 0 km in the scatter plot represents the core location and the right side dots represent the particles arrival in the **early**, the left side dots are the **late** triggered. The red and black lines are the simple AGASA fitting function described by Equation (5.4) where A and B are the AGASA function free parameters.

5.1.3 Examples of events shower using TA SD data

In this section, we are going to illustrate some sample events and we look into these events the characteristics and properties by selecting specific events related to the direction coming from.

Vertical shower event example:

The following event is an air shower registered in 2014-06-18 at 15:32:41.071341 with direction $\sim 20^\circ$ in zenith angle (in $\sec\theta = 1.06$) and azimuth angle 192° and energy $1.8 \times 10^{20.0}$ eV which is the maximum energy registered during 11 years with TA SD. The average length between 1st and the 18th SD is ~ 7 [μs]. Figures 5.5 show the shower event map (the black star mark is the core location), the lateral distribution

and the arrival time distribution by the FADC waveforms. Figure 5.6 shows the residual time measured of this event observed by TA SD.

Middle shower event example:

Figure 5.7 is an event example of real data of TA SD registered in 2019-04-18 at 16:42:57. This event represents an UHECR event with energy $10^{19.3}$ eV with zenith and azimuthal angle of $\sim 43^\circ$ (in $\sec\theta = 1.36$) and $\sim 137^\circ$ with large SDs hit (15 SDs). These plots show the shower event map, the lateral distribution and the waveforms corresponding to the event. In case of residual time it should be taken into account that the curvature of middle zenith angle shower starts to be less curved comparing with showers with zenith nearly close to zenith, the residual time are fitted the early and late side where A free parameter show 1.40 and 1.43 respectively as shown in Figure 5.8 in comparison with the event of zenith $\theta \sim 8^\circ$ is less than ~ 1.5 and in case of power law of density the free parameter B also vary depending on the different condition in case of early or late.

Inclined shower event example:

The next sample event consists of an inclined shower $\theta \sim 50^\circ$ (in $\sec\theta = 1.57$) coming from the south-east side with primary energy $10^{19.40}$ eV recorded 2018-09-15 at 02:23:05, and it is observed in the event map (top right panel of Figure 5.9) where the dash line shows the separation of the number of SDs hit in the early stage (8 SDs) and the late triggered (5 SDs). The bottom left Figure shows the lateral distribution of particles which most of SDs hit have low particle density and the right Figures show the arrival time distribution sequence. Figure 5.10 shows an asymmetry respect to the core position in the early (8 SDs) part of the curvature and the late part of curvature with fewer SDs (5) hit. The characteristic of inclined shower shows the shower front is less curved by showing the A parameter fitted, A is the power-law of R , for early and late with 1.33 and 1.35 respectively. And B parameter for early and for late are -0.42 and -1.05 respectively, B being the power-law of particle density in case of late curvature shows less particle density.

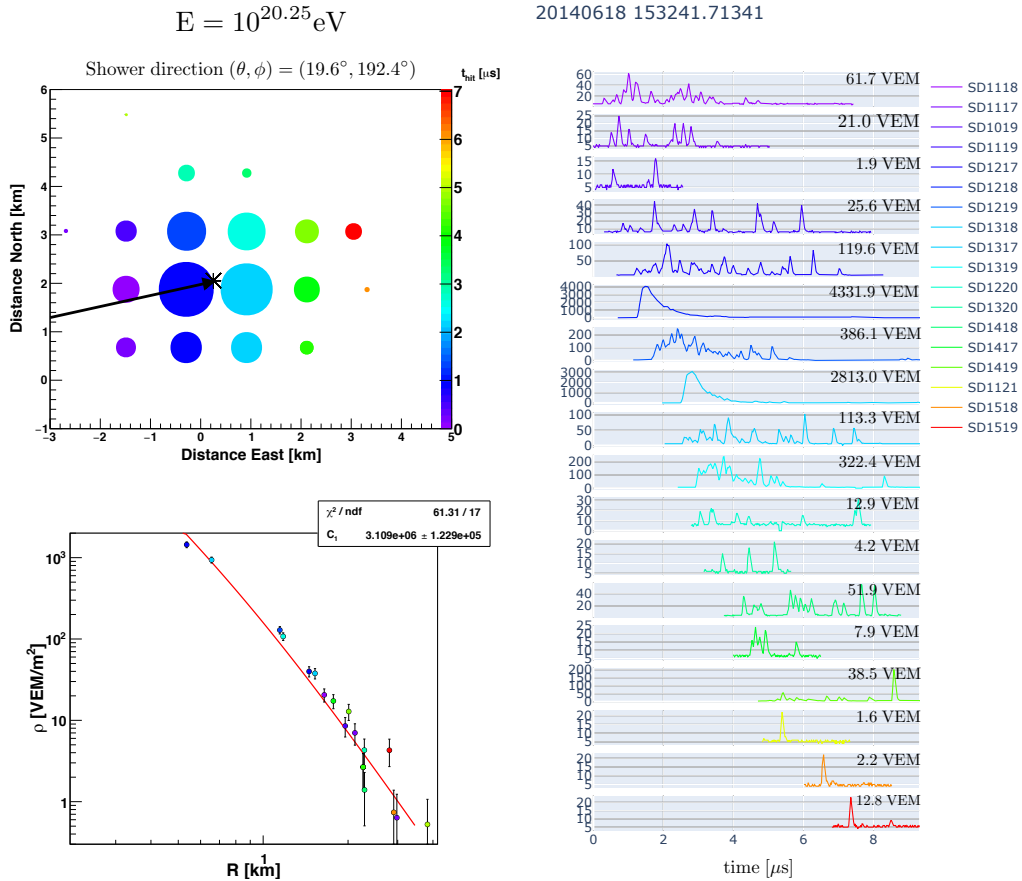


FIGURE 5.5: This event air shower is the highest primary energy found $E = 10^{20.25}$ eV observed with 18 SDs triggered. The left top show the map event display where color bar show the arrival time sequence. Bottom figure shows the lateral distribution fitted with the AGASA LFD function. Right plots show all FADC traces showing the arrival delay.

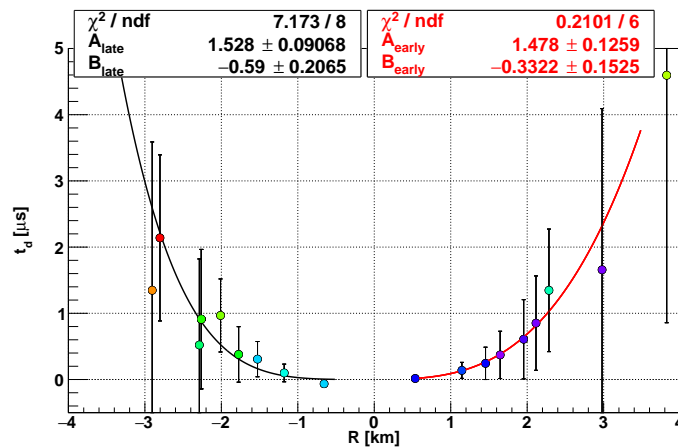


FIGURE 5.6: This plot is the corresponding residual time measured for the large air shower detected versus the distance to core. Primary energy $E = 10^{20.25}$ eV and arrival direction $(\theta, \phi) = (19.6^\circ, 192.4^\circ)$.

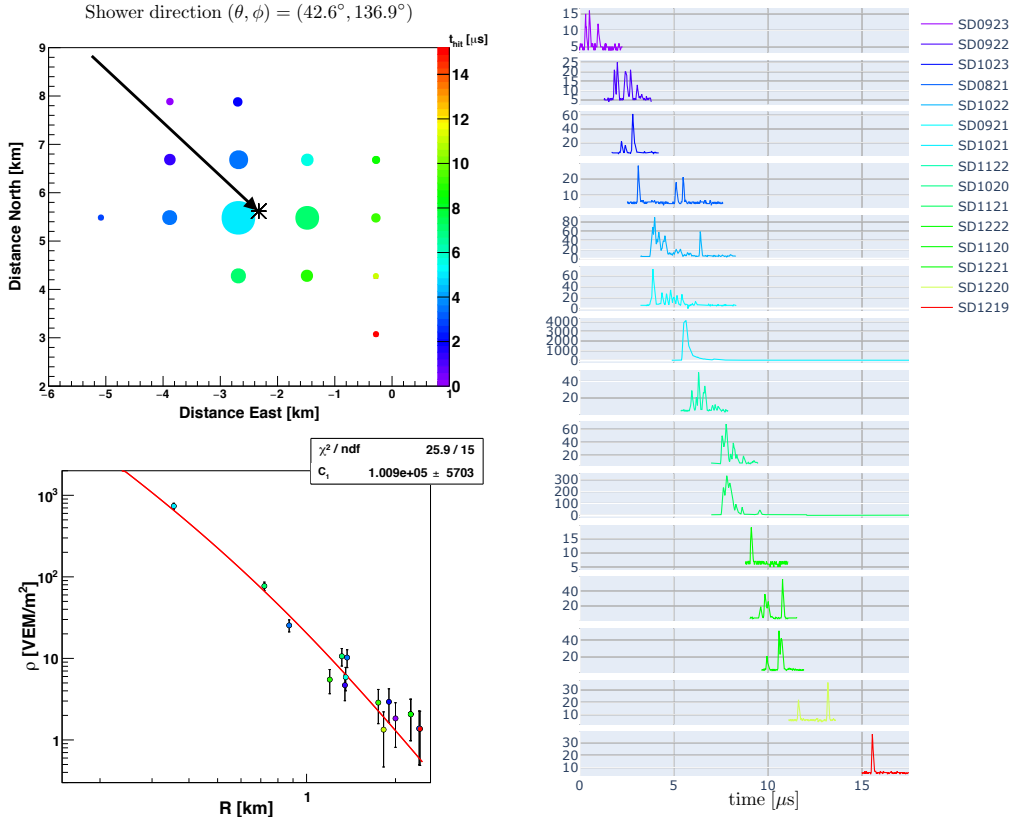


FIGURE 5.7: One event shower sample recorded in 2019-04-18 at 16:42:57.524175 $(\theta, \phi) = (42.9^\circ, 136.9^\circ)$ with primary energy of $10^{19.30}$ eV. Left top: show the event map. Left bottom: Scatter plot of particle density versus distance to shower axis. Right panel: the footprint recorded represented by the waveforms traces.

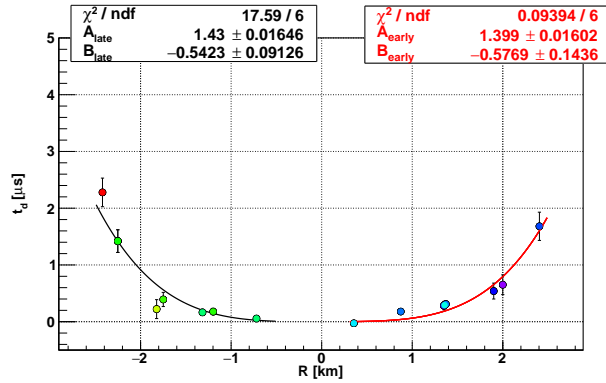


FIGURE 5.8: Distribution of the residual time respect to the air shower plane measured by the event recorded in 2019-04-18 $(\theta, \phi) = (42.9^\circ, 136.9^\circ)$ $E=10^{19.30}$ eV. The red line is the AGASA fitting function for the early hit SDs and the black line the AGASA function fitted for late SDs hit.

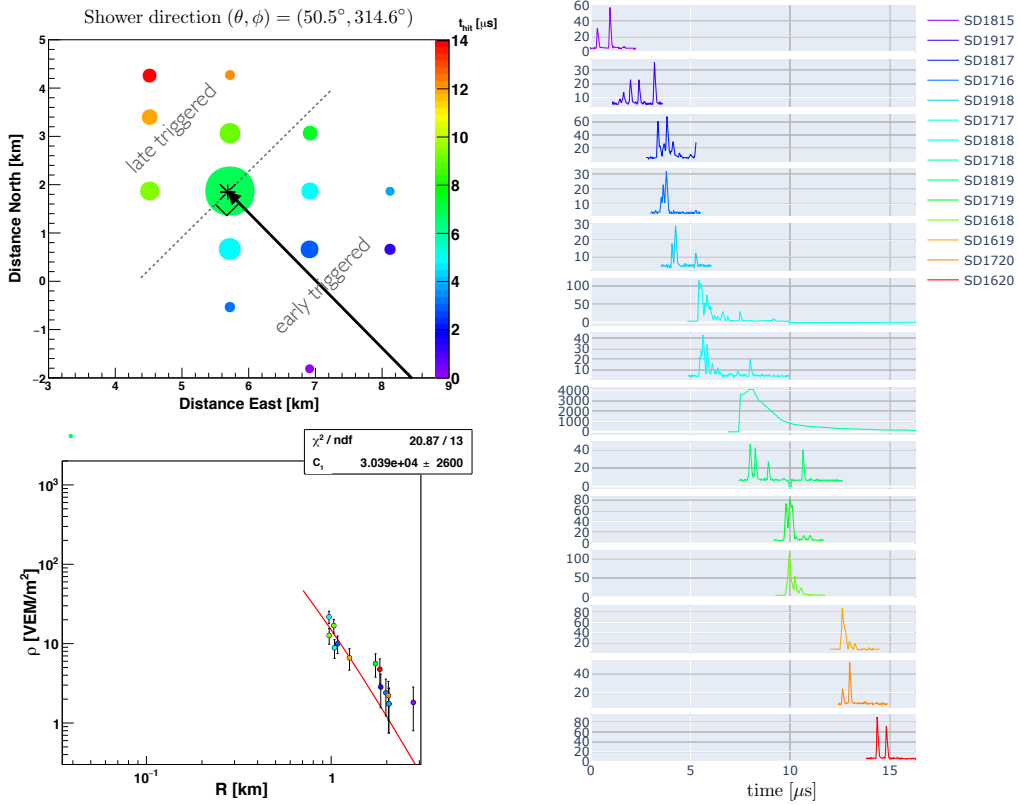


FIGURE 5.9: This example represents to an inclined event shower $(\theta, \phi) = (50.5^\circ, 314.6^\circ)$ of energy $E = 10^{19.40}$ eV with 14 SDs triggered. Left top figure is showing the event map where the arrow show the direction of UHECR event and the dash line shows the separation from the early and late hits SDs. Bottom left show the particle density versus to core distance. Right panel shows the corresponding FADC traces showing the delay time distribution.

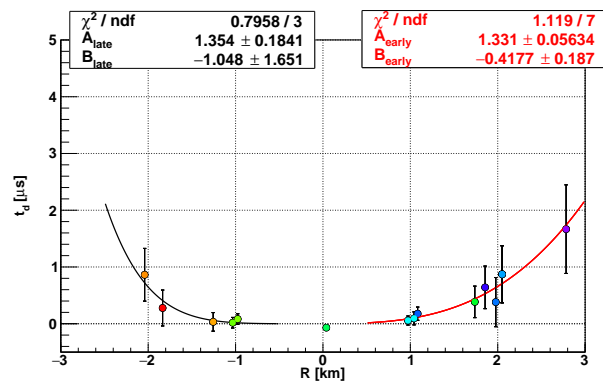


FIGURE 5.10: The residual time distribution as function of R for inclined shower $(\theta \sim 50^\circ)$ with $E = 10^{19.40}$ eV, the positive x-axis represents the curvature for early SDs hit and the negative x-axis are the latest arrival particles.

5.2 Residual time dependence on zenith angle (θ)

This section, it is dedicated to study hundreds of shower events, whose method consists in selecting specific zenith and energies intervals to analyze the zenith angle dependence by using data taken between May 2008 to May 2019 with 3 intervals of energy in logarithmic scale $18.90 \leq \log(E/eV) \leq 19.08$, $19.15 \leq \log(E/eV) < 19.45$ and $19.45 \leq \log(E/eV) \leq 20.05$ with $0 < \theta \leq 60^\circ$ which corresponds to $1.0 < \sec\theta \leq 2.0$, this zenith angle interval is divided in 5 intervals of $\sec\theta$ in step of 0.2.

In order to estimate the residual time with respect to the shower plane, all the total time distributions have been processed in a standard way. We determine the mean of t_d residual time in a specific range of R as,

$$\langle t_d \rangle = \sum_{i=1}^N t_{d,i}/N, \quad (5.6)$$

where $t_{d,i}$ is the residual time of the i -th data, and N is the total number of data in the bin of R . Figure 5.12 show an example of a collection of shower particle arrival delays in an interval of energy of $18.90 \leq \log(E/eV) \leq 19.08$ with zenith interval of $\sec\theta = 1.18 - 1.20$.

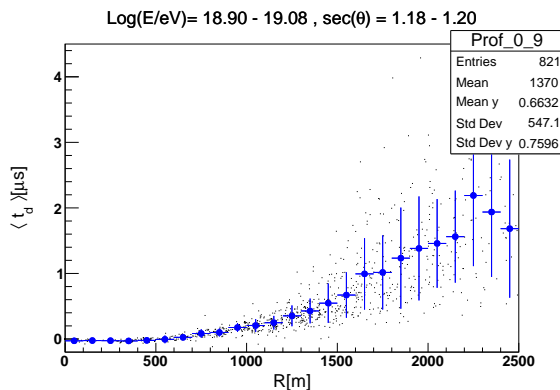


FIGURE 5.11: Example of residual time distribution as a function of distance from the shower core for a specific zenith interval in $\sec\theta = 1.18 - 1.20$ ($\theta = 32.1^\circ \sim 33.5^\circ$) including early and late part of shower front. The black dots is the residual time for each SD and blue dots correspond to the average of t_d in an interval of R of 100 m, and the y-axis error bar correspond to RMS.

The next set of plots show a sequence of zenith angle interval from $\sec\theta = 1.0 - 1.18$ (equivalent to $0^\circ - 32.1^\circ$), it is divided in 9 intervals in step of 0.02

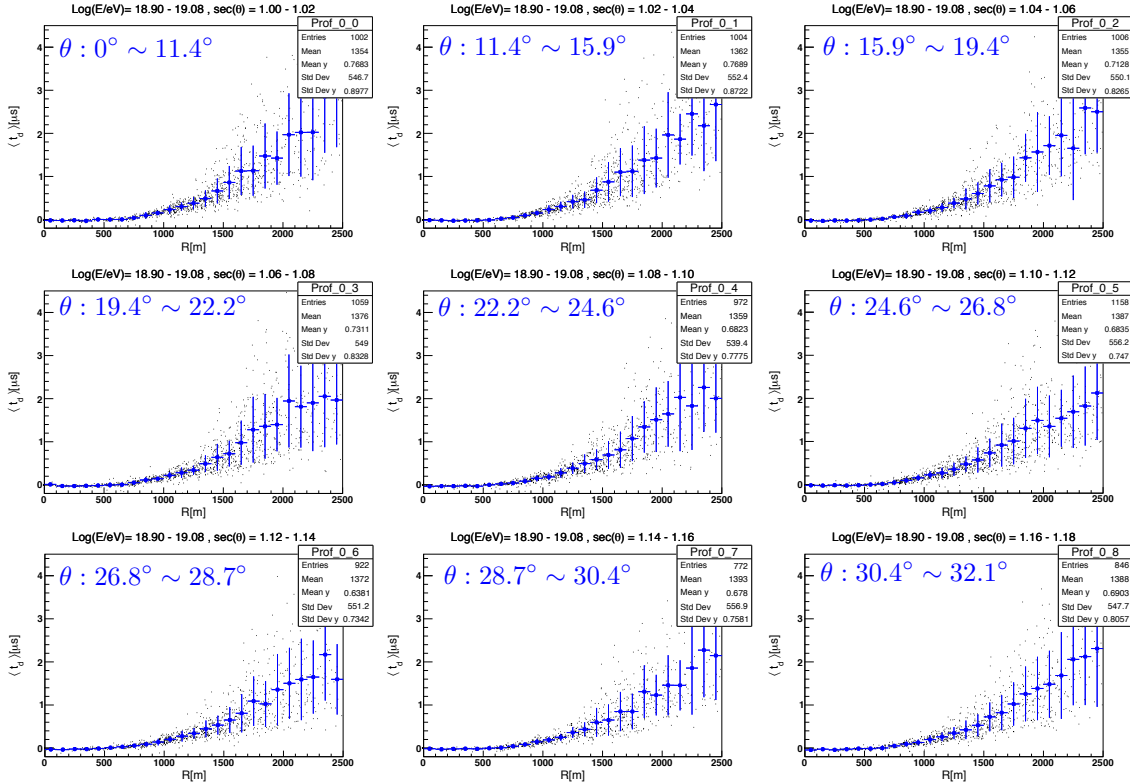


FIGURE 5.12: This set of plots correspond t_d vs. R for zenith angle intervals in $\text{sec}\theta = 1.00 - 1.18$ divided in step of 0.02.

covering all showers with the short atmospheric depth, the numbers of events in this interval is ~ 800 events (Figure 5.12). According to Figure 5.12 the curvature of shower front is modified slightly while increase the zenith and R .

The following plots correspond to shower events for energy interval of $10^{18.90} - 10^{19.08}$ eV two examples of residual time as function of core distance for two zenith angle intervals. Figure 5.13, the left scatter plot shows zenith interval $\text{sec}\theta = 1.0 - 1.2$ ($\theta = 0^\circ - 33.6^\circ$) including 848 selected events and the right side plots show the histograms of t_d distribution in a specific range of R . Figure 5.14 is for events corresponding to inclined showers in $\text{sec}\theta = 1.8 - 2.0$ ($\theta = 56.2^\circ - 60.0^\circ$) with 160 events showers selected.

Figure 5.15 presents the residual time binned scatter fitted by the AGASA residual time function where A and B are free parameters. The zenith angle interval is $1.0 < \text{sec}\theta \leq 1.2$ this interval corresponds to $0^\circ < \theta \leq 33.6^\circ$ for energy interval between $10^{18.90} \leq E \leq 10^{19.08}$ eV which corresponds to energy centered at $10^{19.0}$ eV with $\pm 20\%$ error.

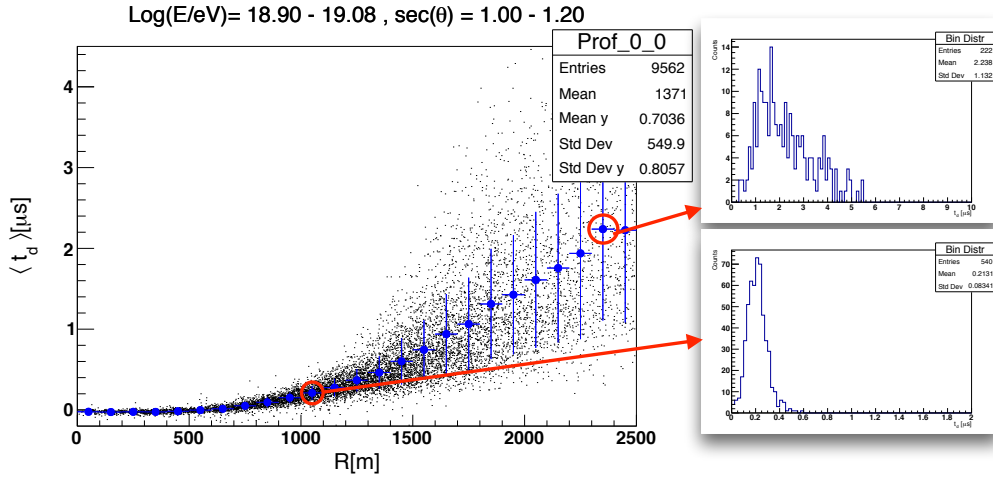


FIGURE 5.13: Left plot is an example of residual time distribution for $\sec\theta = 1.0 - 1.2$ and the two histograms attached to it represents to the distribution of t_d in a bin of 100 m which is shown the red circle.

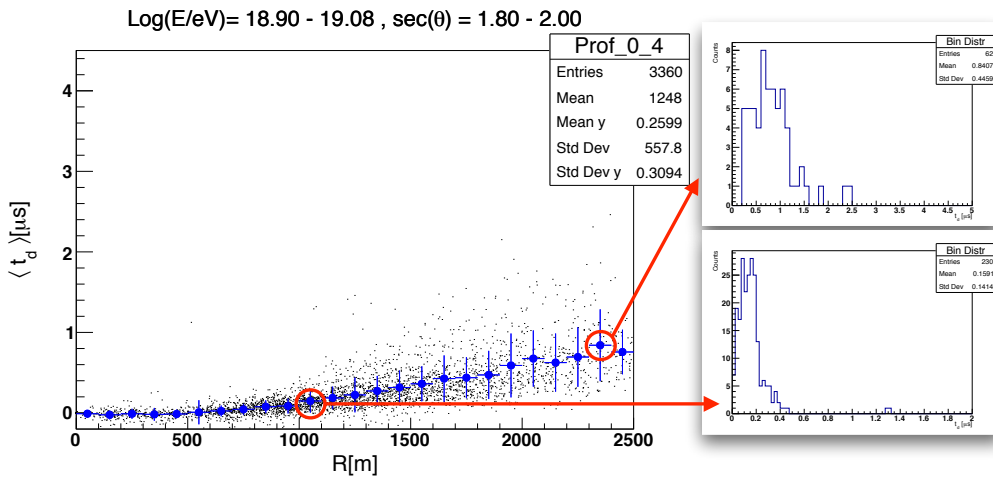


FIGURE 5.14: Left panel is an example of $\sec\theta = 1.8 - 2.0$ inclined event showers. Right plots are the respective histograms of red circles bins of t_d .

In the Equation (5.4) A and B are the free parameters to be fitted, and the particle density ρ was also considered at the time of fitting. Figure 5.16 represents the particle density versus distance to shower axis in a fix energy and zenith interval which corresponds to the residual time presented in Figure 5.15. The averaged density is fitted by the Equation 5.5. The normalization factor C_n of the AGASA LDF is the free parameter to be fitted. Knowing the free parameter of the averaged density $\langle \rho \rangle$ in the same interval of the residual time distribution, the averaged residual time is fitted.

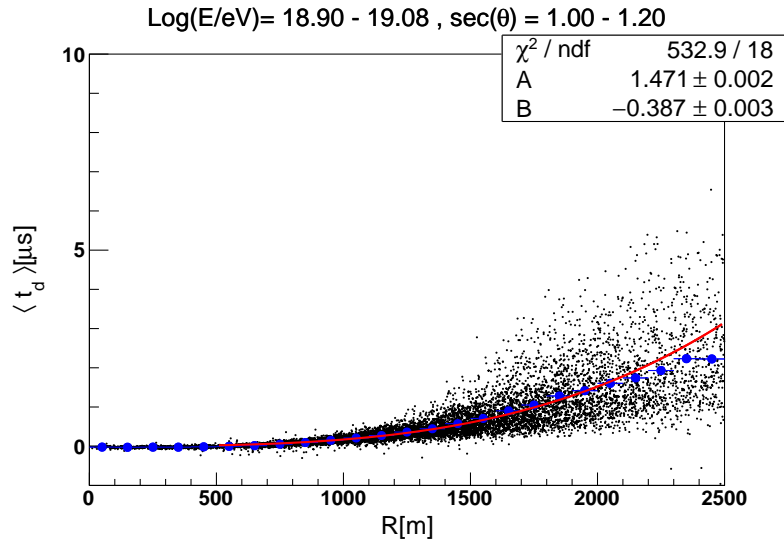


FIGURE 5.15: Residual time distribution in function of distance of core position of an interval of energy $10^{18.90} - 10^{19.08}$ eV and zenith angle interval of $\sec\theta = 1.0 - 1.2$. The red line is the fitted line of AGASA residual time function.

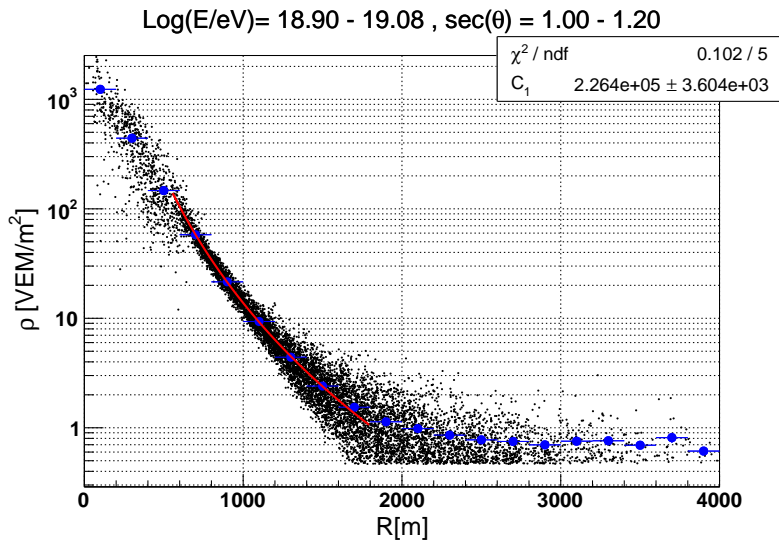


FIGURE 5.16: Particle density distribution as function of distance of core position for the interval of energy $10^{18.90} - 10^{19.08}$ eV and zenith interval $\sec\theta = 1.0 - 1.2$ of each SD (black dots) and the blue dots are the average of particle density binned in each 200 m.

Figures 5.17 (left) show the residual time and core distance distribution for the energy interval $10^{18.90} - 10^{19.08}$ eV and the corresponding particle density as function of core distance (right) for 4 intervals of zenith angle. From top to bottom zenith intervals: $\sec\theta = 1.2 - 2.0$ in step of 0.2. Figures 5.18 and 5.19 show the results of residual time distribution and core distance (left) with the particle density as

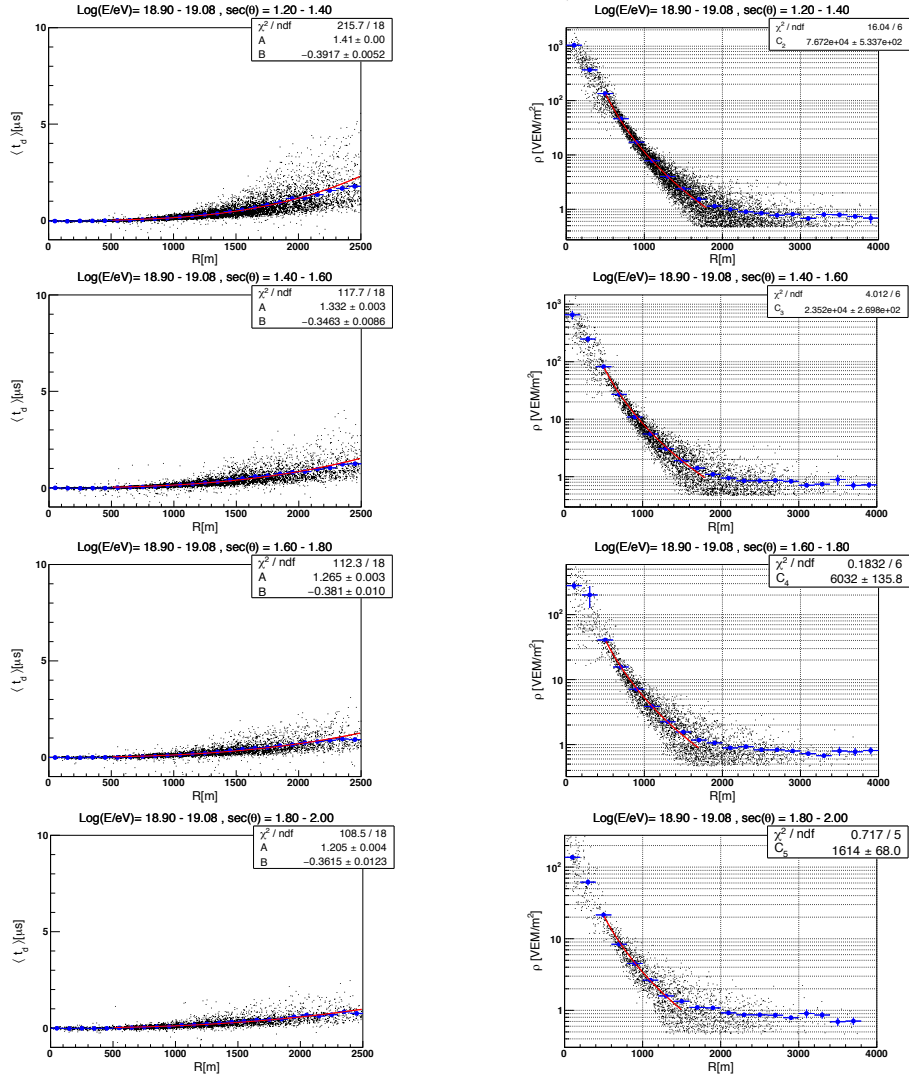


FIGURE 5.17: Left panel: residual time distribution versus core distance, the red line is the residual time AGASA function fitted from 500 to 2500 m. Right panel: particle density versus distance to core, and the red line is the AGASA LDF fitted to the averaged of ρ binned in intervals of R . From top to bottom various zenith angle, $\sec\theta = 1.2 - 2.0$ in step of 0.2. Corresponding to interval of energy $10^{18.90} - 10^{19.08}$ eV.

function core distance (right) for energy intervals of $10^{19.15} - 10^{19.45}$ eV and $10^{19.45} - 10^{20.05}$ eV respectively from top to bottom shows its evolution of t_d and ρ respect to R while zenith angle increases from $\sec\theta = 1.0 - 2.0$ in step of 0.2. These results show the evolution of shower front curvature for different energy intervals.

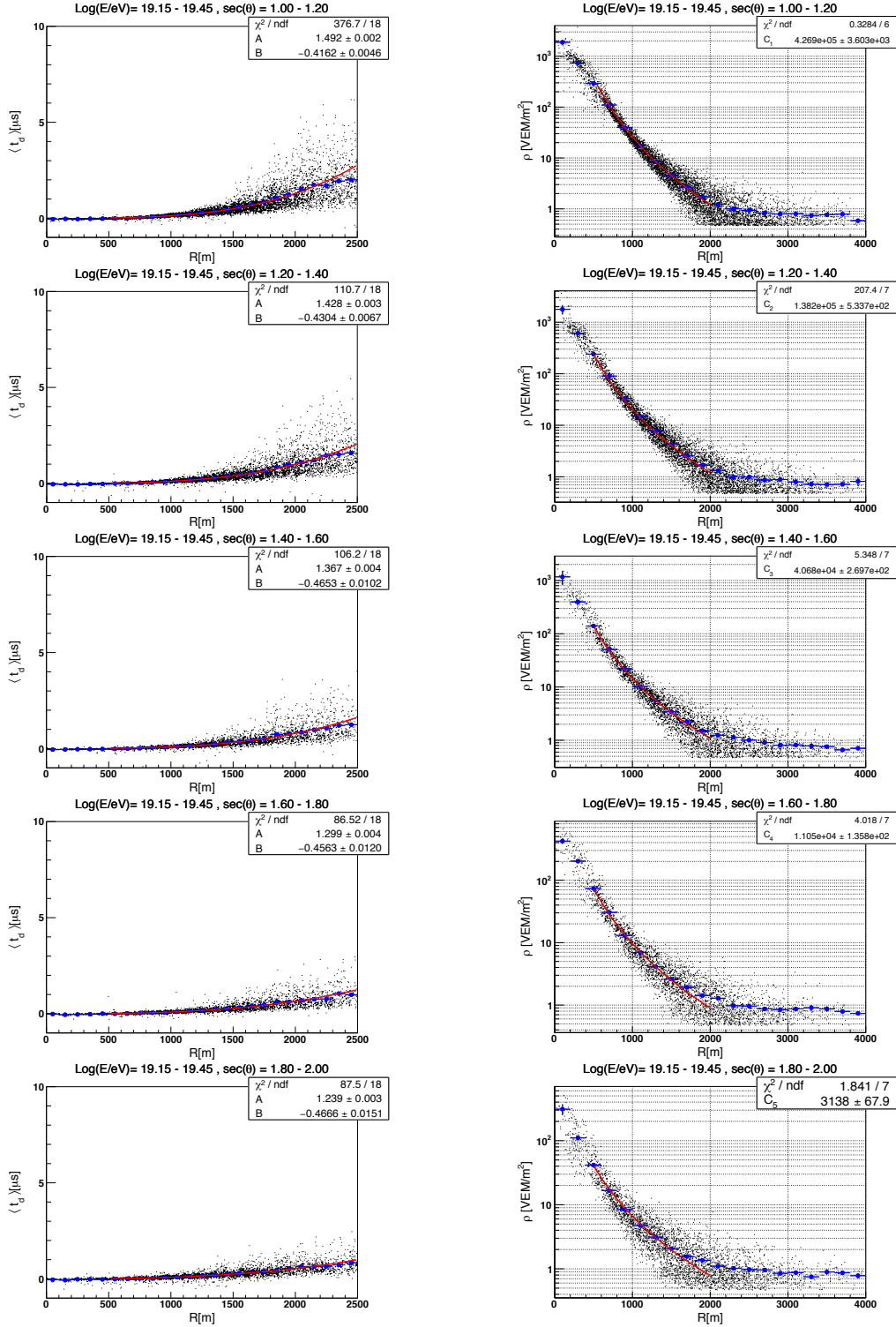


FIGURE 5.18: Left panel: residual time distribution versus distance to the shower core, the red line is the residual time AGASA function fitted from 500 to 2500 m. Right panel: particle density versus distance to the shower core, and the red line is the AGASA LDF fitted to the averaged of ρ binned in intervals of R . From top to bottom various zenith angle, $\sec\theta = 1.0 - 2.0$ in step of 0.2. Corresponding to interval of energy $10^{19.15} - 10^{19.45}$ eV.

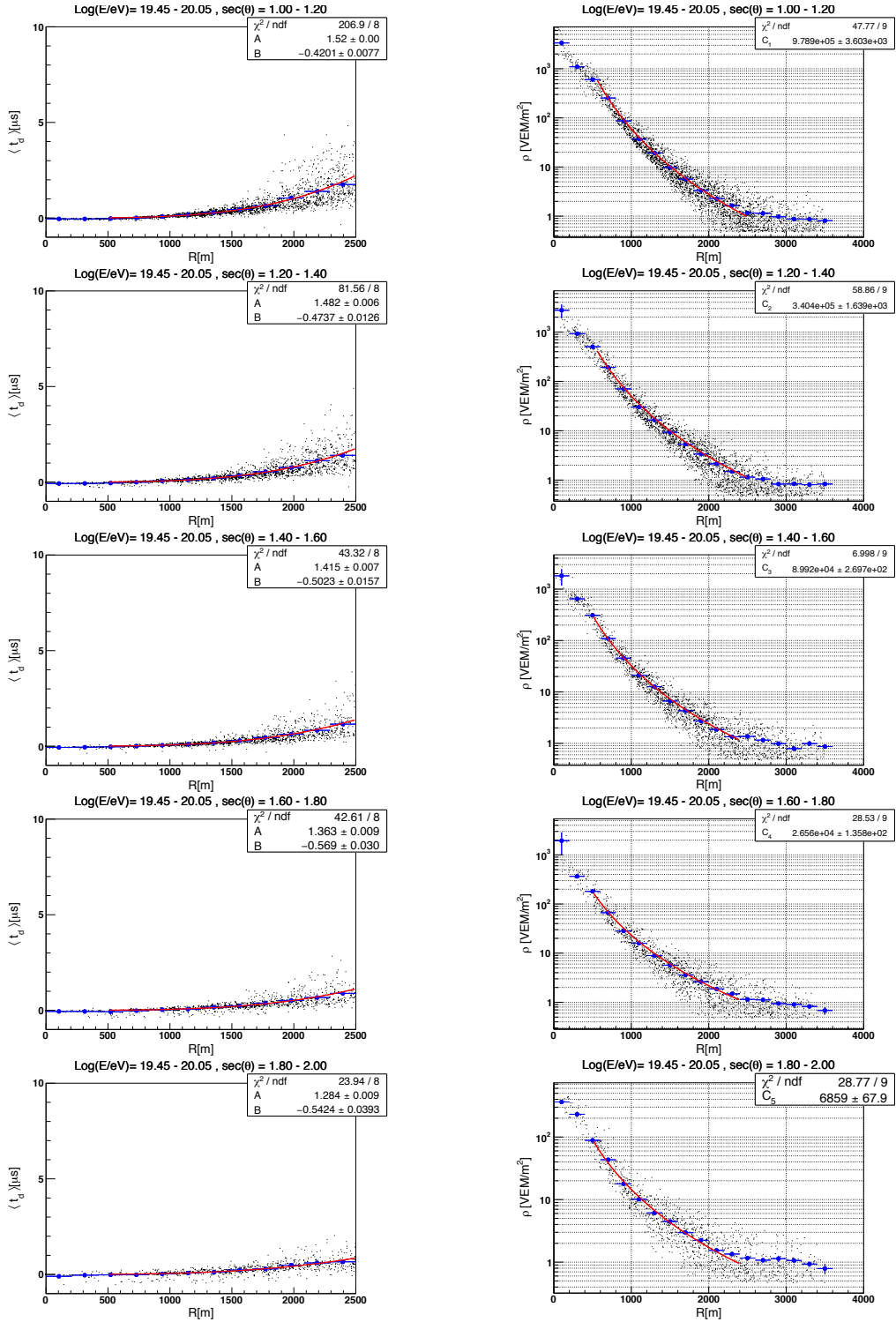


FIGURE 5.19: Left panel: residual time distribution versus distance to the shower core, the red line is the residual time AGASA function fitted from 500 to 2500 m. Right panel: particle density versus distance to the shower core, and the red line is the AGASA LDF fitted to the averaged of ρ binned in intervals of R . From top to bottom various zenith angle, $\sec\theta = 1.0 - 2.0$ in step of 0.2. Corresponding to the highest interval of energy $10^{19.45} - 10^{20.05}$ eV.

5.2.1 Residual time parameters A and B

To describe the distribution of arrival time of particles that reach ground detectors, the residual time parameters, A and B are introduced during the fitting of residual time distribution for different zenith angles intervals. By using TA plastic scintillator surface detectors of 3 m^2 were used, this technique to study shower-to-shower fluctuations of residual time to understand the shower curvature. A and B parameters are considered to attribute some dependence on zenith angle.

Figure 5.20 is the summary of the analysis made on the first interval of energy with average in energy bin of $10^{19.0} \text{ eV}$. Shown on the left of Figure the result of A parameter versus $\sec\theta$ where can be observed there is a clear dependence by zenith angle, the 5 points analyzed, a linear fitting. And the right figure shows the B parameter as function of $\sec\theta$, in this case there is not clear dependence on zenith angle.

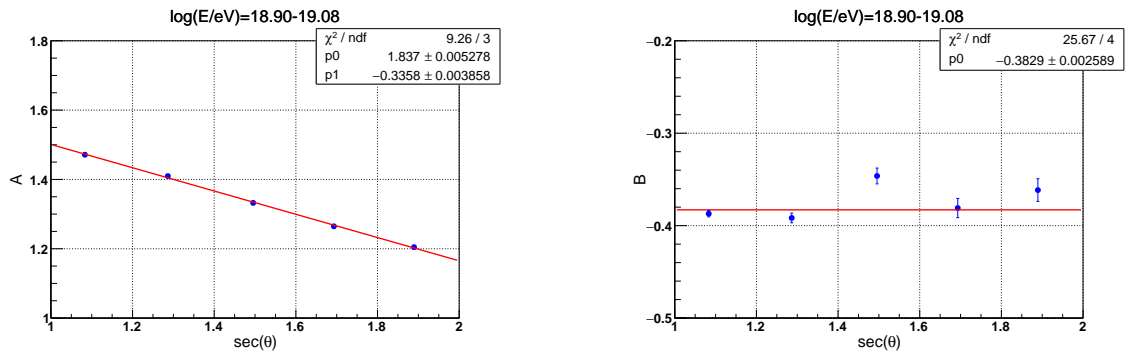


FIGURE 5.20: Parameters A and B as function of $\sec\theta$, blue dots represent for average energies in $\log(E/eV) = 19.0$. Parameter A represents the power-law of curvature shower and B parameter is the power-law of particle density.

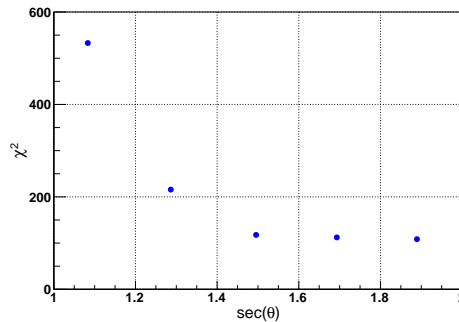


FIGURE 5.21: Values of χ^2 from the AGASA residual time function fitted and the $\sec\theta$ analyzed in the energies $10^{18.90} - 10^{19.08} \text{ eV}$.

Figure 5.21 shows the values of χ^2 (n.d.f. = 18) fitted in the residual time distribution by AGASA function as described in Equation (5.4) with free parameters A and B , and $\sec\theta$. It can be observed that the χ^2 for the first interval of zenith is large it is caused at large R (> 2000 m) between the averaged t_d and the expected residual time in that interval of zenith (see Figure 5.15) and the rest of zenith interval are also high for large R (> 2400 m) (see Figures of left panel 5.17), this can be indicated the AGASA function is good fitted for curvature with the radius with $R < 2000$ m for showers of particles with energies centered at 10^{19} eV.

5.3 Residual time dependence on zeta angle (ζ)

It was studied some samples of shower event on the Section 5.1.3 where it was observed the shower front is not symmetric depending on its geometry by analyzing the early and late part of the curvature. As illustrated in that section by observing with real data, in this section the shower front it is analyzed by considering the azimuthal angle around the shower axis. It was studied that the arrival time has dependence on R , zenith angle θ and now we will introduce the azimuthal angle ζ definition. Considering the a "late" side of the shower, which travelled through more atmosphere than the part "early" side of shower. The concept of azimuthal angle is defined in the plane perpendicular to the shower axis or along to the shower plane, which is represented in the Figure 5.22 (left), and its frontal view of ζ angle in the Figure (right).

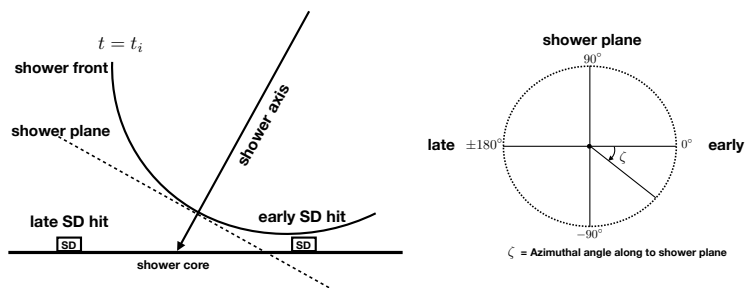


FIGURE 5.22: Description of early and late SD hits and the zeta angle (ζ) on the shower planes definition. The left figure is a side view of air shower curvature with "early" side, and "late" side. Right figure describes the ζ angle definition representing the early/late part of the shower.

The center is the core of the shower and all SDs distributed covering 360° isotropically. The SD that was triggered earliest has $\zeta = 0^\circ$ and the SD that was triggered the latest has $\zeta = \pm 180^\circ$. In the next sections, the method of analysis consists in dividing the zeta angle into 3 main parts of the shower, the "early" that covers $|\zeta| \leq 60^\circ$, the "intermediate" covers the zeta angle $60^\circ < |\zeta| < 120^\circ$ and the interval in zeta angle the "late" covering $120^\circ \leq |\zeta| \leq 180^\circ$.

Figures 5.23 show three examples of residual time binned in 3 intervals of zeta angle. The lateral distribution also was analyzed with the same conditions of residual time distribution for the zeta angle as shown in Figures 5.24, the colored diamond marks are the averaged of particle density and they are fitted with the AGASA LDF (red line).

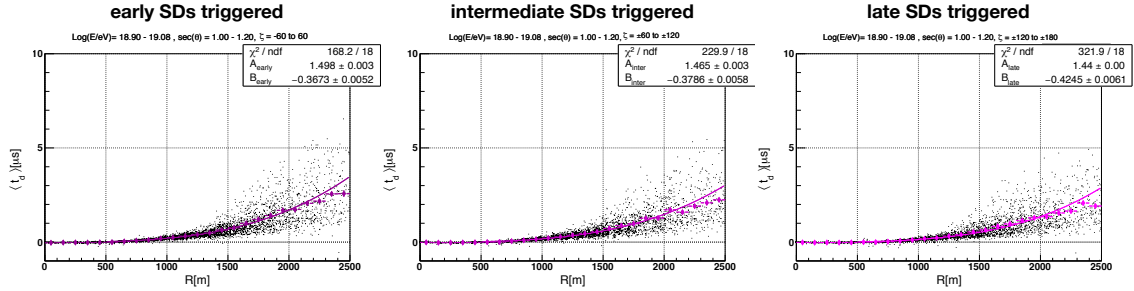


FIGURE 5.23: Residual time distribution versus distance of core shower. From left to right, the early part of shower corresponding the interval of zeta angle $|\zeta| \leq 60^\circ$, the intermediate part of showers $60^\circ < |\zeta| < 120^\circ$, and the late part of the curvature $120^\circ \leq |\zeta| \leq 180^\circ$.

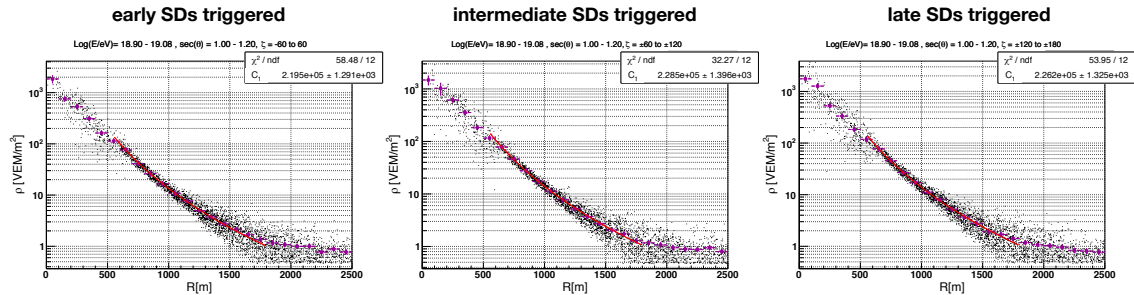


FIGURE 5.24: Particle density versus distance to core. From left to right plots, particle density for the early, intermediate and the early part of showers. For energy in averaged at $10^{19.0}$ eV. In the interval of zenith $1.0 \leq \sec\theta \leq 1.2$.

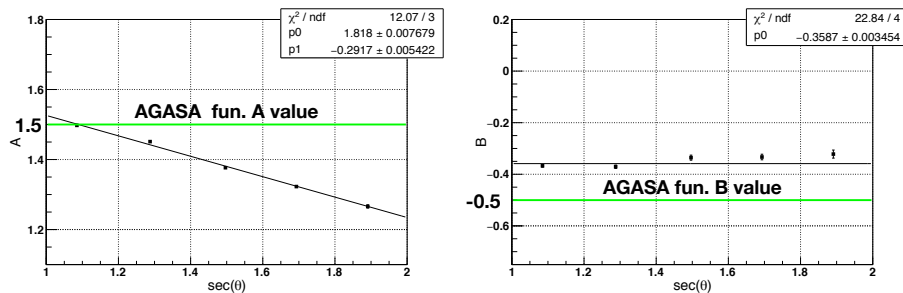


FIGURE 5.25: Parameters A and B as function of $\sec\theta$ for showers of early part of shower front for interval of energy $10^{18.90} - 10^{19.08}$ eV.

Figures 5.25 show the residual time dependence on zenith angle for "early" part of the shower front. By observing the earliest stage of the shower front A and B parameters present more clear tendency than when it is analyzed all showers. The green line in the Figures 5.25, show the values of A and B of AGASA residual time function presented in the Equation 2.16. The A value of AGASA function is valid for the $\sec\theta \simeq 1.1$ ($\theta \simeq 24.6^\circ$) and the B values are different between AGASA ($B = -0.5$) for energies $E > 10^{18.0}$ eV and TA ($B = -0.36$) for energy averaged bin $10^{19.0}$ eV and early part of the curvature.

5.4 Results of shower front analysis

This section is divided into three main parts of showers taking into account the curvature formed by the 3 intervals of zeta angle ζ . Each interval of zeta angle is analyzed for three main energies binned on average of bin $10^{19.0}$ eV, $10^{19.30}$ eV and $10^{19.75}$ eV. In order to understand the evolution of shower front considering the variation of geometry and the energy.

5.4.1 Curvature of the early part of shower front

Figures 5.26 show the results of the early part of the curvature of shower front presented for different energy intervals from left to right, the lower to higher energy respectively. Each plot shows the average of residual time binned in 100 m for 5 intervals of zenith angle $\sec\theta$, the colors from light to dark blue correspond from vertical to inclined shower events respectively. Each interval of zenith angle in $\sec\theta$

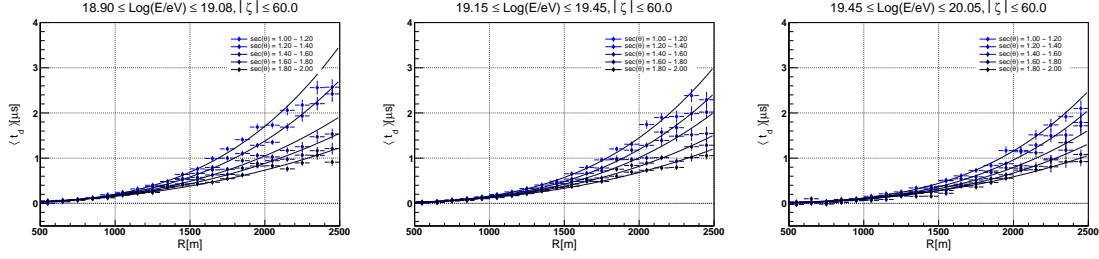


FIGURE 5.26: The curvature of shower front in function of core distance for "early" part of the shower for 3 intervals of energy. In each plot, the color from light to dark blue represents the $\sec\theta$ binned from vertical to inclined shower respectively. Energy interval in logarithmic scale 18.90 – 19.08 (left), higher energy band 19.15 – 19.45 (middle), and the highest energy band 19.45 – 20.05 (right).

shows the fit black line with the AGASA function for the residual time, A and B are the fitting parameters.

The fitted values of A and B are then parametrized with respect to $\sec\theta$ using a linear function as shown in Figures 5.27. These show the summary of A and B with respect to $\sec\theta$ for 3 intervals of energies for the early part of showers. Left Figure shows the summary of A versus $\sec\theta$ for 3 intervals of energies, the black, blue and red dots correspond from lower to highest energy interval respectively and they are fitted to linear functions. It can be seen that A has a clear dependence on zenith angle θ . In the case of B parameter (right) shows, B vs. $\sec\theta$ for 3 bands of energies from lower to higher and it can be observed there are not dependence on $\sec\theta$, where B parameters show a constant tendency.

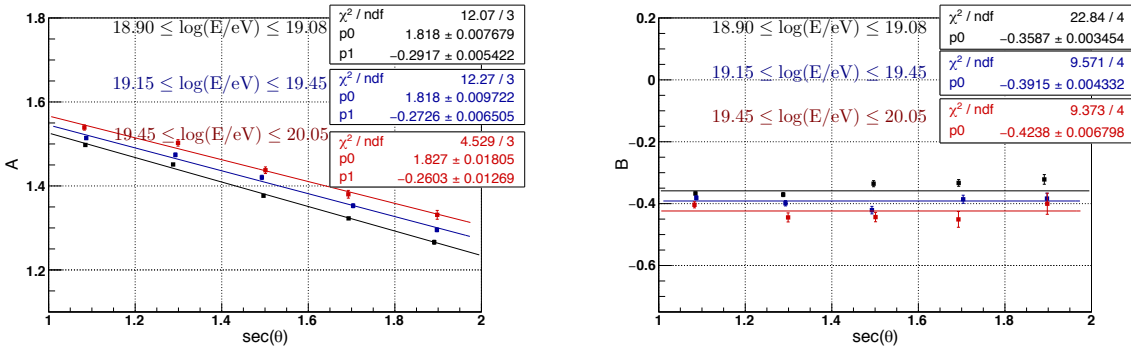


FIGURE 5.27: Parameters A and B of residual time function versus $\sec\theta$ for "early" part of the shower.

5.4.2 Curvature of the intermediate part of the shower front

Figures 5.28 show the results of the "intermediate" part of the curvature of shower front for different intervals of energy, and each "intermediate" part of the shower various zenith angle intervals.

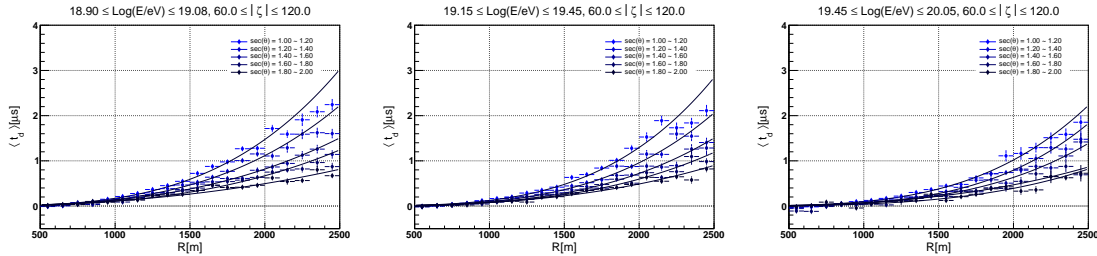


FIGURE 5.28: The curvature of shower front as function of core distance for "intermediate" part of the shower for various zenith intervals. Energy interval in logarithmic scale 18.90 – 19.08 (left), higher energy band 19.15 – 19.45 (middle), and the highest energy band 19.45 – 20.05 (right).

Figures show 5.29 the summary of the analysis fitting to the residual time distribution for intermediate part of the shower, with A and B as free parameters to be analyzed respect to zenith angle. For the case of A parameter, which is the power-law of the radius of the curvature decreases as the energy increases. And in the case B parameter, the power-law of particle density it is shown for low energy centered at ($10^{19.0}$ eV) is constant, but for higher energies, there is not a clear tendency, this can be attributed to low statistics due to two factors, first low statistics of t_d presented in this interval of zeta angle (intermediate) notoriously when zenith angle increases and second factor due to the highest energies, the shower events are low, presenting only the bias.

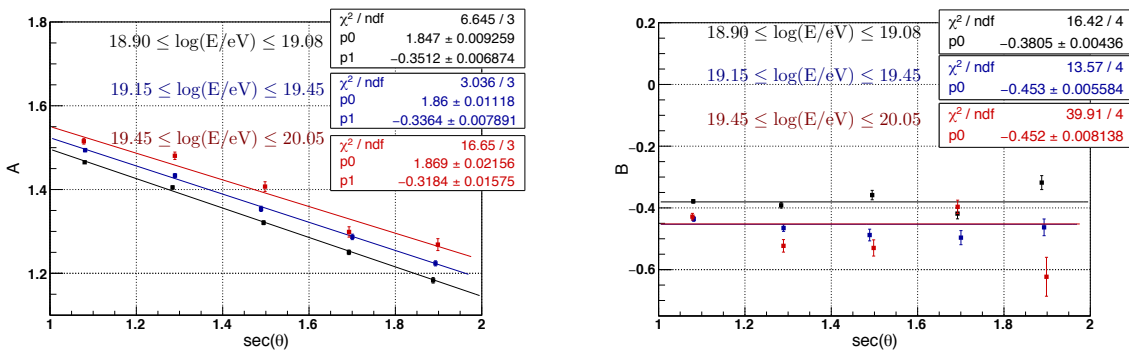


FIGURE 5.29: Parameters A and B of residual time function versus $\sec\theta$ for "intermediate" part of the shower.

5.4.3 Curvature of the late part of the shower front

The complemented part of the shower, the "late" SDs triggered was also analyzed. In the Figures 5.30, show the summary of curvatures of shower front for the "late" SDs triggered for different energies, this part of shower presents a deficit of t_d mainly when increases the zenith angle θ most of the particles are deposited their energies in the atmosphere and it may be only muons remained for more inclined showers. Each "late" part of the shower for different zenith angle intervals.

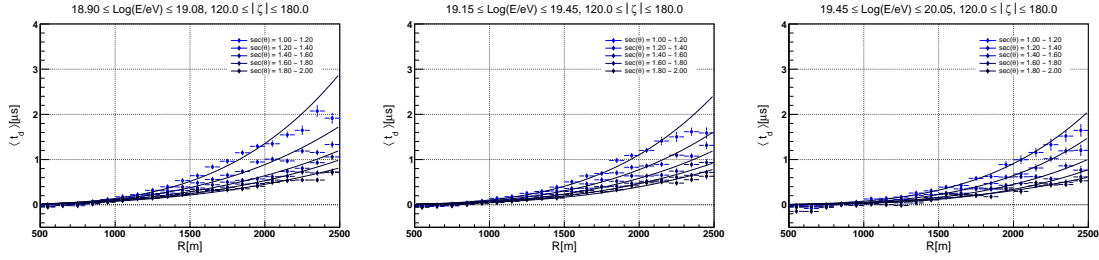


FIGURE 5.30: The curvature of shower front as function of core distance for "late" part of the shower for various zenith intervals. Energy interval in logarithmic scale 18.90–19.08 (left), higher energy band 19.15–19.45 (middle), and the highest energy band 19.45–20.05 (right).

The A and B fitting parameters are analyzed with respect to $\sec \theta$ for the "late" part of the shower as shown in Figure 5.31. The power-law (A) of the radius of curvature for "late" increases slightly while the energy increases, being the curvature wider for higher energies. And the power-law of the particle density B shows large statistics bias, however, the values of B show a reduction for higher energy.

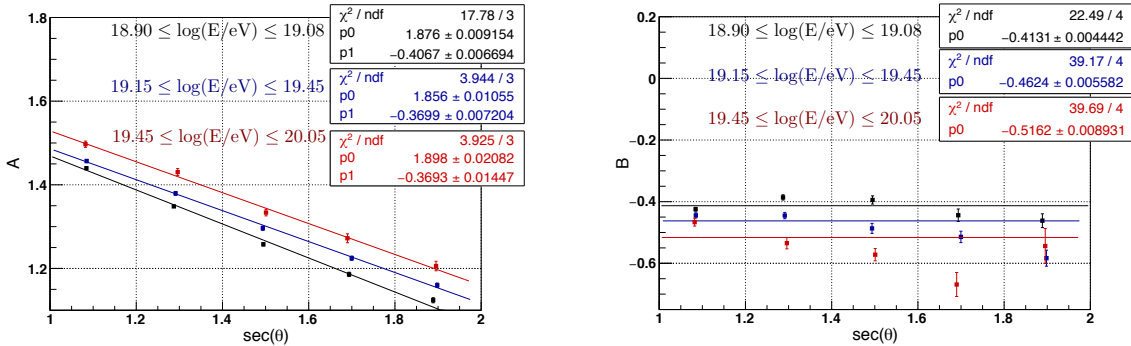


FIGURE 5.31: Parameter A and B of residual time function versus $\sec \theta$ for "late" part of the shower for different energy intervals.

5.5 Results of residual time dependence on zeta angle (ζ)

It was analyzed constants of $A(p_0, p_1)$ and $B(p_0)$ parameters respect to zeta angle (in $\cos\zeta$) for each band of energy. The three intervals of zeta angle averaged for "early" at $\zeta = 0^\circ$ ($|\zeta| \leq 60^\circ$), "intermediate" at $\zeta = 90^\circ$ ($60^\circ < |\zeta| < 120^\circ$) and "late" at $\zeta = 180^\circ$ ($120^\circ \leq |\zeta| \leq 180^\circ$).

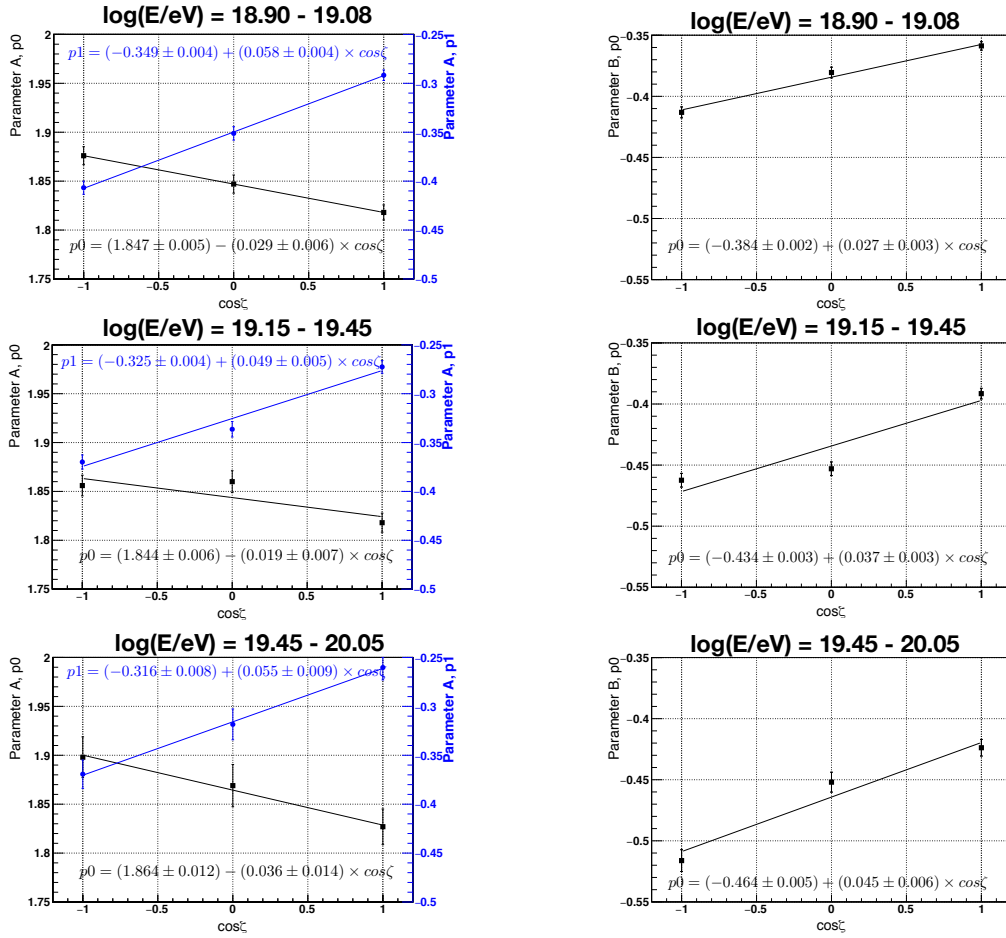


FIGURE 5.32: Results of constants of p_0 , p_1 of A (left) and p_0 of B (right) respect to the zeta angle ($\cos\zeta$). Top to bottom different energy intervals.

The analysis of these constants shows a clear dependence on zeta angle and the Equation form is,

$$t_d = 2.6 \times \left(1 + \frac{R}{30m}\right)^{p_0(\cos\zeta) + p_1(\cos\zeta) \times \sec(\theta)} \times \left(\frac{\rho_i}{m^{-2}}\right)^{p_0_B(\cos\zeta)} [\mu s]. \quad (5.7)$$

5.6 Results of residual time dependence on energy

In Section 5.4 was studied the curvature by parts into zeta angle intervals for different energy bands. As result, linear fits are found for A parameter respect to $\sec\theta$, where A has the form $A = p_0 + p_1 \times \sec\theta$, and B is constant p_0 for 3 intervals of energy. Then it is analyzed the constants p_0 and p_1 of A and p_0 of B parameters with respect to average energy bin in logarithm scale at 19.0, 19.30 and 19.75 for each part of the curvature of shower front as shown in the Figure 5.33.

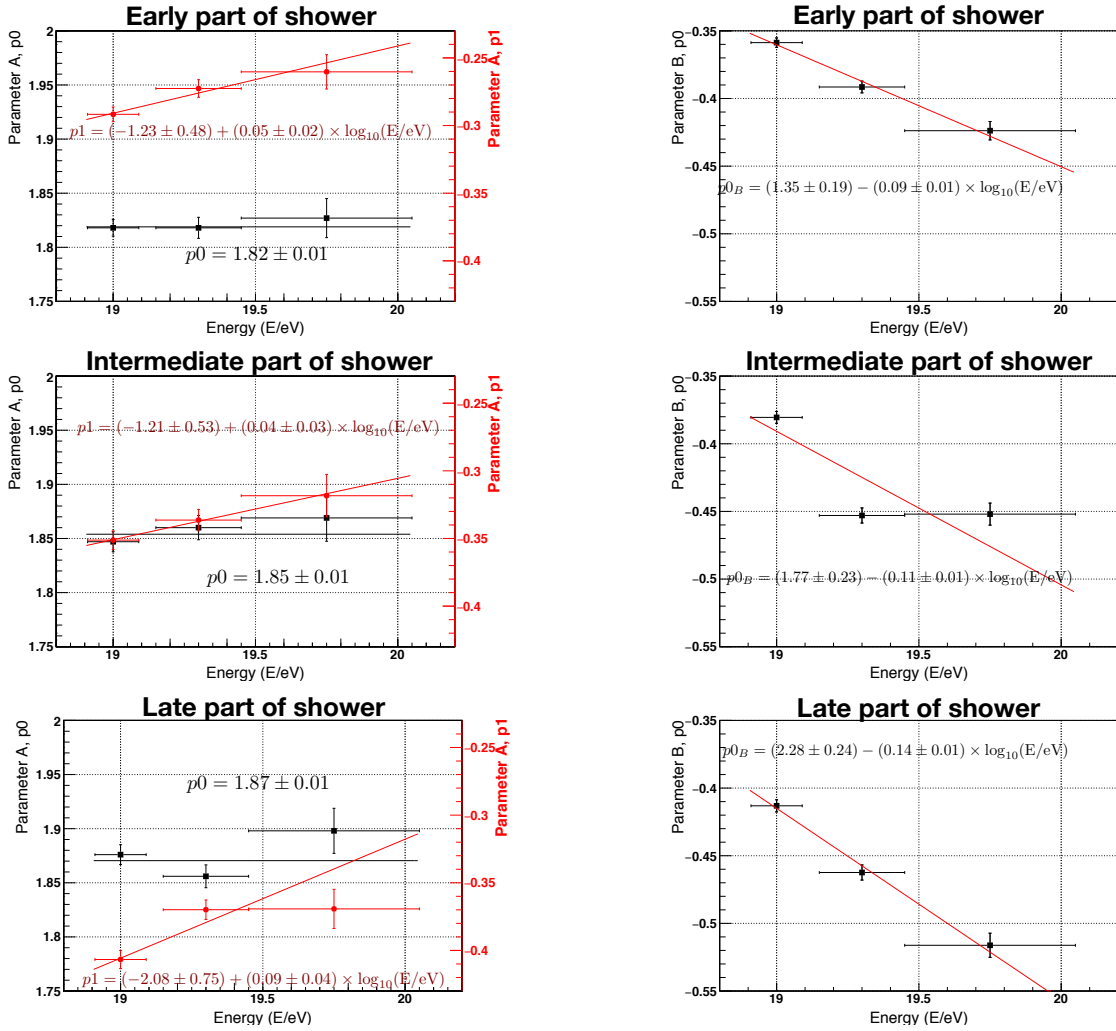


FIGURE 5.33: Results of constants of p_0 , p_1 of A (left) and p_0 of B (right) respect to averaged energy. Top to bottom different zeta angle intervals.

In the case of constants of A and B for the early part of the shower was found

a clear tendency in each constant for $p1$ of A and $p0$ of B parameter show energy dependence but not for $p0$ of A . In the case of the intermediate and late part of the curvature of shower present no clear tendency. In the case of the early part, it was found enough statistics but for the intermediate and late part, there are not good fitting of χ^2 comparing with early (see more details Appendix A.4, A.5, and A.6). In the three parts of the shower studied, the tendency is similar and the Equation is represented by,

$$t_d = 2.6 \times \left(1 + \frac{R}{30\text{m}}\right)^{p0+p1(E) \times \sec(\theta)} \times \left(\frac{\rho_i}{\text{m}^{-2}}\right)^{p0_B(E)} [\mu\text{s}]. \quad (5.8)$$

5.7 Summary of θ , ζ angle and energy dependence

Figures 5.34 show a summary of the curvatures of shower front for different zenith angle intervals, 3 bands of energy from low (top) to high (bottom). From left to right early, intermediate and late part of the curvature of shower front.

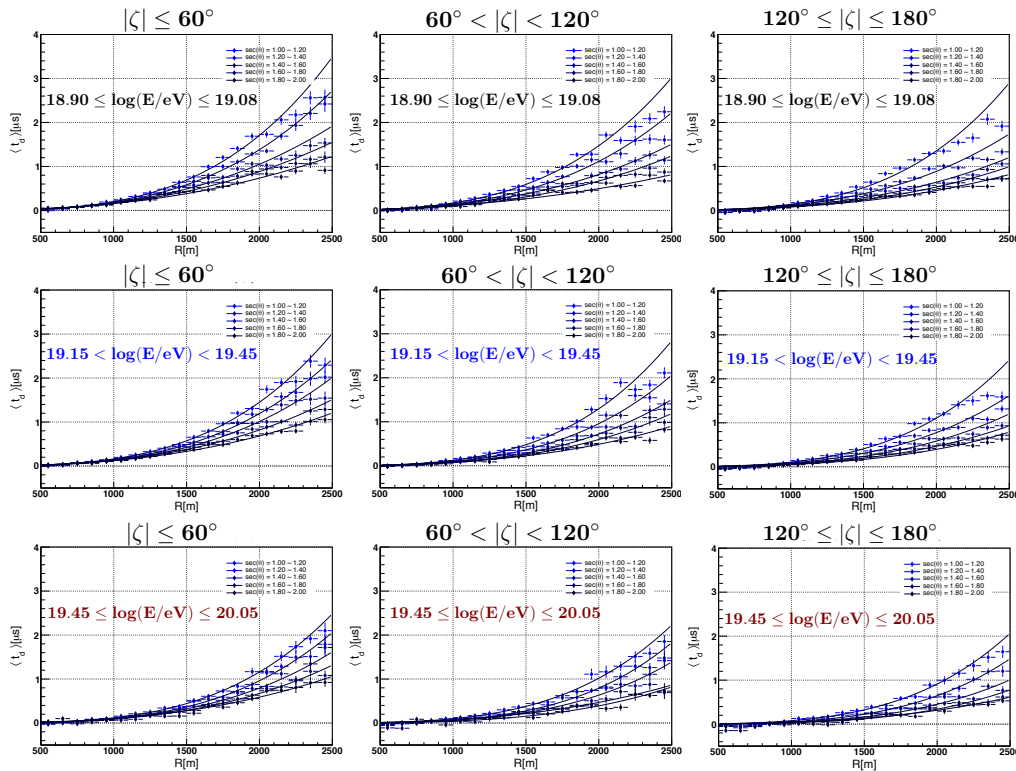


FIGURE 5.34: Curvature of shower front for 5 intervals of zenith angle (by blue color degree, dark blue for large zenith). Top to bottom are for different energy intervals. Left to right presents in different intervals of zeta angle.

Figure 5.35 shows the result of analysis in the curvature of shower front presented in the Figures 5.34, as summary of A and B versus zenith angles respectively by 3 intervals of zeta angle as "early"(top), "intermediate" and "late" (bottom) part of shower front. In each interval of energy was analyzed A and B .

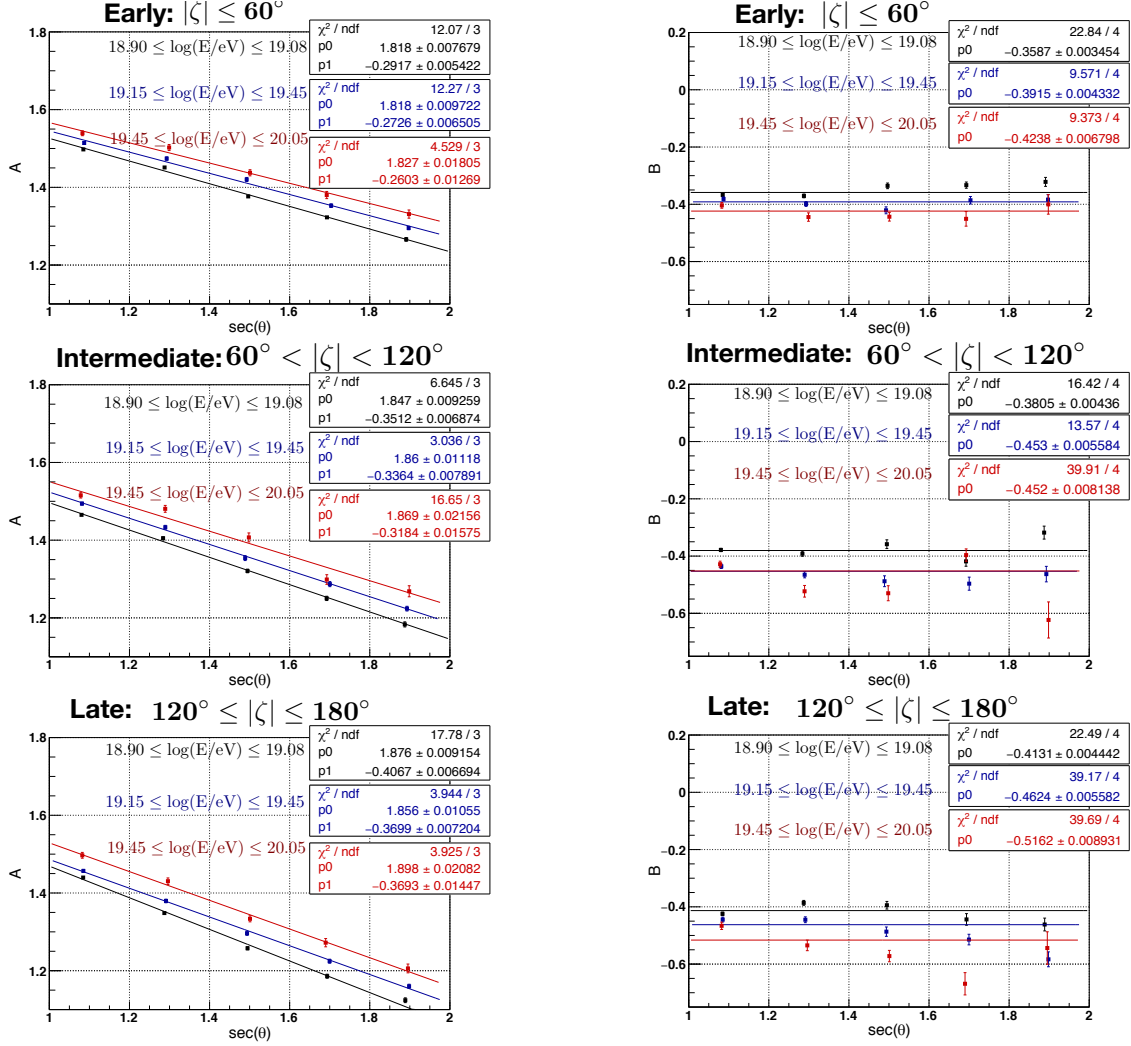


FIGURE 5.35: Results of A (left) and B (right) parameters for various zenith angle intervals binned. Top to bottom early, intermediate and late zeta angle intervals, each one for 3 bands of energies.

Based on this analysis, it was found an zeta angle dependence as described in details in Section 5.5 and it is expressed by the following Equation,

$$t_d = 2.6 \times \left(1 + \frac{R}{30\text{m}}\right)^{p0(\cos\zeta) + p1(\cos\zeta) \times \sec(\theta)} \times \left(\frac{\rho_i}{\text{m}^{-2}}\right)^{p0_B(\cos\zeta)} [\mu\text{s}], \quad (5.9)$$

Table 5.1 presents the functions of $p0$ and $p1$ of A parameter, as well as $p0$ of B from the Equation 5.9 for different energy intervals.

$\log(E/eV)$	$A = p0(\cos\zeta) + p1(\cos\zeta) \times \sec\theta$	$B = p0(\cos\zeta)$
18.90 – 19.08	$p0 = 1.847 - 0.029 \times \cos\zeta$ $p1 = -0.349 + 0.058 \times \cos\zeta$	$p0 = -0.384 + 0.027 \times \cos\zeta$
19.15 – 19.45	$p0 = 1.844 - 0.019 \times \cos\zeta$ $p1 = -0.325 + 0.049 \times \cos\zeta$	$p0 = -0.434 + 0.037 \times \cos\zeta$
19.45 – 20.05	$p0 = 1.864 - 0.036 \times \cos\zeta$ $p1 = -0.316 + 0.055 \times \cos\zeta$	$p0 = -0.464 + 0.045 \times \cos\zeta$

TABLE 5.1: Table of functions found of $p0$ and $p1$ of A and $p0$ of B for different energy intervals.

In this study, it was also found that the residual time function has dependence on energy as shown on the Section 5.6. Each part of the shower was analyzed independently and the generalized Equation is,

$$t_d = 2.6 \times \left(1 + \frac{R}{30\text{m}}\right)^{p0+p1(E) \times \sec(\theta)} \times \left(\frac{\rho_i}{\text{m}^{-2}}\right)^{p0_B(E)} [\mu\text{s}], \quad (5.10)$$

Table 5.2 shows the summary of the functions of $p1$ and value of $p0$ of A and the functions of $p0$ of B parameter for different intervals of zeta angles.

$\log(E/eV)$	$A = p0 + p1(E) \times \sec\theta$	$B = p0(E)$
$ \zeta \leq 60^\circ$	$p0 = 1.82$ $p1 = -1.23 + 0.05 \times \log(E)$	$p0 = 1.35 - 0.09 \times \log(E)$
$60^\circ < \zeta < 120^\circ$	$p0 = 1.85$ $p1 = -1.21 + 0.04 \times \log(E)$	$p0 = 1.77 - 0.11 \times \log(E)$
$120^\circ \leq \zeta \leq 180^\circ$	$p0 = 1.87$ $p1 = -2.08 + 0.009 \times \log(E)$	$p0 = 2.28 - 0.14 \times \log(E)$

TABLE 5.2: Table of functions found of $p0$ and $p1$ of A and $p0$ of B for different zeta angle intervals.

Chapter 6

Shower disk thickness analysis using SD data

An air shower induced by a UHECR primary develops in the atmosphere, contains several types of secondary particles induced by hadron. The Telescope Array array allows measuring, with the hybrid design (FD and SD), the longitudinal development of the shower and the footprint of signals of charged particles mainly electrons and muons on the ground with the SD array. The observables from the data have been taken from SD is the time profile. The aim of this chapter is to study the temporal structure of air showers by exploring the thickness of the shower disk. There are few studies about the thickness of shower disk, this analysis can be related to shower development and then it derived to infer the type of cosmic rays. However, there is not exists yet a detailed material from the simulation or data to make this interpretation. The main motivation to use this definition is to understand the phenomena of air shower through its thickness formed on the shower disk and how it affected by its different geometry conditions, its development of the secondary particles in the atmosphere when hit on the ground. One of the pioneering works, to study the longitudinal development features of extensive of air showers using the definition of width time of the signal deposited on the detector, were the Volcano Ranch and the Haverah park groups [55, 52] in the 1963s with a small array of CRs focussing at highest energies. A recent study was reported by Auger experiment [44] in 2016 with the purpose to investigate the mass composition of UHECR. However, this work is focused to understand the characteristics of EAS initiated by an UHECR using good statistics of TA SD data. This analysis has specifically been focussed to

explore the information on the waveforms of the FADC signals. The entire chapter will be dedicated to analyze data of the TA SD observed during 11 years from 2008-05-11 to 2019-05-10.

As introduced in Section 5.1.3 FADC traces which are used to measure the signal responses from SD. Figure 6.1 shows the FADC waveforms stored in one event shower, where the typical TA SD signals response to the upper and lower layer as is shown the black and red area respectively.

20081009 194547.790110

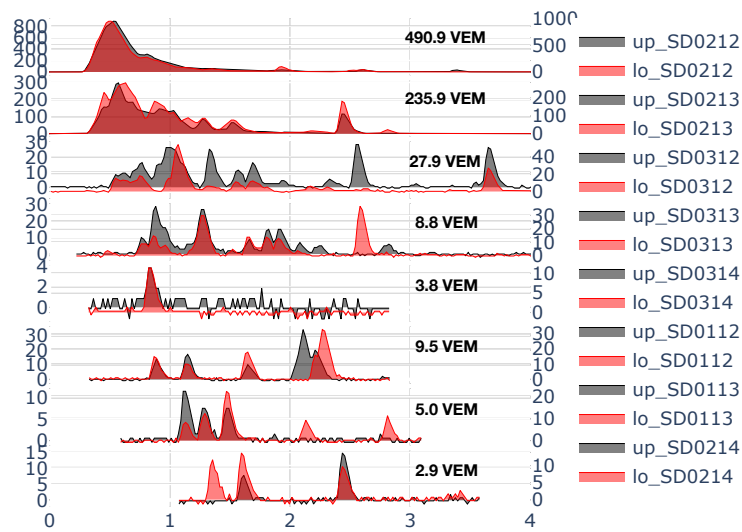


FIGURE 6.1: An example of FADC waveforms of one vertical event shower. The black area fill represents the upper layer and the red area is the lower layer of the SD counter.

This is an illustration of the traces from a vertical event shower with zenith $\theta \sim 1^\circ$ by showing both signals of response, upper and lower layer. The standard way in TA to measure the charge VEM is the average of the integral area of both signals in each SD. In the analysis of the thickness of shower disk uses each signal upper/lower layer independently.

6.1 Definition of risetime (t_R)

In the early the risetime definition ($t_{1/2}$) was introduced during Haverah Park experiment based on water-Cherenkov detectors to study the mass composition using

$t_{1/2}$, but it was impossible to deduce it due to limited data [55]. Today it is still in debate to use this definition of risetime as parameter to understand the mass composition. However, the risetime is rather useful to understand the features of the EAS. The main idea of the risetime definition t_R is that the time takes for signal trace to rise to 10%, which is the pulse generated when at least pass one particle through of detector, from the total signal is t_{10} and the time it takes for the signal to rise to 50% of the total signal is t_{50} , the point of the half of the total pulse is deposited on the detector [87, 55]. The thickness of the shower disk increases with the distance from the shower axis and this arises because the primary CRs particles at a large axial distances moves deeper in the atmosphere [54]. Therefore, the t_R is defined as the width of a certain time of accumulated waveform. In this study we use the risetime defined as the time interval in which the accumulated waveform reaches from 10% to 50% of the total SD signal as represented in the right panel of 6.2.

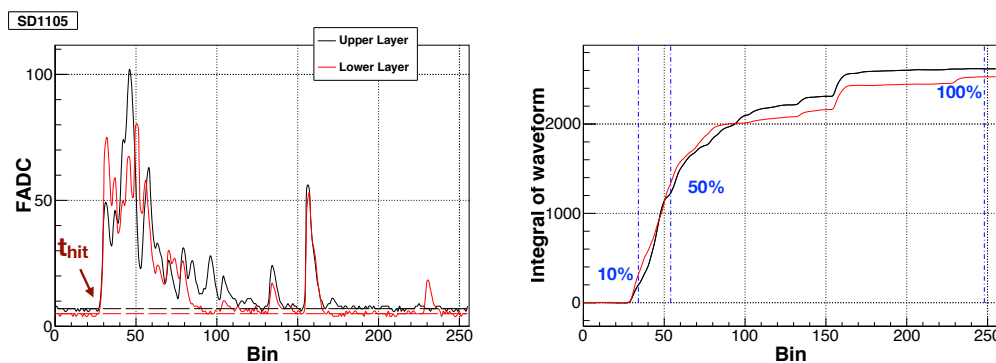


FIGURE 6.2: (Left) Typical FADC waveforms of a TA SD counter as a function of time-bin. The black and red lines represent the upper and lower layers response signals of PMTs of one SD. (Right) The accumulated waveforms of the left figure.

6.2 Quality of waveform to determine the risetime

Before starting the analysis it was studied some events to verify the quality of the FADC traces for the calculation of the risetime. In this section, two types of signals of waveform do not contribute to the study of the risetime t_R .

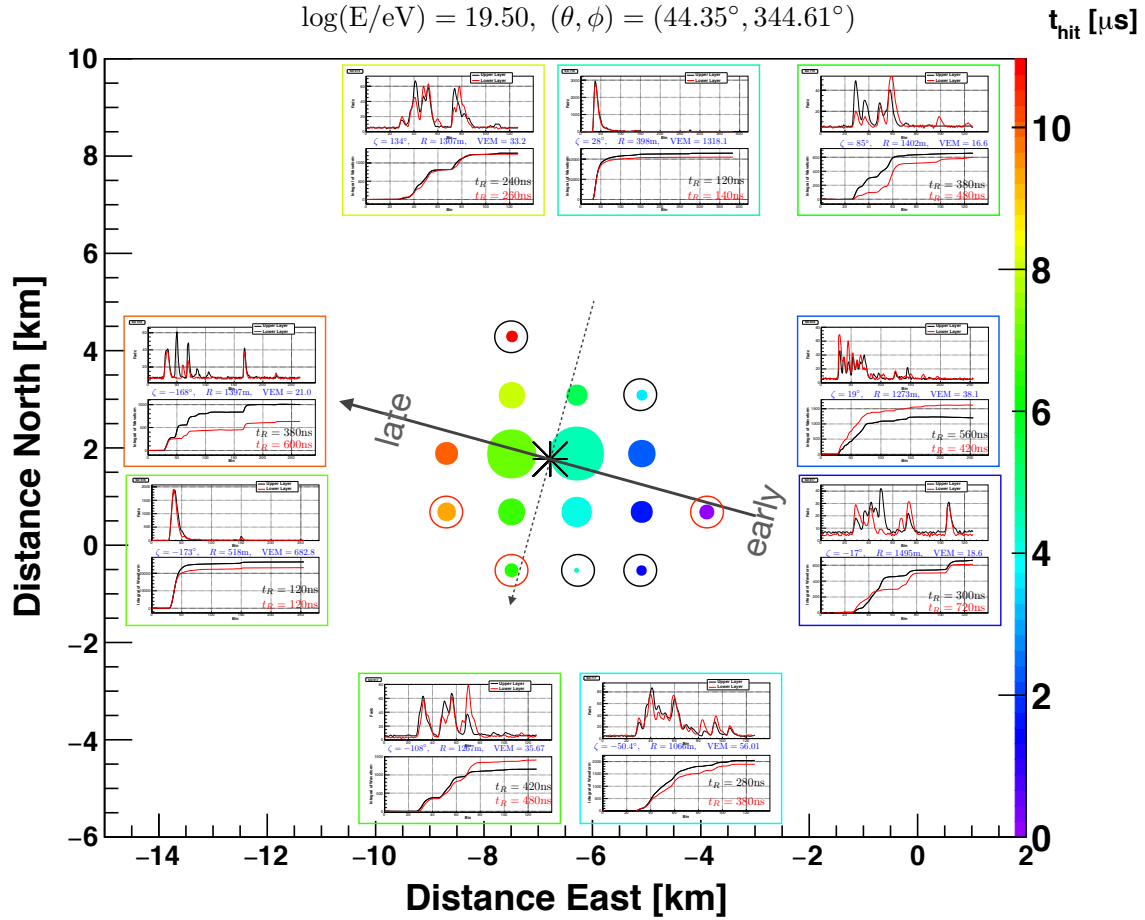


FIGURE 6.3: An example of an event map with 16 SDs triggered. Around the map, the waveforms FADC with the integration of signals. The black star mark is the core location and the waveforms correspond to all SDs close to the core. The SDs marked in circles with red represent those weak signals and those with black circles are possible accidental particles.

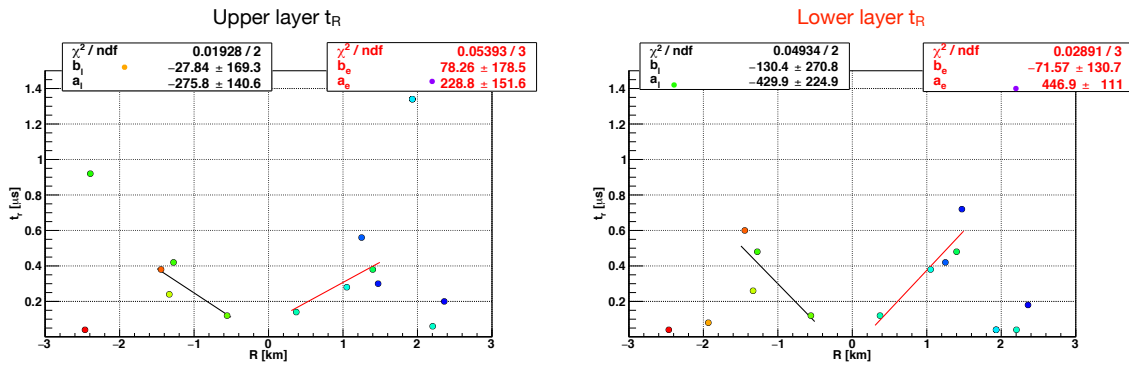


FIGURE 6.4: These plots are the scatter plot is the risetime versus R measured for the upper and lower layer.

Figure 6.3 is one example of event with the respective waveforms and the calculation of the width time of risetime through of the integrated waveform from 10 %

to 50 %. The risetime as function core distance is calculated for upper and lower signals respectively as shown on Figure 6.4. At 0 km is located the core and the right side of risetime are the early SDs hit and the left are the late and both data are fitted with a linear function.

While the distance to core increases the signals become weaker, in the event example at distance closely to 2 km and higher, the FADC pulses decrease which causes the width of risetime, (t_R), become smaller as shown in the Figure 6.4 for both cases of the upper and lower layer. Figures 6.5, both the VEM charge are 4.7 and 1.9 respectively. And the risetime calculated for the respective is also low in the order of 0.04 [μ s] and this example vary considering the primary energy, this case corresponds to $10^{19.50}$ eV, but for energy ($E < 10^{19.00}$ eV) the signals of secondary particles also are become weak signals starting at a close distance to core e.g. at 1200 m.

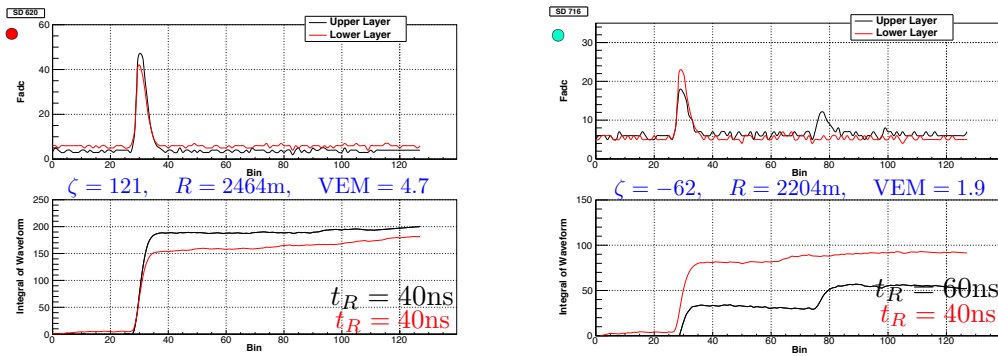


FIGURE 6.5: The FADC waveforms and the corresponding integration of the weak signals at higher distance to core the color marked match with the map event display.

Figures 6.6 are the FADC traces formed for the shower event in the map display (Figure 6.3) for the possible accidental signals, the second or third peaks in the waveforms. In the case SD 517 ID (shown in the top left of Figure 6.6) the second peak isolated from the first is produced at bin 110 (1 bin = 20 ns) with high pulse by the upper layer (black line) than lower layer, which corresponds to 2200 ns or 2.2 [μ s]. The corresponding integration of FADC signals fluctuate more for the upper layer that causes the width of risetime correspond to 76 bin between 10% to 50% and the bin-time is 1520 ns, in case of lower layer is 80 ns. In case of SD 616 ID (bottom left side of Figure 6.6) shows 3 single FADC pulses for upper/lower layer

and the integration of the waveforms fluctuates producing high risetime of $0.92 \mu\text{s}$ and $1.42 \mu\text{s}$ for up/lo layer respectively. The SD 917 ID (top of right Figure 6.6) with VEM charge 7.3 shows 3 extra FADC pulses after first peak, the risetime is 1.44 and $1.4 \mu\text{s}$ up/lo layer respectively, this case probably considered as miscalculated of risetime. Last SD 816 (bottom of right 6.6) located at 2360 m from core with VEM charge 4.0, it has two consecutive FADC pulses determining the risetime of 0.2 and $1.8 \mu\text{s}$ being not enough but also in this example of FADC trace and for cases of weak pulses can cause an unstable from the baseline due the constant fluctuation of signal.

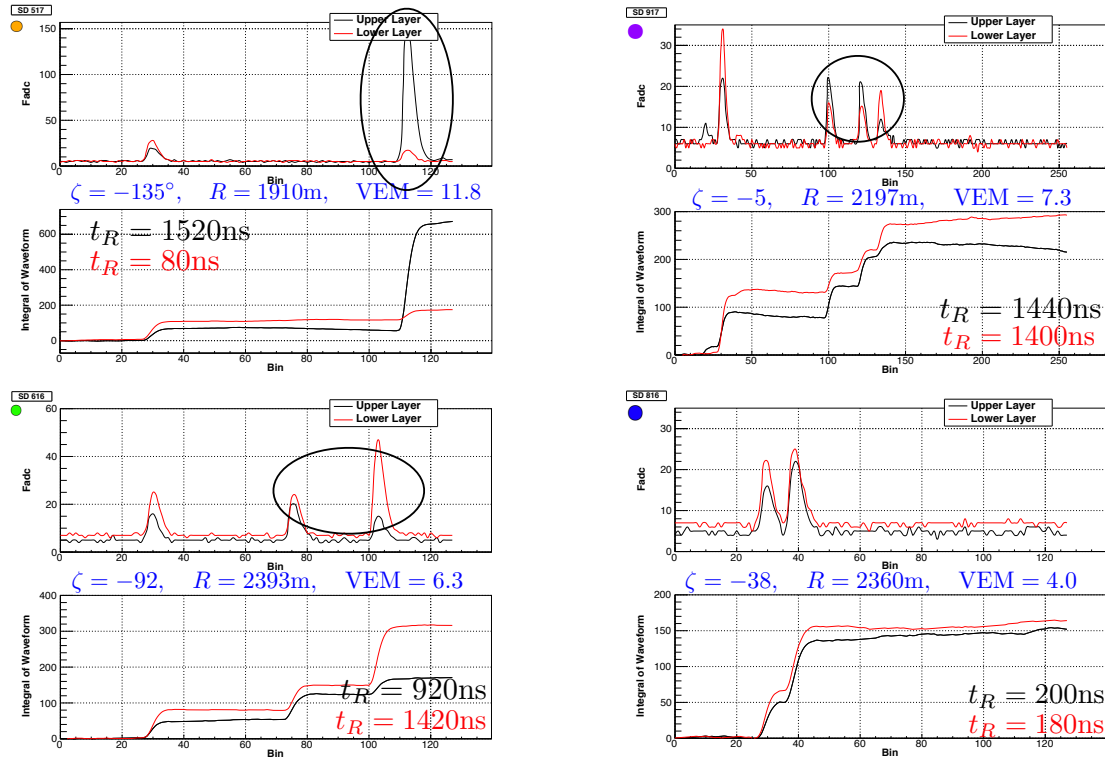


FIGURE 6.6: The FADC waveforms and the corresponding integrated signal, the color marked matches with the map event display.

Another clear example of a weak FADC signal that can cause a miscalculation of risetime due to fluctuation of baseline is presented in Figure 6.7. This waveform has a single peak and the accumulated waveform is reached at bin ~ 40 , and the accumulated along all bins are found at bin ~ 100 , then the width of risetime can be miscalculated by this last accumulated due to the fluctuation from the baseline FADC.

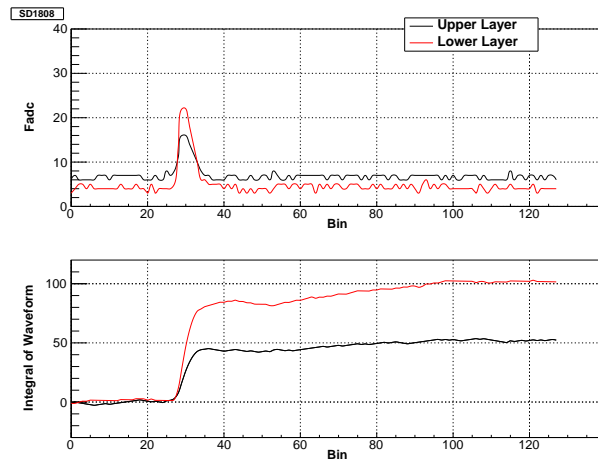


FIGURE 6.7: Example of weak signal (upper panel) and the integrated signal (low panel) the color marked matches with the event map display.

6.2.1 Bad quality of FADC signals

A typical waveform duration is 2.56 microsecond equivalent to 1 frame of waveform stored in 128 time-bins. However, some waveform's duration is extended to several waveform frames. Some cases were found interrupted waveforms during taking data, causing the missing information of the tail of longer FADC traces or in other cases storing accidental FADC traces pulses possible belonging to another event shower. In the present analysis was rejected these pulses with missing information of the waveforms or discontinued waveforms as explained in Section 4.5.

The following FADC traces are examples of interrupted waveform. Figures 6.8 shows examples of waveforms interrupted, by assumig these waveforms stored are accidental-signal.

It was explained in Section 3.2.1, the triggered condition during collecting the waveforms during the event $\pm 32 \mu\text{s}$. In the process of data analysis was applied to reject these accidental signals.

Figure 6.8 (left) is a waveform stored in the 580 bins, with 2 FADC traces interrupted from bin 128 to 450. Figure 6.8 (right) shows the waveform recordered from bin 0 to 1675, the first pulse is weak and the second pulse is big pulse probably cause by other event.

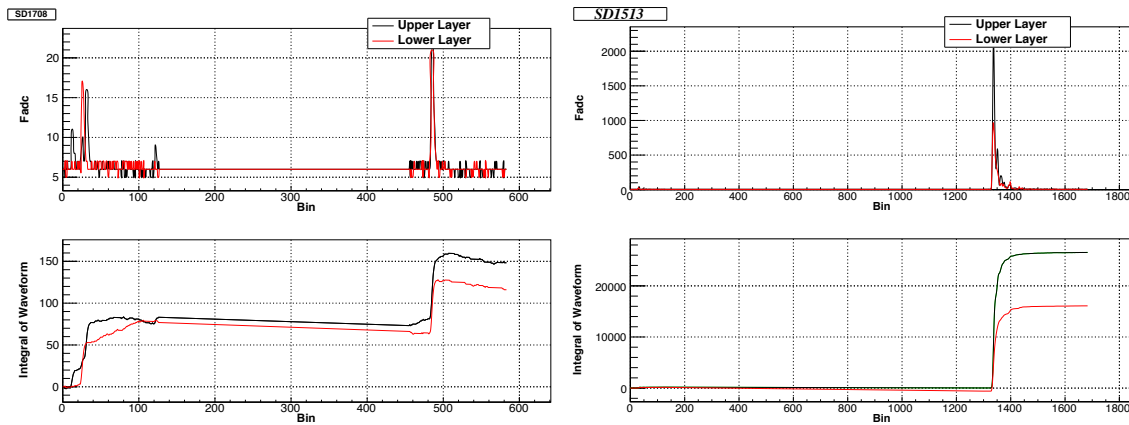


FIGURE 6.8: Two example of interrupted waveforms during collecting data at CT. Left figure shows the waveform interrupted after 1 frame at 129 bin and continue at bin 450 ($\sim 9 \mu\text{s}$) and collecting this accidental-signal. Right figure is other example when the first FADC signal is weak, the total bins are 1675 which correspond $33.5 \mu\text{s}$ and the second big pulse is at bin 1330.

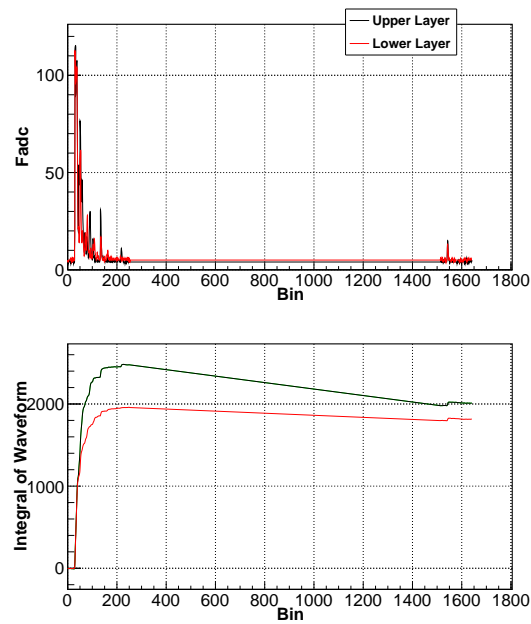


FIGURE 6.9: A FADC trace belongs to a high signal pulse, but the signal is interrupted after the 2nd. frame.

Figure 6.9 represents a high pulse and from the 3rd frame of waveform is interrupted which caused the miscalculation of the risetime.

6.3 Risetime dependence of zenith angle

Results of the risetime as a function of the distance from the shower core is shown in 6.10 for upper and lower layer time-traces. As it can be seen, the risetime increases as R increases at least up to the distance $R = 1200$ m for both cases upper/lower layer. The black and red dots are the average of risetime with a 100 m binning. These examples represent the risetime distribution for events with average energy of $\log(E/eV) = 19.0$ for vertical showers with zenith angles $1.0 < \sec\theta \leq 1.1$ ($0^\circ - 24.6^\circ$). The average of risetime (black and red dots) are fitted with a linear function. $\langle t_R \rangle = b + a \times R$ as a first approximation in an interval of 500 to 1200 m of distance from the core R .

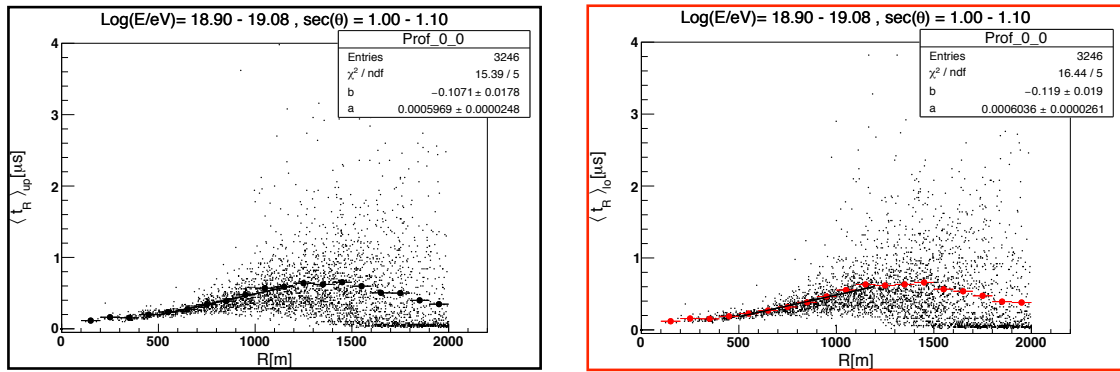


FIGURE 6.10: The distribution of risetime as function of distance to core for an fix interval of energy of $18.90 \leq \log(E/eV) \leq 19.08$ and zenith angle in $1.0 < \sec\theta \leq 1.1$ ($0^\circ < \theta \leq 24.6^\circ$). Left and right plots correspond to upper and lower layer, the black and the red dots represent the averaged of risetime in a bin of 100 m. Both is fitted with a linear function in R range of 500 - 1200 m.

The risetime increases with the core distance and decreases with respect to increasing the zenith angle as it was shown on Figure 6.11. This Figure (left) shows the mean of risetime from the data and it is fitted with the first approximation of first-order-polynomial from 500 to 1200 m, at higher distance of 1200 m the the binned risetime decreased due to the weak time-signal. The averaged risetime can also be fitted to second-order-polynomial from 100 - 1500 m as shown in Figure 6.11(right). For our analysis we have been taken into account the results of linear function fitting in the range of 500 - 1200 m. Figures ?? show the results of linear fitting as function of $\sec\theta$, in both cases of a and b has dependence on zenith angle.

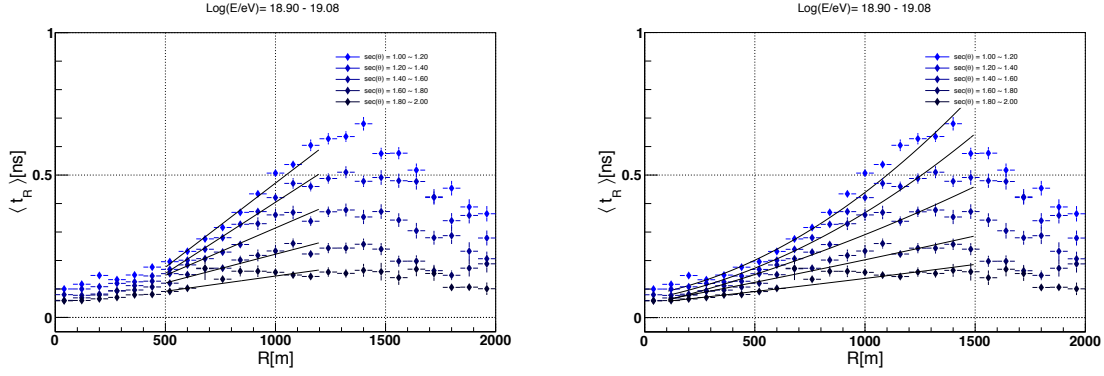


FIGURE 6.11: Mean of risetime for SDs binned in R and $\sec\theta$ for an interval of energy $18.90 \leq \log(E/eV) \leq 19.08$. Left plot is fitted with a linear function in a range of 500 - 1200 m. Right plot is fitted each zenith interval with a quadratic polynomial function in the range 100 to 1500 m.

The thickness of the shower disk refers to the bulk swarm of secondary particles propagating towards the ground. Therefore in this analysis, it is used as parameter of the thickness of the shower disk, the slope a , from linear fitting observed in the interval R (500 – 1200 m). Figures 6.12 show the results of a (left) and b (right) respect to $\sec\theta$ for 3 intervals of energies averaged at $10^{19.0}$ eV (black square marks), $10^{19.30}$ eV (blue square mark) and $10^{19.75}$ eV (red square mark). Comparing these 3 energies averaged, the tendency of dependence in $\sec\theta$ is clearly observed for any energy interval. Thus, the following Equation shows the slope, a , and the offset, b , has dependence on $\sec\theta$,

$$\langle t_R \rangle = b(\theta) + a(\theta) \times R. \quad (6.1)$$

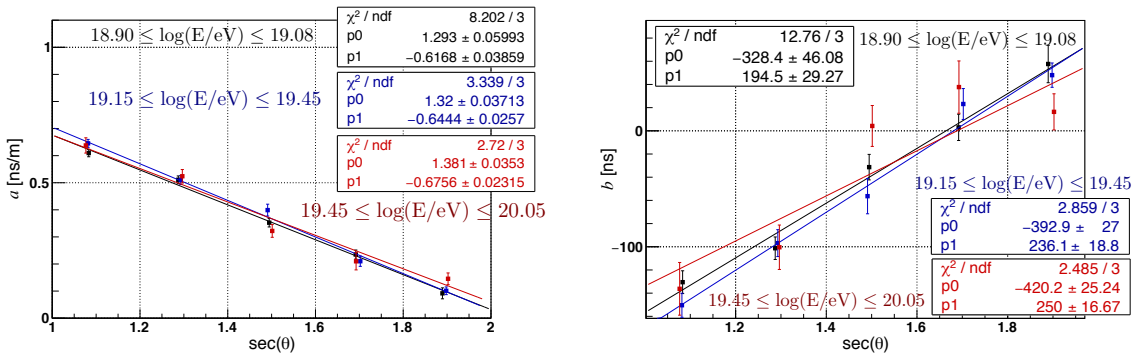


FIGURE 6.12: The superposition of results of the slope, a , and the offset, b versus $\sec\theta$ of 3 intervals of energy averaged in $10^{19.0}$, $10^{19.30}$ and $10^{19.75}$ eV.

However, for understanding the parameter of thickness of shower disk there is not clear variation comparing the 3 intervals of energy.

To understand of the thickness of shower disk has dependence on the zenith angle, it is necessary to look up the lateral distribution to understand this tendency. The Figures 6.13 show the particles densities binned in 150 m for 5 interval of $\sec\theta = 1.0 - 2.0$ in step of 0.2 for 3 intervals of energy (plots from left to right). We can expect for vertical showers the particles density is higher than for inclined shower and the thickness of showers for vertical also should be thicker than that inclined showers.

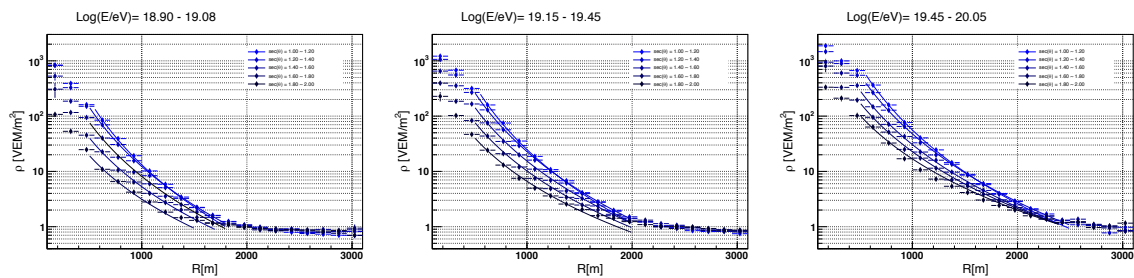


FIGURE 6.13: Particle density distribution averaged as function of core distance binned in bins of 150 m, and various zenith intervals in $\sec\theta$ $1.0 < \sec\theta \leq 2.0$ in steps of 0.2. Lateral distribution of particles in the interval of energy $18.90 \leq \log(E/eV) \leq 19.08$ (left), $19.15 \leq \log(E/eV) < 19.45$ (middle), and $19.45 \leq \log(E/eV) \leq 20.05$ (right).

In order to understand with more details the characteristics of shower disk, in the next section it is decided to make an analysis based on the azimuthal angle (ζ), whose definition was described in the previous Chapter Section 5.3.

6.4 Analysis of azimuthal angle (ζ)

It was made a similar analysis made on residual time, the dependence on zeta angle to analyze the thickness of shower disk calculating the variance of a slope of risetime assuming the angle around the shower axis (ζ). For this purpose, it was studied the distribution of zeta angle for "early", $|\zeta| \leq 60^\circ$, "intermediate", $60^\circ < |\zeta| < 120^\circ$, and "late", $120^\circ \leq |\zeta| \leq 180^\circ$, SDs triggered. Firstly, if we considered an event shower and its azimuthal angle (ζ) is projected on the ground of each SD as shown in the Figure 6.14.

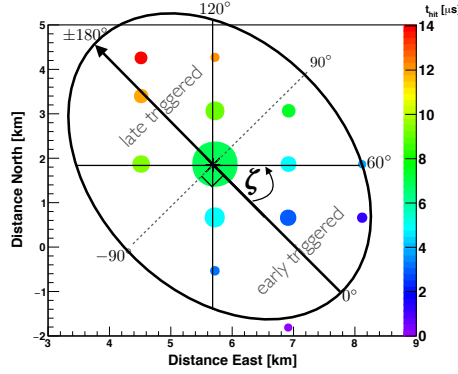


FIGURE 6.14: An event map display with the zeta angle projected on the ground.

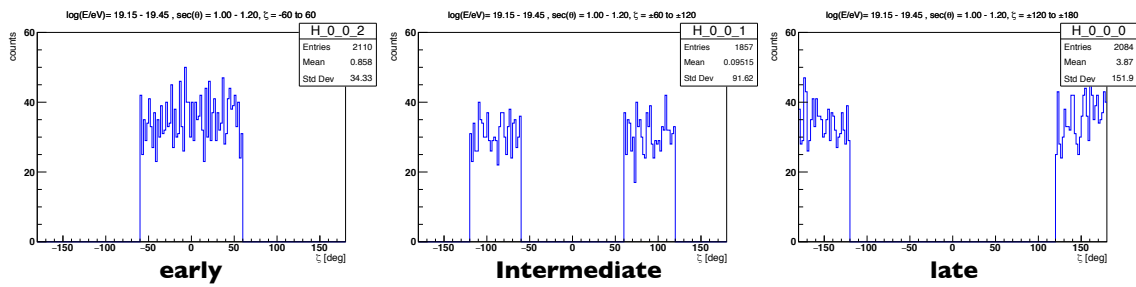


FIGURE 6.15: An example of ζ distribution for **early** ($\zeta = -60$ to 60), **intermediate** ($\zeta = \pm 60$ to ± 120) and **late** ($\zeta = 120$ to -120) triggered SDs for fix interval in energy $10^{19.15} - 10^{19.45}$ eV and zenith angle $1.0 \leq \sec\theta \leq 1.2$.

Figures 6.15 show the zeta angle distribution for the early SDs triggered ($|\zeta| \leq 60^\circ$) (left), the intermediate SDs triggered ($60^\circ < |\zeta| < 120^\circ$) (middle), and for late $120^\circ \leq |\zeta| \leq 180^\circ$) (right) for all event of showers in the energy range of $10^{19.15} - 10^{19.45}$ eV for a fix zenith interval $\sec\theta = 1.0 - 1.2$. Figures 6.16 show all distribution of zeta angle for various intervals of zenith angle in $\sec\theta = 1.0 - 2.0$ in steps of 0.2 from top to bottom, and from left to right different intervals of energy. And Figures 6.17 show the distribution of core distance respect to zeta angle for various intervals of zenith angle and different intervals of energy.

As introduced previously the azimuthal angle, ζ , close at 0° are triggered the "earliest" SDs counters, ζ close at $\pm 90^\circ$ corresponds to SDs triggered in the "intermediate" part of shower event, and ζ close at $\pm 180^\circ$ corresponds to all triggered "lately". It was observed from the distribution of zeta angle in Figure 6.16, when zenith increases the distribution of zeta changes gradually observing a deficit in the distribution at "intermediate", for zeta angle around $\zeta = \pm 90^\circ$ as zenith is going to

be large and its tendency is presented in different intervals of energy. In the same way, the distribution of core distance R has the same tendency along to the all ζ distribution, for vertical showers, R is distributed uniformly but while increasing the zenith angle this distribution becomes asymmetric.

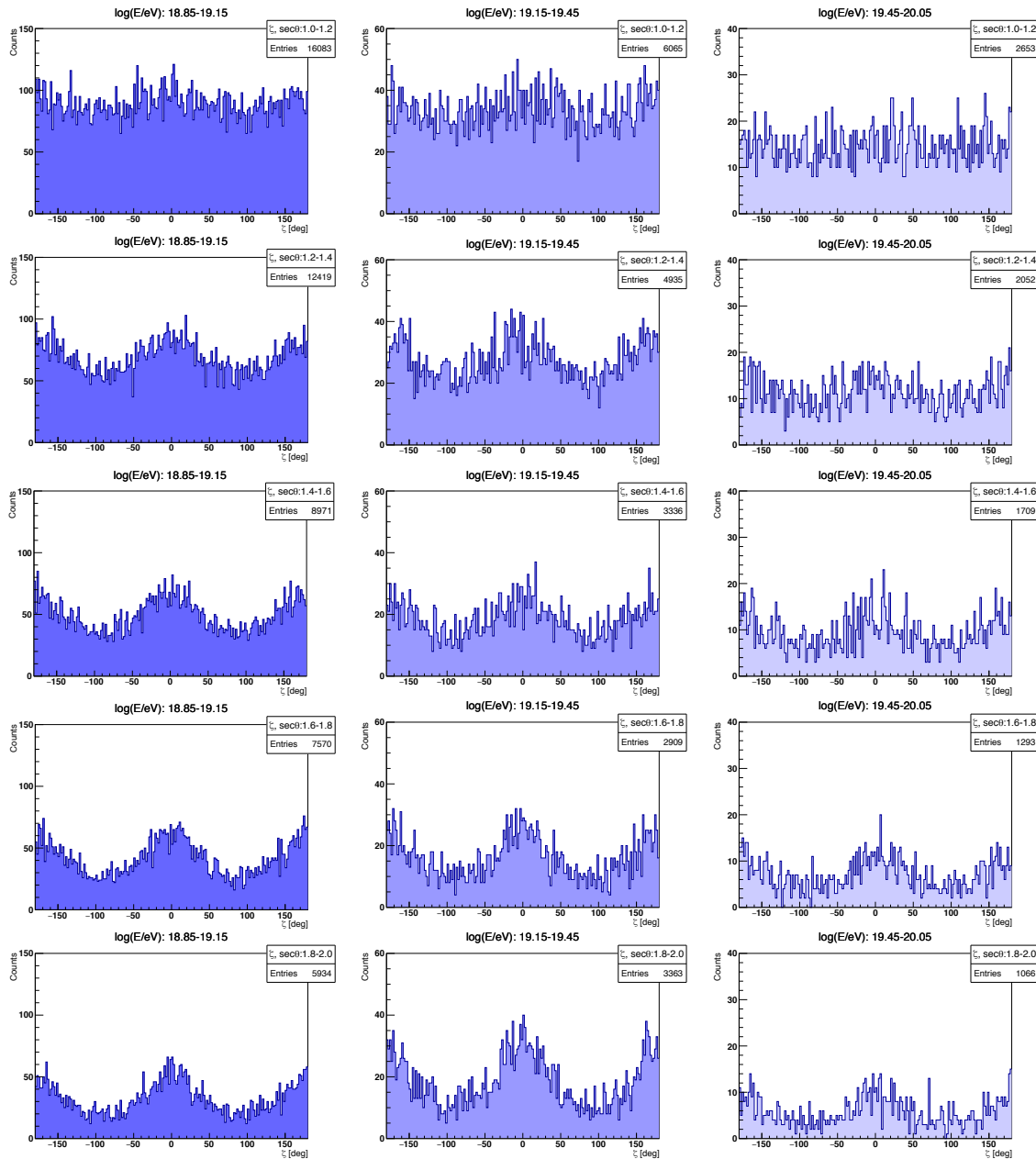


FIGURE 6.16: Histograms of ζ distribution in bins of $\log(E/eV)$ for various zenith angle intervals. Left column of plots show at interval $18.90 \leq \log(E/eV) \leq 19.15$. Middle column of plots show at interval $19.15 < \log(E/eV) < 19.45$. Right column of plots at interval $19.45 \leq \log(E/eV) \leq 20.05$. From top to bottom binned: $1.0 \leq \sec\theta \leq 1.2$, $1.2 < \sec\theta < 1.4$, $1.4 < \sec\theta < 1.6$, $1.6 < \sec\theta < 1.8$ and $1.8 < \sec\theta \leq 2.0$.

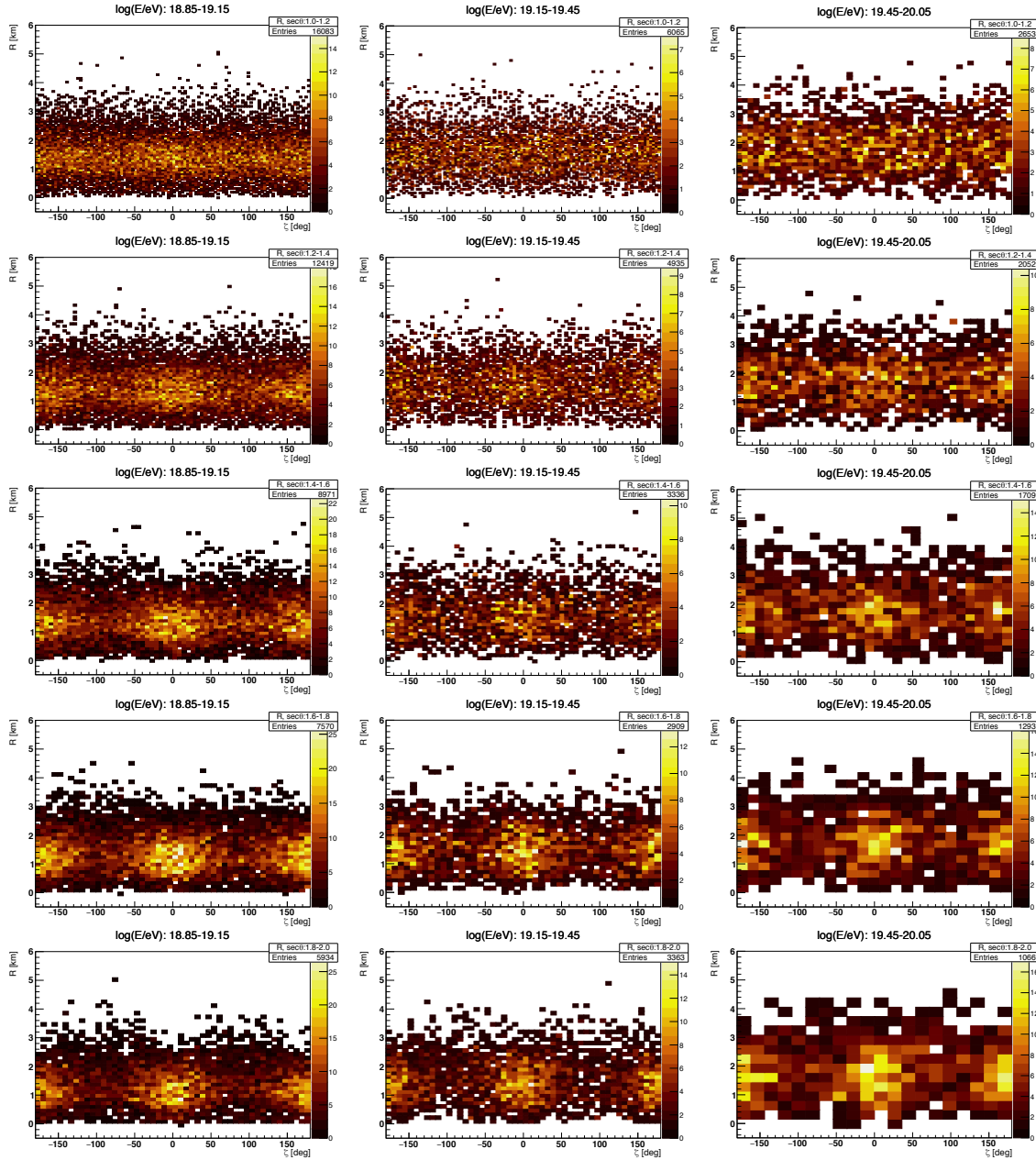


FIGURE 6.17: Scatter distribution of core distance (R) values and azimuthal angle (ζ) in bins of $\log(E/eV)$ for various zenith angle intervals. Left plots correspond to energy interval $18.90 \leq \log(E/eV) \leq 19.15$. Middle plots in bins at interval of $19.15 < \log(E/eV) < 19.45$. Right plots in energy bins $19.45 < \log(E/eV) \leq 20.05$. From top to bottom: $1.0 \leq \sec\theta \leq 1.2$, $1.2 < \sec\theta < 1.4$, $1.4 < \sec\theta < 1.6$, $1.6 < \sec\theta < 1.8$ and $1.8 < \sec\theta \leq 2.0$.

Figures 6.18 show some cartoons that represent the shape roughly projected on the ground when the EASs hit the ground considering the different zenith angles condition according to the zeta angle distribution shown on 6.16.

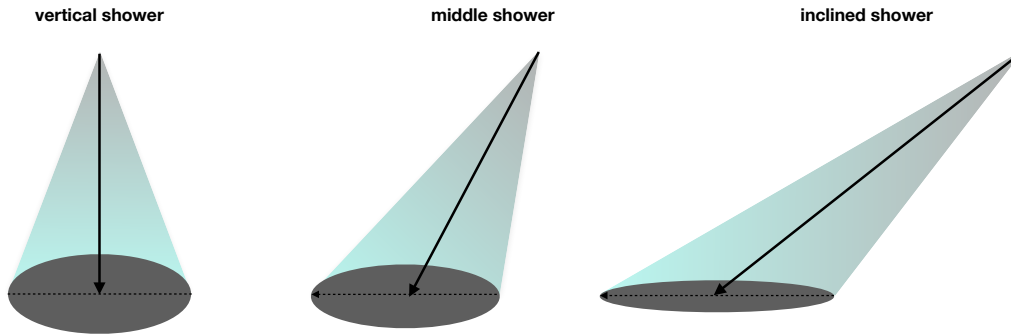


FIGURE 6.18: Scheme of shower shape and the effect of zeta angle projected on the ground.

6.5 Thickness of shower disk dependence on ζ

Data used in the thickness of shower disk are from May 2008 to May 2019 using different selection rules detailed in Section 4.5. We have performed the risetime profile to analyze the thickness using the slope a variation on the zenith angle, R and zeta angle. Considering a determined band of energy, those events showers are selected into 5 intervals of zenith angle and each one is divided into the SDs triggered by "early", "intermediate" and "late" triggered as parts of an event shower, and t_R is analyzed. The FADC traces of TA SDs have two signals and in the present analysis were considered both independently as the upper and lower layer for the calculation of the risetime t_R . The next measurement of risetime is based on lower layer results.

The set of plots presented in Figures 6.19 shows an example of how is the variation of risetime, t_R , for three intervals of zeta angle and for a fix interval of energy between $19.15 \leq \log(E/\text{eV}) \leq 19.45$. From the top to bottom panel of plots are measured for 5 intervals of zenith angle and the 3 columns divided are intervals of zeta angle from early (left), intermediate (middle) and late (right).

In all cases of risetime of analysis, we have focused in a specific range of R from 500 to 1200 m for the linear fitting. The next step is to parameterize the thickness parameter, a , with the zeta angle. To understand it, we can see a simple case from the Figure 6.19 the third row, which corresponds to showers with middle zenith angle $44.4^\circ \leq \theta \leq 51.3^\circ$, the fitting in the 3 cases for early, intermediate and late, it can be observed the slope a changes clearly in the 3 cases for "early" $a = (0.52 \pm 0.02)$

[ns/m], intermediate $a = (0.32 \pm 0.02)$ [ns/m] and late $a = (0.23 \pm 0.01)$ [ns/m] respectively.

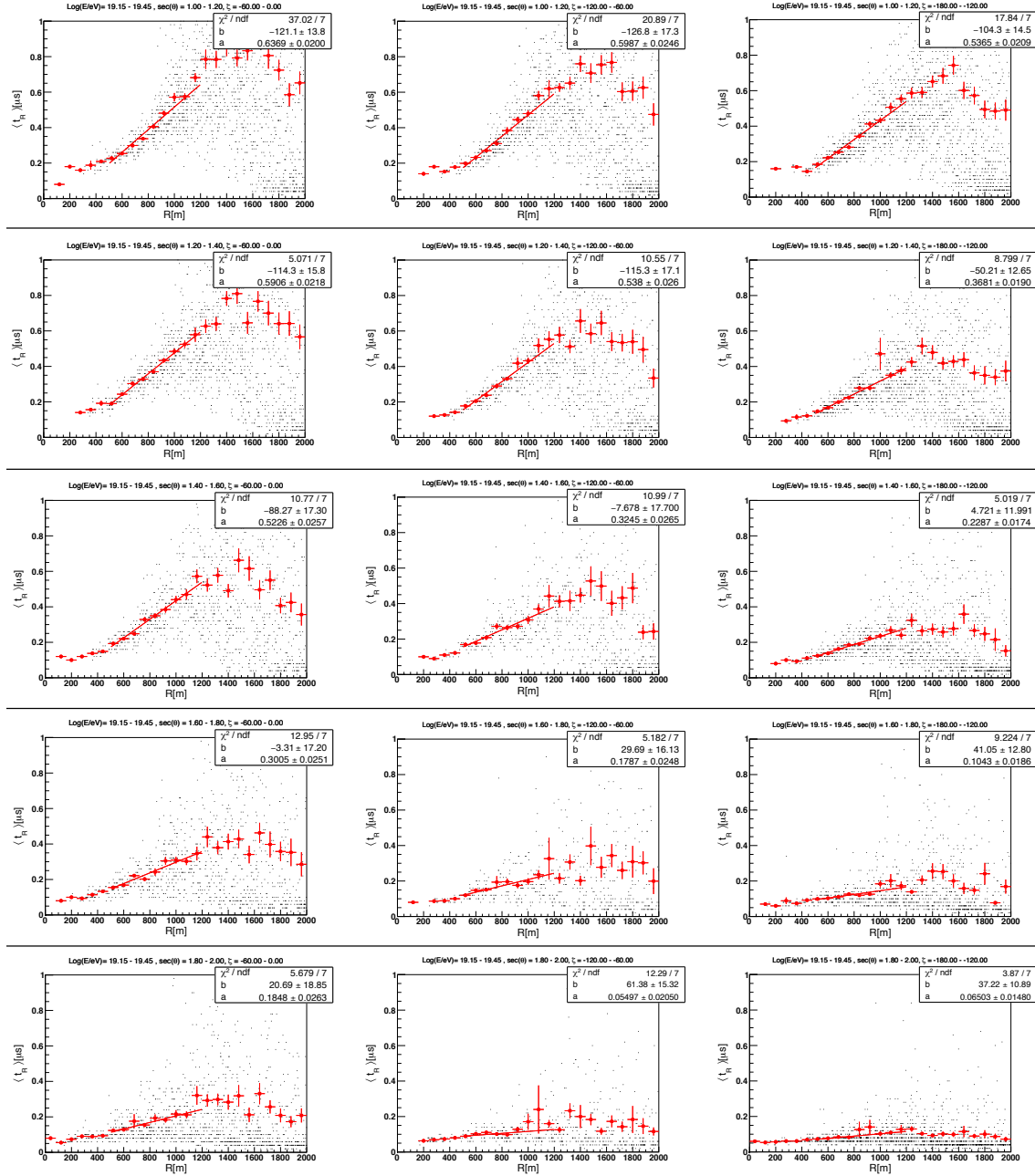


FIGURE 6.19: The scatter plots of the risetime vs. core distance for an interval of the energy of $10^{19.15} - 10^{19.45}$ eV. Divided into 5 intervals of zenith angle from top to bottom in $\text{sec} \theta = 1.0 - 2.0$ in steps of 0.2. From left to right different intervals of zeta angle for "early", $|\zeta| \leq 60^\circ$, (left), "intermediate", $60^\circ < |\zeta| < 120^\circ$, (middle), and "late", $120^\circ \leq |\zeta| \leq 180^\circ$ (right). Each plot with linear fits in the range of R of 500 - 1200 m.

6.5.1 Thickness parameter parameterized to zeta angle

In order to study the thickness parameter, a , from the following analysis, the showers are divided into 6 bands of zeta angle. The following example is based in 6 intervals of zeta angle in steps of 60° .

Then the fitted values of a are parameterized with respect to ζ (left) and $\cos\zeta$ (right) as shown in the Figures 6.20. This is an example analyzed for a fix energy interval centered at $10^{19.30}$ eV and fix zenith close to vertical showers. Both cases are fitted with a second and first order cosine function expressed in the Equations (6.2) and (6.3) respectively.

$$a = (c_0 + c_1 \cos\zeta + c_2 \cos^2\zeta) \text{ [ns/m]} \quad (6.2)$$

$$a = (a_0 + a_1 \cos\zeta) \text{ [ns/m]} \quad (6.3)$$

For the case of early, from the Figures 6.20 the gray area, the thickness parameter is higher than for late, it can be interpreted as the thickness of shower disk for early is slightly thicker than for late thickness.

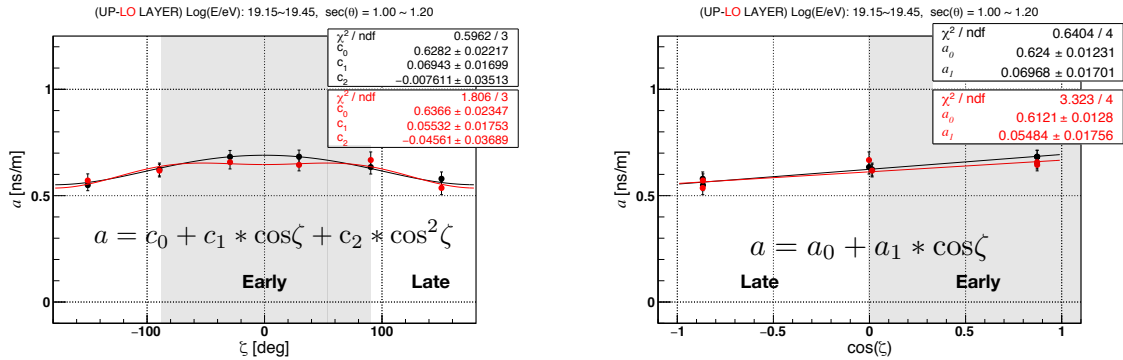


FIGURE 6.20: Thickness parameter a and azimuthal angle ζ , for the interval of energy $10^{19.15} - 10^{19.45}$ eV, and zenith angle band in $\sec\theta : 1.0 - 1.2$. Left plot a vs. zeta, the upper layer FADC traces result (black dots) and the lower layer FADC traces result (red dots). Right plot a vs. $\cos\zeta$, the upper and lower layer results are represented by black and red dots respectively.

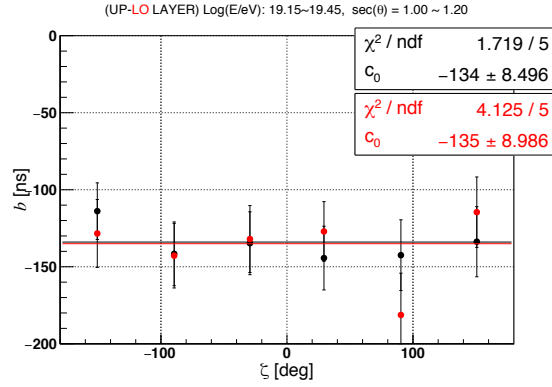


FIGURE 6.21: The values of offset, b , respect to zeta angle ζ , for the interval of energy $10^{19.15} - 10^{19.45}$ eV, and zenith angle band in $\sec\theta = 1.0 - 1.2$.

Figure 6.21 shows the values of b parameterized with respect to ζ . In case of the offset, b , parameterized with zeta angle as shown on the Figure 6.21, shows it does not have dependency on zeta angle for this zenith angle interval, it was observed for others intervals of zenith angle, the values of b show a variation in zeta, but it does not hold a specific tendency as in case of a . It should be noted that the distribution of t_R respect to R is not linear from the origin, being the values of b negative by this zenith interval and as zenith interval change b is also changed. In this work has not analyzed the offset time, b , of the risetime t_R .

The following figures show the results the thickness parameter a variation with zeta angle, for 4 intervals of energy by using 6 intervals of zeta angle ζ in steps 60° , the details of the risetime distribution for the corresponding zeta angle are shown in the Appendix A.8 ($E = 10^{19.0}$ eV) and Appendix A.9 ($E = 10^{19.75}$ eV).

The next set of Figures 6.22 6.23 6.24 6.25 show the values a respect to zeta angle (left) and respect to $\cos\zeta$ (right) for the intervals of energy $10^{18.60} - 10^{18.85}$ eV, $10^{18.85} - 10^{19.15}$ eV, $10^{19.15} - 10^{19.45}$ eV, and $10^{19.45} - 10^{20.05}$ eV respectively. From top to bottom for various intervals of zenith angle in $\sec\theta = 1.0 - 2.0$ in steps of 0.2. Each distribution is fitted by the Equation 6.2 (left) and Equation 6.3 (right). It should be noted for the highest energy interval the numbers of events are small, thus, SDs data also are reduced. Then, the first division of zeta angle are 6 for $\zeta = 0^\circ - 180^\circ$ in steps of 30° and considering the symmetry of the shower axis line the 6 intervals of $\zeta = 0^\circ - (-180^\circ)$ are included in the first zeta division as observed in Figure 6.25 (left).

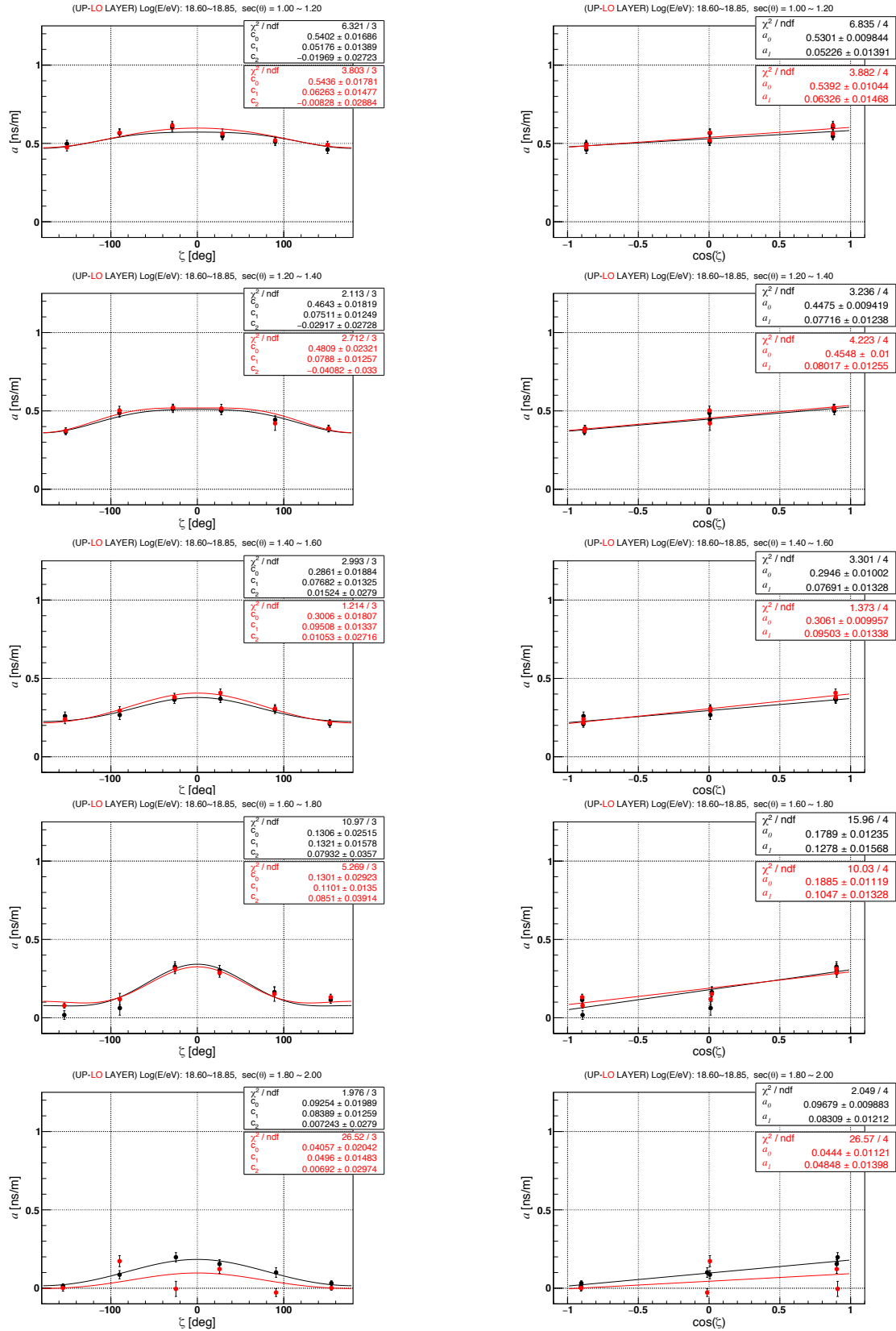


FIGURE 6.22: Thickness parameter a as function of ζ (left plot) and $\cos\zeta$ (right plot) for various $\sec\theta$ for the lower energy interval $10^{18.60} - 10^{18.85}$ eV. Top to bottom plots for intervals of $\sec\theta = 1.2 - 2.0$ in steps of 0.2. The results for upper layer (black mark) and lower layer (red marks).

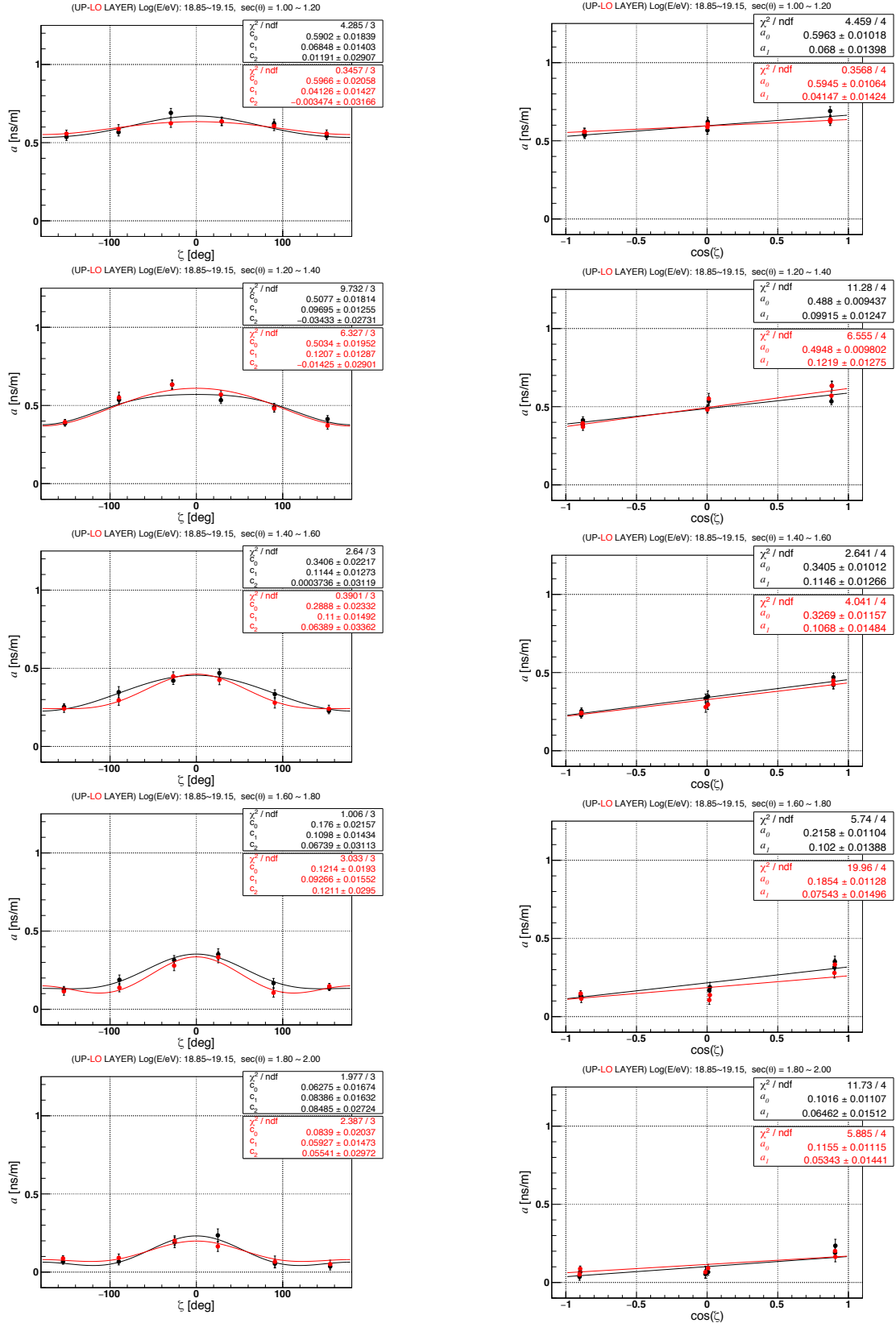


FIGURE 6.23: Thickness parameter a as function of ζ (left plot) and $\cos\zeta$ (right plot) for various $\sec\theta$ for the lower energy interval $10^{18.85} - 10^{19.15}$ eV. Top to bottom for intervals of $\sec\theta = 1.2 - 2.0$ in steps of 0.2. The results for upper layer (black mark) and lower layer (red marks).

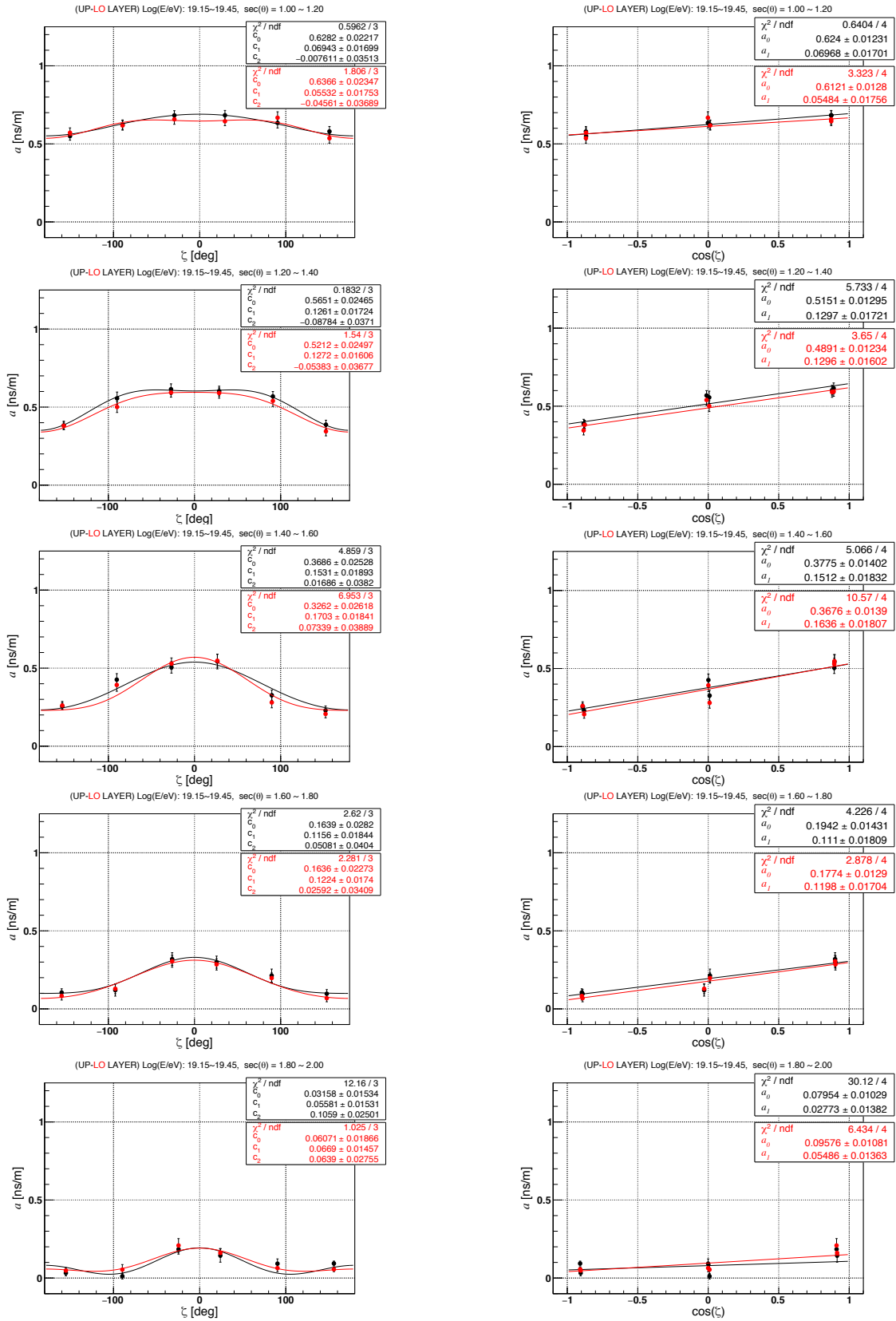


FIGURE 6.24: Thickness parameter a as function of ζ (left plot) and $\cos\zeta$ (right plot) for various $\sec\theta$ for the lower energy interval $10^{19.15} - 10^{19.45}$ eV. Top to bottom for intervals of $\sec\theta = 1.2 - 2.0$ in steps of 0.2. The results for upper layer (black mark) and lower layer (red marks).

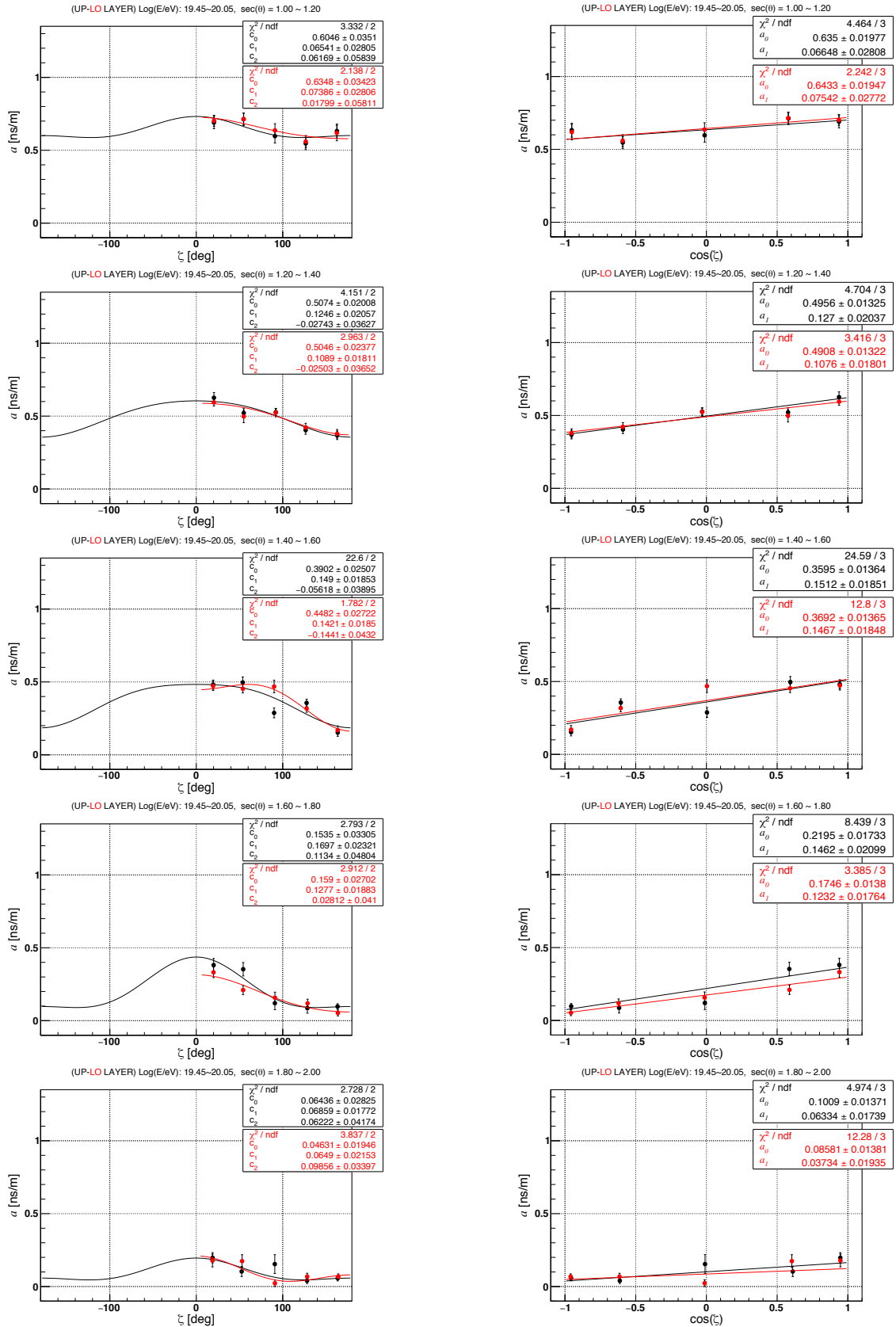


FIGURE 6.25: Thickness parameter a as function of ζ (left plot) and $\cos\zeta$ (right plot) for various $\sec\theta$ for the lower energy interval $10^{19.45} - 10^{20.05}$ eV. Top to bottom for intervals of $\sec\theta = 1.2 - 2.0$ in steps of 0.2. The results for upper layer (black mark) and lower layer (red marks).

From these results 3 main conclusions are considered:

1) The thickness of the air shower disk change according to zenith angle, e.g. for the showers close to $\theta \sim 0^\circ$ the thickness of the disk is thicker and while the zenith angle increases the thickness of shower disk become less thick in the shower front.

2) The thickness of the shower also varies along azimuthal angle in almost all cases of zenith, the early part of the thickness of shower disk is thicker than the late part of the shower, depending on the zenith angle. This variation of the thickness of shower disk may be attributed to the path of the shower axis in case of vertical showers the atmospheric depth is the shortest that travels the formed secondary particles leaving their traces in the SDs, the bulk of secondary particles are thicker. For showers with large zenith angles are affected twice. Firstly, the shower axis is longer, then, the thickness of the shower disk also decreases. Secondly, considering the inclined showers' path the early and late part of the shower, the path of secondary particles in the early is relatively short than the late path, being the late part of the shower is more affected due to the secondary particles are absorbed in the atmosphere. Thus, this asymmetry is formed along to the zeta angle.

3) The thickness of the shower disk also changes for different energies, the thickness of shower disk increases when energies are higher as it was shown in the last Figures. But the tendency of asymmetry along zeta angle is observed in any energy.

6.6 Summary of thickness dependence on zeta angle

The next Figures 6.26 show a summary of the results presented in Section 6.5.1, the thickness parameters a as function of azimuthal angle ζ (left) and $\cos\zeta$ (right) for various bands of zenith angle and 4 intervals of energy analyzed $10^{18.60} - 10^{18.85}$ eV, $10^{18.85} - 10^{19.15}$ eV, $10^{19.15} - 10^{19.45}$ eV, and $10^{19.45} - 10^{20.05}$ eV. The lower layer results are presented by red marks.

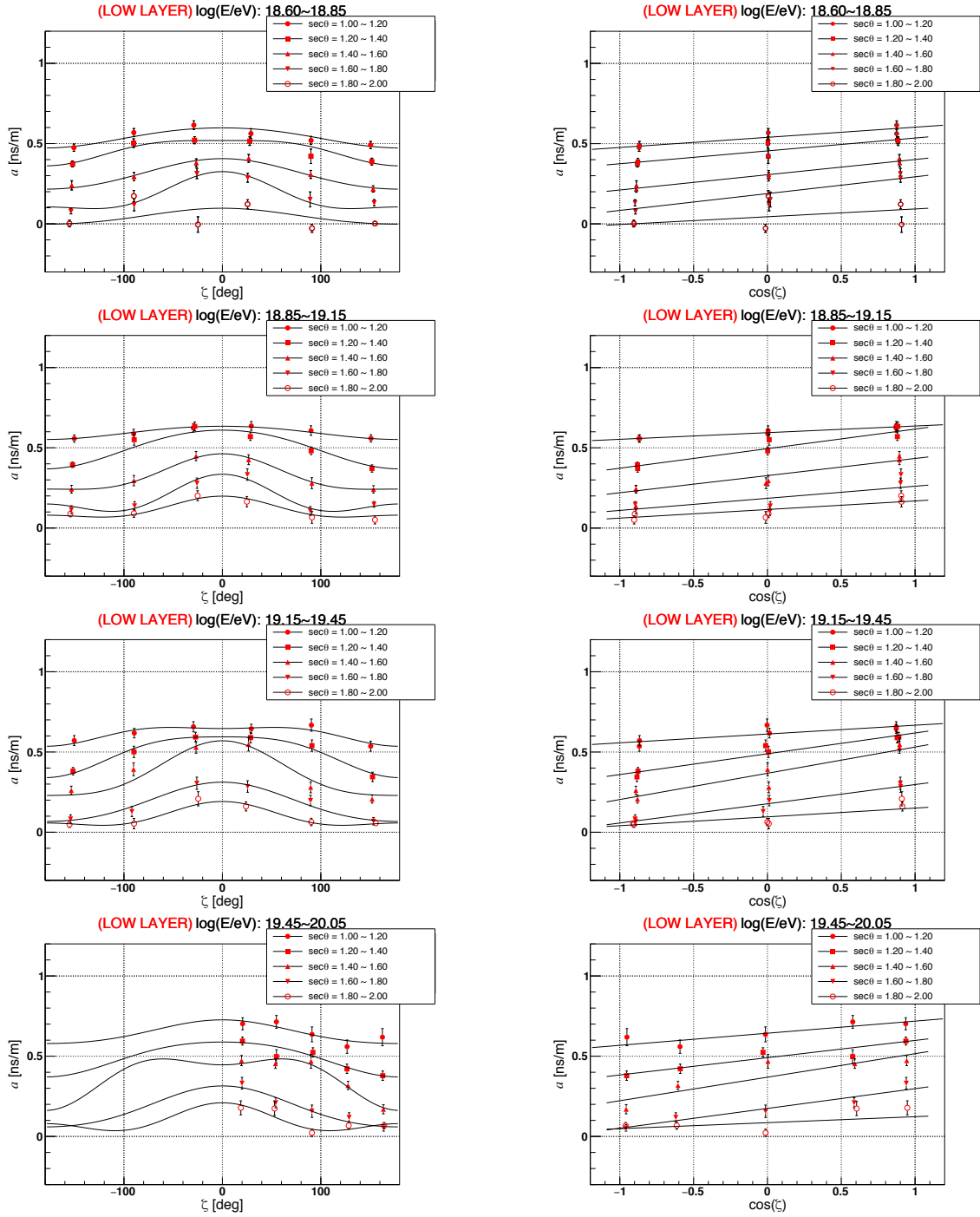


FIGURE 6.26: Thickness parameter (a) versus zeta angle (left) and $\cos\zeta$ (right) for various $\sec\theta$ in each plot. From top to bottom, 4 intervals of energy $10^{18.60} - 10^{18.85}$ eV, $10^{18.85} - 10^{19.15}$ eV, $10^{19.15} - 10^{19.45}$ eV, and $10^{19.45} - 10^{20.05}$ eV. All evaluated for linear fits in a range of 500 - 1200 m.

From the summary of the plots, it can be concluded that the thickness of the shower disk increases for higher energies and it more evident in the plots of a vs. $\cos\zeta$, the thickness in the early regions ($\cos\zeta = 1$) of shower is thicker than for

late regions of shower ($\cos\zeta = -1$) in cases for large zenith angles. These analyses through linear fits can be seen for intermediate and middle zenith angle, the slope is steeper than for showers of small zenith angles and larger zenith angles. According to the report presented by Auger group this effect of asymmetry can be caused by geometric effects till a point of inflection of zenith angle ($\theta > 30^\circ$), after this point, the attenuation is the main factor to reduce this asymmetry, by means secondary particles, electrons, and positrons are absorbed in the atmosphere and only remaining the muonic component [44].

The following Tables 6.1,6.2 and 6.3 show the numerical values obtained for 3 intervals of energy from linear fits on thickness parameter a and $\cos\zeta$, these results from lower layer signals.

$\sec(\theta)$	θ	$10^{18.85} - 10^{19.15}$ eV
1.0 - 1.2	0 - 33.6	$a = (0.59 \pm 0.01) + (0.04 \pm 0.01) \times \cos\zeta$
1.2 - 1.4	33.6 - 44.4	$a = (0.49 \pm 0.01) + (0.12 \pm 0.01) \times \cos\zeta$
1.4 - 1.6	44.4 - 51.3	$a = (0.32 \pm 0.01) + (0.11 \pm 0.01) \times \cos\zeta$
1.6 - 1.8	51.3 - 56.2	$a = (0.18 \pm 0.01) + (0.07 \pm 0.01) \times \cos\zeta$
1.8 - 2.0	56.2 - 60.0	$a = (0.11 \pm 0.01) + (0.05 \pm 0.01) \times \cos\zeta$

TABLE 6.1: Summary of function fitted in the a and $\cos\zeta$ for the energy interval $10^{18.85} - 10^{19.15}$ eV for each interval of $\sec\theta$.

$\sec(\theta)$	θ	$10^{19.15} - 10^{19.45}$ eV
1.0 - 1.2	0 - 33.6	$a = (0.61 \pm 0.01) + (0.05 \pm 0.01) \times \cos\zeta$
1.2 - 1.4	33.6 - 44.4	$a = (0.50 \pm 0.01) + (0.13 \pm 0.01) \times \cos\zeta$
1.4 - 1.6	44.4 - 51.3	$a = (0.37 \pm 0.01) + (0.16 \pm 0.01) \times \cos\zeta$
1.6 - 1.8	51.3 - 56.2	$a = (0.18 \pm 0.01) + (0.12 \pm 0.01) \times \cos\zeta$
1.8 - 2.0	56.2 - 60.0	$a = (0.09 \pm 0.01) + (0.05 \pm 0.01) \times \cos\zeta$

TABLE 6.2: Summary of function fitted in the a and $\cos\zeta$ for the energy interval $10^{19.15} - 10^{19.45}$ eV for each interval of $\sec\theta$.

$\sec(\theta)$	θ	$10^{19.45} - 10^{20.05}$ eV
1.0 - 1.2	0 - 33.6	$a = (0.65 \pm 0.01) + (0.09 \pm 0.02) \times \cos\zeta$
1.2 - 1.4	33.6 - 44.4	$a = (0.49 \pm 0.01) + (0.12 \pm 0.01) \times \cos\zeta$
1.4 - 1.6	44.4 - 51.3	$a = (0.35 \pm 0.01) + (0.16 \pm 0.01) \times \cos\zeta$
1.6 - 1.8	51.3 - 56.2	$a = (0.18 \pm 0.01) + (0.12 \pm 0.01) \times \cos\zeta$
1.8 - 2.0	56.2 - 60.0	$a = (0.09 \pm 0.01) + (0.65 \pm 0.01) \times \cos\zeta$

TABLE 6.3: Summary of function fitted in the a and $\cos\zeta$ for the energy interval $10^{19.45} - 10^{20.05}$ eV for each interval of $\sec\theta$.

6.7 Thickness of shower disk dependance on energy

It was studied the variation of thickness parameter as a function of energy measured with the lower layer FADC traces. The set of Figures 6.27 show the values of the thickness parameter a as function of energy for the different intervals of zenith angle in $\sec\theta = 1.0 - 2.0$. The top panel shows the results of the early region $|\zeta| \leq 60^\circ$ of a vs. energy. The middle panel shows the values of a vs. energy for the intermediate part of shower $120^\circ < |\zeta| < 180^\circ$. And the bottom panel is the result of a vs. energy for the late region of the shower $120^\circ \leq |\zeta| \leq 180^\circ$.

The result of the early part, the thickness of the shower disk shows a tendency to increase as energy is higher for small zenith intervals. In the case of the intermediate region of the shower, the dependence on energy not increases as in the early case. For the late case, there is no clear dependence on energy due to the low statistics presented.

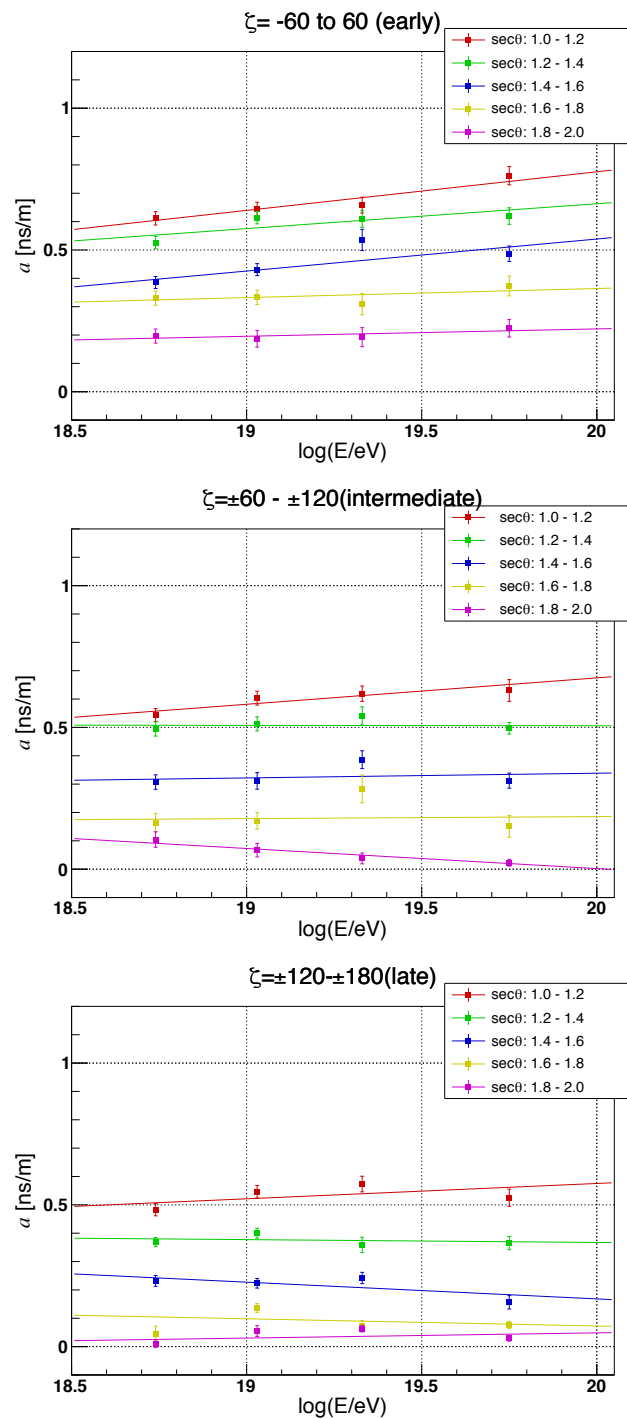


FIGURE 6.27: Thickness parameter a as a function of energy measured by lower layer signals for various $\sec\theta$ intervals. Top plot is the result of early part of shower. Middle plot is the intermediate part of shower. Bottom plot is for late part of shower results.

Chapter 7

Summary and conclusions

The work in this thesis is focused on studying the structure of the extensive air shower produced by ultra high energy cosmic rays based on the observations with the Telescope Array surface detectors data, to reveal the nature and features of extensive air showers. It was examined air shower data of TA had taken in observation from 2008 to 2019.

The time structure analysis was separated into two chapters by using two definitions through the FADC signal pulses footprinted by the event showers of UHECR.

An overview of recent progress in cosmic ray studies, especially to understand from the curvature of the shower front for different geometrical delays condition and energies. However, the general residual time function for the time delay can be expressed as a simple convolution of three residual times as it summarized in the Section 5.7. On the other hand, modeling the thickness of the shower disk by using the risetime t_R has not been measured before and now we present an analysis by using selected events showers and selected SDs FADC traces information. It was found interesting results based on the developed of extensive air shower in the atmosphere by observing the thickness of shower disk at a different part of shower by means at $\zeta = 0$, and $\zeta = \pm 180$ in the interval of core distance R of 500 to 1200 m. From these measurements it was found a certain asymmetry of the shower thickness for a different zenith angle.

In order to summarize and conclude this analysis, it is presented both analyses by using two observables of time profile: 1) the curvature of the shower front and 2) the thickness of shower disk. From the two methods used it has been proven that the extensive air shower has clearly effects on geometrical conditions such as the

zenith angle, azimuthal angle, distances to shower core and energy.

7.1 The curvature of the shower front

From each event shower data has been used to extract particle arrival time distributions with respect to the arrival time of the shower core. The typical time fluctuations along the shower plane was studied by the empirical residual time of AGASA experiment. Figures 7.1 show $\langle t_d \rangle$ and distance to core, these plots show the curvature of shower front for different intervals zenith angles, the blue area around the averaged t_d shows the fluctuation of shower-to-shower in each interval of zenith.

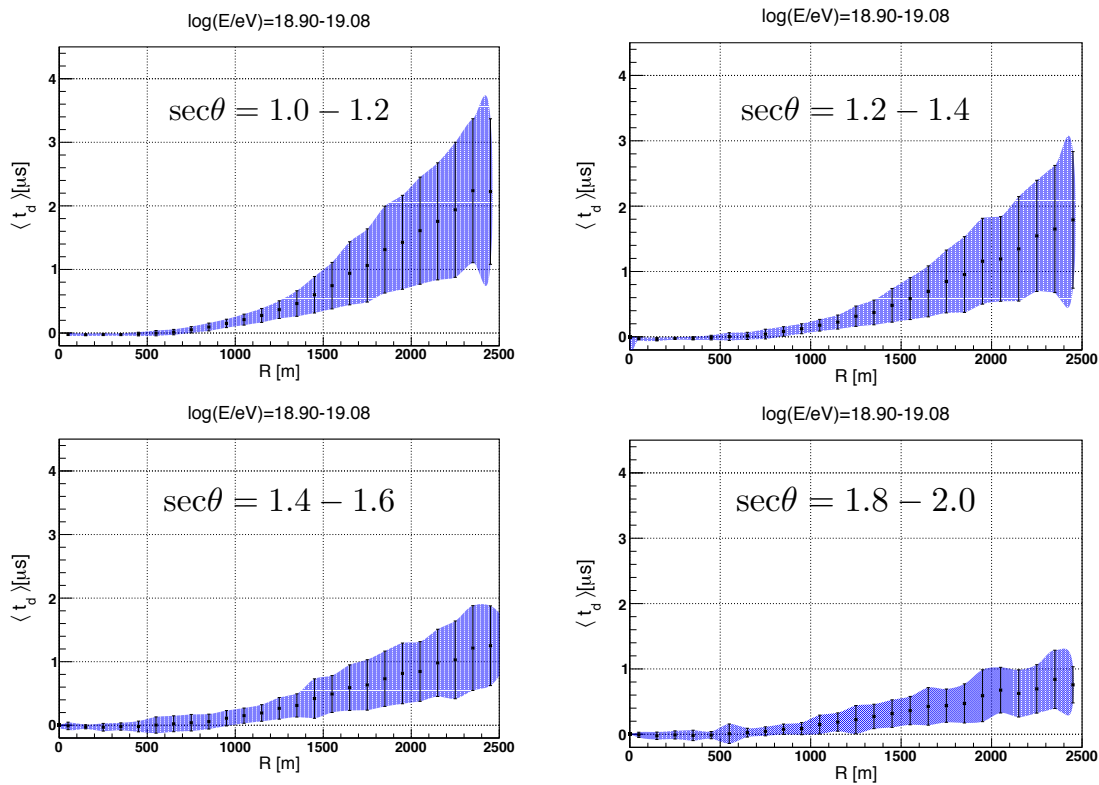


FIGURE 7.1: The evolution of the curvature of shower front for various $\sec\theta$ in lower energy interval of $10^{18.90} - 10^{19.08}$ eV. The area of curvature shows the fluctuation of all event showers in the $\sec\theta$ binned presented by the RMS in the y-error bar and the dots is the average of t_d .

For air showers with zenith angles $\theta < 33^\circ$ the radii of the curvature are less than 2500 m, for showers with zenith $\theta > 56^\circ$ the radii are extended making the curvature more wider.

7.2 Comparison of risetime investigation with other experiment

The analysis of risetime by using the definition of integrated of FADC waveform from 10% to 50% with the TA SD was investigated to study shower structure is the first time. In 2016 the Auger experiment has reported an analysis of data with the water-Cherenkov surface detector in this report is used the risetime to study the mass composition of UHECR [44]. The next set of plots 7.2 show both results from TA and Auger experiment with the t_R scatter distribution and R in the same interval of energy $10^{19.20} - 10^{19.50}$ eV and the same interval of zenith angle $42^\circ - 48^\circ$ respectively.

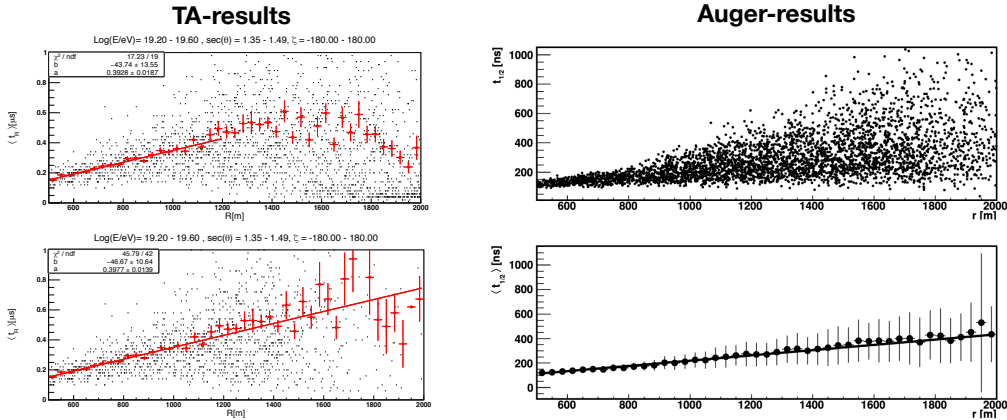


FIGURE 7.2: Left panel: Risetime calculated by TA SD. Right panel: The risetime measured by AUGER experiment by water-Cherenkov detector.

The left upper and lower Figures 7.2 show the results obtained with TA SD, the upper plot shows the t_R distribution with a loose cut selection of SD, and the lower plot shows the t_R distribution with tight cut selection by using FADC signal higher than 10 VEM. In both cases, the linearity are kept but showing more fluctuation at higher of 1500 m caused by weak signals.

The upper right plot shows the result of Auger result of t_R distribution and the lower plot shows the averaged t_R in small bins of R . In case of Auger result shows this linearity is hold in the R range of 500 to 2000 m and TA in the range of R 500 - 1200 m. Both results of TA and Auger show similar linear correlation in different intervals of R .

It can also be observed from both results the slope for TA is steeper than for Auger. The reason for this difference may be attributed to the response of the detector, TA's detector is smaller (3 m^2) than the Auger detector ($\sim 34 \text{ m}^2$) being this last more sensitive to muons.

Figures 7.3 show the results of the variation slope a , thickness parameter, respect to the azimuthal angle ζ . Figures 7.3 (left) show TA SD results for an interval of energy $10^{18.85} - 10^{19.15} \text{ eV}$ for 5 intervals of $\sec\theta$ in the steps of 0.2. Figures 7.3 (right) show the Auger results in the interval of energy $10^{18.55} - 10^{18.75} \text{ eV}$ for various intervals of zenith angle.

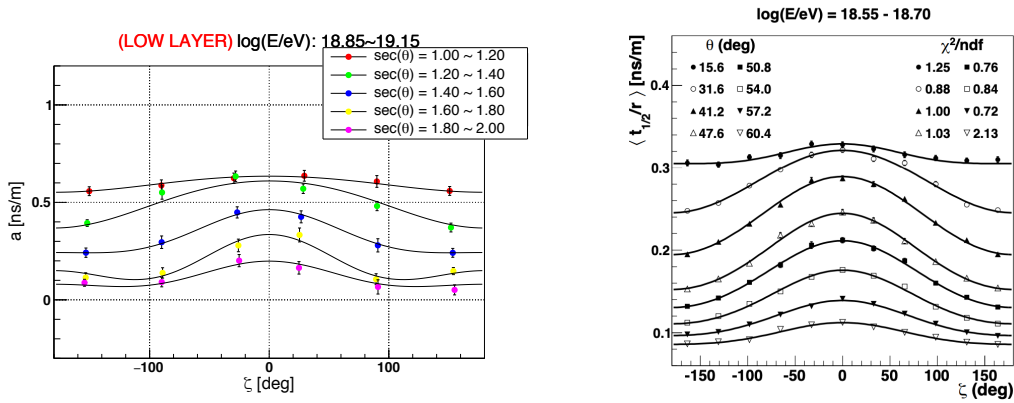


FIGURE 7.3: The asymmetry along the azimuthal angle calculated for 5 intervals in $\sec\theta$ for TA SD (left). Asymmetry measured by Auger experiment (right).

The asymmetry of the shower thickness on the azimuthal angle is observed for both experiments, and this asymmetry appear more strongly for showers with middle zenith angles.

It is important to mention that the result of Auger group, the asymmetry is observed for several intervals of zenith angles because it counts with more events of showers, attributing this to the area of Auger experiment being 4 times larger in statistics than TA data. Nevertheless, in both results can be observed the asymmetry on the azimuthal angle of ζ with same tendency.

7.3 Asymmetry in the curvature of the shower and the thickness of shower disk

We have studied the characteristics of air shower of UHECRs by using two definitions via FADC signal pulses. Firstly, we used the relative arrival time distribution information to study the curvature of the shower front with the definition of residual time t_d . Secondly, we used a certain time width of FADC signal pulse to study the thickness of the shower disk. From both analyses, we conclude that there is evidence that the air shower development in the shape of the shower curvature is not symmetric, it respects the azimuthal angle. In the case of the thickness of the shower disk, it is observed an asymmetry in the shower thickness in the early and late part of the air showers. This asymmetry observed in both cases depends on several factors of each event shower such as its geometry, zenith angle, zeta angle, distance to the core, particle density, and energy of the UHECR.

Figure 7.4 shows the zeta angle definition, which was used to analyze the air shower structure where it was found an asymmetry on ζ . Through the analyses, the shower front and thickness of shower disk were divided into 3 parts the showers denoted by "early", "intermediate" and "late". The left Figure 7.4 shows the shower plane and the zeta angle, view from side. And the right Figure shows the front view of the zeta angle, divided the zeta angles in 3 parts.

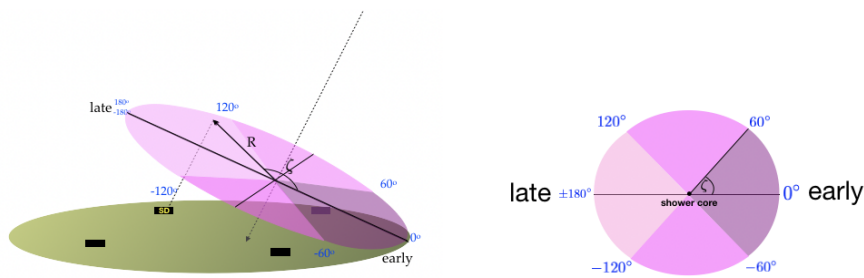


FIGURE 7.4: Side view of definition of the azimuthal angle (ζ) (left image) and the front view of the zeta angle projected on the ground. The color shows the early part of the shower (dark purple), intermediate (purple) and late triggered part of the shower (light purple).

Figures 7.5 show the analyzed results in the interval of energy $10^{19.15} - 10^{19.45}$ eV for 3 intervals of zenith angle; residual time (left plots) and rise time (right plots) distribution binned in an interval of R and the distance to core. The upper plots

are for zenith interval in $\sec\theta = 1.0 - 1.2$ ($\theta = 0^\circ - 33.6^\circ$). The second-row plots are for the middle zenith interval in $\sec\theta = 1.4 - 1.6$ ($\theta = 44.4^\circ - 51.3^\circ$). And the bottom plots are for inclined showers in $\sec\theta = 1.8 - 2.0$ ($\theta = 56.2^\circ - 60.0^\circ$).

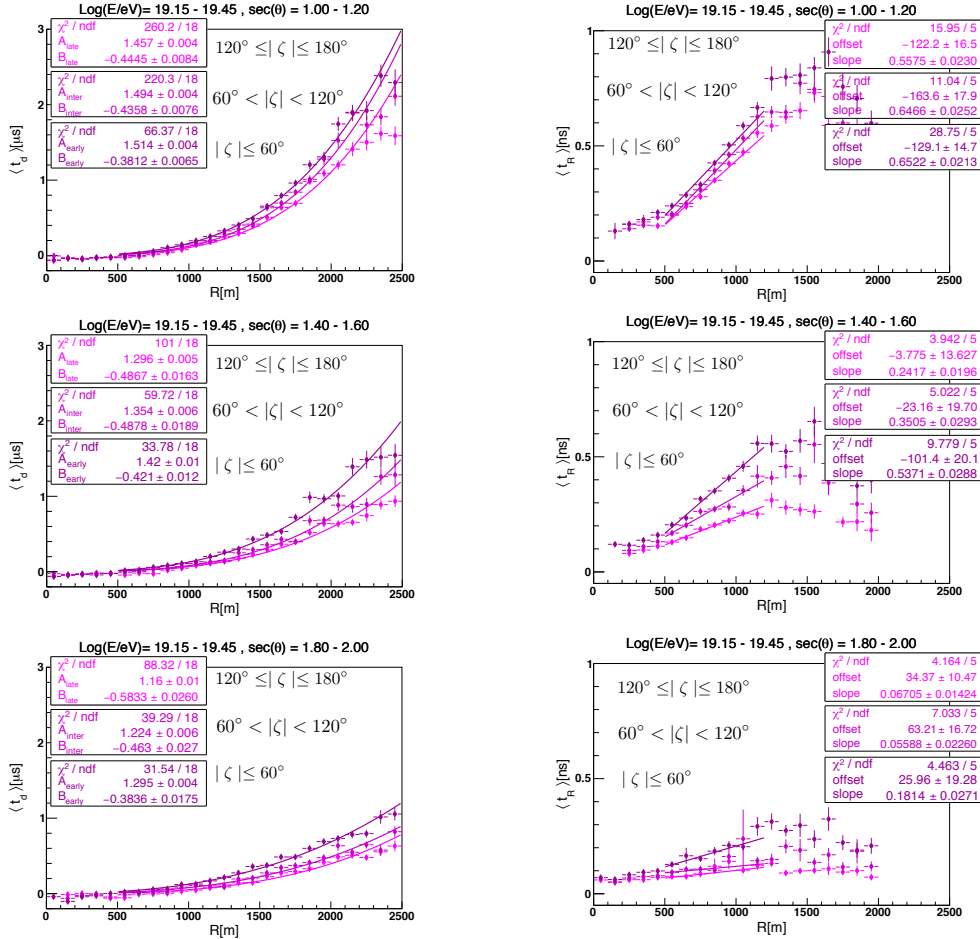


FIGURE 7.5: Residual time (left) and risetime (right) distribution as function of distance to shower axis. The early shows the dark color, and the late part of shower shows by the light color.

In each plot shows the comparison of the 3 parts of the shower denoted by the colors, from dark to light, represent the early ($|\zeta| \leq 60^\circ$), intermediate ($60^\circ < |\zeta| < 120^\circ$), and late ($120^\circ \leq |\zeta| \leq 180^\circ$) part of the showers.

It can be noted for the first interval of zenith there is not much variation, thus, showing these features is almost symmetric in the curvature and the thickness of showers. The second interval of zenith allows us to see a clear difference between the earliest and latest part of the shower. The showers of interval correspond to $\theta = 44.4^\circ - 51.3^\circ$ traveling middle atmospheric depth the early part is less affected by the atmosphere due to short length of trajectory comparing with the late part

which is quenched. Third case zenith interval, inclined showers are the longest path that traverses and these showers are dominated by weak signals. Its curvature and its thickness of the disk are reduced in case of the late part of the shower show the statistical bias due to low SDs triggered.

Figures 7.6 show the summary of the results studied for the highest energy interval $10^{19.45} - 10^{20.05}$ eV with 3 intervals of $\sec\theta$ of curvature of the shower front and the risetime distribution for early, intermediate and late part of the shower.

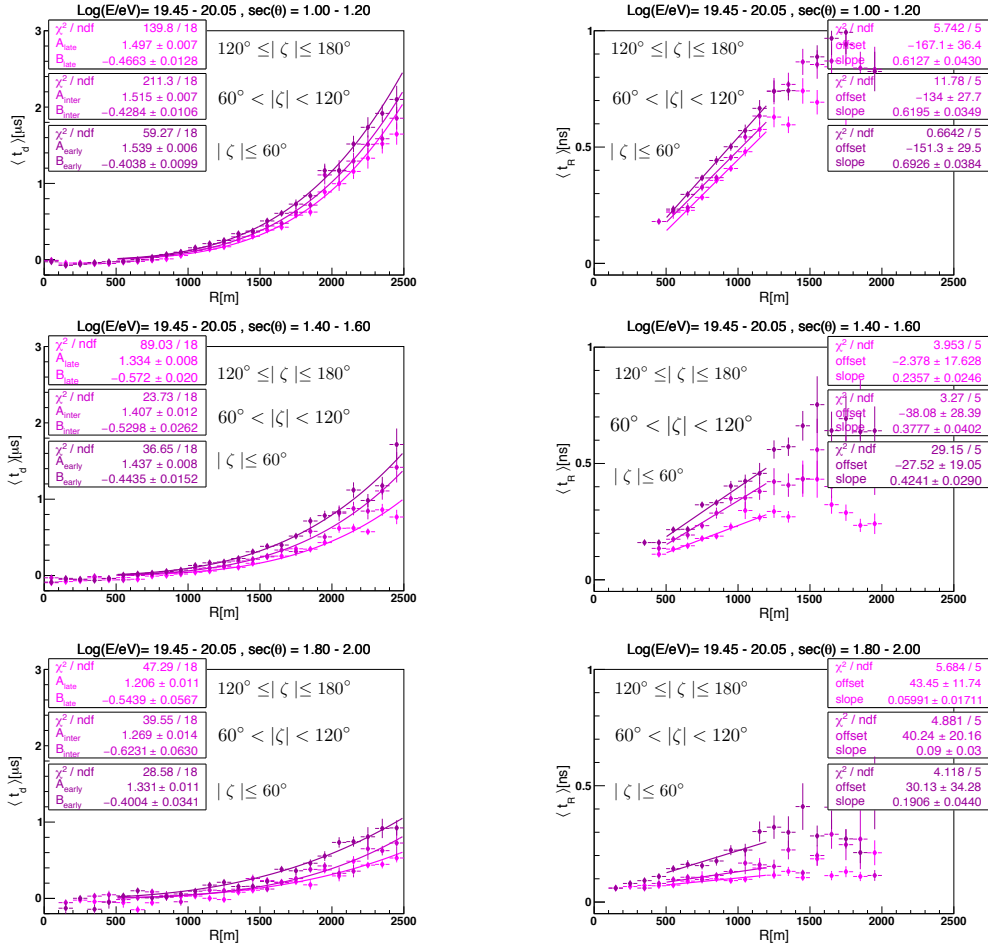


FIGURE 7.6: Averaged of residual time and risetime as function of distance to core for energy $10^{19.45} - 10^{20.05}$ eV. Left panel: residual time for early, intermediate and late part of curvature of shower. Right panel: risetime distribution for early, intermediate and late SDs triggered.

The flux of UHECR at this interval of energy is low. The feature of the curvature of shower disk shows the shower front is big comparing with low energies. And the thickness of showers also shows the average t_R can be extended to 1500 m in its

linearity. For a large zenith angle, the statistics also decreases which affects to high fluctuation between the earlies and the late part of showers.

The radius of the curvature of an extensive air shower produced by an UHECR with average of energy of 10^{19} eV is extended from 0 to 2500 m, and for the highest primary energy $\sim 10^{20}$ eV the radius goes from 0 to 3500 m. The implications of the thickness of shower disk while it is propagated in the atmosphere is affected by the atmospheric depth. This effect was observed when the larger the zenith angle, the longer the shower develops in the atmosphere and therefore the distance from the ground to the depth of the first interaction point is further away. The latest arrival particles the energy deposited in its trajectory, consequently few particles arrived comparing with the early arrival particles.

7.4 Future prospects

At present, the main tasks have been explored, the features of air showers by using a large experiment with the TA SD data. The next step to accomplish this analysis should be also extended to observe these singularities of EAS with MC data by using the latest hadronic models. Also, it is important to consider the performance of TA SD detector for a better understanding of the thickness of the air shower at a large distance of shower core to check the type particle sensitivity at beyond distance of 1200 m, especially at low energies.

During the analysis two quantities which have been measured, but it was observed large statistical bias for inclined showers and for late parts of showers, for a better EAS modeling we need to accumulate more showers data to reduce the limits of errors. The TAx4 project which is an extension in area of TA, TAx4 is currently under construction, which aims to observe the UHECR at 10^{20} eV. Therefore it will be ideal to extend this analysis including high statistics.

Further work of interest in cosmic rays astrophysics is to touch other issues related to understanding the origin of cosmic rays. There are several and important experiments to trying to investigate the nature of cosmic rays and their mechanisms of propagation in the universe. One issue is currently, the identification of sources by observing the distribution of the arrival direction of cosmic rays to find the sources of

cosmic rays. TA has also been examining event showers with UHECR by observing the northern sky and with TAx4 will have been benefited to observe more events.

Another promising experiment, to study the nature of the origin of cosmic rays, is the new experiment under construction called ALPACA (Andes Large area PArticle detector for Cosmic ray physics and astronomy) located in Bolivia with the aim to observe gamma-ray source by observing the southern sky. This project has been proposed to observe sources through gamma-ray as well as cosmic rays by using a conventional type of detection using surface detectors of plastic scintillation and water-Cherenkov detectors. The expectation of looking at sources of gamma-ray with energies higher of 100 TeV is to identify PeV accelerating objects.

Appendix A

A.1 Rise time measured by Haverah Park experiment

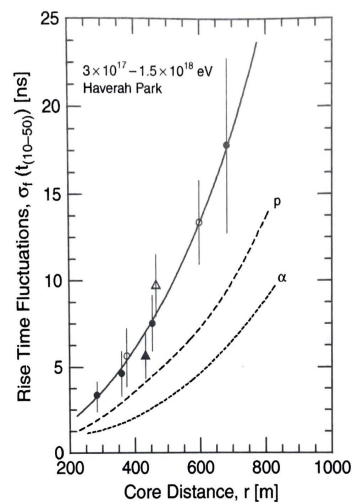


Fig. 14.45 Fluctuations, $\sigma_f(t_{10-50})$, of the rise time measurements, $t_{(10-50)}$, of the shower front as defined in the text, obtained with the Haverah Park installation versus core distance in showers of an estimated primary energy range from $3 \cdot 10^{17}$ to $1.5 \cdot 10^{18}$ eV. \bullet , \circ , Barrett et al. (1975a, b); \blacktriangle , \triangle , Watson and Wilson (1974). The *full symbols* were obtained in showers where only two individual measurements of $t_{(10-50)}$ met the required shower selection criteria, for the *open symbols* three measurements met the criteria. *Curves p and α* show results of simulations for primary protons and alpha particles, respectively (Lapikens, 1975; Hillas et al., 1971a). The *solid line* is an approximate fit to the experimental points, drawn by the author

FIGURE A.1: Rise time measured by Haverah Park experiment [90].

A.2 Angular resolution

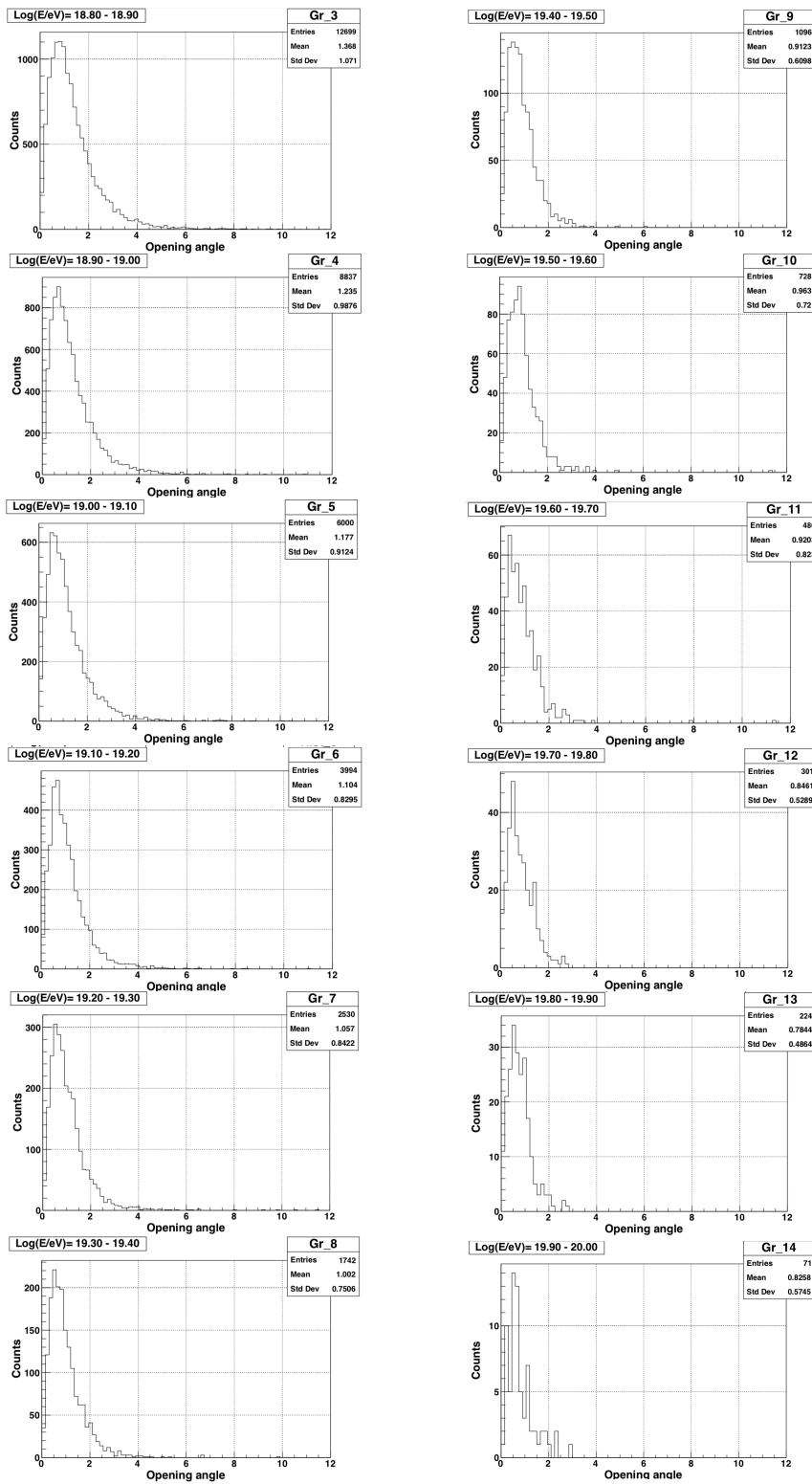


FIGURE A.2: Histograms of opening angle σ_θ for various energy bins.

A.3 Resolution of core location

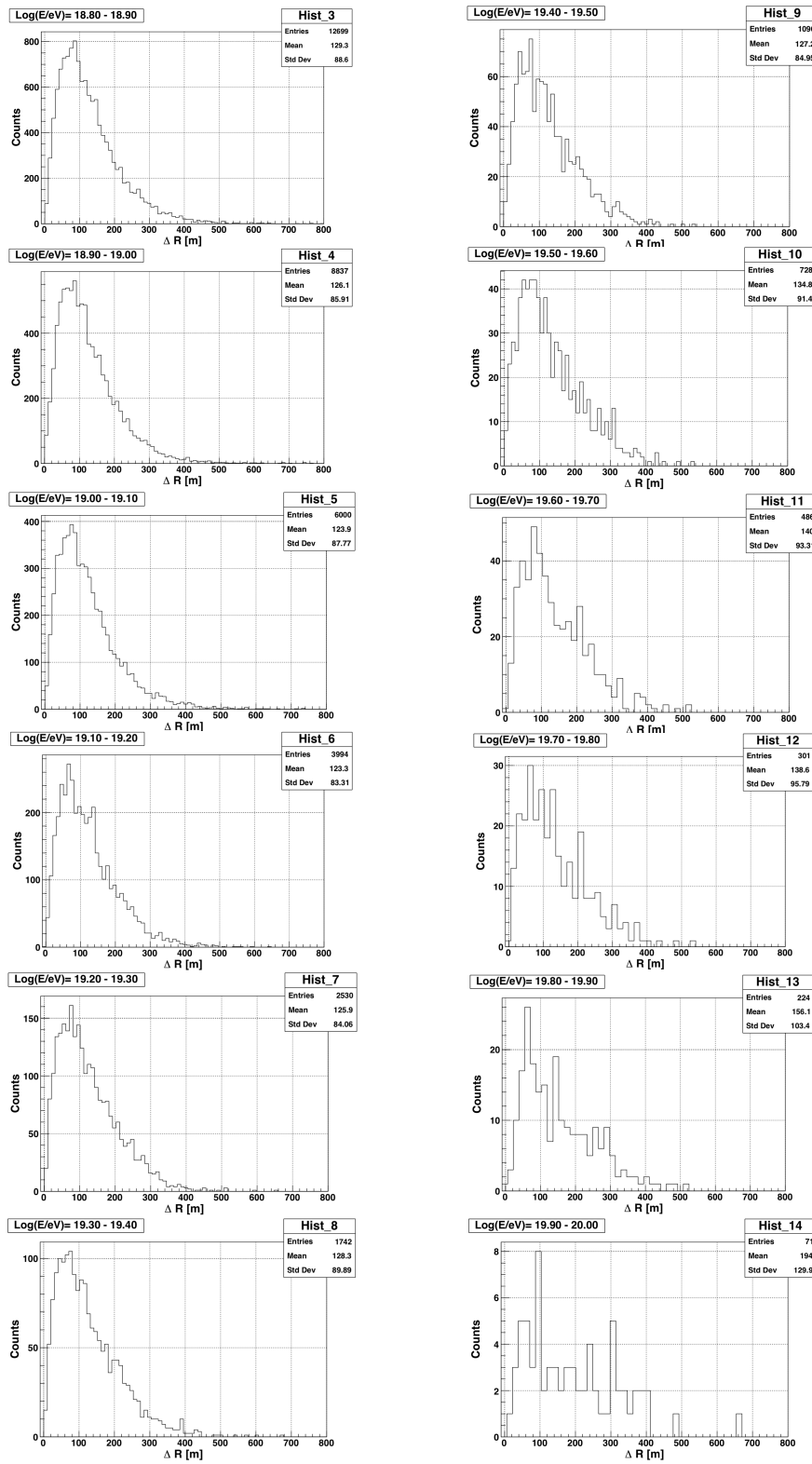


FIGURE A.3: Histograms of ΔR for various energy bins.

A.4 Residual time for averaged energy $\sim 10^{19.0}$ eV

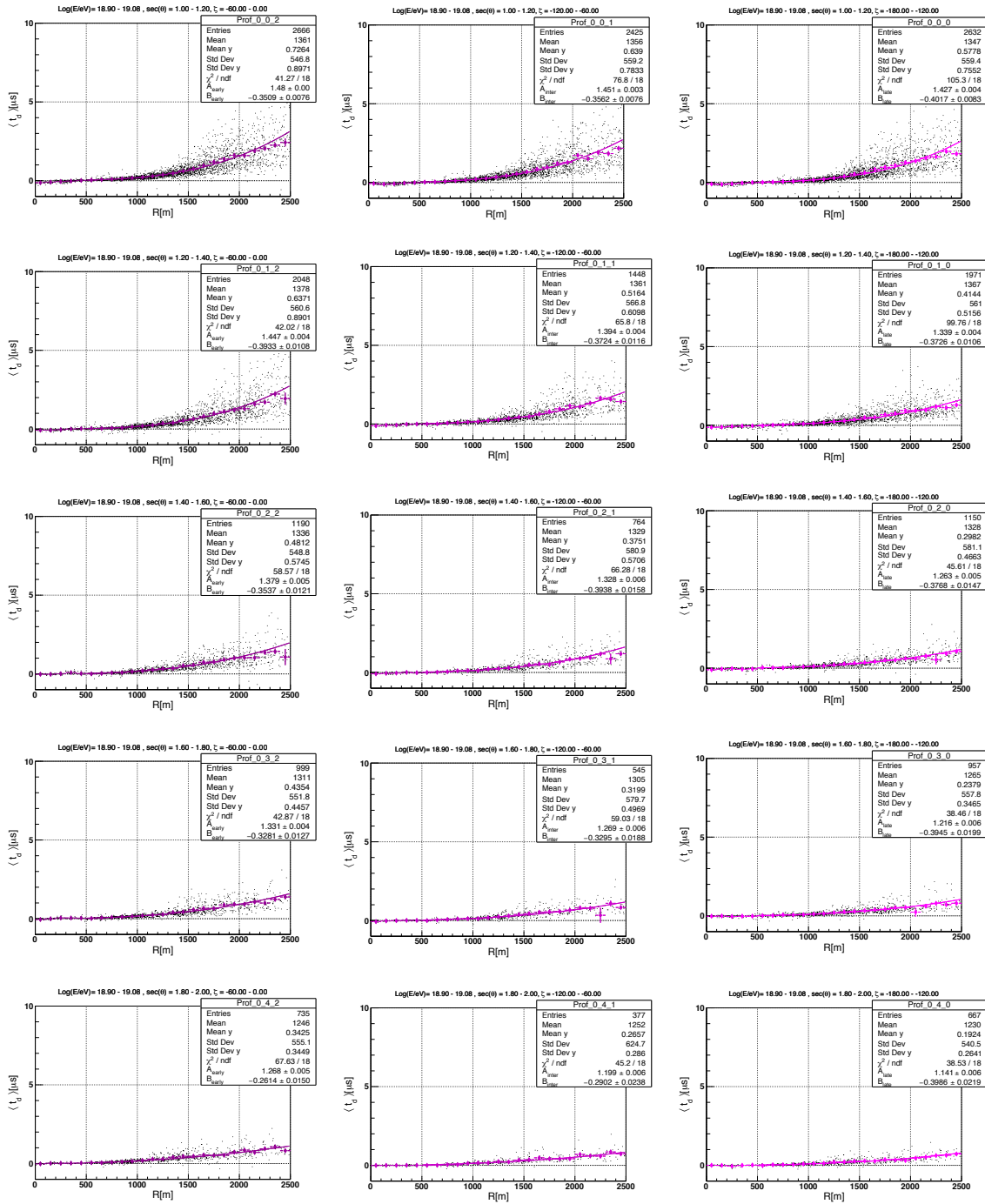


FIGURE A.4: t_d vs. R profile for energy interval $10^{18.90} - 10^{19.08}$ eV for early(left), intermediate(middle), and late(right) side showers.

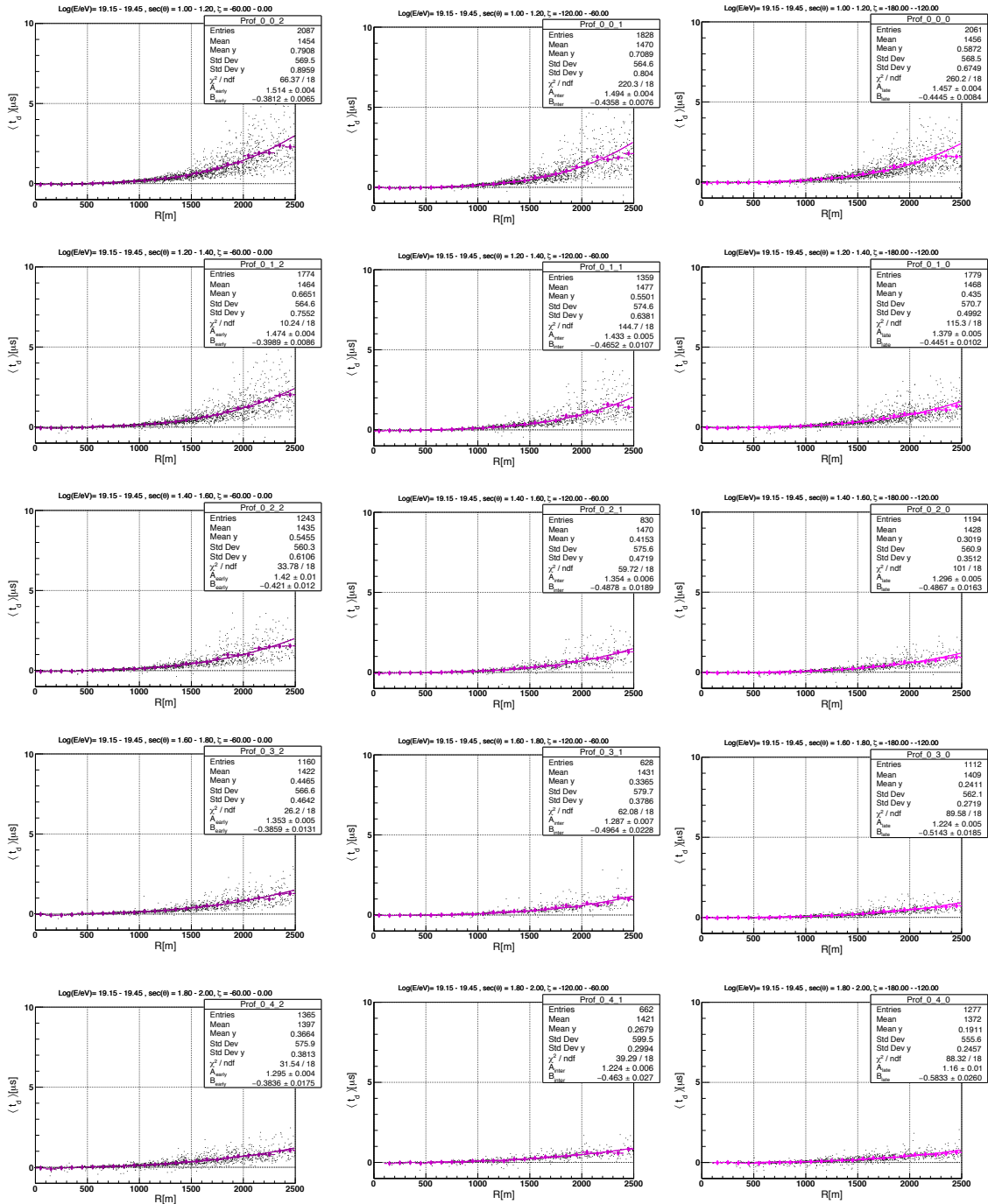
A.5 Residual time for averaged energy $\sim 10^{19.3}$ eV

FIGURE A.5: t_d vs. R profile for energy interval $10^{19.15} - 10^{19.45}$ eV for early(left), intermediate(middle), and late(right) side showers.

A.6 Residual time for averaged energy $\sim 10^{19.8}$ eV

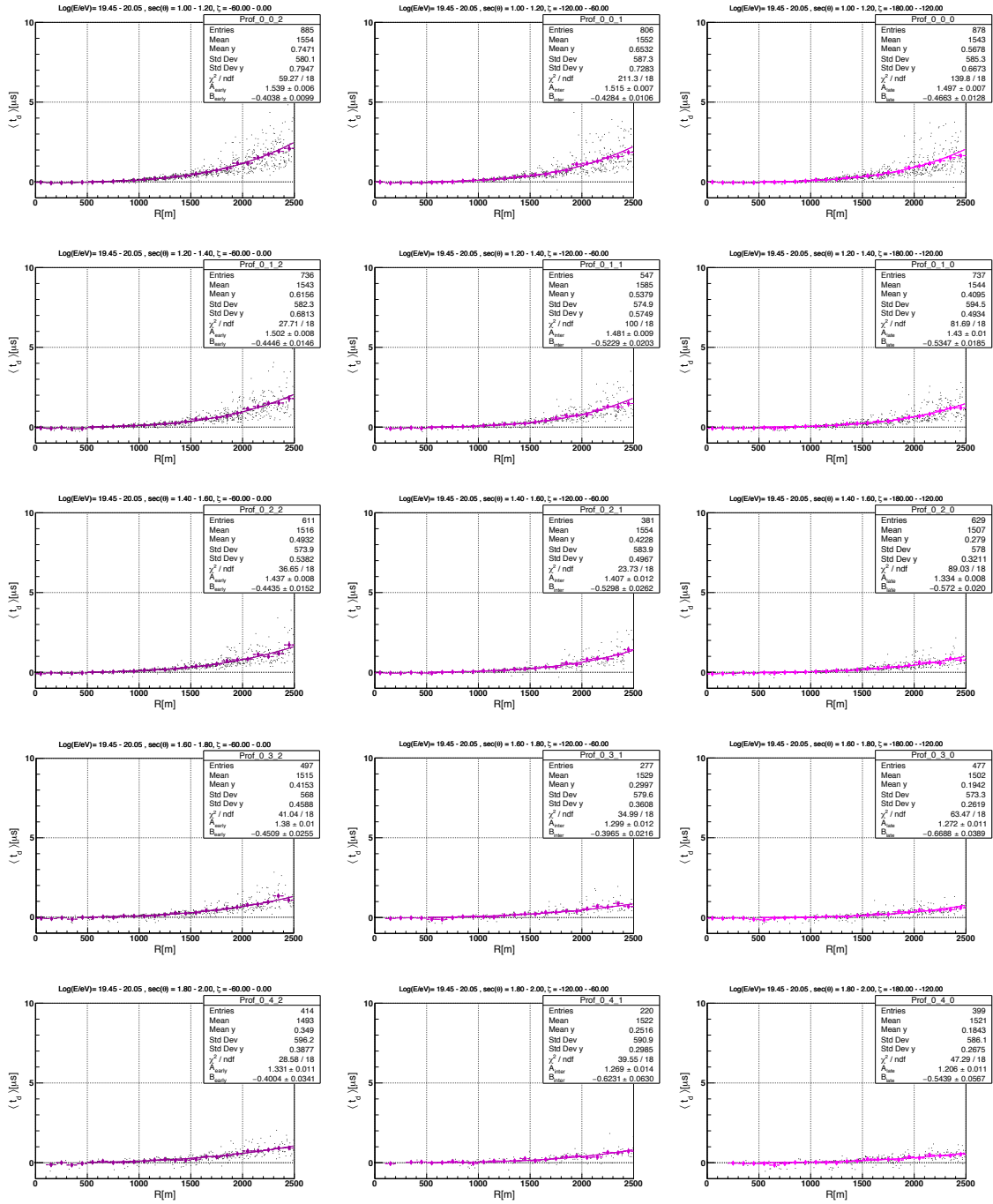


FIGURE A.6: t_d vs. R profile for energy interval $10^{19.45} - 10^{20.05}$ eV for early(left), intermediate(middle), and late(right) side showers.

A.7 Lateral distribution for averaged energy 10^{19} eV

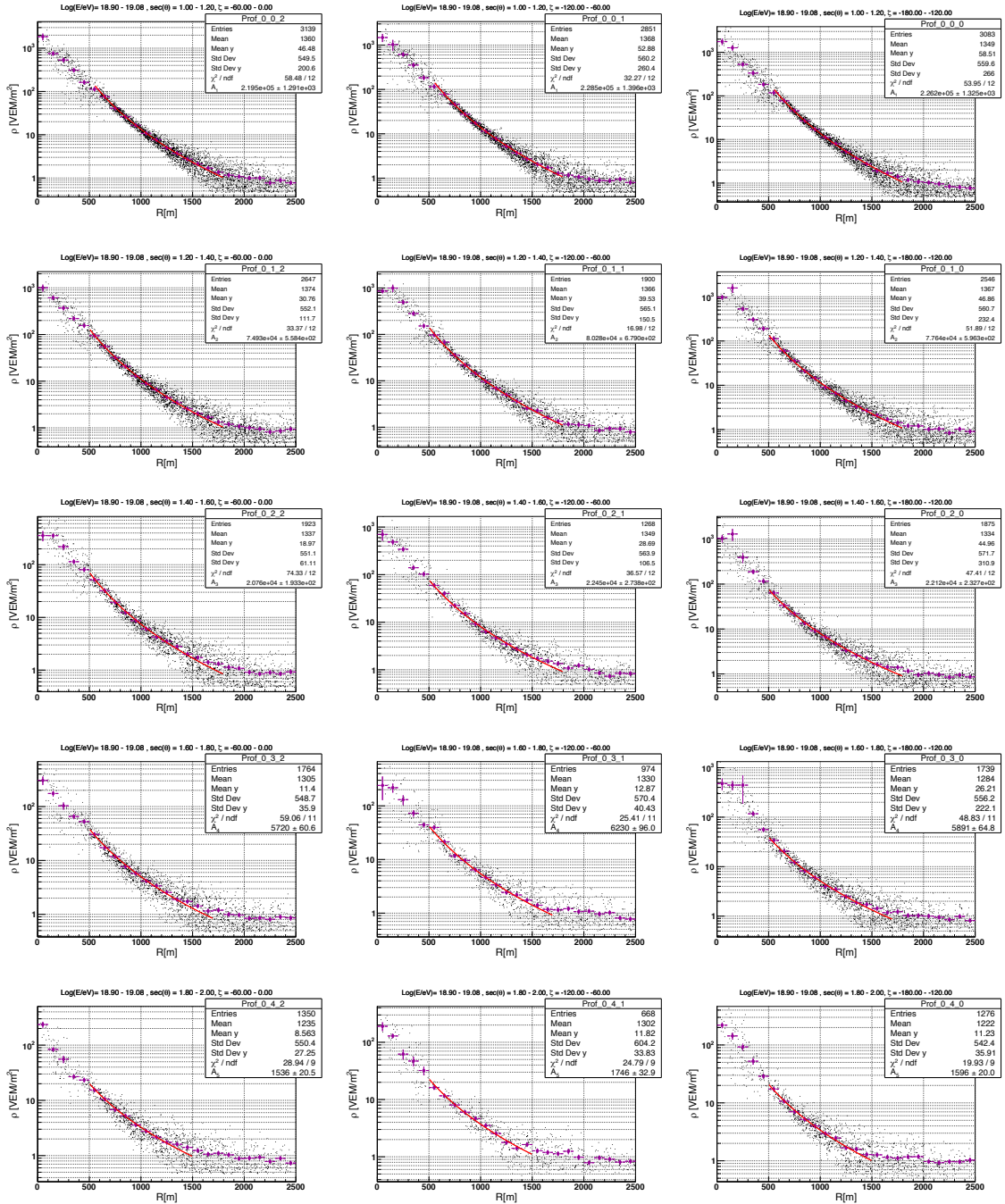


FIGURE A.7: ρ vs. R profile for energy interval $10^{18.90} - 10^{19.08}$ eV for early(left), intermediate(middle), and late(right) side showers.

A.8 t_R distribution for averaged energy $10^{19.0}$ eV

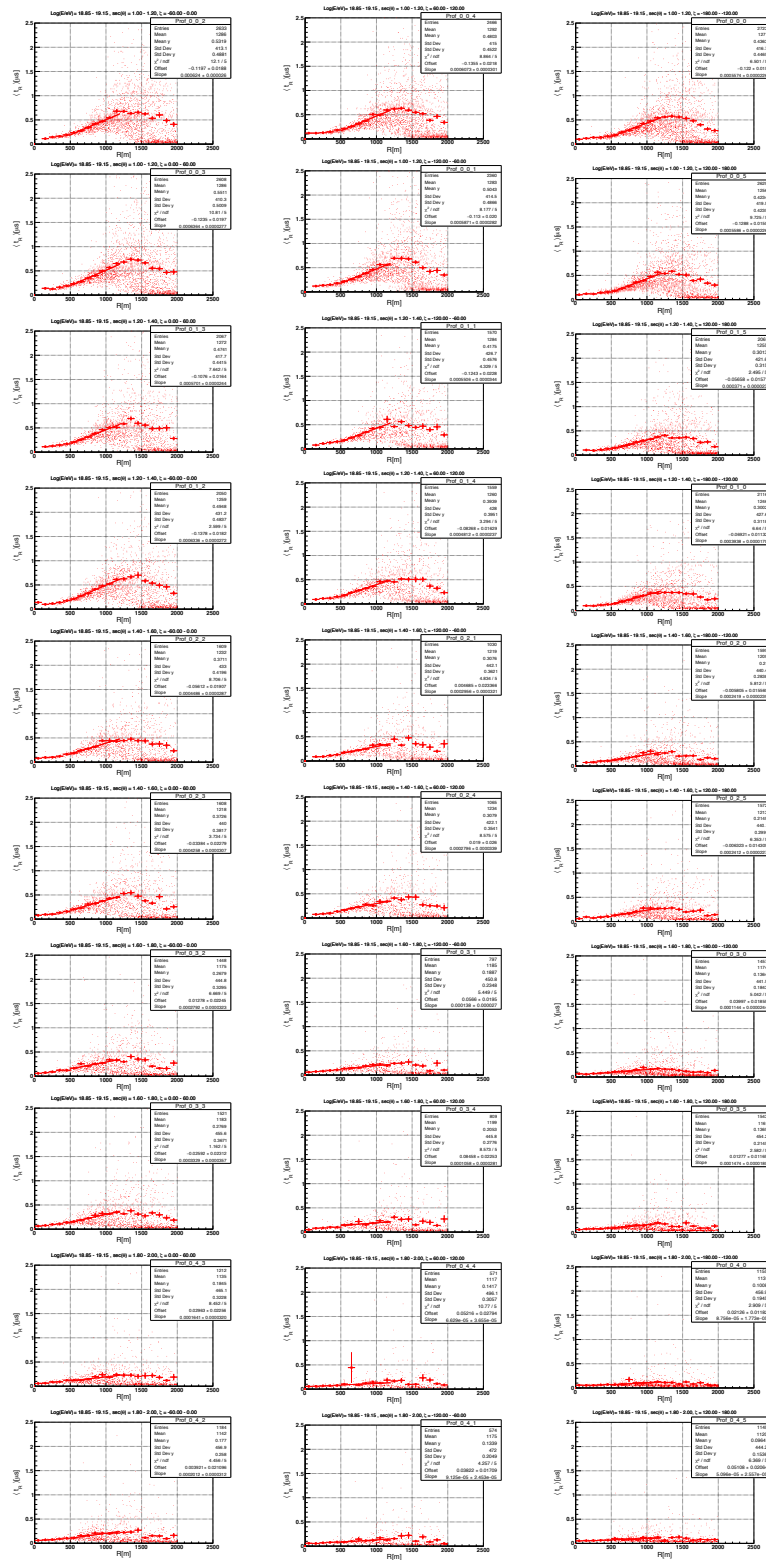


FIGURE A.8: t_R vs. R profile for energy interval $10^{18.85} - 10^{19.15}$ eV for 5 intervals of zenith angle and 6 intervals of zeta angle.

A.9 t_R distribution for averaged energy $10^{19.75}$ eV

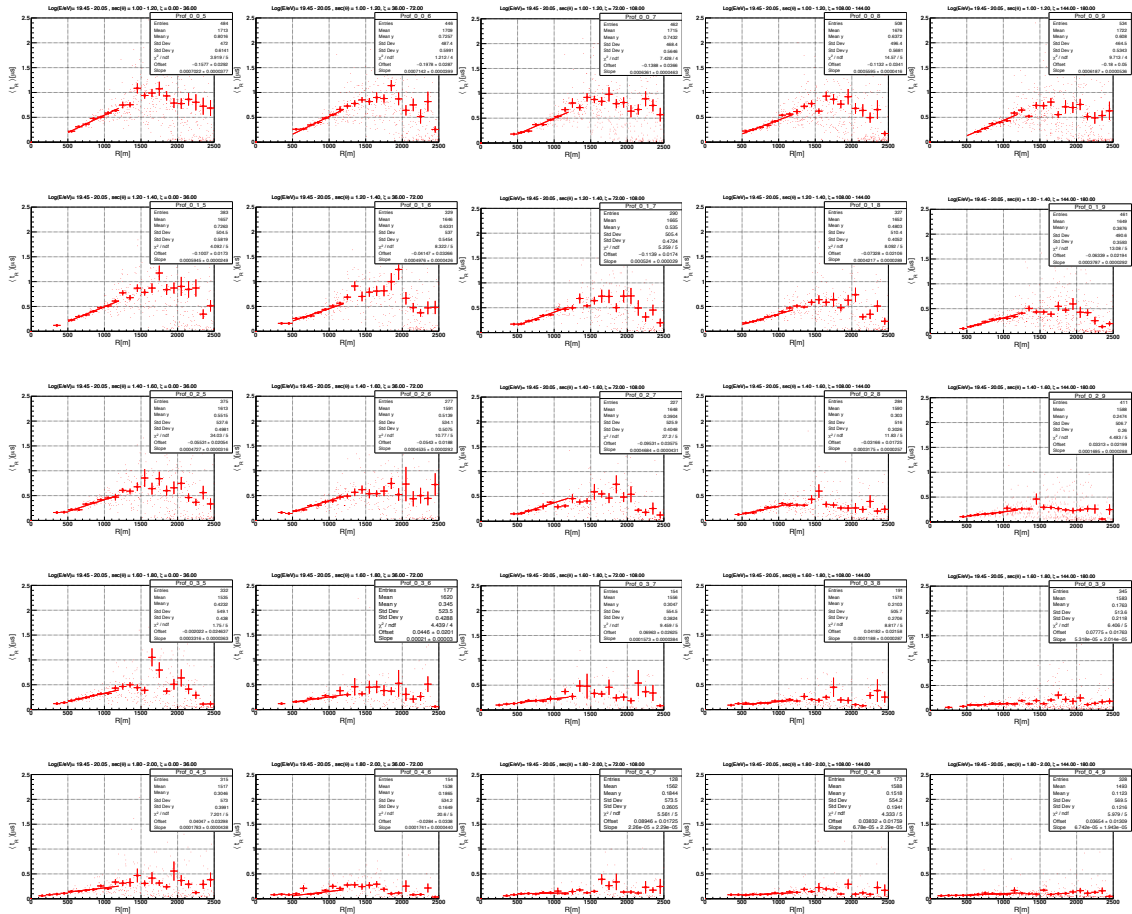


FIGURE A.9: t_R vs. R profile for energy interval $10^{19.45} - 10^{20.05}$ eV for 5 intervals of zenith angle and 5 intervals of zeta angle.

Bibliography

- [1] V. F. Hess. “Penetrating Radiation in Seven Free Ballon Flight”. In: *Z. Phys.* 13 (1912), p. 1084.
- [2] P. Auger and R. Maze. “Extensive cosmic showers in the atmosphere”. In: *Compt. Rend. Acad. Sci. (Ser. II)* 2.207 (1938), pp. 228–229.
- [3] P. A. M. Dirac. “The Quantum Theory of the Electron”. In: *proc. Roy. Soc. Lond.* II (Feb. 1928), pp. 351–361.
- [4] C. D. Anderson. “The Positive Electron”. In: *Phys. Rev.* 43 (Mar. 1933).
- [5] S. H. Neddermeyer and C. D. Anderson. “Note on the nature of Cosmic Ray Particle”. In: *Phys. Rev.* 51 (May 1937), pp. 884–886.
- [6] B. Rossi and K. Griesen. “Cosmic ray theory”. In: *Rev. Mod. Phys* 13.13 (Jan. 1941), pp. 240–309.
- [7] John Linsley. “Evidence for a primary cosmic-ray particle with energy 10^{20} eV”. In: *Phys. Rev. Lett.* 10 (Jan. 1963), pp. 146–148.
- [8] L. R. Evans. “The Large Hadron Project”. In: *LHC Project Report 53* (Sept. 1996). URL: <https://cds.cern.ch/record/313675/files/lhc-project-report-53.pdf>.
- [9] K. Greisen. “End to the Cosmic-Ray Spectrum?” In: *Phys. Rev. Lett.* 16.17 (Apr. 1966), pp. 748–750.
- [10] G. T. Zatsepin and V. A. Kuzmin. “Upper limit of the spectrum of cosmic rays”. In: *Jetp Lett.* 4 (Aug. 1966), pp. 78–80.
- [11] G. Gamow. “The Origin of Elements and the Separation of Galaxies”. In: *Phys. Rev.* (June 1948), pp. 505–506.
- [12] R. A. Alpher and R. C. Hernan. “On the Relative Abundance of the elements”. In: *Phys. Rev.* 74.12 (Dec. 1948), pp. 1737–1742.
- [13] A. A. Penzias and R. W. Wilson. “A measurement of excess antenna temperature at 4080 Mc/s”. In: *Astrophys. J.* 142 (Jan. 1965), pp. 419–421.
- [14] P. Noterdaeme et al. “The Evolution of the Cosmic Microwave Background Temperature* Measurements of T_{CMB} at high redshift from carbon monoxide excitation”. In: *Astr. and Astrophys.* (Dec. 2010).
- [15] L. Archondoqui and H. Golberg. “Footprints of super-GZK cosmic rays in the Pilliga State Forest”. In: *Phys. Lett. B* 583 (Dec. 2004), pp. 213–221.
- [16] M. I. Pravdin et al. “Energy Spectrum of Primary Cosmic Rays in the Energy Region of 10^{17} - 10^{20} eV by Yakutsk Array Data”. In: *ICRC, Lodz* 28.31 (Jan. 2009), p. 389.
- [17] A. Bunner. “Cosmic Ray Detection by Atmospheric fluorescence NYO-3038”. In: *Doctoral Thesis* (Feb. 1967).
- [18] K. Shinozaki and M. Teshima. “AGASA results”. In: *Nucl. Phys. Proc. Suppl.* 136 (Jan. 2004), pp. 18–27.

- [19] M. Takeda et al. “Energy determination in the Akeno Giant Air Shower Array experiment”. In: *Astroparticle Physics* 19 (Sept. 2003), pp. 447–462.
- [20] R.U. Abbasi et al. “First observation of the greisen-zapsep-in-kuzmin suppression”. In: *Phys. Rev. Lett.* 101101 (Mar. 2008), p. 101101.
- [21] M. Tanabashi et al. “2018 Review of Particle Physics”. In: *Physics Review D* 98.98 (June 2018), p. 57.
- [22] J. R. Horandel. “Models of the Knee in the Energy Spectrum of Cosmic Rays”. In: *Astropart. Phys.* 41 (Feb. 2004), pp. 241–265.
- [23] D. Ivanov et al. “Energy Spectrum measured by the Telescope Array experiment”. In: *ICRC 2019* 1 (Aug. 2019), p. 7.
- [24] M. S. Longair. *High Energy Astrophysics*. New York: Cambridge University Press, 2011, pp. 564–574.
- [25] M. Bustamante et al. “High-energy cosmic-ray acceleration”. In: *CERN Latinamerican* (Mar. 2009), pp. 533–539.
- [26] M. S. Longair. *High Energy Astrophysics*. New York: Cambridge University Press, 2011, pp. 314–317.
- [27] Vickas Joshi. “Reconstruction and Analysis of Highest Energy gamma-ray and its Application to Pulsar Wind Nebulae”. In: *PhD thesis* (2019), p. 5.
- [28] M. S. Longair. *High Energy Astrophysics*. New York: Cambridge University Press, 2011, pp. 568–572.
- [29] G. B. Gelmini. “High energy cosmic rays”. In: *Journal of Physics Conference Series* 171(1) (Mar. 2009), p. 9.
- [30] M. R. George et al. “On active galactic nuclei as sources of ultra-high energy cosmic rays”. In: *Mon. Not. R. Astron. Soc.* 388 (2008), pp. L59–L63.
- [31] R.U. Abbasi et al. “Indications of intermediate-scale anisotropy of cosmic rays with energy greater than 57 EeV in the northern sky measured with the surface detector of the telescope Array experiment”. In: *The astrophysical journal letters* 790:L21 (Aug. 2014), p. 2.
- [32] L. S. Sparke and J. S. Gallagher III. *Galaxies in the Universe*. New York: Cambridge University Press, 2007, p. 289.
- [33] A. di Matteo et al. “Investigating an angular correlation between nearby starburst galaxies and UHECRs with the Telescope Array experiment”. In: *The european physical journal conference* 210:01007 (Jan. 2019), pp. 1–5.
- [34] T. Jacobson, S. Liberati, and D. Mattingly. “Lorentz violation at high energy: Concepts, phenomena, and astrophysical constraints”. In: *Annals Phys.* 1.321 (Jan. 2006), pp. 150–196.
- [35] A. Dar. “Can Fireball Models Explain Gamma-Ray Bursts?” In: *Astrophysical journal Letters* 1 (Jan. 1998), p. L93.
- [36] A. de Rujula. “GRBs in the cannonball model: an overview”. In: *New Views on Microquasars* 1 (Jan. 2002), p. 177.
- [37] Anna Uryson. *Ultra High Energy Cosmic Rays*. New York: NOVA Science Publisher, Inc., 20, pp. 26–27.
- [38] V. A. Kuzmin and I. I. Tkachev. “Ultra-high-energy cosmic rays, superheavy long-lived particles, and matter creation after inflation”. In: *JETP LETTERS* 68.4 (Aug. 1998), pp. 271–272.
- [39] Manuel Drees. “Particle physics explanations for ultra-high energy cosmic rays”. In: *Pramana* (Feb. 2004), pp. 208–209.

- [40] M. V. S. Rao and B. V. Sreekantan. *Extensive Air Shower*. Singapore: World Scientific, 1998, p. 33.
- [41] Reinhard Schlickeiser. *Cosmic Ray Astrophysics*. Germany: Springer, 2002, p. 27.
- [42] J. Matthews. “A Heitler model of extensive air showers”. In: *Astroparticle Physics* 1.22 (Oct. 2004), pp. 387–397.
- [43] L. Cazon. “Probing High-energy hadronic interactions with Extensive Air Showers”. In: *ICRC 2019* 1 (Aug. 2019), pp. 1–16.
- [44] A. Aab et al. “Azimuthal asymmetry in the risetime of the surface detector signals of the Pierre Auger Observatory”. In: *Physical Review D* 1.93 (Apr. 2016), p. 072006.
- [45] C. Song et al. “Energy estimation of UHE cosmic rays using the atmospheric fluorescence technique”. In: *Astroparticle Physics* 14 (2000), pp. 7–13.
- [46] J. Linsley. “Spectra, anisotropies and composition of cosmic rays above 1000GeV”. In: *ICRC* (Sept. 1983), pp. 135–191.
- [47] T. K. Gaisser. *Cosmic Rays and Particle Physics*. New York: Cambridge University Press, 1990, p. 46.
- [48] K. Nakamura et al. “Review of particle physics”. In: *J.Phys.G* G37 (2010), p. 075021.
- [49] D. A. Suprun, P. W. Gorham, and J. L. Rosnera. “Synchrotron Radiation at Radio Frequencies from Cosmic Ray Air Showers”. In: *Astroparticle Physics* 1 (Nov. 2003), pp. 157–168.
- [50] R. Engel, D. Heck, and T. Pierog. *Extensive Air Showers and Hadronic Interactions at High Energy*. Annual Review of Nuclear and Particle Science, 2011, p. 470.
- [51] S. Yoshida et al. “The cosmic ray energy spectrum above 3×10^{18} eV measured by the Akeno Giant Air Shower Array”. In: *Astroparticle Physics* (Sept. 1995), pp. 105–127.
- [52] J. Linsley and L. Scarci. “Arrival Times of Air Shower Particles at Large Distances from the Axis”. In: *Phys. Rev.* 128.10 (Dec. 1962), pp. 2382–2392.
- [53] J. Linsley. “Thickness of the particle swarm in cosmic ray air showers”. In: *In NASA. Goddard Space Flight Center 19th Intern. Cosmic Ray Conf.* 7 (1985), pp. 359–362.
- [54] M. A. Lawrence, A. A. Watson, and A. A. West. “The thickness of the shower disc as observed in showers produced by primaries above 10 (19)eV”. In: *ICRC 1985* 7 (Jan. 1985), pp. 332–335.
- [55] A. A. Watson and J. G. Wilson. “Fluctuation studies of large air showers : the composition of primary cosmic ray particles of energy $E_p \sim 10^{18}$ eV”. In: *J. Phys* 7.10 (Feb. 1974), pp. 1199–1212.
- [56] <http://www.telescopearray.org/index.php/about//telescope-array>.
- [57] H. Schoorlemmer, J. Hinton, and R. Lopez-Coto. “Characteristics of extensive air showers around the energy threshold for ground-particle-based γ -ray observatories”. In: *The European Physical Journal C* 79 (May 2019), p. 427.
- [58] <http://www.telescopearray.org/index.php/about/surface-detection>.
- [59] <https://alchetron.com/Pierre-Auger-Observatory>.

- [60] <http://www.telescopearray.org/index.php/about/fluorescence-detection>.
- [61] D. R. Bergman and T. A. Stroman et al. “TA 10 Year Stereo Composition Measurement”. In: *International Cosmic Ray Conferences ICRC 2019* (Aug. 2019).
- [62] D. Gora et al. “The Pierre Auger Observatory: Review of Latest Results and Perspectives”. In: *Universe 2018* 4 (Nov. 2018).
- [63] W. Hanlon et al. “Depth of Ultra High Energy Cosmic Ray Induced Air Shower Maxima Measured by the Telescope Array Black Rock and Long Ridge FADC Fluorescence Detectors and Surface Array in Hybrid Mode”. In: *The Astrophysical Journal* 858:76 (May 2018), pp. 8–9.
- [64] W. Hanlon. *Telescope Array 10 Year Composition*. https://www.icrc2019.org/uploads/1/1/9/0/119067782/telescope_array_10_year_composition.pdf.
- [65] <https://spie.org/news/6098-searching-for-a-cosmic-ray-hotspot-with-the-telescope-array?SS0=1>.
- [66] R.U. Abbasi et al. “Air fluorescence measurements in the spectral range 300–420 nm using a 28.5 GeV electron beam”. In: *Astroparticle Physics* 29 (Jan. 2008), pp. 77–86.
- [67] M. Ave et al. “Precise measurement of the absolute fluorescence yield of the 337 nm band in atmospheric gases”. In: *Astroparticle Physics* 42:42 (Feb. 2013), pp. 90–102.
- [68] B. Shin. “Energy Scale Calibration of Ultra High Energy Cosmic Rays for the Telescope Array experiment with Electron Light Source”. In: *Doctor Thesis* (Feb. 2016), pp. 76–77.
- [69] T. Fujii. “Measurements of the Energy Spectrum and the Mass Composition of Ultra-High Energy Cosmic Rays with Telescope Array Fluorescence Detectors in Monocular Mode”. In: *Doctor Thesis* (Sept. 2012), p. 78.
- [70] T. A. Stroman et al. “The energy spectrum of ultra-high-energy cosmic rays measured by the Telescope Array FADC fluorescence detectors in monocular mode”. In: *Astroparticle Physics* 48 (June 2013), pp. 16–24.
- [71] D. Ivanov. “ENERGY SPECTRUM MEASURED BY THE TELESCOPE ARRAY SURFACE DETECTOR”. In: *Doctor Thesis* (Oct. 2012), p. 102.
- [72] T. Nonaka et al. “The surface detector array of the Telescope Array experiment”. In: *Nuclear Instruments and Methods in Physics Research A* 689 (2012), p. 2.
- [73] M. S. Longair. *High Energy Astrophysics*. New York: Cambridge University Press, 2011, p. 143.
- [74] A. Taketa et al. “Measurement of the spectrum of ultra-high energy cosmic rays by the Telescope Array Surface detector”. In: *ICRC 2009* (Sept. 1999), pp. 17–25.
- [75] R. Takeishi. “Study of muons from ultra-high energy cosmic ray air showers measured with the Telescope Array experiment”. In: *Doctoral Thesis* (Dec. 2016), p. 37.
- [76] R. Takeishi. “Study of muons from ultra-high energy cosmic ray air showers measured with the Telescope Array experiment”. In: *Doctoral Thesis* (Dec. 2016), p. 42.
- [77] D. Ivanov. “ENERGY SPECTRUM MEASURED BY THE TELESCOPE ARRAY SURFACE DETECTOR”. In: *Doctor Thesis* (Oct. 2012), p. 78.

-
- [78] M. Teshima et al. “Properties of 10^9 GeV - 10^{10} GeV Extensive Air Showers at Core Distances Between 100 m and 3000 m”. In: *Journal Physics G12* (Jan. 1986), p. 1097.
- [79] D. Ivanov. “ENERGY SPECTRUM MEASURED BY THE TELESCOPE ARRAY SURFACE DETECTOR”. In: *Doctor Thesis* (Oct. 2012), p. 101.
- [80] D. Heck et al. “CORSIKA: A Monte Carlo Code to Simulate Extensive Air Showers”. In: FZKA 6019 (1998).
- [81] S. Ostapchenko. “QGSJET-II: results for extensive air showers”. In: *Nucl. Phys. B Proc. Suppl.* 151 (2006), pp. 147–150.
- [82] B. T. Stokes et al. “A simple parallelization scheme for extensive air shower simulation”. In: *arxiv:1103.4643* (2011), pp. 1–10.
- [83] R. Takeishi. “Study of muons from ultra-high energy cosmic ray air showers measured with the Telescope Array experiment”. In: *Doctoral Thesis* (Dec. 2016), p. 55.
- [84] B. T. Stokes et al. “Dethinning extensive air shower simulations”. In: *arxiv:1104.3182* (2012), pp. 1–9.
- [85] D. Ivanov. “ENERGY SPECTRUM MEASURED BY THE TELESCOPE ARRAY SURFACE DETECTOR”. In: *Doctor Thesis* (Oct. 2012), p. 104.
- [86] D. Ivanov. “ENERGY SPECTRUM MEASURED BY THE TELESCOPE ARRAY SURFACE DETECTOR”. In: *Doctor Thesis* (Oct. 2012), pp. 103–108.
- [87] F. Kakimoto et al. “Arrival time distributions of electrons in air showers with primary energies above 10 (18)eV observed at 900m above sea level”. In: *ICRC 19 7.19* (Aug. 1985), pp. 328–331.
- [88] G. Battistoni et al. “Monte Carlo study of the arrival time distribution of particles in extensive air showers in the energy range 1-100 TeV”. In: *Astropart. Phys* 9 (Sept. 1998), pp. 277–295.
- [89] G. Agnetta et al. “Time structure of the extensive air shower front”. In: *As-troparticle Physics* 6 (Oct. 1997), pp. 301–312.
- [90] Peter K.F. Grieder. *Extensive Air Shower, Vol II*. New York: Springer, 2010, p. 775.